Numerical and Experimental Investigation of Higher Capacity Cold Formed Steel Shear Walls

by

Ghaith Abdulrahman Alshamsi

A thesis

presented to the University of Waterloo

in the fulfillment of the

thesis requirement for the degree of

Doctor of Philosophy

in

Civil Engineering

Waterloo, Ontario, Canada, 2024

© Ghaith Abdulrahman Alshamsi 2024

Examining Committee Membership

The following served on the Examining Committee for this thesis. The decision of the Examining Committee is by majority vote.

External Examiner	Dr. Colin Rogers Professor, Department of Civil Engineering, McGill University
Supervisor	Dr. Lei Xu Professor, Department of Civil & Environmental Engineering University of Waterloo
Internal Member	Dr. Wei-Chau Xie Professor, Department of Civil & Environmental Engineering University of Waterloo
Internal Member	Dr. K. Eugene Kim Assistant Professor, Department of Civil & Environmental Engineering University of Waterloo
Internal-External Examiner	Dr. Kaan Inal Professor, Department of Mechanical and Mechatronics Engineering University of Waterloo

Author's Declaration

This thesis consists of material all of which I authored or co-authored: see Statement of Contributions included in the thesis. This is a true copy of the thesis, including any required final revisions, as accepted by my examiners.

I understand that my thesis may be made electronically available to the public.

Statement of Contributions

The work presented in this report, unless otherwise specified, has been accomplished solely by the author with guidance from the supervising professor, Dr. Lei Xu. Particularly, the experimental program discussed in Chapter 3 and Chapter 4 has been conducted in collaboration with Dr. Xinmei Yao [1]. The finite element modeling assumptions and results of the concentric-sheathed shear wall as well as parts of the parametric study presented in Chapter 5 and Chapter 6 were published in [2] and [3].

Abstract

In this research project, three unique, higher-capacity cold-formed steel (CFS) shear wall configurations are proposed and examined, with the aim of extending CFS framing applications into mid-to-high rise buildings. The shear wall configurations consist of a concentric-sheathed shear wall with built-up hat section studs, a concentric-sheathed shear wall with an intermediate stud located at mid-span, and a diagonally strapped concentric sheathed shear wall with built-up hat section studs.

A preliminary, full-scale testing program was carried out in collaboration with Chongqing University that included monotonic and cyclic tests of the shear wall specimens, cyclic tests of screw connection assemblies in double shear, and coupon material tests. The test results were analyzed using the Equivalent Energy Elastic Plastic (EEEP) method and the analysis results indicate that the shear walls investigated herein attained substantially higher strengths and ductility than code approved shear walls.

Numerical non-linear shell finite element models of each specimen was established and calibrated using the experimental results. To overcome convergences issues, the explicit solver was employed. The finite element results demonstrated good correlation with the experimental results for all shear wall configurations, with the exception of the diagonally-strapped specimen. The verified numerical models were then used to conduct an extensive parametric study, where several factors such as screw spacing, stud and sheet thickness, and aspect ratio were assessed.

An analytical model for predicting the monotonic response of the concentric-sheathed wall and a simplified method for determining the axial force and bending moment demand on the

boundary studs are proposed. Both methods consider semi-rigid behaviour in the boundary frame of the shear wall and have showed good agreement with the shell finite element results, suggesting that the methods can be used for preliminary design purposes.

Acknowledgments

First and foremost, I would like to extend my warmest and sincere gratitude to my supervisor and mentor, Professor Lei Xu. Professor, your expertise, kindness and patience made finishing this research project an extremely pleasant and memorable journey.

I would also like to thank the Ministry of Education in the UAE for funding my graduate studies. Special thanks are due to Mrs. Rania Al-Haj and Mr. Mohammed Al Shamsi.

To my friends, Linbo, Ryan, Daniel, and my close friend and roommate Ahmad, thank you for all your help.

And last but most definitely not least, I would like to thank my wonderful family for their unconditional love. Mom, Dad, and Nawary, this work would not have been possible without your constant encouragement and endless support.

Table of Contents

List of Figures xii

List of Tables xix

Chapter 1: Introduction 1

1.1 Background 1
1.2 Problem Statement 2
1.3 Objectives and Scope 4
1.4 Organization of Thesis 5

Chapter 2: Literature Review 7

2.1 Introduction 7
2.2 Hot-rolled Special Plate Shear Walls (SPSW) 7
2.3 Conventional Cold-Formed Steel (CFS) Shear Walls 14
2.4 Higher-Capacity Cold-Formed Steel Shear Wall 19
2.5 Numerical Studies on CFS Shear Walls 24
2.6 Semi-Rigid Connections in Steel Frames 28

Chapter 3: Preliminary Testing Program 32

3.1 Introduction 32
3.2 Shear Wall Specimen Configuration 33
3.3 Test Frame Apparatus and Cyclic Loading Protocol 44
3.4 Data Acquisition 46
3.5 Test Observations and Failure Modes 47
3.5.1 Monotonic Test (specimen GD-06). 48
3.5.2 Cyclic Test (concentric-sheathed specimen, GD-19 & C-SW-2). 51
3.5.3 Cyclic Test (diagonally strapped specimen, GD-10). 57
3.6 Connection Tests in Double Shear 60
3.7 Coupon Material Tests 63

Chapter 4: Analysis and Interpretation of Test Results 64

4.1 Introduction 64
4.2 Hysteretic Behaviour 64
4.2.1 Base Shear versus Lateral Drift Curves 64
4.2.2 Energy Dissipation 69
4.2.3 Cyclic Stiffness Degradation 71
4.3 Test Analysis by the EEEP Method 72
4.4 Comparison and Discussion of Results 79
4.5 Connection Test Results 82
4.6 Concluding Remarks 84
Chapter 5: Finite Element Modeling 85
5.1 Introduction 85
5.2 Implicit Solution using ABAQUS/Standard 87
5.3 Initial Model Details 89
5.4 Finite Element Analysis using Explicit Dynamics 92
5.4.1 Determining a Stable Time Step for Explicit Dynamics 93
5.4.2 Obtaining a Quasi-static solution with ABAQUS/Explicit 95
5.4.3 Validating a Quasi-static solution with ABAQUS/Explicit 96
5.5 Explicit Finite Element Model Details 98
5.5.1 Element Selection and Mesh Details 98
5.5.2 Boundary Conditions 102
5.5.3 Material Properties and Constitutive Material Modelling 104
5.5.4 Screw Modelling 110
5.5.5 Geometric Imperfections and Residual Stresses 113
5.6 Verification of Benchmark Finite Element Models 114
5.6.1 Monotonic Finite Element Analysis of Specimen GD-06. 115
5.6.2 Cyclic Finite Element Analysis of Specimens GD-19 & C-SW-2. 122
5.6.3 Cyclic Finite Element Analysis of Specimen GD-10. 132
5.7 Concluding Remarks 136
Chapter 6: Parametric Study 138
6.1 Introduction 138

6.2 Framing Thickness 139
6.3 Sheathing Thickness 143
6.4 Strap Thickness 149
6.5 Screw Spacing 150
6.6 Aspect Ratio 158
6.7 Construction Details 167
6.7.1 Sigma-Stiffened Studs 167
6.7.2 Hold-down Placement 168
6.7.3 Corrugated Sheathing 171
6.7.4 Walls with Multiple Panels 173
6.8 Concluding Remarks 175
Chapter 7: Design Procedure 177

7.1 Introduction 177
7.2 General Behaviour of Concentric-Sheathed CFS Shear Wall 178
7.3 Prediction of Shear Wall Capacity 181
7.3.1 Effective Strip Method [8]: 181
7.3.2 Modified Effective Strip Method [11], [12]: 182
7.3.3 Steel Plate Shear Walls [25]: 183
7.3.4 Concluding Remarks 183
7.4 Derivation of the Analytical Model 184
7.4.1 Introduction 184
7.4.2 Inclination Angle (α): 185
7.4.3 Height and Length of the Partial Tension Field: 188
7.4.4 Equivalent Strip Area 190
7.4.5 Analytical Model Details 192
7.4.6 Discussion of Analytical Model Results 197
7.5 Simplified Analysis 198
7.6 Summary 206
7.6.1 Analytical Method 207
7.6.2 Simplified Method 208
7.6.3 Numerical Example: 208

Chapter 8: Conclusions and Recommendations 222

8.1 Conclusions 222

8.2 Recommendations for Future Work 224

References 226

Appendices 238

Appendix A: Sample Calculations 238

A.1 Effective Strip Method [8]: 238

A.2 Modified Effective Strip Method [11], [12]: 241

A.3 Special Steel Plate Walls: 242

Appendix B: Semi-rigid Structures and Beam Design Tables [90]: 244

List of Figures

Figure 1.1: Typical CFS steel shear wall assembly, retrieved from [7] & [8]. 2

Figure 2.1: Vertical plate girder analogy (left); typical SPSW during construction (right) [17]. 8

Figure 2.2: Strip model illustration by Thorburn et al. [16]. 10

Figure 2.3: Free body diagram of the vertical boundary elements in a four-storey SPSW [24], [26]. 14

Figure 2.4: Effective Strip Model [8]. 19

Figure 2.5: Centre-sheathed wall assembly tested by [11] & [12]. Centre-sheathed wall (top left); reinforcing scheme (top right); double-sheathed wall (bottom). 21

Figure 2.6: Modified tension field width for the proposed method [6]. 24

Figure 2.7: Linear and quadratic elements with the corresponding mesh densities assessed in the study by Schafer et. al [44]. 25

Figure 2.8: Pinching4 material model [49]. 26

Figure 2.9: Semi-rigid connected beam [54]. 29

Figure 3.1 :Cold-formed steel shear wall specimens. (a) GD-06; (b) GD-10; (c) C-SW-2. 40

Figure 3.2: Structural details of specimens GD-06 & GD-19. 41

Figure 3.3: Structural details of specimen C-SW-2. 42

Figure 3.4: Structural details of specimen GD-10. 43

Figure 3.5: Damage due to eccentric placement of the sheathing [13]. 34

Figure 3.6: Sheathing pull-over (left) and screw pull-out (right) failure modes [12], [13]. 35

Figure 3.7: Screw shear damage (left); chord separation damage (right) [11]. 36

Figure 3.8: Test Frame Apparatus. 45

Figure 3.9: Loading protocol for specimens GD-19 and C-SW-2. 46

Figure 3.10: Arrangement of displacement sensors. 47

Figure 3.11: Elastic shear buckling of the sheathing for specimen GD-06. 48

Figure 3.12: Inelastic shear buckling of specimen GD-06 due to high displacements. 49

Figure 3.13: Buckling of end studs for specimen GD-06. 50

Figure 3.14: : Local buckling of the stud (left); severe inelastic buckling of the sheet and stud (right) in specimen GD-06. 50

Figure 3.15: Specimen GD-06 at the end of the monotonic test. 51

Figure 3.16: Development of cross shaped folds, specimen GD-19 (left); specimen C-SW-2 (right). 52

Figure 3.17: Permanent deformations in specimen GD-19 at a displacement level equal to 54 mm. 52

Figure 3.18:Buckling of end studs due to cyclic loading, specimen GD-19 (left); specimen C-SW-2 (right). 53

Figure 3.19: Tension field development across the full length of the panel, specimen GD-19 (left); specimen C-SW-2 (right). 53

Figure 3.20: Development of cross shaped tears and tearing of the end studs in specimen C-SW-2 due to accumulation of plastic strain. 55

Figure 3.21: Fracture and screw bearing damage in the studs. Specimen C-SW-2 (right); specimen GD-19 (right). 56

Figure 3.22: Final failure of specimen GD-19 and specimen C-SW-2. 56

Figure 3.23: Cross shaped folds and inelastic shear buckling of the sheathing (left); buckling of the diagonal straps (right). 57
Figure 3.24: Failure modes of specimen GD-10 at high displacements. (a) Shear damage to screws; (b) Tear and fracture to end studs; (c) Bending deformations to the hold-downs. 58
Figure 3.25: Final failure of specimen GD-10. 59
Figure 3.26: Screw connection test setup and failure modes. 62
Figure 4.1: Base shear vs storey drift plot for specimen GD-06. 65
Figure 4.2: Base shear vs storey drift plot for specimen GD-19. 65
Figure 4.3: Base shear vs storey drift plot for specimen C-SW-2. 66
Figure 4.4: Base shear vs storey drift plot for specimen GD-10. 66
Figure 4.5: Isolated hysteresis loops for specimen GD-19 at different stages of loading. (a) Elastic stage; (b) Sheathing post-buckling stage; (c) End studs post-buckling stage. 68
Figure 4.6: Energy dissipated per cycle. 70
Figure 4.7: Cumulative energy absorbed by each specimen through the test. 71
Figure 4.8: Cyclic stiffness degradation for each specimen. 72
Figure 4.9: Equivalent energy elastic-plastic (EEEP) curve, retrieved from [63]. 73
Figure 4.10: EEEP curve for monotonic test (GD-06). 76
Figure 4.11: Backbone curves for the shear wall specimens. 76
Figure 4.12: : EEEP curves for specimens C-SW-2, GD-10, and GD-19. 77
Figure 4.13: Screw connection test results (specimen 2-3) 83
Figure 4.14: Screw connection test results (specimen 2-4) 83
Figure 5.1: Automatic stabilization scheme when instabilities are encountered. 89

Figure 5.2: Experimental versus FEM results, general static step. 91

Figure 5.3: Energy output using the general static step with automatic stabilization (monotonic). 91

Figure 5.4: Energy output using the general static step with automatic stabilization (monotonic). 92

Figure 5.5: Displacement-controlled load amplitude definition using a smooth step curve. 96

Figure 5.6: a) Fully integrated element; (b) Reduced integration element; (c) Hour-glass mode [77]. 100

Figure 5.7: Discretized shear wall specimen. 101

Figure 5.8: Boundary condition of shear wall models. 103

Figure 5.9: Loading model. 103

Figure 5.10: Conventional and true stress-strain diagram for sample 4-2. 105

Figure 5.11: Isotropic hardening yield surface and resulting stress-strain curve [75]. 109

Figure 5.12: Kinematic hardening displaying the rigid body translation of the yield surface, the resulting stress-strain curve and the associated Bauschinger effect [80]. 109

Figure 5.13: Screw connection test finite element model. 111

Figure 5.14: Results of the screw connection test finite element model. 112

Figure 5.15: Frequency analysis for specimen GD-06. 116

Figure 5.16: Energy history output for specimen GD-06. 116

Figure 5.17: Kinetic energy history output for the monotonic simulation. 117

Figure 5.18: Comparison between FEM and experimental results for specimen GD-06. 119

Figure 5.19: Comparison between failure modes in the experiment and the numerical model for specimen GD-06. 120
Figure 5.20: Base shear vs drift results with varying mass scaling factors. 121
Figure 5.21: Kinetic energy history output for different mass scaling values. 122
Figure 5.22: Frequency analysis for specimen C-SW-2. 123
Figure 5.23: Energy output for specimen C-SW-2. 124
Figure 5.24: Comparison between FEM and experimental results for specimen GD-19. 127
Figure 5.25: Comparison between FEM and experimental results for specimen C-SW-2..... 127
Figure 5.26: Failure modes comparison between the FEM model and experiment for specimen C-SW-2. 128
Figure 5.27: : Failure modes comparison between the FEM model and experiment for specimen C-SW-2. 129
Figure 5.28: Cyclic energy output comparisons between the experimental and numerical results for specimen GD-19. (a) The elastic stage; (b) pre-stud tearing stage; (c) post-stud tearing stage; (d) cumulative energy dissipated..... 130
Figure 5.29: Cyclic energy output comparisons between the experimental and numerical results for specimen C-SW-2. (a) The elastic stage; (b) pre-stud tearing stage; (c) post-stud tearing stage; (d) cumulative energy dissipated..... 131
Figure 5.30: Comparison between FEM and experimental results for specimen GD-10. 132
Figure 5.31: Failure modes comparison between the FEM model and experiment for specimen GD-10..... 134

Figure 5.32: Cyclic energy output comparisons between the experimental and numerical results for specimen GD-10. 135

Figure 6.1: Comparison between different framing sizes for specimen GD-06. 139

Figure 6.2: Comparison between different framing sizes for specimen C-SW-2. 140

Figure 6.3: Comparison between different framing sizes for specimen GD-10. 140

Figure 6.4: Variation of peak load vs. moment of inertia (major axis bending). 143

Figure 6.5: Comparison between different sheathing sizes for specimen GD-06. 144

Figure 6.6: Comparison between different sheathing sizes for specimen C-SW-2. 145

Figure 6.7: Comparison between different sheathing sizes for specimen GD-10. 145

Figure 6.8: Variation of peak load vs. sheathing thickness. 147

Figure 6.9: Development of tension field under different framing to sheathing ratios. (a) $\beta = 0.55$; (b) $\beta = 0.32$ (benchmark); (c) $\beta = 0.2$; (d) $\beta = 0.19$. 148

Figure 6.10: Comparison between different bracing sizes for specimen GD-10. 150

Figure 6.11: Variation of peak load vs. bracing thickness. 150

Figure 6.12: FEM results using different screw spacing for specimen GD-06. 152

Figure 6.13: FEM results using different screw spacing for specimen C-SW-2. 152

Figure 6.14: FEM results using different screw spacing for specimen GD-10. 153

Figure 6.15: Effect of aspect ratio on the behaviour of specimen GD-06. 158

Figure 6.16: Influence on varying the screw spacing for the narrow configuration of specimen GD-19. (a) Monotonic; (b) Cyclic; (c) Energy absorption. 162

Figure 6.17: Influence on varying the screw spacing for the wide configuration of specimen GD-19. (a) Monotonic; (b) Cyclic; (c) Energy absorption. 163

Figure 6.18: Influence on varying the screw spacing for the narrow configuration of specimen C-SW-2. (a) Monotonic; (b) Cyclic; (c) Energy absorption. 164

Figure 6.19: Influence on varying the screw spacing for the wide configuration of specimen C-SW-2. (a) Monotonic; (b) Cyclic; (c) Energy absorption. 165

Figure 6.20: Sigma-stiffened end studs. 167

Figure 6.21: Cyclic analysis using sigma-stiffened studs. 168

Figure 6.22: Deformed shape comparison between benchmark model (left) and model with both sides of the studs (right). 170

Figure 6.23: Cyclic analysis using hold-downs on both sides of the studs. 170

Figure 6.24: Monotonic analysis using corrugated sheathing as infill panel. 172

Figure 6.25: Deformed shape of wall models with corrugated sheathing. 172

Figure 6.26: Monotonic analyses of multi-panel walls with different mid-span sheathing connections 173

Figure 6.27: Stress contour plots for the multi-panel walls. (a) Cut-off wall; (b) continuous wall. 174

List of Tables

Table 1: Test Matrix. 39

Table 2: Screw connection test schedule. 61

Table 3: Coupon material test results. 63

Table 4: EEEP design parameters....78

Table 5: Energy dissipated and design shear flow values. 78

Table 6: Design parameters for the screw connection test. 82

Table 7: Summary of input parameters for the explicit numerical analyses. 136

Table 8: Summary of experimental and numerical results. 136

Table 9: Effects of varying the thickness of the framing members. 154

Table 10: Effects of varying the thickness of the sheathing.....155

Table 11: Effects of varying the spacing of the screws. 156

Table 12: Effects of varying the thickness of the bracing straps. 157

Table 13: Summary of varying the aspect ratio for specimen GD-06.....160

Table 14: Summary of varying the screw spacing for the wide and narrow configurations of specimen GD-19 & C-SW-2. 166

Table 15: Comparison of results (force values in *kN*, bending moment values in *kN.mm*).....205

Table 16: Moment distribution for the bare frame (bending moments unit are in *kN.mm*). 217

Table 17: Comparison of results (force values in *kN*, bending moment values in *kN.mm*).....221

Table 18: End-reactions of semi-rigid members.....244

Chapter 1: Introduction

1.1 Background

Owing to its high strength and stiffness, ease of transportation, non-combustibility, and high durability [4], cold-formed steel (CFS) has recently emerged as a cost-effective construction material in commercial, industrial, and residential buildings in North America. Early uses of CFS frames were limited to non-structural components such as partition walls. However, with increased demand and research from the industry, CFS framing applications have expanded to lateral force and seismic force resisting systems [5]. In particular, the high strength to weight ratio of CFS structures make it an attractive alternative for regions that are prone to seismic activity. Typical code-approved CFS lateral load systems include strap braced walls, wood sheathed shear walls, and steel sheathed walls [6]; the latter being the main focus of this research. A steel sheathed shear wall consists of boundary tracks and studs, steel sheathing, fasteners, and hold-downs [7]. In conventional construction, open C-shaped channel sections make up the boundary frame while the steel sheathing is mechanically fastened to the frame using self-tapping screws. Finally, hold-downs are installed on the boundary studs. A hold-down is the structural element of the system that resists the overturning forces and anchors the wall to the foundation using high strength bolts. The system resists lateral forces in the plane of the wall through a combination of sheathing yielding due to tension field action, and screw-to-framing bearing deformations. A conventional CFS steel sheathed shear wall is displayed in Figure 1.1.

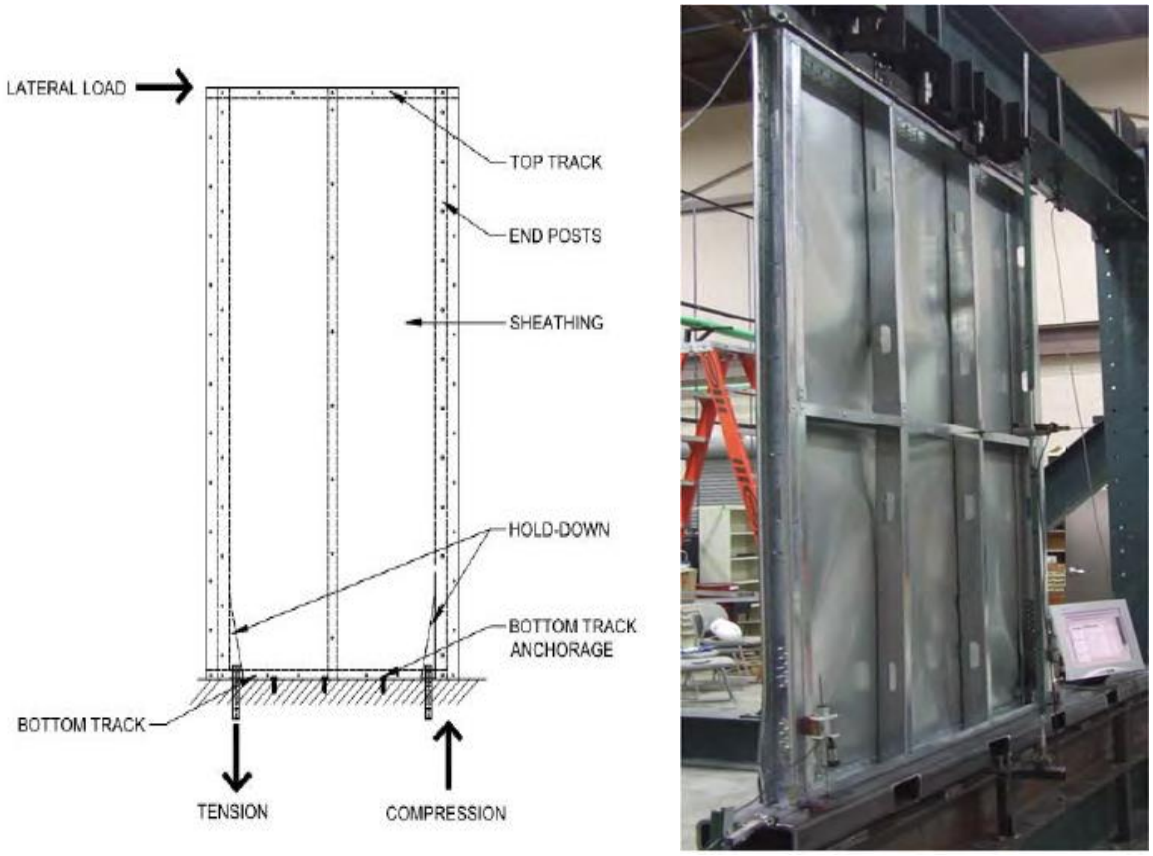


Figure 1.1: Typical CFS steel shear wall assembly, retrieved from [7] & [8].

1.2 Problem Statement

Even though the use of CFS as a seismic force resisting system (SFRS) has gained popularity in recent years, design standards still restrict the use of CFS steel sheathed shear walls to low-rise and mid-rise construction (up to 6 storeys). For instance, the National Building Code of Canada [9] limits the height of CFS structures to 20 meters. Moreover, the AISI S400-20 standard [10] offers design values for steel sheathed CFS shear walls. The nominal shear resistance and building parameters (material thickness, screw size and spacing, and aspect ratio), which are based on previous testing programs, are presented in a tabulated format [11]. Unfortunately, the available design values are suitable for low-rise buildings only. Furthermore, they are limited by member thicknesses and screw spacing.

The AISI S400 standard also permits the design of CFS shear walls through the effective strip method which was developed by Yanagi and Yu [8]. This analytical method assumes that the nominal wall resistance is provided by a partial width of the steel sheathing through tension field action [12]. While this method does offer some degree of flexibility, it is only permitted for use in the US and Mexico. Additionally, the analytical method was based on a specific wall configuration and restricted building parameters, thus confining the design of such systems to these parameters.

Based on the brief discussion presented in this section, it is evident that the current design guidelines limit the use of steel sheathed CFS walls to mid-rise construction. There is a pressing need to come up with innovative design alternatives that can attain higher forces and ductility and thus bridge the gap between CFS and hot-rolled steel seismic force resisting systems. Consequently, three novel shear wall configurations are proposed in this research, a concentrically-sheathed shear wall with built-up hat section studs, a concentrically-sheathed shear wall with an intermediate stud, and a diagonally strapped concentric sheathed shear wall with built-up hat section studs. The design of the shear walls investigated in this report are inspired by previous higher capacity cold-formed shear walls originally proposed by Professor Colin Rogers [6], [11], [12], [13]. The concentrically-sheathed wall specimens were subjected to both monotonic and cyclic loads, while the diagonally strapped specimen was subjected to cyclic loads only.

1.3 Objectives and Scope

As previously mentioned, the purpose of this research is to push the state-of-the-art and expand CFS seismic force resisting systems (SFRS) applications to mid-to-high rise buildings. The specific objectives of the study are summarized as follows:

- Propose a novel cold-formed steel high-capacity shear wall configuration that is capable of attaining higher strength and ductility.
- Carry out monotonic and cyclic loading tests on the proposed, single-storey steel sheathed shear wall specimens, this includes supplementary experiments such as connection test in double shear and coupon tests.
- Analyze the test data to come up with relevant design parameters.
- Develop and validate high fidelity shell finite element models of the wall specimens using the commercial software ABAQUS [14]. This includes monotonic and cyclic testing of the walls.
- Conduct parametric studies by assessing different building parameters (such as but not limited to sheathing thickness, aspect ratio, screw spacing) to provide efficient design alternatives.
- Propose an analytical method and a simplified, hand-based method to determine the force demand on the boundary studs of the concentric-sheathed CFS shear wall.

In North America, the process of introducing an original SFRS requires several phases. To begin with, a preliminary design concept that complies with the capacity-based design approach is proposed, followed by preliminary testing. Next, the performance of the structural system is

evaluated through a series of data analyses (such as strain data) and numerical analyses (FEM). The subsequent steps involve presenting a design procedure/design equations to aid designers in assessing the strength and serviceability of the system, as well as performing confirmatory test to validate the proposed design procedure. Finally, the appropriate seismic design provisions for the system are developed by determining the seismic force modification factors (R_d and R_o). Unfortunately, since the unforeseen COVID-19 pandemic made it impossible to travel and conduct further testing, the scope of this project does not include confirmatory laboratory experiments. The project was originally initiated at University of Waterloo where the preliminary design concept was proposed, however the preliminary testing of the wall specimens was conducted in collaboration with Chongqing University in China [1]. Hence, this study focuses on the first four steps, and confirmatory tests and development of seismic design provisions are outside the scope of this study and are recommended for future research in this field.

1.4 Organization of Thesis

Chapter 2 of the report outlines the existing literature related to steel sheathed shear walls which includes a summary of experimental, analytical, and numerical investigations. Moreover, it provides a brief introduction to hot-rolled steel plate shear walls (SPSW) and semi-rigid connections since the concepts derived from SPSW research are used as a foundation for the simplified procedure presented in chapter 7. Chapter 3 introduces the experimental setup and describes the shear wall assemblies along with supplementary test and highlights the main failure modes. The test data is analyzed subsequently in Chapter 4 on a cycle-by-cycle basis and by using the Equivalent Energy Elastic Plastic (EEEP) [15] method to extract relevant design parameters.

Chapter 5 is concerned with explaining the finite element modeling assumptions for the shear wall assemblies as well as validating benchmark FEM models against the experimental data. A series of parametric studies is then conducted on the benchmark models in chapter 6 in order to evaluate the contribution of different elements and construction details on the performance of the wall. A simplified analytical model is proposed in Chapter 7 to aid designers in determining the monotonic response of the concentric-sheathed shear wall as well as the force demand of the studs. Finally, chapter 8 summarizes the main observations and conclusions and presents recommendations for future research.

Chapter 2: Literature Review

2.1 Introduction

This chapter provides a brief overview of the literature pertaining to steel sheathed shear walls. The first section of this chapter examines relevant analytical and numerical studies related to SPSW. The subsequent section discusses the experimental work performed on conventional shear walls as well as the current analytical design methods of CFS shear walls. As previously mentioned, a conventional CFS shear wall comprises of a boundary frame made from open sections (typically C-shape sections) where the steel sheathing is fastened to one side or two sides of the frame. On the other hand, the third section discusses higher capacity steel sheathed CFS shear walls that were first proposed by the research efforts at McGill University [6], [11], [12], [13]. This configuration of shear walls makes use of built-up back-to-back C-shape sections to form the boundary frames, with the sheathing either placed on both sides of the frame or confined centrally between the built-up studs. The following section outlines previous work on numerical analyses of CFS shear walls. Finally, the chapter concludes with a brief review on semi-rigid connections in steel structures.

2.2 Hot-rolled Special Plate Shear Walls (SPSW)

A special plate shear wall (SPSW) is a structural system that is made up of a slender steel diaphragm (plate), two boundary columns (vertical boundary elements) and two boundary beams (horizontal boundary elements) [16]. The main function of an SPSW is to counter the

overturning moment and storey shear due to lateral loads. The system can be idealized as a vertical plate girder, as depicted in Figure 2.1.

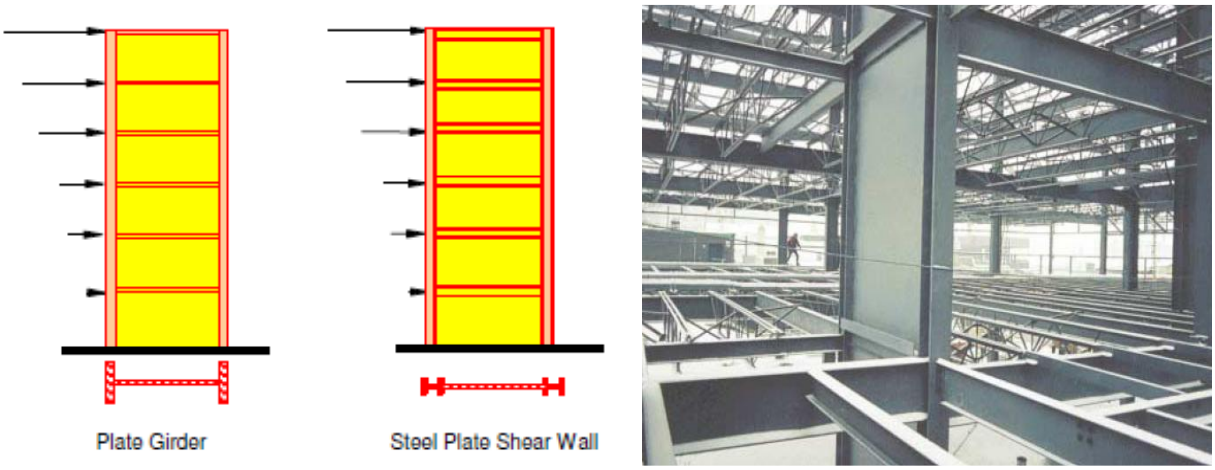


Figure 2.1: Vertical plate girder analogy (left); typical SPSW during construction (right) [17].

In Japan and North America, SPSWs have been used as the main lateral force resisting system in high-rise structures as early as the 1970's [18], even prior to their standardization. Initially, the infill plate of SPSW was heavily reinforced with stiffeners in order to prevent elastic buckling. It was later widely accepted that shear walls employing thin unstiffened plates possess considerable post-buckling strength due to tension field action, making unstiffened SPSWs an attractive alternative due to their economy. Since then, a significant amount of research work has been dedicated to unreinforced SPSW systems [19], [20], [21], [22], [23], [24], [25], [26]. One of the early efforts to quantify the behaviour of unstiffened SPSW systems is the analytical work by Thornburn et al. [19]. In this study, the authors proposed analytical models for unstiffened shear walls based on the tension field theory originally postulated by Wagner [27]. Recognizing that the compressive resistance of the plate is negligible, an analytical model was derived where the tension field of the buckled plate is replaced by a series of tension-only strips. The strips are

modelled as pinned-truss members oriented at the same inclination angle of the diagonal tensile stress in the plate. Also, individual strip members have a cross-sectional area that is equivalent to the product of the strip width and plate thickness. The number of strips was varied for a range of panel dimensions and based on plane frame analysis; it was determined that a minimum of 10 strips per panel were sufficient to represent the tension field action of the shear wall. The strip model is adopted by both CSA/CAN S16:19 [28] and AISC 341-16 [29].

To determine the angle of inclination of the tension field, Thorburn et al. [19] applied the principle of least work on a one-storey, one-bay shear wall that is bounded by infinitely rigid beams. The rationale behind this assumption is that in a multi-storey structure, the tension field for two adjacent stories will oppose each other and hence the vertical deflection of the beam can be neglected. Moreover, the derivation did not include the bending strain energy of the columns. Figure 2.2 illustrates the strip model with infinitely rigid beams, while the resulting inclination angle expression is displayed in Eq. (2.1).

A testing program was undertaken by Timler & Kulak [20] in order to substantiate the analytical method proposed by Thornburn et. al [19]. A large-scale single storey steel plate shear walls consisting of two panels was subjected to load reversals at service levels, then to a monotonic load to failure. The plate was framed with built-up members that are approximately equivalent in size and structural properties to typical hot-rolled wide flange sections. Another objective of the testing program was to investigate the development of the tension zone in the web plate and to examine the drift behaviour of the web plate under cyclic loads at service levels.

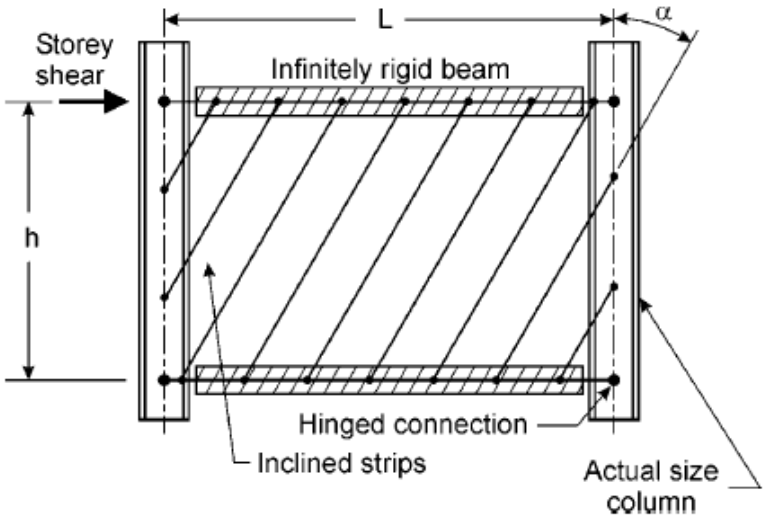


Figure 2.2: Strip model illustration by Thorburn et al. [16].

$$tan^4\alpha = \frac{1 + \frac{Lw}{2A_c}}{1 + \frac{Hw}{A_b}} \qquad \textbf{(2.1)}$$

where; α = inclination angle between the vertical and tension strips (degrees)

A_c = areas of columns (mm^2)

A_b = areas of beams (mm^2)

L = length of panel (mm)

w = thickness of the steel plate (mm)

h = height of panel (mm).

The framing members employed fully continuous connections at the interior beam-column intersection and true-hinged connections at the bottom and top levels. According to Timler &

Kulak [20], the use of fully continuous inter-storey connections greatly reduced the deflections of the web which resulted in an uncomplicated test set up.

The test specimen was set up as a simply supported deep beam with the load applied vertically at mid-span. The service cyclic load that was applied to the specimen was equivalent to h/400 or 6.25 mm. The stresses were monitored at the center of each panel at identical locations. The general stress distribution showed reasonable agreement which indicated that the load distribution throughout the plate was symmetrical. Furthermore, the inclination angle of the tension field that was retrieved from the strain readings varied between 44° and 56°. The authors also report that the axial and bending strains that are obtained from the framing members exhibited a linear relationship with the applied loading scheme.

The specimen was then incrementally loaded until a connection failure appeared. The web plate stresses at the ultimate load had a similar pattern of stress distribution as the service load stress distribution, however the stresses were in excess of the yield stress of the web plate. The strain readings and observation of the boundary frame indicate that there was a gradual decrease in stiffness beyond the elastic limit with adequate ductile behaviour until the ultimate load was reached. It is worth noting that the failure in this test consisted of the tearing in the web plate to fish plate connection rather than a failure in the framing members.

Lastly, the inclination angle equation that was derived previously by Thornburn et al. [19] was re-evaluated. Based on the stress distribution and observation made from the physical test, the authors included the bending strain energy of the columns in the energy expression, as displayed in Eq. (2.2). The proposed formula showed reasonable agreement with the inclination angle that

was measured from the experiment. In addition, it is implemented in CSA/CAN S16:19 [28] and AISC 341-16 [29].

$$\tan^4 \alpha = \frac{1 + \frac{wL}{2A_c}}{1 + wh(\frac{1}{A_b} + \frac{h^3}{360I_cL})} \quad \textbf{(2.2)}$$

where; I_c = inclination angle between the vertical and tension strips (degrees).

Behbahanifard et al. [30] conducted an extensive experimental and numerical study on multi-storey unstiffened shear walls. The experimental program consisted of the upper three storeys of a four-storey steel plate shear wall that was previously tested by Driver et al. [31]. During previous testing programs, only the lower storey showed considerable damage and plastic deformation, for that reason, the lower storey was removed along with the beam and the remaining structure was welded to a 90 mm thick base plate. The main purpose of the large-scale test was to monitor the performance of the framing members and to increase the database of steel plate shear wall tests. The specimen was subjected to 10 cycles of cyclic loading in the elastic range and 14 cycles up to the inelastic range. The authors report that even though a beam-column connection has ruptured during the test, it did not compromise the ability of the frame to resist the shear load, indicating an adequate level of redundancy. The angle of inclination was also obtained during the application of load cycles in the elastic range, though showed poor agreement when compared with the results obtained from Eq. (2.2) [20]. The justification is that

the inclination angle equation was based on simple pinned connections at the top level of the shear wall, while the testing specimen was fabricated with moment resisting connections.

A shell finite element model of the shear wall specimen was developed in order to perform a parametric study on different structural properties and geometric dimensions of the shear wall. Due to convergence issues, the explicit solver of the commercial software ABAQUS was utilized. The finite element model showed good correlation with the experimental results in terms of peak load, energy dissipated and tension field orientation, and the benchmark models were used to perform dimensional analyses on the steel plate shear wall.

Recognizing the complexity involved with constructing a uniform strip model to analyze SPSWs, Berman and Bruneau [25] proposed a capacity design method to calculate the axial force and bending moment demand in the vertical boundary columns of SPSWs. The method assumes that if the web plate undergoes uniform yielding, a simple free body diagram of the vertical boundary columns subjected web forces inclined at an angle α can be used to estimate the column's axial forces and bending moments. As displayed in Figure 2.3 below, the applied loads due to the web yielding forces on the columns (ω_{yci} and ω_{xci}) and beams (ω_{ybi} and ω_{xbi}) at each story i are as follows:

$$\omega_{yci} = 0.5F_{yp}t_{wi}\sin 2\alpha \qquad \omega_{xci} = F_{yp}t_{wi}(\sin\alpha)^2 \qquad \textbf{(2.3)}$$

$$\omega_{ybi} = F_{yp}t_{wi}(\cos\alpha)^2 \qquad \omega_{xbi} = 0.5F_{yp}t_{wi}\sin 2\alpha \qquad \textbf{(2.4)}$$

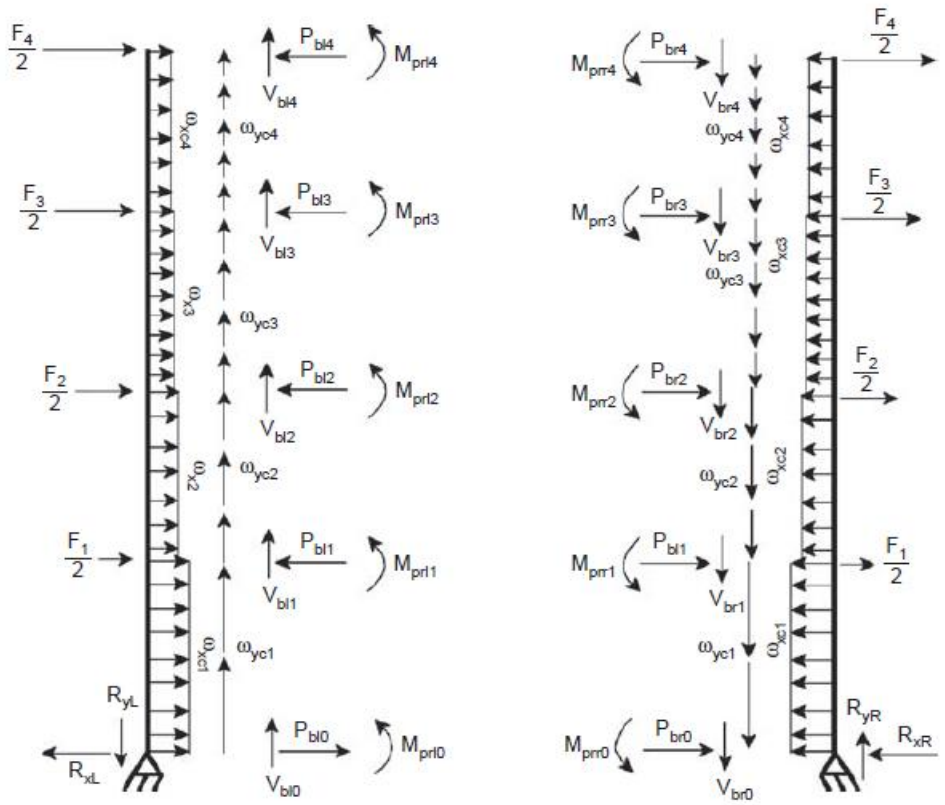


Figure 2.3: Free body diagram of the vertical boundary elements in a four-storey SPSW [24], [26].

2.3 Conventional Cold-Formed Steel (CFS) Shear Walls

The first attempt at assessing the performance of CFS sheathed shear walls is the work carried out by Serette et al. [5] at Santa Clara University. The research program included a series of 16 static and 28 cyclic tests that were performed on flat strap cross-braced, steel sheathed CFS walls, high aspect ratio walls and walls framed with 16- (1.6 mm) and 18-gauge studs (1.2 mm), respectively. The main objective of the research was to study the behaviour of the walls and come up with strength values for design purposes. The specimen consisted of a frame constructed with back-to-back studs, a single interior inner stud, boundary tracks, and sheathing or strap-bracing fastened to one side of the frame only through evenly spaced screws. Lateral

displacement was applied at the top plate and uplift, mode of failure, and maximum loads were monitored and recorded. Serette et al. [5] reported that the dominant mode of failure was a combination of fastener pullout, unzipping of the steel sheathing and buckling of the chord studs. It was concluded that steel sheathed assemblies behaved well and that using thicker sheets resulted in higher capacities. It is worth noting that the design values of this study were incorporated in the earlier versions of the AISI standard for lateral design [32].

To supply engineers with further nominal shear values for CFS steel sheathed shear walls, Yu et al. [33] carried out an additional test on CFS shear walls at the University of North Texas. The tested specimens investigated a wide array of structural parameters and dimensions including sheathing thicknesses of 27 mil (0.68 mm), 30 mil (0.76 mm) and 33 mil (0.84 mm). Each test was conducted on walls with aspect ratios corresponding to 2:1 and 4:1; alongside three fastener spacing schemes: 6-in (150mm), 4-in (100 mm), and 2-in (50mm). The specimens were subjected to a displacement controlled cyclic loading as well as monotonic loading to failure.

Additional tests were also performed on a supporting group of specimens to assess the difference between No.8 screws and No. 10 screws, and to investigate the effects of the screw installation pattern on the boundary studs (staggered pattern on the end studs and screw on the inner stud). The main observations of the test results indicate that when subjected to monotonic loading, that wall assemblies with screws spacing equal to 4-in (100 mm) and 6-in (150 mm) failed from a combination of steel sheet buckling and screw pullout, while specimen fabricated with 2-in (50 mm) screw spacing failed due to buckling of the outer flange of the boundary stud only. Conversely, when subjected to cyclic loads, the main failure mode that was encountered in all

specimens was the sheathing fasteners pullout from the interior studs. The authors also state that alternative screw patterns yielded slightly higher shear strength than the original screw pattern (about 7%). The testing program also confirmed the validity of the reduction factor recommended by the AISI Lateral Standard [32] for shear wall with higher aspect ratios (4:1).

To address the lack of design provisions for CFS steel shear walls in Canada, an extensive research program was initiated at McGill University by Balh & Rogers [34], and Ong-tone & Rogers [35]. In this study, monotonic and reverse cyclic loading were carried out on single-storey shear walls constructed from several framing and sheathing thicknesses. The walls ranged in size from 610 mm by 2440 mm (1:4) to 2440 mm to 2440 mm (1:1). The material thicknesses that were investigated were 0.46 mm and 0.76 mm for the steel sheet, and 0.84 mm and 1.09 mm for the framing members. During the tests, the major failure modes that were observed were the sheathing connection failure and buckling and distortion of framing studs. A few exploratory tests investigated the use of bridging elements to control the buckling of the end stud, however it failed in limiting damage to the stud. The test results were then analyzed using the Equivalent Energy Elastic Plastic (EEEP) method [15] with the aim of establishing a limit state design procedure. Test results from Yu et al. [33] and Ellis [36] were incorporated at this phase. The overstrength factor for walls longer than 1220 mm was also obtained by dividing the shear resistance from the test by the shear resistance from the EEEP curve. A seismic design procedure that conforms to the FEMA P695 [37] methodology was also proposed. The methodology involves the selection and modelling of representative buildings with varying heights in Vancouver (high seismicity). Input ground motion records are then selected and scaled to different intensities to determine the collapse probability of each model building. The main findings of this research

imply that a material resistance factor, Φ = 0.7 was suggested for steel sheathed shear walls, and that the reserve capacity of a shear wall is equal to 1.4. Finally, a height limit of 15 m was recommended for buildings with CFS shear walls, and the proposed R_d and R_o values are 2.5 and 1.3, respectively.

The seismic design provisions for steel sheathed CFS shear wall in Canada were first introduced to the AISI S213 [38] and AISI S400 [10] design standards thanks to the efforts of Shamim & Rogers [39], [40]. This study consisted of a full-scale dynamic shake table testing of five single and five double-storey steel sheathed CFS walls, as well as three single and four double-storey wood sheathed walls. The main aim of the dynamic test was to observe and measure the dynamic properties of the shear walls. As such, each wall was subjected to impact test to obtain the linear viscous damping ratio, harmonic excitation to determine the natural frequency, and lastly ground motion records representative of the seismic hazard in Quebec. The steel sheathed specimens comprise of a 1220 mm by 2440 mm frame with the sheathing attached to one side of the frame. The nominal shear resistance of the walls was estimated from the data retrieved from the studies previously mentioned in this section. The shear wall specimens were constructed with 0.46 mm and 0.76 mm steel sheathings and varying screw spacing. The failure modes that were encountered in the dynamic tests followed the same trend of the failure modes encountered in previous static tests. Several specimens endured severe bending in the studs due to out of plane forces caused by the eccentricities of sheet placement, these specimens were reconstructed with thicker studs and the subsequent tests showed no damage to the studs in the lower storey. The next step involved establishing OpenSees models of the shear walls and calibrating them to the data obtained from the dynamic tests. The model utilized linear beam-column elements as

framing members, uplift and rotational springs for the hold-downs, and a hysteretic truss element as the shear wall to replicate capture strength and stiffness degradation. The FEMA P695 [37] methodology was then applied on twelve archetype buildings located in three zones with different seismic intensities. The results of this study confirmed the accuracy of the seismic force reduction factors of R_d = 1.3 and R_o = 2.0.

In the United States and Mexico, the AISI S400 [10] permits the use of the effective strip method proposed by Yanagi and Yu [8]. As shown in Figure 2.4, the effective strip method assumes that a partial width of the steel sheathing in the diagonal direction provides lateral shear resistance through tension field action. Therefore, the nominal resistance of a shear wall system is limited by the maximum tension in the effective width of the sheathing. The tension strength in the sheathing is in turn attributed to two components: the capacity of sheathing-to-framing connections at both ends of the effective strip, and the yield strength of the effective strip.

Xu & Martinez [41] proposed an analytical method to determine the ultimate lateral strength of CFS shear walls and its associated displacement. The method considers factors that influence the behaviour and strength of CFS shear walls such as: mechanical material properties, thickness of steel sheet and studs, and spacing of mechanical fasteners. Based on previous observations, the authors recognized that the failure mode of CFS walls may be initiated either by sheathing-to-framing connections or failure of the steel studs. As such, they proposed an analytical method where the lateral strength of the sheathing is calculated based on a simplified inelastic method for evaluating the strength of eccentrically loaded bolted connections originally proposed by Brandt [42]. Alternatively, the lateral strength of the CFS wall that corresponds to the

compressive strength of the end studs can be calculated based on the geometry of the wall and the nominal compressive strength of the end stud, which can be evaluated using cold-formed steel design procedures as per CSA 136 [43]. The predicted lateral strengths calculated through the analytical procedure showed good agreement with test results.

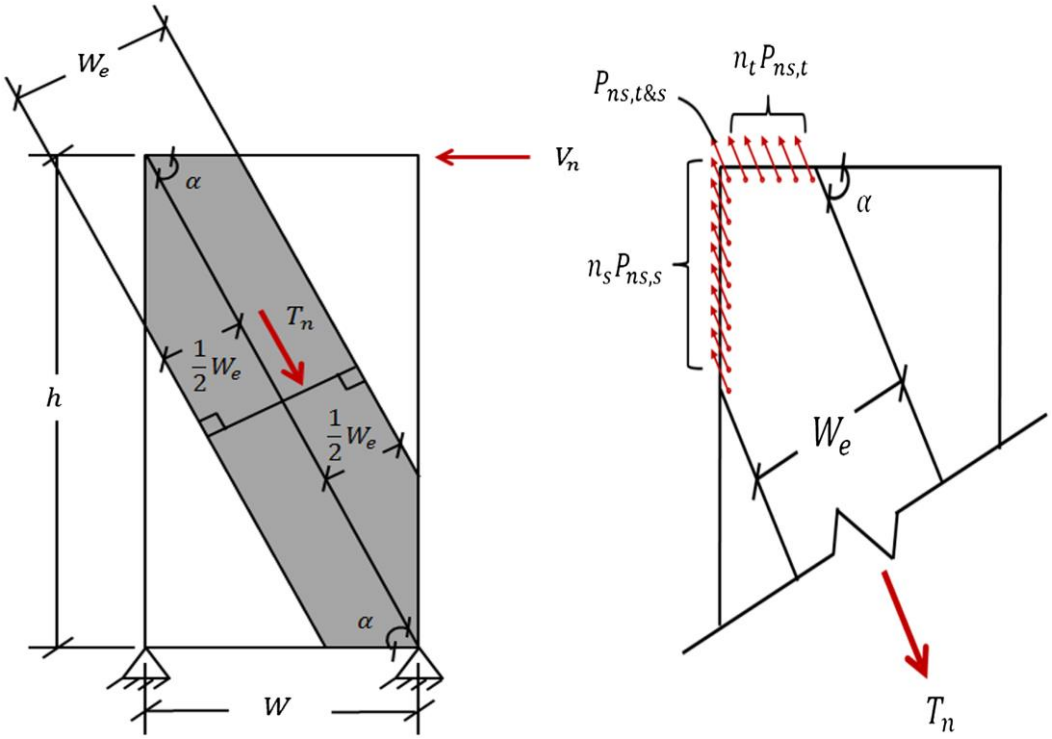


Figure 2.4: Effective Strip Model [8].

2.4 Higher-Capacity Cold-Formed Steel Shear Wall

In order to expand the applications of CFS steel sheathed shear walls into mid-rise construction, a multi-phase testing program was carried out in McGill University during 2017 by Santos & Rogers [11] and Briere & Rogers [12] (phase 1); and by Wu [6] in 2019 (Phase 2). The laboratory test program of phase 1 consisted of 31 specimens with varying construction parameters. Two original configurations capable of attaining considerable higher forces than the walls listed in current standards were proposed: a double sheathed configuration and a centre-sheathed

configuration. The double sheathed configuration was built with two steel sheets installed on both sides of the wall. The rationale behind this construction detail was to eliminate the eccentricities associated with tension field forces and thus reduce the torque on the end studs. Conversely, the centre-sheathed configuration comprised of a steel sheathing confined and concentrically placed between two built-up back-to-back channel studs and built-up tracks. The centre-sheathed wall was designed with the aim of avoiding sheathing pull through which would allow for more ductile screw-bearing deformations. The centre-sheathed wall underwent a design change through the testing phase as the chords had to be reinforced with box section end studs since failure was initiating in the studs. The specimens were fabricated with 0.36 mm and 0.47 mm thick sheathing for the double-sheathed configuration, and 0.84 mm and 1.09 mm for the centre-sheathed configuration. The frame thicknesses on the other hand were 1.73 mm and 2.46 mm, and lastly the screw spacing varied between 50 mm, 100 mm, and 150 mm with the centre-sheathed specimen employing a staggered screw pattern. The specimens were loaded monotonically and cyclically following an asymmetric loading protocol or the Consortium of Universities for Research in Earthquake Engineering (CUREE) reversed cyclic protocol. The configurations, along with the reinforcing scheme are shown in Figure 2.5.

Some of the unique failure modes that were encountered include shear failure of the screws in the centre-sheathed specimen where the screw had to penetrate three or five layers of sheets. Furthermore, the confinement of the sheathing led to tear-out sheathing failure and the formation of pinched holes due to accumulated plastic strain during load reversal. Regarding the framing members, at the beginning of the tests the centre-sheathed shear wall failed to reach its full capacity due to flexural buckling of the framing members. Another type of framing failure

was the separation of built-up chord members attributed to the out-plane-forces caused by the buckled sheathing. This type of failure was observed in specimen that were assembled with screw spacing equal to 150 mm.

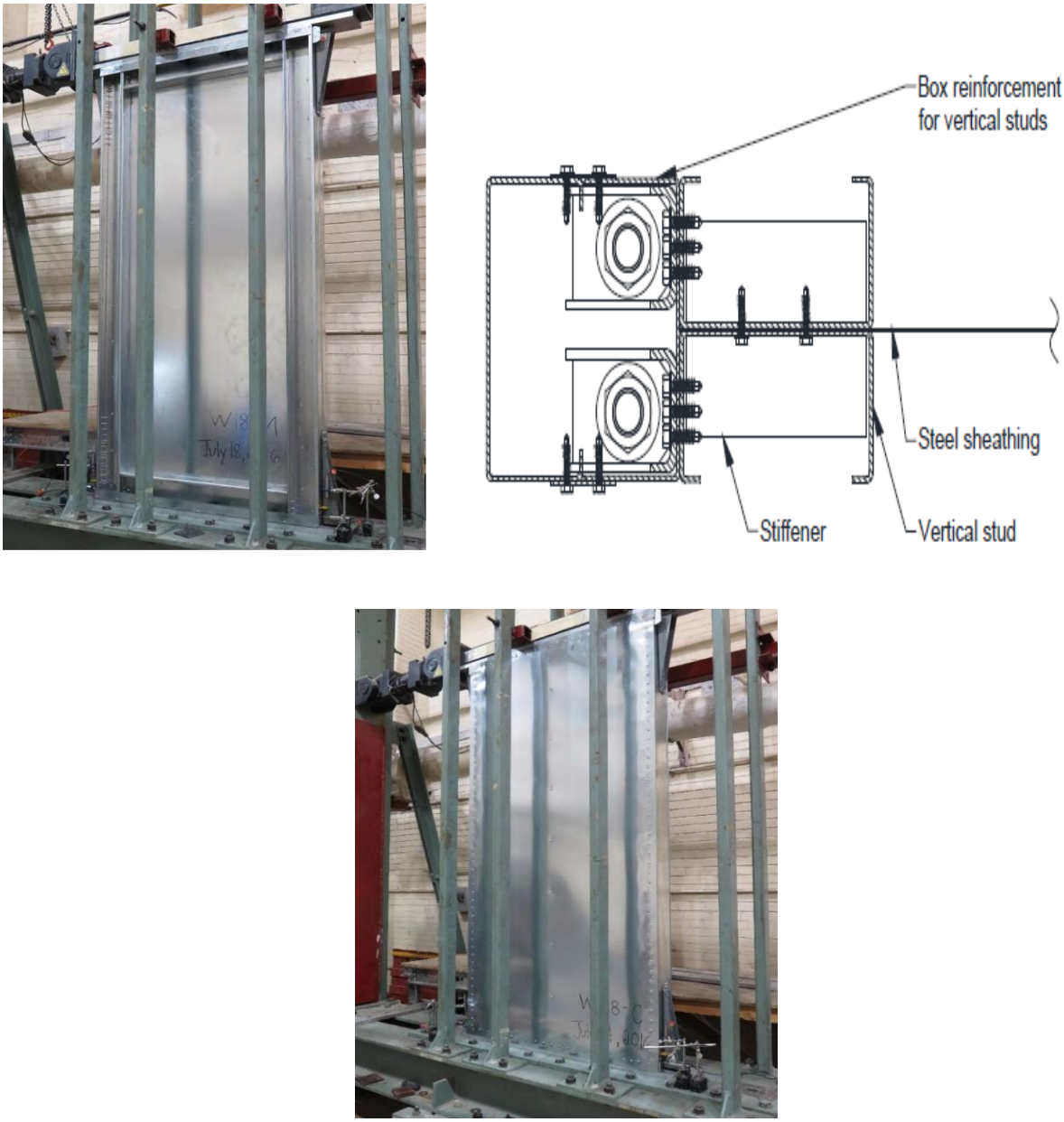


Figure 2.5: Centre-sheathed wall assembly tested by [11] & [12]. Centre-sheathed wall (top left); reinforcing scheme (top right); double-sheathed wall (bottom).

The test data were then analyzed and interpreted using the EEEP method for the purpose of developing a Limit State Design (LSD) approach and a Load and Resistance Factor Design (LRFD) approach. The procedure generally followed the same steps outlined above, however some adjustments had to be made since substantial shear forces and drift values were attained by the centre-sheathed specimen. The authors also proposed a preliminary design method, called the modified effective strip method (MESM), to calculate the nominal shear resistance of the centre-sheathed wall. As explained in Eq. (2.5),the MESM assumes that all the sheathing screws around the perimeter of the wall contribute to the shear resistance of the wall through bearing deformation. This assumption is based on the observation that there was bearing damage in the sheathing, to a different extent, at every screw connection. The preliminary design method estimates the bearing resistance of each connection by using the bearing strength equation for bolts in double shear since at the time of proposing the preliminary design method, there were no methods to determine screws' bearing resistance in double shear. Overall, the double sheathed configuration exhibited increased shear strength (two times higher than what is available in AISI S400 [10]) although the ductility was not improved. The centre-sheathed wall, however, reached a shear capacity four times higher than what is currently listed in the code; and the shear capacity was achieved at large drifts (7%) which show the high ductility of the system.

$$S_{n(MESM)} = \frac{(n/2)P_{nb}cos\alpha}{W} \quad \textbf{(2.5)}$$

where; n = Total number of sheathing-to-framing fasteners.

α = Tension force inclination angle.

W = width of the wall.

P_{nb} = Nominal bearing strength of a single connection, described in Eq. (2.6) below:

$$P_{nb} = Cm_f dtF_u \quad \textbf{(2.6)}$$

In which C represents the bearing factor (Table J3.3.1 [43]), m_f stands for the modification factor (Table J3.3.2 [43]), d is the nominal diameter of the bolt, t is the thickness of the metal sheet, and F_u is the ultimate strength of the sheet.

The second phase of the project [6] aimed at expanding the test data of the centre-sheathed configuration. As such, nine additional full-scale tests were built using the same configuration and material properties discussed in [11] & [12], although the maximum screw spacing was limited to 125 mm so as to eliminate the separation of built-up studs. Phase two also included full-scale tests of the bare frame and connection tests in double shear. The results from the aforementioned tests were also utilized to formulate a new approach, labeled the MESM + Frame method. The method that is displayed below in Eq. (2.7) and Figure 2.6, includes a provision for the frame effect which is additive to the resistance provided by the screws. Design parameters were also obtained for Limit State Design and Load and Resistance Factored Design.

$$S_{n(MESM)} = \frac{(n_{reduced}/2)P_{nb}cos\alpha}{W} + S_{Frame} \quad \textbf{(2.7)}$$

$$S_{Frame} = \begin{cases} 18.2\,kN/m\ for\ no\ stud\ reinforcement \\ 26.8\,kN/m\ for\ R2\ reinforcement \\ 38.2\,kN/m\ for\ R3\ reinforcement \end{cases}$$

where;

$n_{reduced}$ = Total number of sheathing-to-framing fasteners excluding the corners as displayed in Figure 2.6.

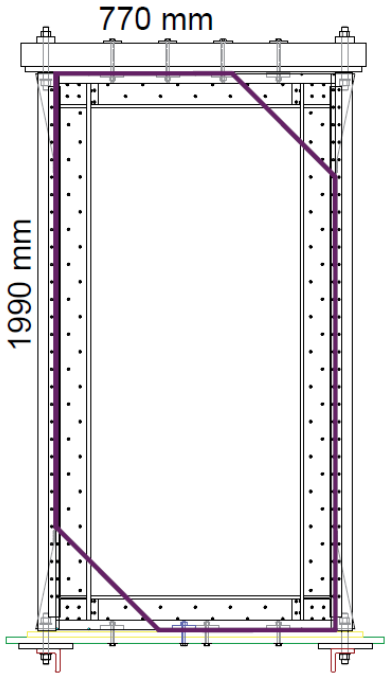


Figure 2.6: Modified tension field width for the proposed method [6].

2.5 Numerical Studies on CFS Shear Walls

Schafer et al. [44] presented an overview of nonlinear collapse modeling of cold-formed steel members using shell elements. A numerical study involving a 1,200 mm long CFS steel lipped channel stud was performed to evaluate the collapse modeling sensitivity to several parameters. The sensitivities of the following parameters were assessed: element selection and mesh density, plasticity model, solution scheme, and lastly, software implementation (ABAQUS [14] and ADINA [45]). As displayed in Figure 2.7, three shell elements with varying mesh densities were explored, S4, S4R and S9R5. S4 and S4R are four-node shell elements with linear shape functions, while the

S9R5 is a nine-node element that utilizes quadratic shape functions. Quadratic elements offer greater flexibility in constructing a mesh, especially in models with curved edges. The mesh densities that were chosen included coarse, medium and a fine mesh. When a coarse mesh was used, the model reached a capacity that was 9% higher than the fine mesh. Also, models with a coarse mesh were unable to capture local buckling modes reliably. However, once an adequate mesh was established, the difference in the response of the elements was insignificant.

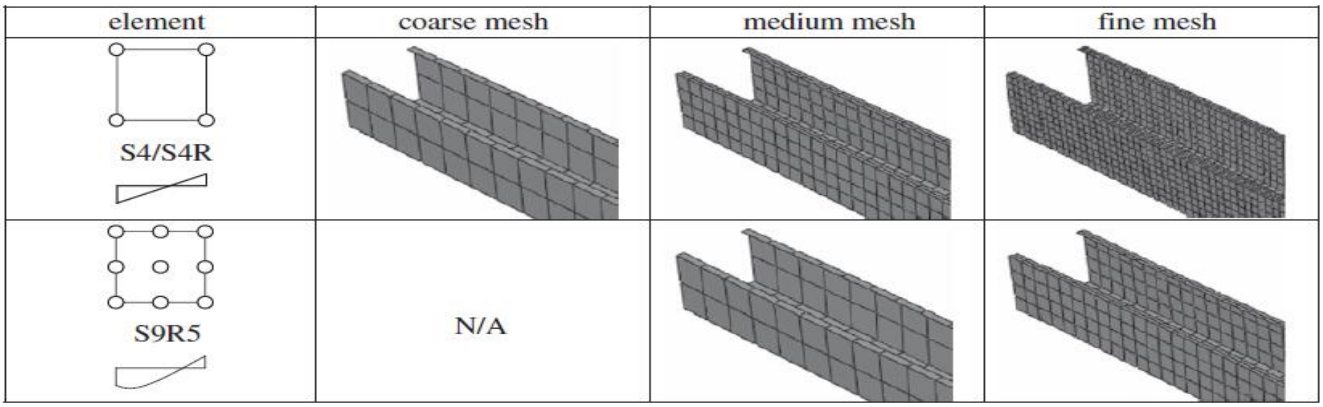


Figure 2.7: Linear and quadratic elements with the corresponding mesh densities assessed in the study by Schafer et. al [44].

Two solution schemes were compared, the arc-length solver scheme (Riks), and a displacement-based Newton Raphson supplemented with artificial damping. The authors generally recommend the arc-based scheme since it's based on increments of work rather than increments of force/displacement and has proven to be more robust when resolving problems that involve buckling. However, for the studs investigated in this study, when a sufficient number of steps was used, the artificial damping solution provided a higher peak load but identical post-buckling response. Since the Riks algorithm solves the equilibrium equation without adding artificial energy, it is preferred method for such a case. A tri-linear material model was deployed to the models to observe the sensitivity of the plasticity model. The results indicated that the choice of

plasticity model has a substantial effect on the peak load, since the capacity was decreased by 13% when a 1% reduction was applied to the modulus of elasticity (0.99E). The drop in peak load was independent of element type, mesh density, solution scheme and number of integration points. This led the authors to conduct a brief comparative study with ADINA. When the same material model was implemented in the ADINA model, the decrease in the modulus of elasticity had minimal impact on the strength of the channel.

As previously stated, the behaviour of CFS walls is greatly influenced by the sheathing-to-framing connections. One of the limitations of ABAQUS is the inability to completely capture the hysteretic behaviour of CFS sheathed connections [46]. To address this issue, Ding [47] performed a comprehensive study on the modeling of monotonic and cyclic response of screw fastened connections. A user element (UEL) subroutine was written and verified for a nonlinear hysteresis model that can simulate pinching and strength and stiffness degradation for CFS fastened screws. The user element is based on the OpenSees [48] Pinching4 material model. A typical Pinching4 backbone curve is shown in Figure 2.8.

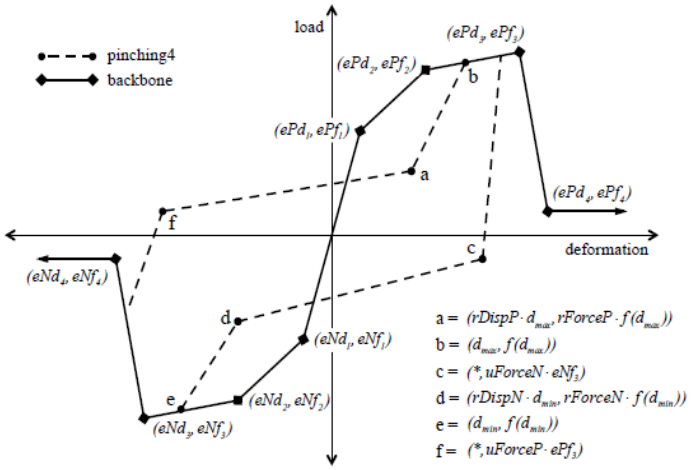


Figure 2.8: Pinching4 material model [49].

Pinching4 is a multi-linear, one-dimensional material model written by Lowes et al. [49]. The model's behaviour is simulated by pinching paths. The paths in turn are controlled by the user input parameters and material loading history. The model is also characterized by four states. State 1 and 2 represent loading of the material along the positive and negative backbone branch; while state 3 and 4 represent reloading and unloading cases where the pinching and degradation occur. State change occurs when the material is loaded beyond the boundaries of the state or when loading changes direction. The updated material behaviour in the new state is then used in the analysis. The model was incorporated in ABAQUS as a user element (UEL) and tested on shear wall models of recent cyclic experiments [50] & [51]. All simulations were consistent with the shear-deformation response and strength degradation, confirming the validity of the subroutine and displaying its potential in performing future cyclic simulations of CFS framed steel sheathed walls.

Zhang & Schafer [52] developed a model using ABAQUS to simulate the behaviour of the double-sheathed wall that was tested by Briere & Rogers [12]. The wall assembly was modeled with 8-node double curved reduced integration shell element (S8R) and discretized with a fine mesh equivalent to a global seed of 12.7 mm. Frame-to-frame connections were modeled as multi-point pin constraint while sheathing-to-framing connections were simulated using linear elastic springs in three translations directions. Using the dynamic implicit solver, the authors reported that the initial stiffness of the model is reasonable, and that the response of the steel sheet is qualitatively similar to the test. However, a more robust model of the sheathing-to-framing fasteners must be incorporated to match the experiments' results. Rouaz et al. [53] developed FEM models for CFS shear walls tested by Balh & Rogers [34]. All elements were modeled as 4-

node shell elements with reduced integration scheme (S4R). A mesh size of 50 x 50 mm was used for all framing members. To simulate the screw connections, mesh-independent fasteners were used. The authors state that good agreement was achieved between the experimental and numerical results in terms of force-displacement and failure modes.

2.6 Semi-Rigid Connections in Steel Frames

It is widely accepted in current practice to idealize connections in steel frames as either fully pinned or fully rigid. While this assumption greatly reduces the design procedure of such frames, the resulting response of the idealized structure might vary greatly from the real structure. Several experimental programs have repeatedly proven that fully fixed connections retain some extent of flexibility while fully pinned connections exhibit a certain degree of rotational stiffness [54]. Hence, in reality, connections in steel frames display semi-rigid deformation behaviour which in turn greatly affects the distribution of internal stresses in the actual members.

Semi-rigid connections in steel frames can be introduced through the concept of the "r-factor" or "end-fixity factor" [55]. As displayed in Figure 2.9, joint flexibility is incorporated through a rotational spring that is attached to the end of the beam. The end-fixity factor can then be defined as:

$$r = \frac{\alpha}{\phi} = \frac{1}{1 + \frac{3EI}{RL}} \quad \textbf{(2.8)}$$

Where R is the rotational stiffness of the end-connection, $\frac{EI}{L}$ is the flexural stiffness of the connected member, α is the rotation of the end member, and finally, ϕ is the combined rotation

of the member and the connection due to a unit end-moment. For a pinned connection, the rotational stiffness at the ends of the beam is idealized as 0, therefore the end-fixity factor is equal to 0 as well. On the other hand, the rotational stiffness for a rigid connection is assumed as infinity, as a result the end-fixity factor is equivalent to unity. Lastly, a semi rigid connection possesses an end-fixity factor between zero and one.

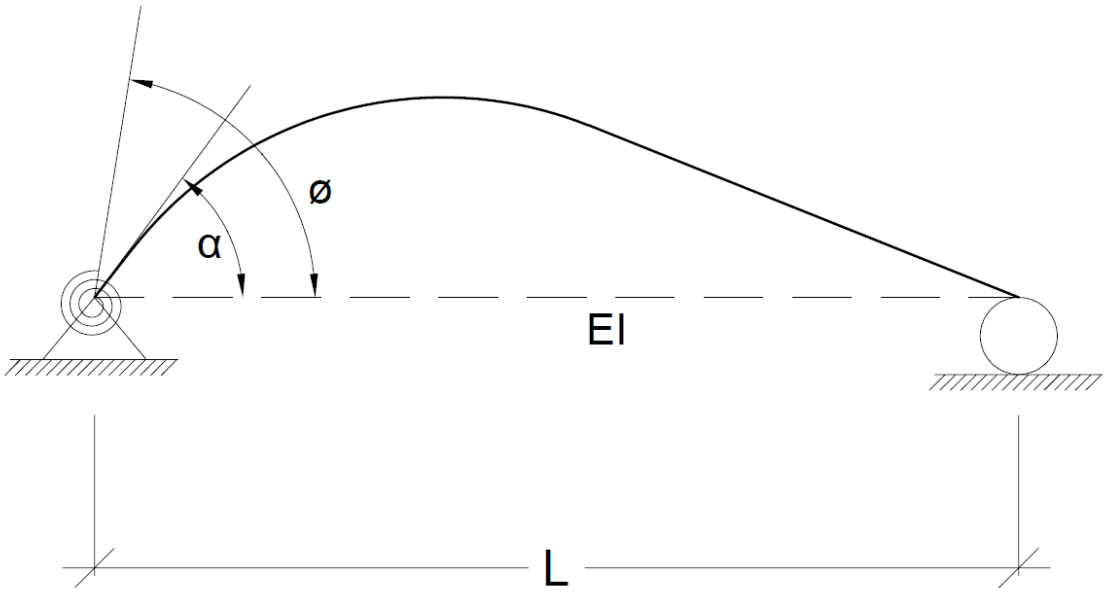


Figure 2.9: Semi-rigid connected beam [54].

Structural analysis of indeterminate beams and frames can be performed using various techniques. Of these techniques, the moment distribution method, which was proposed by Cross [56], is perhaps the most popular. The advantage of the moment distribution method is that it's based on successive approximations that can be worked out to any desired degree of accuracy and that it does not require solving a set of simultaneous equations. Through the incorporation of the end-fixity factor, the analysis of semi-rigid frames can be carried out using the moment

distribution method. The overall procedure is similar, however as discussed below, some minor modifications are applied to consider semi-rigid behaviour.

- **Member-End Moments:** The initial moments of the members assuming the ends of those members are partially fixed against rotation due to varying types of loadings can be found in the tables in Appendix B.
- **Member Stiffness Factor:** For a member with different connection stiffnesses at each end, R_a & R_b, assume that the end-fixity factors for ends a and b as defined by Eq. (2.8) are r_a & r_b, respectively. Consequently, the members stiffness factors K_{ab} & K_{ba} are expressed as:

$$K_{ab} = s_{ab}\frac{4EI}{L} \quad \textbf{(2.9)}$$

$$K_{ba} = s_{ba}\frac{4EI}{L} \quad \textbf{(2.10)}$$

where s_{12} & s_{21} account for the end-connection flexibility and are defines as follows:

$$s_{ab} = \frac{3r_a}{4 - r_a r_b} \quad \textbf{(2.11)}$$

$$s_{ba} = \frac{3r_b}{4 - r_a r_b} \quad \textbf{(2.12)}$$

- **Distribution Factor (DF):** If n number of members are connected at a joint, and an arbitrary moment is applied at that joint, then each connected member will supply a portion of the resistive moment in order to satisfy the moment equilibrium at the joint [57]. The fraction of resistant moment, called the distribution factor, can be defined as:

$$D_{12} = \frac{K_{ab}}{\sum^{n} K_{ab}} \quad \textbf{(2.13)}$$

- **Carry-Over Factor:** If a member, whose far end is partially restrained from rotation, is acted upon by a moment at its near end, then a moment must be applied at its far end to resist the rotation of the member end. The ratio of far-end moment to near-end moment which is known as the carry-over factor can be expressed as:

$$C_{ab} = \frac{r_b}{2} \quad \textbf{(2.14)}$$

$$C_{ba} = \frac{r_a}{2} \quad \textbf{(2.15)}$$

-

Chapter 3: Preliminary Testing Program

3.1 Introduction

Experimental testing is essential in capturing key parameters and failure modes that aid in evaluating the structural behaviour of a proposed system. The main objective of the preliminary testing program is to provide information about the performance of the cold-formed steel high-capacity shear wall specimens under the effects of monotonic and cyclic displacements representing wind and seismic loading. As stated in chapter 1, the initial design of the specimen was proposed at the University of Waterloo, however the preliminary tests were conducted in collaboration with Chongqing University in China under the supervision of Professor Xu. The testing program consisted of a full-scale monotonic test, three full-scale cyclic tests of the shear wall specimens, cyclic connection tests in double shear, and coupon material tests. Since they were conducted in China, the tests were carried out according to the Chinese Standards of cold-formed steel [58], material tensile-testing [59], and testing methods for earthquake resistant buildings [60].

A detailed description of the shear wall specimens is first introduced, including lessons learned from previous testing programs that influenced several design decisions. Then, the test frame setup and loading protocol are presented, followed by a discussion regarding the main test observations and failure modes of each specimen. The chapter finally concludes with a brief discussion of the supplementary tests that include the cyclic screw connection tests and coupon tests.

3.2 Shear Wall Specimen Configuration

Three configurations were proposed and assessed in this research, a concentric-sheathed shear wall with built-up hat section studs, a concentric-sheathed shear wall with an intermediate stud located at mid-span, and a diagonally strapped concentric sheathed shear wall with built-up hat section studs. Three concentric-sheathed specimens were tested, while one diagonally strapped specimen was tested.

The first configuration comprised of a thin steel sheet concentrically confined between built-up studs at each end and built-up tracks at the top and bottom of the wall. Two hat sections are attached face-to-face to form box-shaped built-up vertical studs. The sheathing is fastened to both flanges of the built-up studs using #12 self-tapping screws spaced at 50 mm. The horizontal boundary elements consist of two angle tracks attached back-to-back. Two rows of #12 self-tapping screws spaced at 50 mm are then used to restrain the sheathing between the webs of the tracks. A square connector plate is used to fix the tracks and studs at the corners of the wall and to ensure continuity of the frame using M12 high-strength bolts. The hold-downs are rigidly connected through their spine to the exterior face of each individual stud using two rows of M8 bolts. Hold-downs were placed at the bottom and top of the wall at each end; therefore the assembly contained a total of 8 hold-downs. The concentric-sheathed specimens were subjected to a displacement-controlled monotonic test (specimen GD-06) and a displacement-controlled cyclic test (specimen GD-19).

In terms of structural configuration, building parameters and element sizes, the recent work that was carried out at McGill University [6], [11], [12] concerning centre-sheathed high-capacity

shear walls can be considered as the most comparable to the concentric-sheathed shear wall specimen. In previous studies where the sheathing was attached to the framing members from one side only [13], [34], major failure modes encountered in the frame include distortional and torsional buckling of the studs. Placing the sheathing on one side imposes eccentricities which induce torsional forces on the studs. Also, as displayed in Figure 3.1, the horizontal component of the tension field that develops in the sheet leads to distortional unwrapping of the stud's lips.

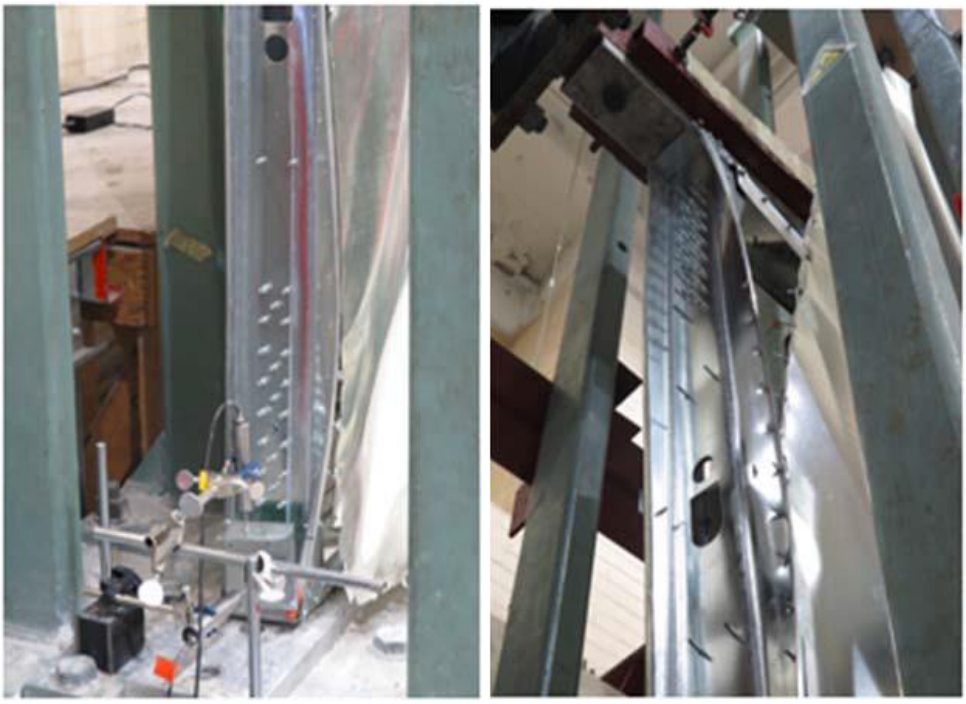


Figure 3.1: Damage due to eccentric placement of the sheathing [13].

The shear buckling of the sheathing also generated out-of-plane forces on the frames which caused the sheathing to pull-over and "unzip" from the screws. Additionally, since the sheathing was attached to the framing through two-ply connections, several walls were prone to screw pull-out, as displayed in Figure 3.2.



Figure 3.2: Sheathing pull-over (left) and screw pull-out (right) failure modes [12], [13].

Another observation that was made by Briere [12] and Santos [11] was the separation of built-up channel sections when the screw spacing was too large (150 mm), and the shear failures of the screws located at the corners of the walls, as depicted in Figure 3.3. These screws had to penetrate three or five layers of steel and as a result are subjected to higher shear forces due to the formation of the tension field across the diagonals. The design and detailing of the proposed shear walls presented in this research aims to address these shortcomings in order to attain higher forces and lateral drift.



Figure 3.3: Screw shear damage (left); chord separation damage (right) [11].

For the proposed concentric-sheathed specimens, the main energy dissipation mechanism is a combination of sheathing-to-framing screw bearing deformations and yielding of the sheathing itself. Accordingly, the screw spacing was limited to 50 mm in all specimens as previous research and code-approved walls indicate that the walls' capacity increase as fastener spacing decrease. Utilizing a small screw spacing would also prevent the studs from separating due to ripple effect of the shear buckling of the steel sheathing. Additionally, confining the sheathing between built-up studs eliminates several failure modes associated with screws such as sheathing pull-over, screw tilting and screw pull-through. Hence the shear capacity of the proposed system is anticipated to increase due to the improved bearing contact of the screws. Also, shear failure of the screws at the corners of the walls was avoided since the plate connections at the corners were realized through high-strength bolt rather than self-tapping screws, as displayed in Figure

3.7. On the other hand, the use of built-up box-like studs would prevent the torsional buckling of the end studs since closed sections inherently possess high torsional rigidity. In addition, the placement of the sheathing in the centre-line of the wall eliminates eccentricities and thus the studs would be subjected to forces in their strong axis of bending. Finally, the shear wall specimen were all constructed using a mild grade of steel for the sheathing. A mild-grade of steel was utilized for the sheathing in order to reduce the forces on the studs due to the sheathing pull-in effects and to ensure that the failure initiates in the sheathing at the screw locations, thus satisfying capacity design principals.

Based on the design of the concentric-sheathed specimen, another specimen was constructed with an intermediate stud attached on both sides of the sheathing and subjected to cyclic loading (specimen C-SW-2). The intermediate stud consists of a lipped hat section that was placed at the mid-span of the wall. The diagonally strapped shear wall specimen on the other hand (GD-10) is made up of the exact same configuration as the concentric-sheathed walls, however it is assembled with two diagonal braces on each side attached to the outside of the top flange of the hat sections. The connections of the bracing members to the studs were realized using M8 bolts at each end. It should be noted that the intermediate stud is installed for non-structural reasons such as installing gypsum boards. However, as will be outlined in the following sections, the addition of the intermediate stud improves the cyclic performance of the specimen considerably. Regarding the diagonally strapped wall, while the same advantages apply to this configuration (no eccentricity, higher stud capacity), the addition of diagonal bracing is anticipated to increase the redundancy and shear capacity of the wall since the system now boasts an additional inelastic fuse element. Where in the concentric-sheathed specimens the main energy dissipation

mechanism is the yielding of the sheathing and the sheathing-to-frame screw connections, this type of shear wall has the added advantage of dissipating energy through yielding of the diagonal straps in tension.

As displayed in Table 1, the overall height of the cold-formed steel shear walls is 2,400 mm while each specimen spanned a total bay width of 1,210 mm, resulting in an aspect ratio equal to 2:1. The connector plate, boundary frame, and bracing members were 2.5 mm thick, with the exception of the intermediate stud being 1.5 mm thick. The thickness of the steel sheathing was kept the same for all specimens at 0.8 mm. The thickness of the components, along with the dimensions of the shear wall specimens were selected based on past experience and the dimensions of a typical building. The three specimens, along with their structural details, are shown in Figure 3.4 through Figure 3.7.

Table 1: Test Matrix.

Specimen ID	Sheathing Thickness (mm)	Bay Width (mm)	Wall Height (mm)	Framing Thickness (mm)	Intermediate Stud Thickness (mm)	Screw Spacing (mm)	Loading Type
GD-6	0.8	1210	2400	2.5	-	50	Monotonic
GD-19	0.8	1210	2400	2.5	-	50	Cyclic
C-SW-2	0.8	1210	2400	2.5	1.5	50	Cyclic
GD-10	0.8	1210	2400	2.5	-	50	Cyclic



(a) (b) (c)

Figure 3.4 :Cold-formed steel shear wall specimens. (a) GD-06; (b) GD-10; (c) C-SW-2.

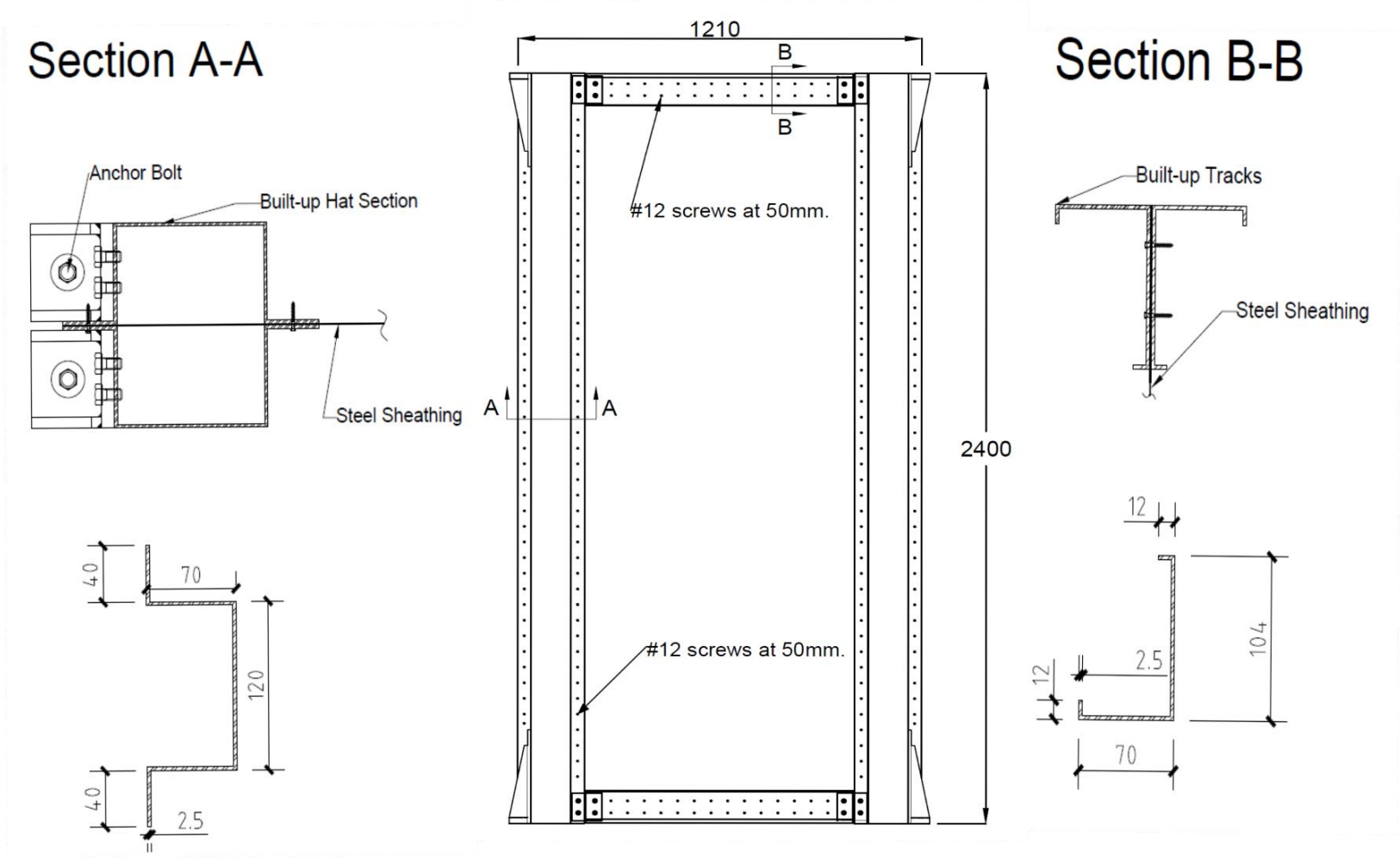


Figure 3.5: Structural details of specimens GD-06 & GD-19.

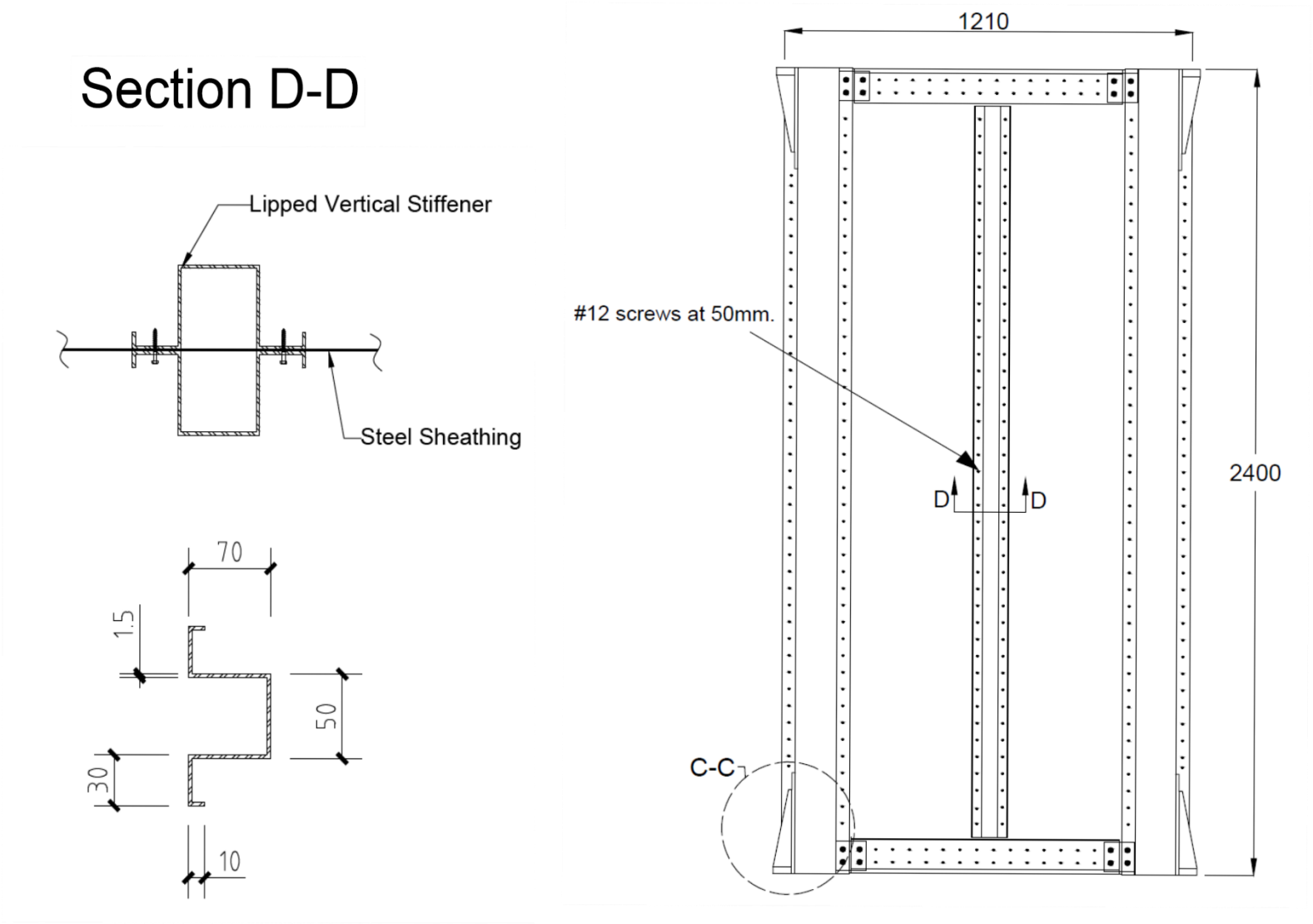


Figure 3.6: Structural details of specimen C-SW-2.

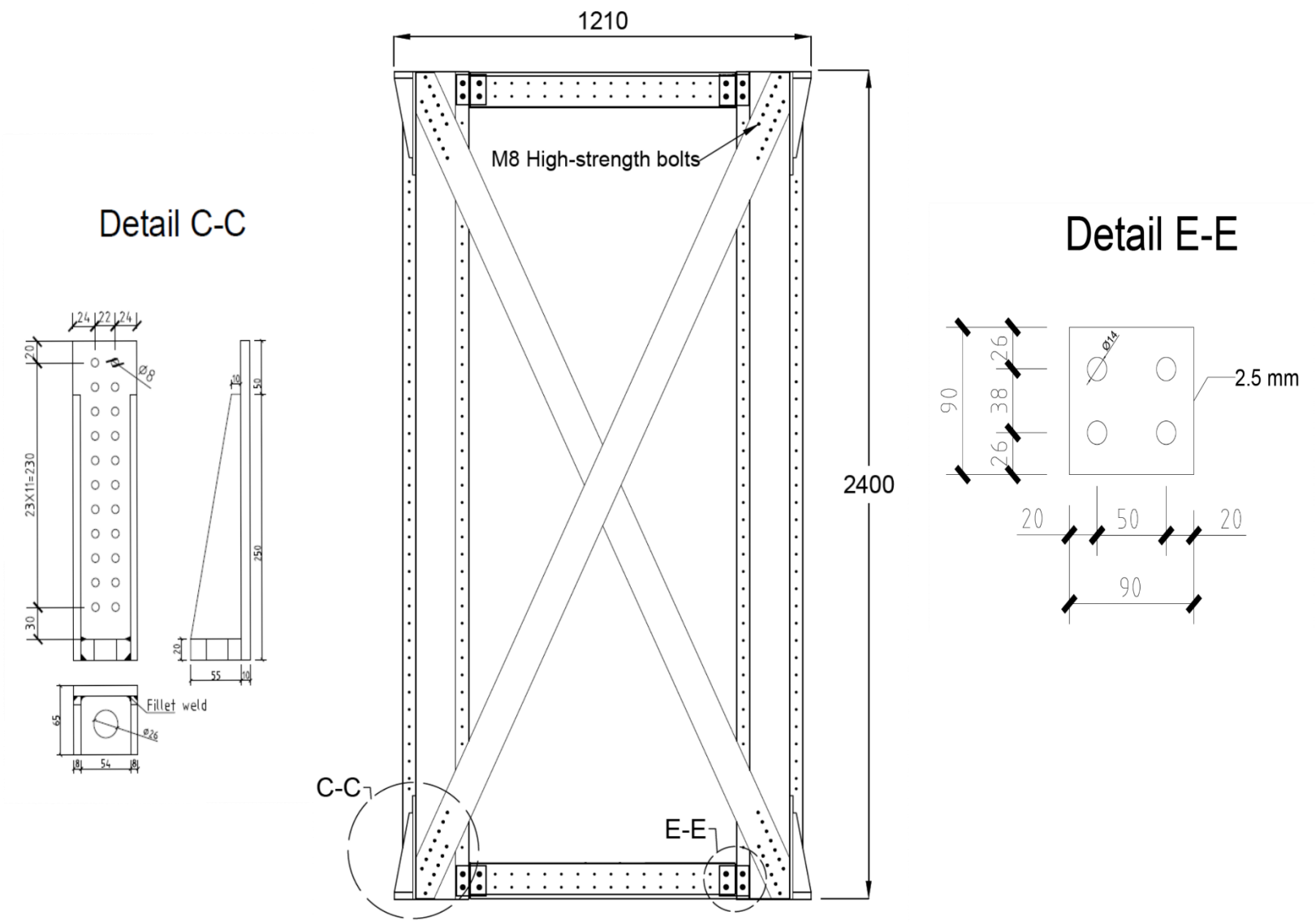


Figure 3.7: Structural details of specimen GD-10.

3.3 Test Frame Apparatus and Cyclic Loading Protocol

As displayed in Figure 3.8, the test frame adopts a dual channel electro-hydraulic servo program-controlled structure testing machine system. The system is capable of performing force-controlled or displacement-controlled testing. The test frame is equipped with an actuator with a ±300 mm horizontal stroke; and a displacement-loading speed of 0.1~3mm/s. The whole experimental process is controlled by an electro-hydraulic servo controller and a microcomputer.

The shear wall assembly is connected to the testing frame through the hold-downs and tracks. The hold-downs are attached to the top control beam and the bottom base beam through M24 high strength hexagonal anchor bolts, while the tracks are connected to the beams using M12 anchor bolts. The testing was only concerned with lateral loads hence gravity loads were not applied in this experiment. The horizontal displacement is applied to the top of the wall through the horizontal actuator. The rigidity of the control beam can ensure that the horizontal load is transferred evenly to the top of the wall. Also, a rolling support is attached to the loading device which restricts the wall's out-of-plane movement, simulating the support of a floor slab.

The loading protocol followed the specifications of the Chinese standard for seismic tests of buildings, JGJ/T 101-2015 [60]. Based on a preliminary finite element analysis, the yield displacement (δ_y) was determined to be 18 mm. Consequently, the shear wall specimens were subjected to a displacement increment equivalent to 3 mm and cycled once until the yield displacement was achieved. Post-yield, the concentric-sheathed specimens were subjected to an increasing displacement increment equal to 18 mm and cycled three times per increment, while the diagonally strapped specimen was subjected to an increasing displacement increment equal

to 9 mm ($0.5 \times \delta_y$). When the shear capacity of the specimens dropped to 85% of the maximum load, the test was terminated, and the wall assembly was considered to be destroyed. A sample of the loading protocol for the concentric-sheathed specimens is shown in Figure 3.9.

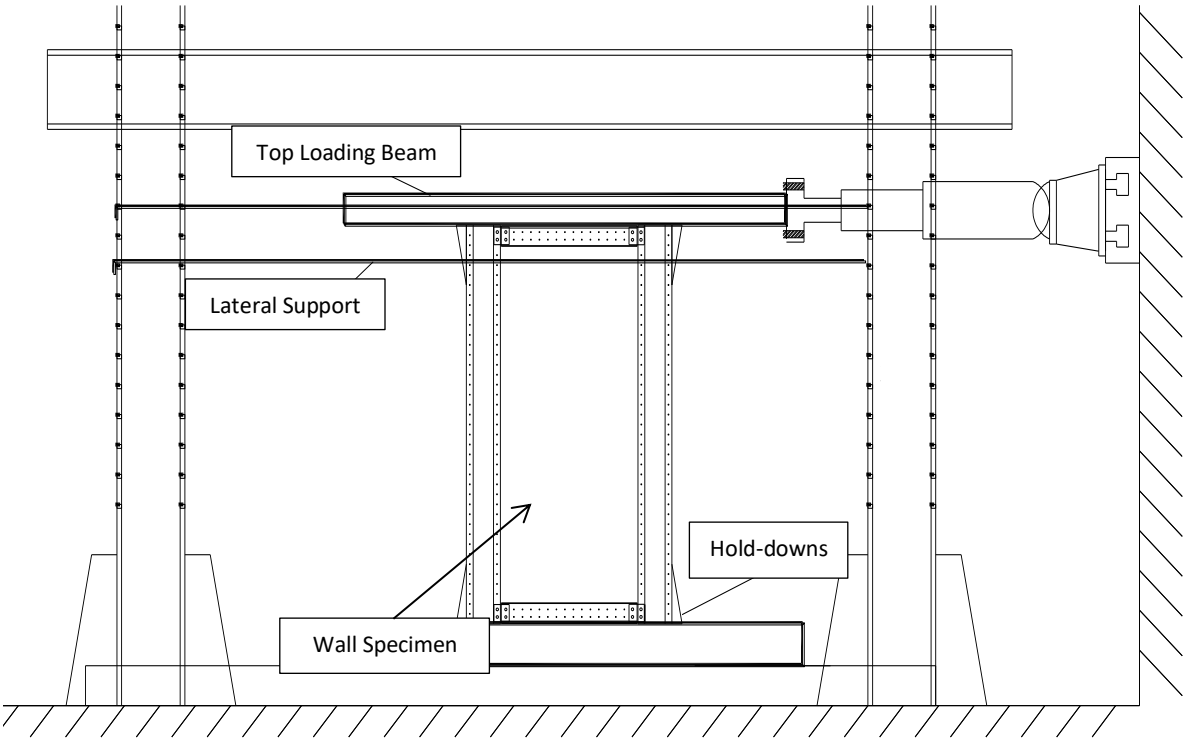


Figure 3.8: Test Frame Apparatus.

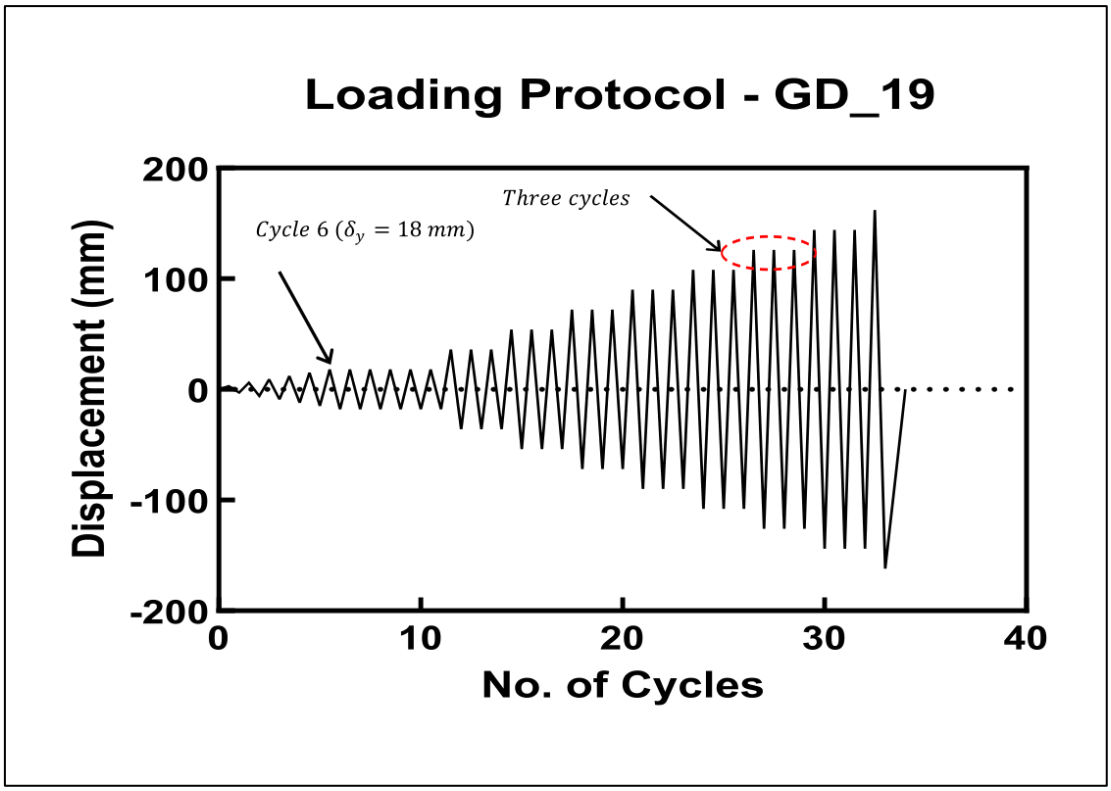


Figure 3.9: Loading protocol for specimens GD-19 and C-SW-2.

3.4 Data Acquisition

Based on the Chinese Standard for low-rise cold-formed steel buildings [58], the testing frame was installed with ten displacement sensors as displayed in Figure 3.10 below. The sensors designated D1, D2 and D3 are used to measure the horizontal displacement of the specimen. D4 and D5 measure the vertical displacement of the specimen with respect to the ground. D6 and D7 on the other hand measure the horizontal displacement of the specimen relative to the ground, while D8 and D9 are employed to measure the vertical displacement of the bottom beam relative to the ground. Finally, sensor D10 measures the vertical displacement of the base beam with respect to the ground.

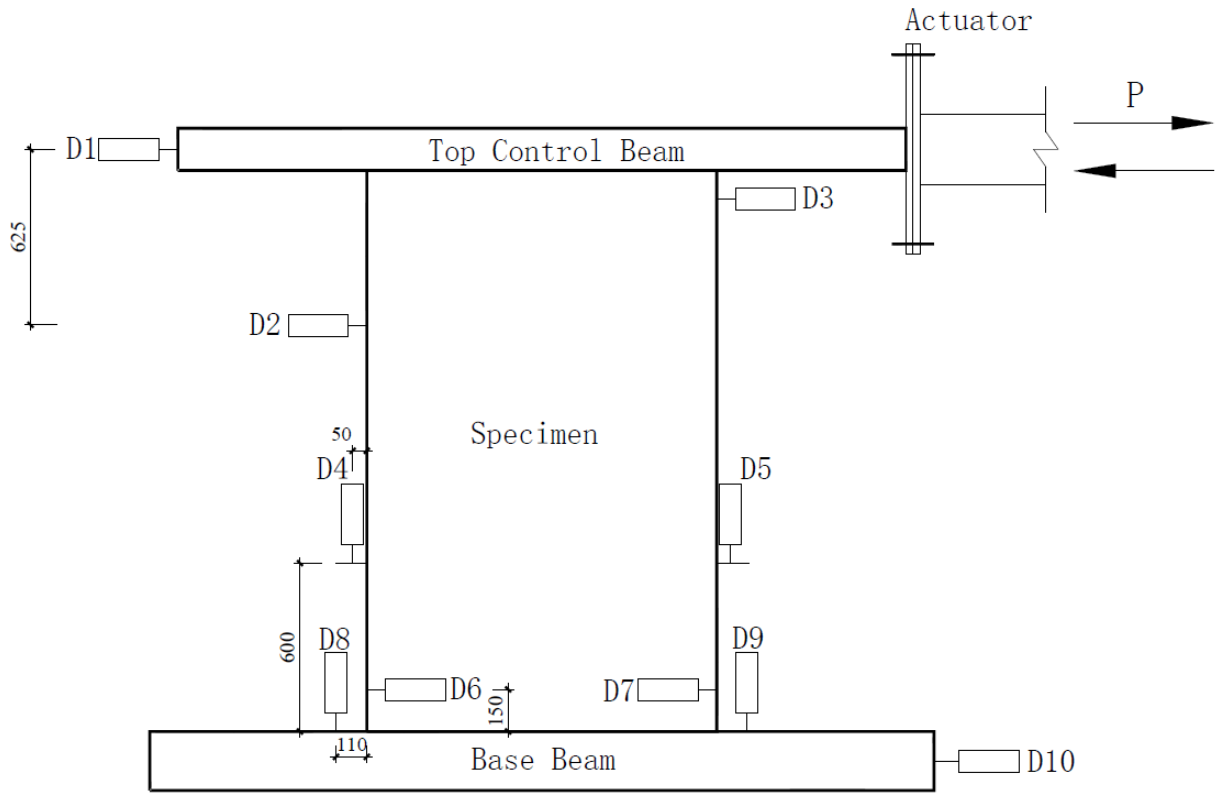


Figure 3.10: Arrangement of displacement sensors.

3.5 Test Observations and Failure Modes

The main observations and failure modes for the monotonic and cyclic test are presented in the following subsections. Various key parameters such as the specimen's ductility and wall resistance can be obtained from a monotonic test. Alternatively, cyclic testing is essential in capturing the degradation in strength and stiffness at high shear deformations, as well as determining the energy dissipation capacity which is important for seismic design.

3.5.1 Monotonic Test (specimen GD-06).

As illustrated in Figure 3.11, the tension field started developing across the diagonal of the steel sheet due to the elastic shear buckling of the sheathing at displacements as low as 6 mm. The lateral displacement changes the rectangular aspect of the frame, resulting in the lengthening of one diagonal of the sheet due to tension forces and shortening of the perpendicular diagonal due to compressive forces. The compressive forces induce ripples in the sheathing and causes it to buckle out of plane. This behaviour is typical of cold-formed steel shear wall and was encountered in several previous experimental programs [6], [11], [12]. At higher displacements (36 mm), the tension bands became more defined and were followed by loud tremors. The shear buckling has entered the inelastic zone at this stage and the out-of-plane deformations can be visible in the corners of the wall, as shown on Figure 3.12.



Figure 3.11: Elastic shear buckling of the sheathing for specimen GD-06.

At a displacement of 90 mm, which corresponds to a base shear equal to 93 kN, the built-up stud under compression buckled in flexure, as displayed in Figure 3.13. The amplitude of the flexural buckles grew as the deformation at the top of the wall increased, and there was local buckling in the studs on the other end due to the inelastic formation of the tension field and due to (**Figure 3.14**). The buckling of the end stud was located 770 mm from the bottom of the wall. Visible out-of-plane "bulging" of the sheet was also observed in the portion adjacent to the compression stud. The specimen's bearing capacity had dropped to 85% of its ultimate bearing capacity at this level (225 mm displacement) and the test was terminated. The final "destroyed" specimen is shown in Figure 3.15 after the actuator position was returned to zero, displaying obvious permanent deformations in the sheathing and end stud.



Figure 3.12: Inelastic shear buckling of specimen GD-06 due to high displacements.



Figure 3.13: Buckling of end studs for specimen GD-06.



Figure 3.14: : Local buckling of the stud (left); severe inelastic buckling of the sheet and stud (right) in specimen GD-06.



Figure 3.15: Specimen GD-06 at the end of the monotonic test.

3.5.2 Cyclic Test (concentric-sheathed specimen, GD-19 & C-SW-2).

Regarding the cyclic test, at displacements equal to ±18 mm (the first cycle with $\delta = \delta_y$), there were some localized yielding near the corners of the walls and cross-shape folds started developing as a result of cyclical fatigue. The cross shaped folds became denser as the load increased to ±36 mm and they were more defined and scattered throughout the sheathing in specimen C-SW-2, as shown in Figure 3.16. In addition, at a displacement level equal to ±54 mm, the formation of inelastic tension field across both diagonals has already resulted in deformations in the sheathing, as indicated in Figure 3.17. Both specimens reached their peak loads at a displacement equal to ±72 mm and a base shear of 105 kN and 117 kN for specimens GD-19 and C-SW-2, respectively. Furthermore, at this displacement level, the studs at both ends of the walls started buckling in flexure as displayed in Figure 3.18.



Figure 3.16: Development of cross shaped folds, specimen GD-19 (left); specimen C-SW-2 (right).



Figure 3.17: Permanent deformations in specimen GD-19 at a displacement level equal to 54 mm.



Figure 3.18:Buckling of end studs due to cyclic loading, specimen GD-19 (left); specimen C-SW-2 (right).



Figure 3.19: Tension field development across the full length of the panel, specimen GD-19 (left); specimen C-SW-2 (right).

The difference in specimen behaviour due to the addition of the intermediate stud is visibly demonstrated by Figure 3.19. The intermediate stud does retain considerable stiffness when compared to the thin steel sheathing and thus it is capable of providing a certain degree of

anchorage to the tension field. Hence the added stiffness led to the development of two tension field accros the length of the sheathing. This phenomenon can be also observed by re-examing Figure 3.16 where at similar displacements, specimen C-SW-2 developed several cross-shaped folds when compared to specime GD-19.

When the next block of three horizontal cycles were applied (corresponding to a displacement equal to ±108 mm), the cross shaped folds in the sheathing advanced into tears, and tears near the bottom of the studs were also apparent, 50 mm above the hold-down. This phenomenon only took place in specimen C-SW-2 and specimen GD-19 hadn't exhibited any fracture or tear at this displacement level (refer to Figure 3.20). The addition of the intermediate stud provided additional support for a more uniform tension field to develop at this displacement level and as a result there were higher forces on the end studs. The load reversals at this displacement level caused the stud to buckle in compression and then straighten in the subsequent cycle. The repition of severe cyclic bending eventually resulted in tearing of the material.



Figure 3.20: Development of cross shaped tears and tearing of the end studs in specimen C-SW-2 due to accumulation of plastic strain.

At very high displacement levels (±144 mm), specimen GD-19 suffered tearing due to bearing screw deformations, in addition to shear failure to several high-strength bolts at the location of the hold-down. Similarly, the end stud of specimen C-SW-2 underwent severe tearing and shearing off of the screw connections, which led to separation of the built-up members (Figure 3.21). The load bearing capacity of both specimens dropped to 85% of their respective peak load at this level and the test was terminated. The final failure of each specimen is shown in Figure 3.22.

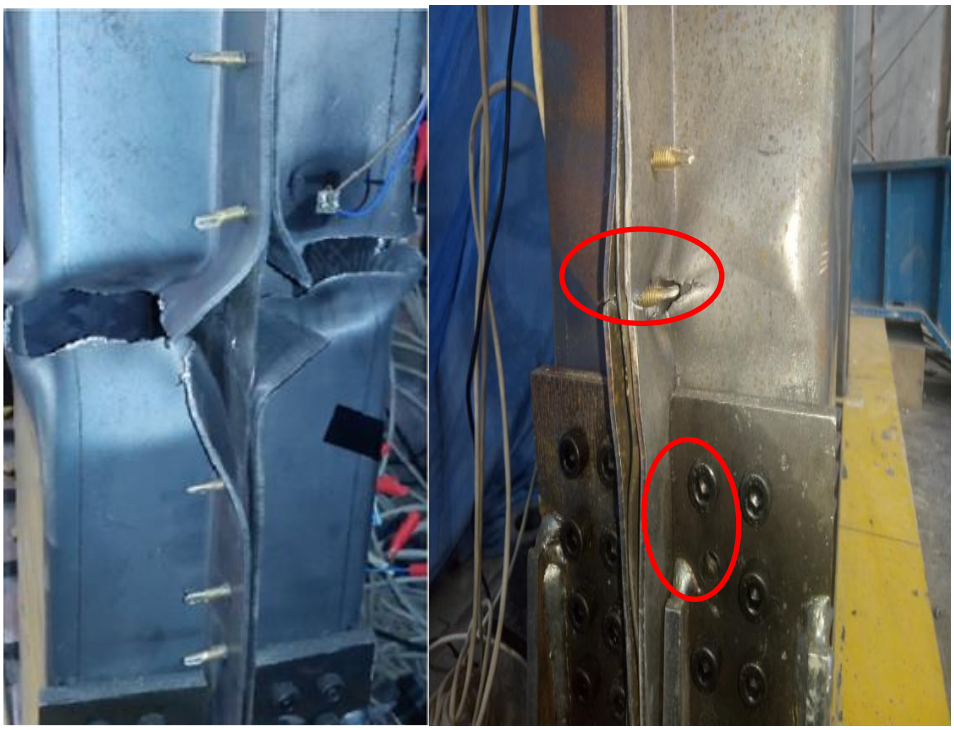


Figure 3.21: Fracture and screw bearing damage in the studs. Specimen C-SW-2 (right); specimen GD-19 (right).



Figure 3.22: Final failure of specimen GD-19 and specimen C-SW-2.

3.5.3 Cyclic Test (diagonally strapped specimen, GD-10).

The failure modes that were observed in the diagonally strapped specimen were generally similar to the ones observed in the concentric-sheathed specimens. As displayed in Figure 3.23, these failure modes include cross-shaped folds due to inelastic load reversals, and localized yielding at the corners of the shear wall. A key difference observed in this specimen was the buckling and elongation of the strap braces, which occurred at low displacement levels due to the high slenderness ratio of the straps.



Figure 3.23: Cross shaped folds and inelastic shear buckling of the sheathing (left); buckling of the diagonal straps (right).

A unique failure mode was encountered in this specimen in the form of plastic bending deformations to the hold-downs. At displacement levels equal to ± 72 mm, the end studs were subjected to flexural buckling that occurred just above the location of the hold-downs. When the drift was increased to 81 mm in the next cycle, the buckling of the studs was extremely severe

such that it ensued in bending deformations in the top spine of the hold-down. The vertical component of the tension field is largest at the column base, combined with axial forces due to the bracing members resulted in a large force at the face of the hold-down that caused flexural buckling in the stud along with inelastic bending deformations in the hold-down. In addition, the accumulation of plastic strains due to the load reversals caused fracture damage in the studs and shearing damage to the screws, as displayed in Figure 3.24. The aforementioned failures resulted in a substantial deterioration of the specimen's load bearing capacity and the test had to be terminated. The final failure of specimen GD-10 is presented in Figure 3.25.

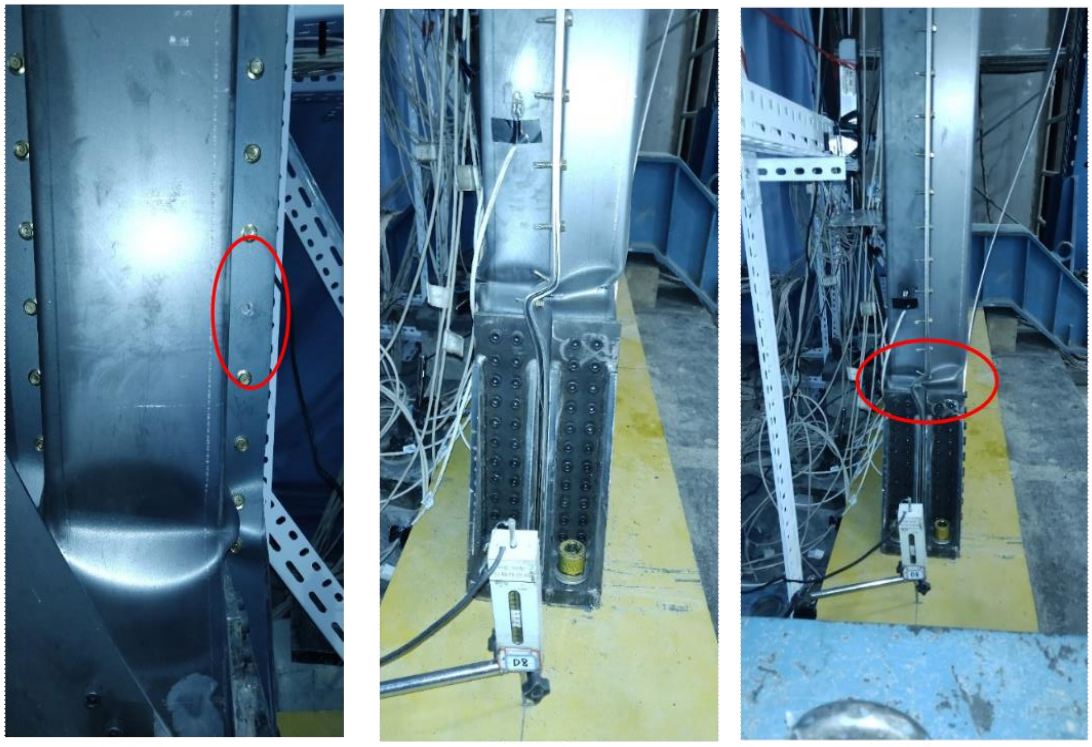


Figure 3.24: Failure modes of specimen GD-10 at high displacements. (a) Shear damage to screws; (b) Tear and fracture to end studs; (c) Bending deformations to the hold-downs.



Figure 3.25: Final failure of specimen GD-10.

Based on the preceding discussion, it can be inferred that the controlling failure mode in all specimens is the buckling of the end studs. The storey shear is mainly resisted by a combination of tension field action in the sheathing and portal frame action. The tension field in turn brought upon a combination of axial forces and bending moments on the end studs, which exceeded the end stud's capacity and resulted in premature buckling thus preventing the sheathing from developing its full resistance. These findings were consistent with previous high-capacity CFS shear wall testing programs conducted at McGill university [11], [12], where the framing failure was remedied by installing reinforcing studs to the frames as discussed in Chapter 2. Unfortunately, the work presented herein does not include any modifications to the design of the specimen, mainly due to the pandemic. It should be also noted that in all experiments, no

damage was observed in any of the tracks (no uplift or any sort of screw deformation), particularly due to the rigid connection to the control beams of the test frame.

Framing failure is highly undesirable since it compromises the gravity load-bearing capacity of the frame which may eventually lead to a sudden collapse of the whole system. Furthermore, to be consistent with capacity-based design approach as recommended by AISI S400 Standard [10], framing failure has to be avoided in order for the system to develop inelastic displacements through a fuse element. For the concentric-sheathed specimen, the designated energy dissipating mechanism is the sheathing-to-framing screw bearing deformations while for the diagonally strapped specimen, the mechanism is a combination of strap yielding and screw bearing deformations.

Even with the premature failure of the studs, the specimen exhibited considerable shear capacity and ductility, especially when compared to code-approved walls (more on that subject in the following chapter). While the concentric placement of the sheathing between built-up studs was advantageous in improving the screw bearing deformations and preventing the sheathing from detaching from the studs, attaching the sheathing through both flanges of the built-up studs resulted in higher forces on the frame that were unaccounted for. This issue will be further addressed in Chapter 6.

3.6 Connection Tests in Double Shear

Two unique connection assemblies for screws in double shear were constructed and tested in this research to determine the capacity of screw connections in double shear (3-ply

configuration). To replicate the connection conditions in the CFS shear walls, six self-tapping screws were drilled through a piece of sheathing (0.8 mm) confined between built-up hat sections (2.5 mm). As shown in

Figure 3.26, the steel sheathing is reinforced using 5 mm thick connection plates and 10 M8 high-strength bolts to prevent the sheathing from buckling under compressive loads. Similarly, connection plates were also attached to both sides of the flanges and webs of the hat-sections. The connecting plates were then welded to the connection test apparatus and the assembly was loaded repeatedly at low cycles. The minimum end distance for each specimen was 50 mm.

The testing apparatus consists of a Servo-Hydraulic Universal Testing Machine which adopts a displacement-controlled loading protocol. The yield displacement was first obtained from a separate monotonic test [1]. For the cyclic tests, the yield displacement was first applied in four cycles. Post-yield, the specimen was subjected to three cycles of increasing displacement load with an increment equal to $0.5 \times \delta_y$ per increment. The test was completed when the load dropped to 85% of the peak load. The details of the screw test schedule can be found in Table 2.

Table 2: Screw connection test schedule.

Test ID	Screw Diameter	Screw Spacing	No. of Screws	Sheathing Thickness	Loading
2-3	5.5 mm	50 mm	6	0.8 mm	Cyclic
2-4	5.5 mm	50 mm	6	0.8 mm	Cyclic

During the test, the screws did not exhibit any tilting or shear failure. Hence the bearing strength

of the confined sheathing was the controlling failure mode in both tests. The connection plates prevented any buckling in the sheathing or the studs and as a result there was no visible damage in the studs. As the cyclic load was being applied to the sheathing, bearing damage started to form around the fasteners. When the displacement was increased, the bearing damage diameter around the holes gradually increased until severe tears were visible and the test had to be terminated, as displayed in Figure 3.26.

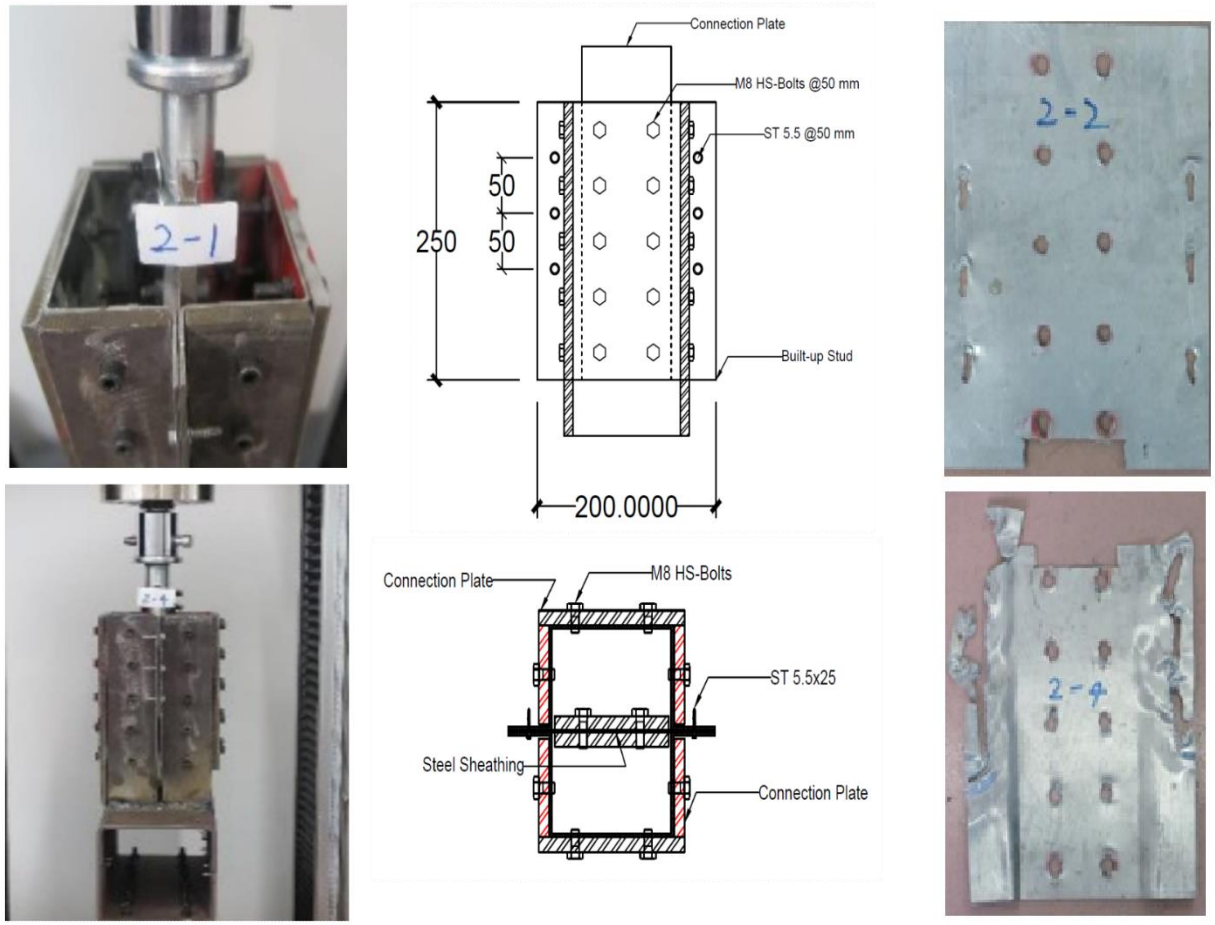


Figure 3.26: Screw connection test setup and failure modes.

3.7 Coupon Material Tests

The materials that make up the assembly of shear wall specimen were subjected to material characterization coupon tests according to the Chinese Standard for metallic materials tensile test [59]. Four coupon tests corresponding to virgin steel thickness of 0.8, 1.5, and 2.5 were conducted. For each thickness, three samples are reported in Table 3 below with one sample being discarded and considered as an outlier.

Table 3: Coupon material test results.

Sample Number	Nominal thickness (mm)	F_y (MPa)	F_u (MPa)	% Elongation	E (MPa)
1-1	0.8	171	300	80	160895
1-2		165	290	81	152597
1-3		165	290	80.5	148477
2-1	1.5	452.5	560	38.5	194385
2-2		450	580	40.5	225219
2-3		452.5	575	38	211716
3-1	2.5	412.5	540	51	192415
3-2		397.5	525	50	172895
3-3		407.5	525	50.5	179406

Chapter 4: Analysis and Interpretation of Test Results

4.1 Introduction

The main objective of this chapter is to quantify the performance of each shear wall specimen and to provide test data for the calibration of finite element models. The base shear versus drift plots for each specimen are first presented. Then, the hysteretic behaviour of the specimens is evaluated on a cycle-by-cycle basis. Aspects of major interest include cumulative dissipated energy and cyclic stiffness. In the following section, the walls are analyzed using the Equivalent Energy Elastic-Plastic (EEEP) method [15], [61], [62] to extract several key design parameters such as ductility, elastic stiffness and load level at which yielding first occurs. The chapter concludes with a summary of the connection test results.

4.2 Hysteretic Behaviour

4.2.1 Base Shear versus Lateral Drift Curves

The global response of each specimen is displayed in Figure 4.1 through Figure 4.4. The response is characterized by pinched hysteresis loops in which the severity of pinching increases as the displacement load increases, which is typical of CFS shear walls. It should be noted that there is a slight asymmetry in the response of specimen C-SW-2 because the right stud (the stud in the "pull" direction) underwent pre-mature tearing before the left stud due to extreme plastic strain reversals. The specimens' response can be divided into several stages based on the main load bearing mechanism. These stages are: elastic stage, sheathing post-buckling stage, end stud post-

buckling stage, and, exclusive for the diagonally strapped specimen, hold-down failure stage. Each stage is indicated on the corresponding base shear-lateral drift plots as illustrated below.

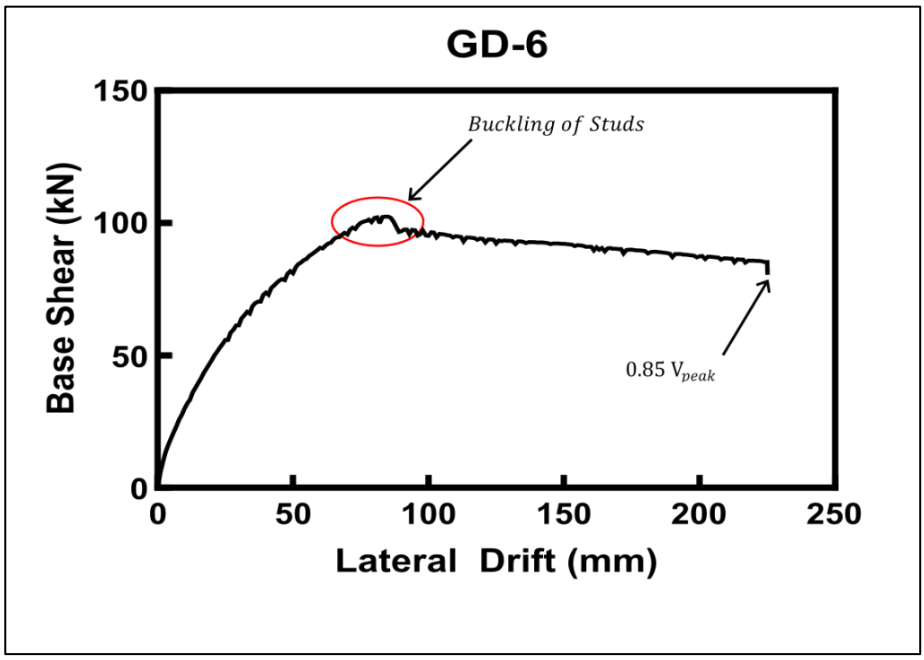


Figure 4.1: Base shear vs storey drift plot for specimen GD-06.

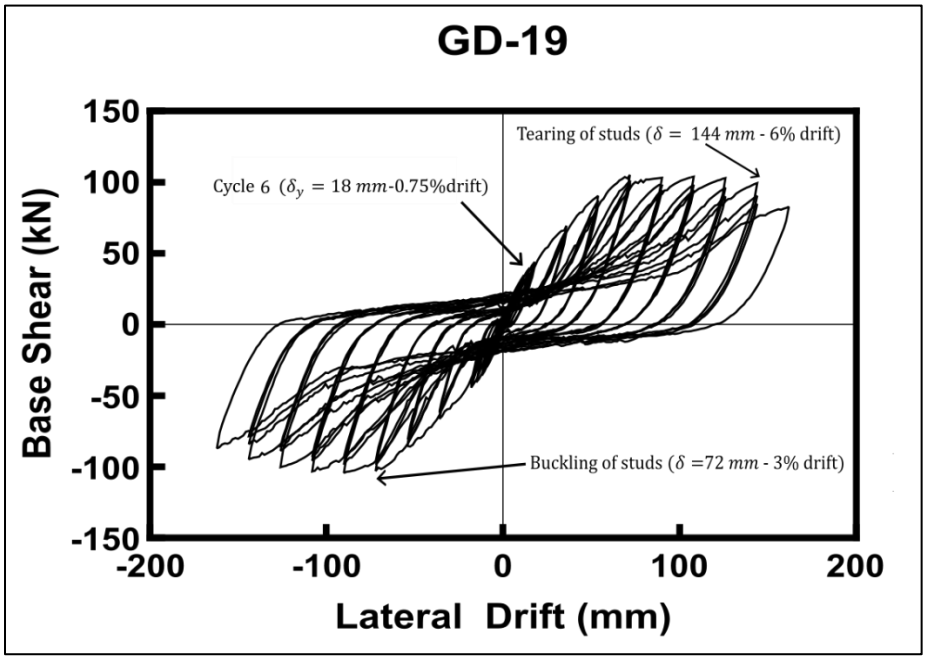


Figure 4.2: Base shear vs storey drift plot for specimen GD-19.

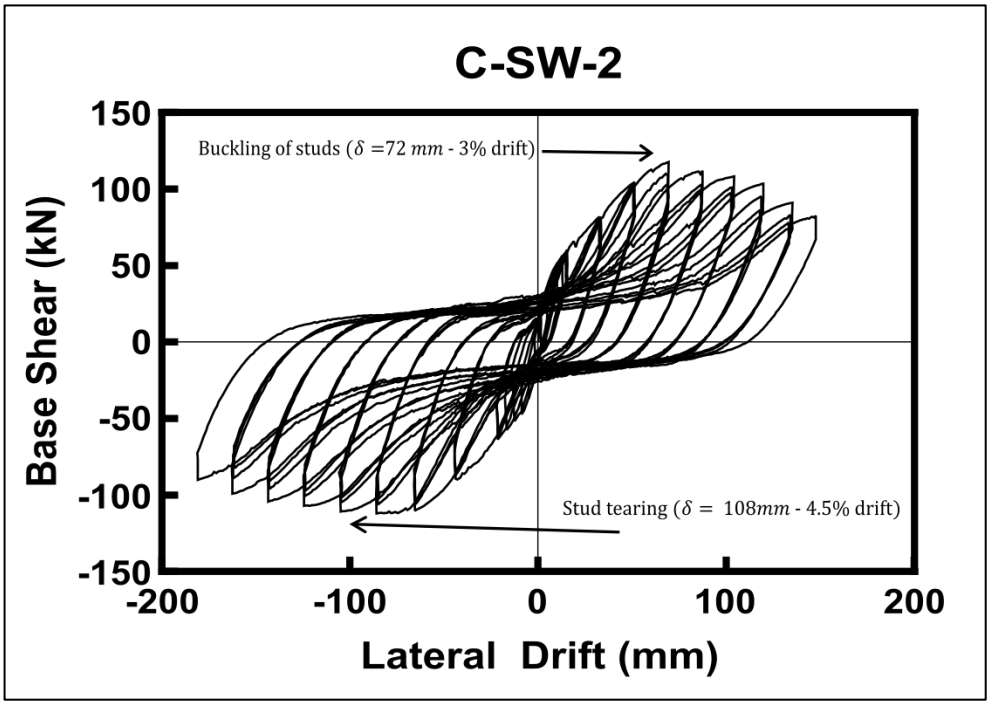


Figure 4.3: Base shear vs storey drift plot for specimen C-SW-2.

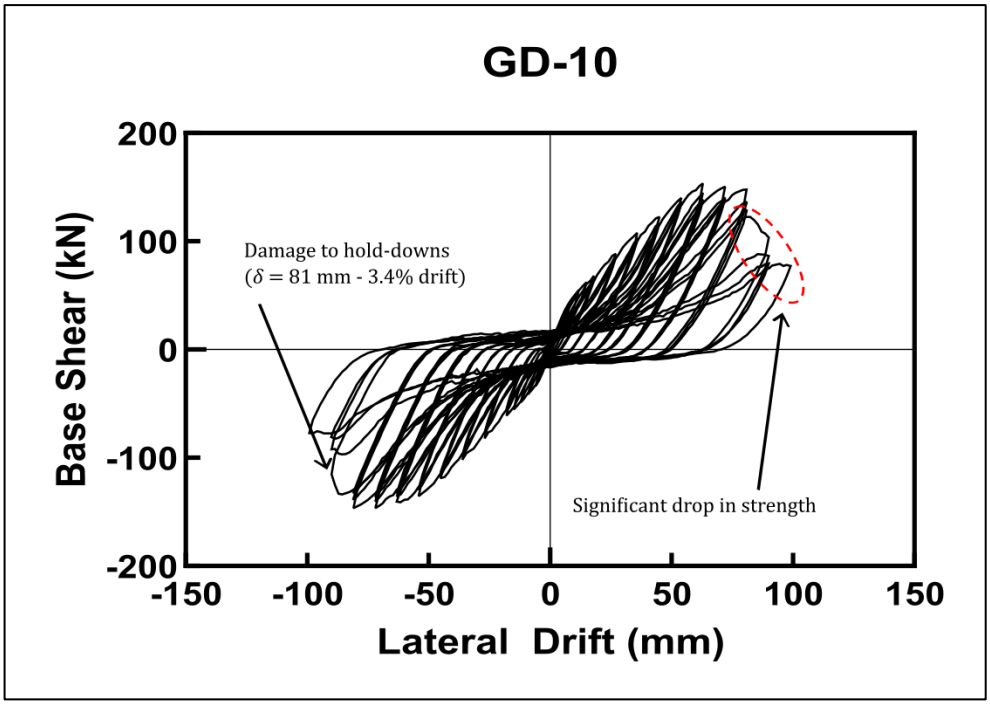


Figure 4.4: Base shear vs storey drift plot for specimen GD-10.

The hysteretic behaviour of the specimens can be understood by analyzing a typical isolated hysteresis loop at each stage. Figure 4.5 shows sample hysteresis loops for specimen GD-19 at the elastic stage (slightly modified to represent a closed curve), sheathing post-buckling stage, and finally, end stud post-buckling stage. During the first 10 cycles, in which the displacement does not exceed the yield displacement ($\delta < 18$ mm), the response of the specimen is linear and relatively stiff, and the loading reversals did not result in any noticeable strength or stiffness degradation. There was some localized yielding in the corners of the sheathing panel, however the local yielding did not have any significant effect on the global base shear versus drift response of the specimen. As the magnitude of displacement was extended beyond the yield stage ($\delta_y \leq \delta \leq 72$ mm), the hysteresis curves started to take shape as the formation of the tension field across the diagonals resulted in consistent but severely pinched hysteresis curves, as shown in Figure 4.5 (b). As the drift is increased and the subsequent displacement increment is applied, the maximum load in the shear wall increases yet there is a slight reduction in stiffness. At this stage, the slight reduction in stiffness is a result of the inelastic deformations that are taking place within the sheathing. At each load excursion, the diagonals of the sheathing undergo plastic strains and thus elongate as the tension field forms. This mechanism of "plastic elongation" can be observed by re-inspecting Figure 3.17 in the previous chapter, where the sheathing displayed multiple out-of-plane buckles when the load returned to zero after the specimen was subjected to a 54 mm displacement.

As the displacement is increased, each displacement cycle attains slightly higher loads until the maximum base shear of 105 kN was reached at a displacement level of 72 mm. The studs have

buckled at this stage ($\delta \geq 72$) and the hysteresis curve resembles an inverted "Z", as displayed in Figure 4.5 (c).

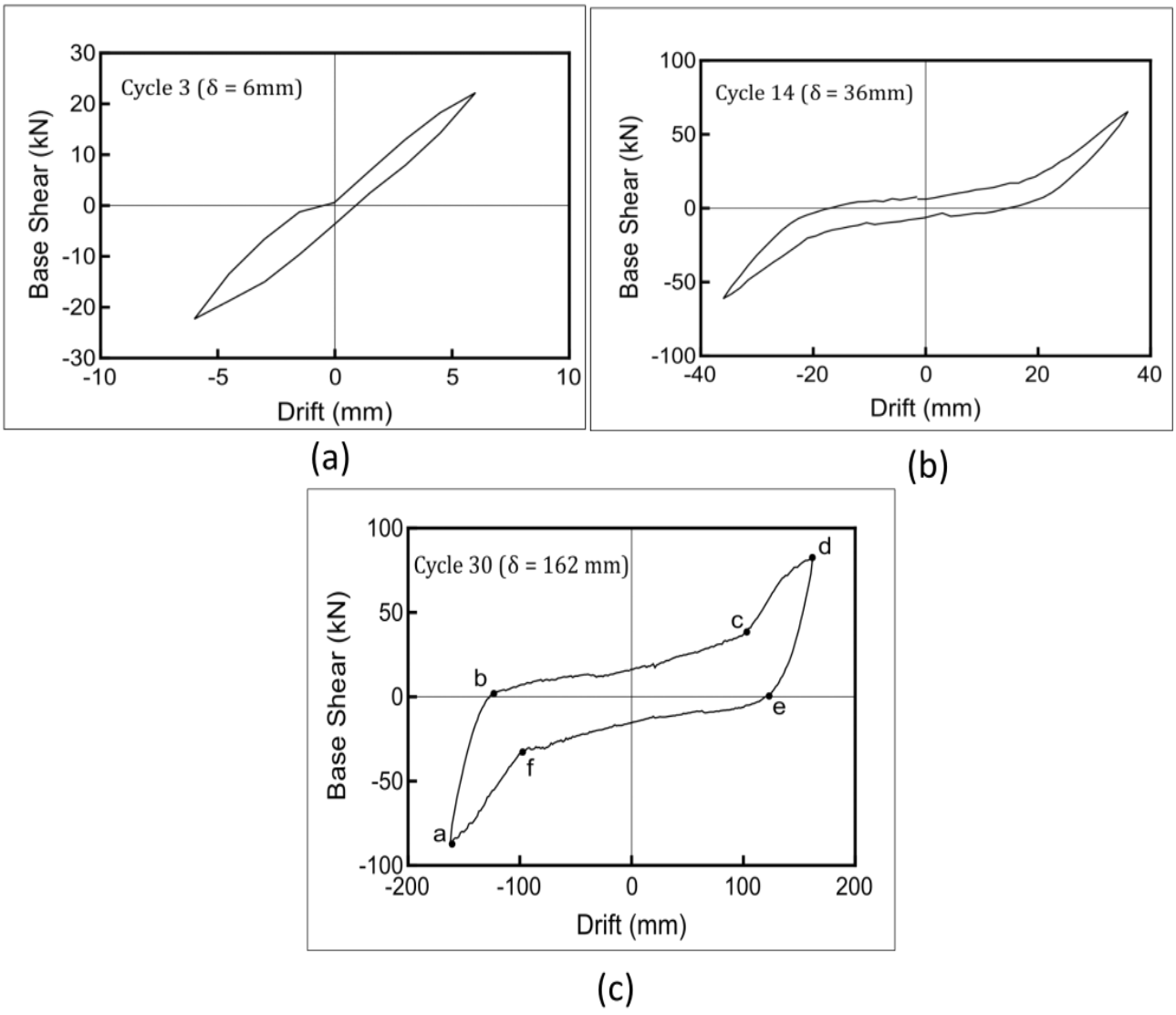


Figure 4.5: Isolated hysteresis loops for specimen GD-19 at different stages of loading. (a) Elastic stage; (b) Sheathing post-buckling stage; (c) End studs post-buckling stage.

Referring to Figure 4.5 (c), point d corresponds to the maximum displacement in this cycle when the specimen is loaded in the "pull" direction. As the loading is reversed, the response follows path $d - e$, which is characterized by a stiffness nearly equivalent to the elastic stiffness. With

increased displacements in the "push" direction, there is a significant drop in the specimen's stiffness which is produced by the re-orientation of the tension field. This phenomenon can be visualized by assessing portion $e - f$, where the stiffness of that portion is relatively flat and the load is being resisted mainly by the boundary frame. Similarly, portion $f - a$ is achieved once the stiffness of the specimen increases due to the formation of the tension field in the other direction. As the next increment is applied, the whole process is repeated although the strength of the wall gradually degrades which manifests in lower attained load. At this stage the drop in maximum load is due to the buckling of the studs. Nonetheless, the strength degradation per cycle is very slow as the base shear only dropped about 7% between successive increments. It wasn't until tears started forming due to bearing screw deformations at higher displacements ($\delta = 144$ mm) that the load bearing capacity dropped below 85% of the maximum base shear. Similar behaviour was observed in specimen C-SW-2, although the tearing of the studs occurred at a lower displacement level and the strength degradation occurred at a slightly faster rate.

Conversely for specimen GD-10, the plastic deformations in the hold-downs which occurred at a displacement equal to 81 mm released a large amount of energy which is reflected in a rather steep drop in the base shear versus drift curve, as annotated in Figure 4.4.

4.2.2 Energy Dissipation

In this section, the total dissipated energy of each specimen is calculated on a cycle-by-cycle basis. As illustrated in Figure 4.6 below, the energy dissipation capacity of each specimen ($\sum E_{TOT}$) was obtained by summing the areas encompassing each hysteresis loop. The area of

each loop was calculated using the trapezoidal rule on MATLAB without differentiating between the energies dissipated during positive or negative cycles.

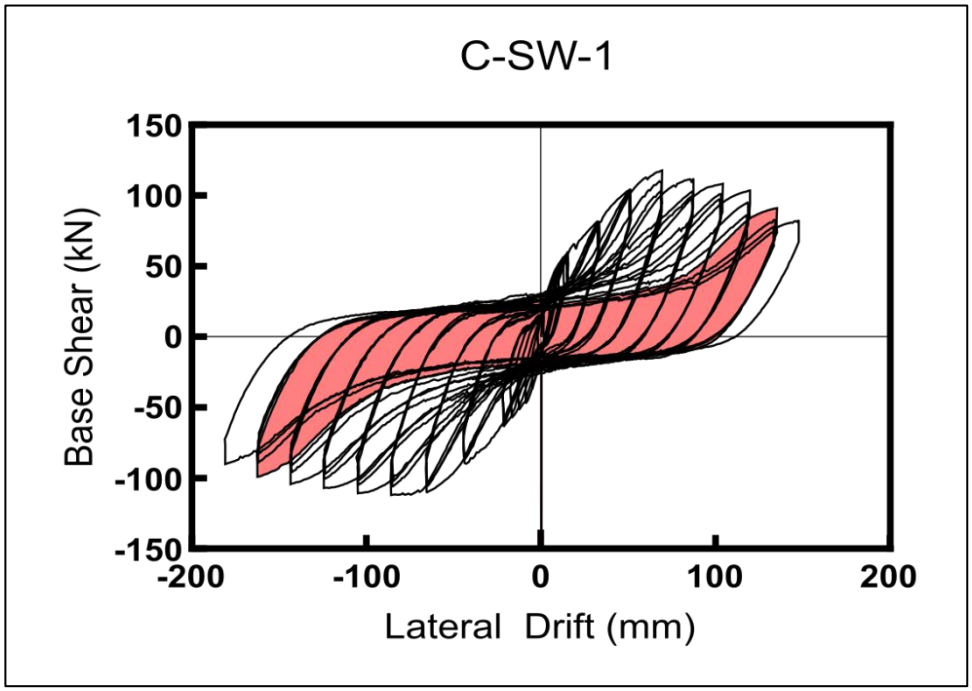


Figure 4.6: Energy dissipated per cycle.

Figure 4.7 shows the cumulative energy absorbed by each specimen per cycle. This value is significant in seismic design as it is a direct indication of the specimen's ductility under inelastic load reversals. The higher the dissipated energy, the more inelastic deformations a specimen can sustain under earthquakes. Since both specimens were subjected to different loading protocols, the cumulative energy is plotted against the overall drift rather than the number of cycles.

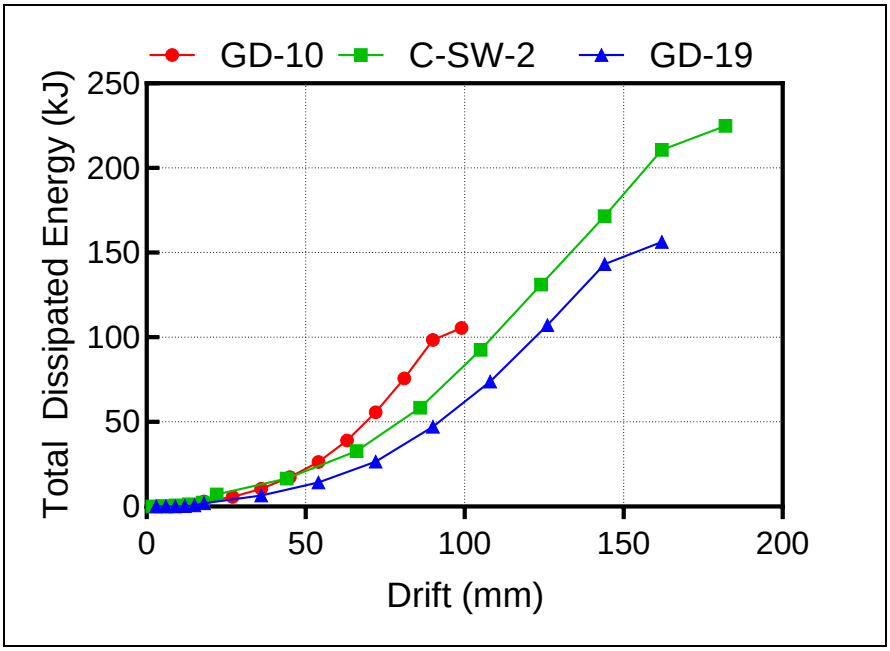


Figure 4.7: Cumulative energy absorbed by each specimen through the test.

4.2.3 Cyclic Stiffness Degradation

The cyclic stiffness degradation of each specimen was calculated next. This parameter represents the stiffness of the specimens at each loading stage and can be used to measure the stiffness degradation of the system, which in turn represents the effects of accumulated damage and non-linear material behaviour during an earthquake. The stiffness of each cycle was calculated based on Eq. (4.1) [60]:

$$K = \frac{|F_i| + |-F_i|}{|\Delta_i| + |-\Delta_i|} \quad \textbf{(4.1)}$$

where F_i is the peak load in the cycle in the positive and negative directions, and Δ_i is the corresponding displacement. Graphically, the cyclic stiffness can be determined by calculating the slope of the line connecting point d and a in Figure 4.5.

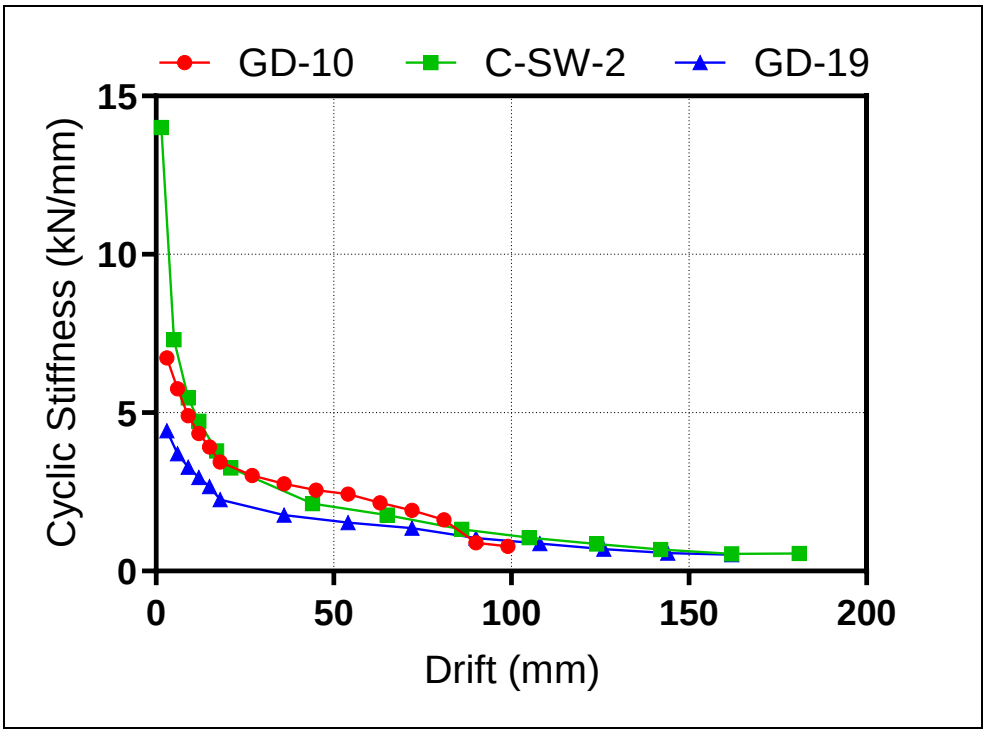


Figure 4.8: Cyclic stiffness degradation for each specimen.

4.3 Test Analysis by the EEEP Method

The EEEP method, which is first introduced by Park [15] then modified by Foliente [61], involves simplifying the highly non-linear base shear-lateral drift curve of a shear wall specimen into a bilinear elastic-perfectly plastic curve. The basic concept of this method states that the energy dissipated during a monotonic or cyclic test, which is equivalent to the area under the force-deformation curve, is equal to the area under the bilinear EEEP curve, as displayed in Figure 4.9. The resulting elastic-perfectly plastic curve is then used to determine the walls' yield resistance and its corresponding drift (V_{yield} & Δ_{yield}), elastic stiffness (k_e), and ductility (μ).

As stated in Chapter 1, the AISI S400 Standard [10] offers design values for steel sheathed shear walls based on various building parameters. The nominal shear resistance values in the Canadian

tables are based on the EEEP method. The method was also adopted by several research programs in Canada on CFS steel sheathed shear walls [6], [11], [12], [13], [34].

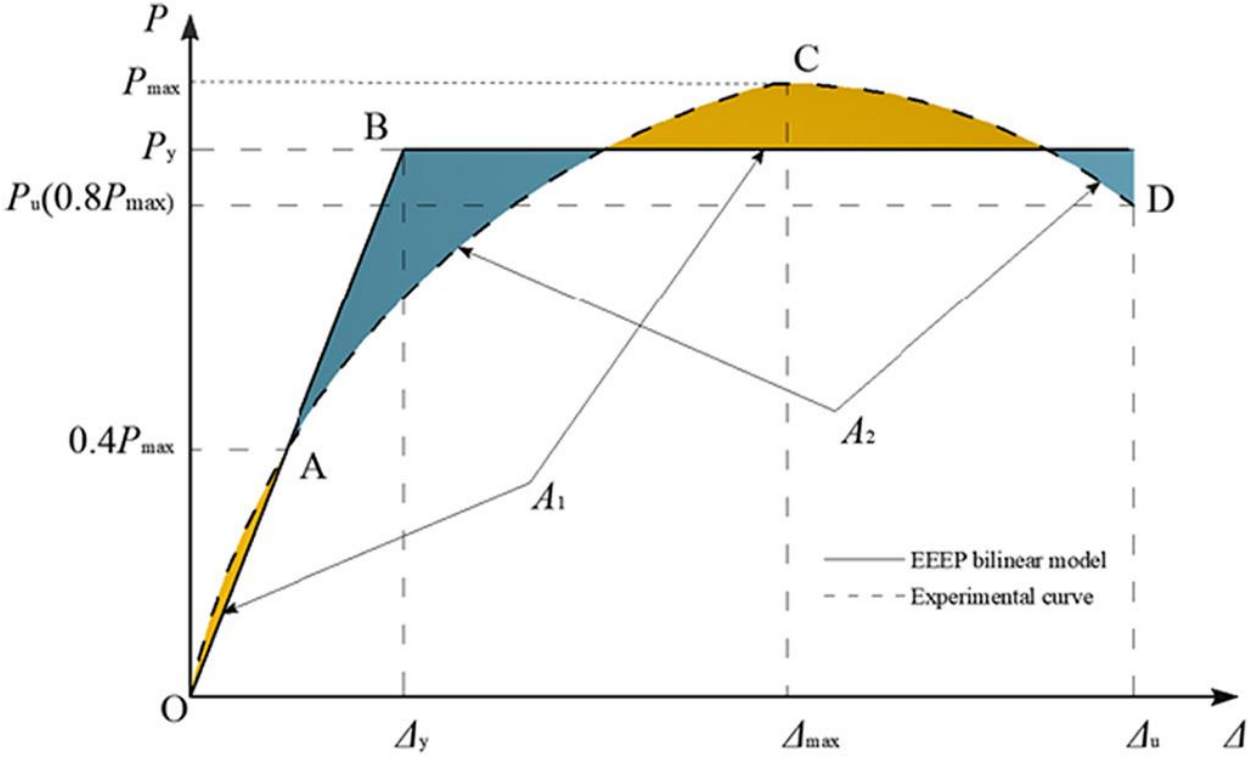


Figure 4.9: Equivalent energy elastic-plastic (EEEP) curve, retrieved from [63].

Based on the procedure stipulated in ASTM E2126-19 [62], the design parameters required for constructing an EEEP curve are the peak resistance (V_{peak}), 80% post-peak resistance ($V_{0.8}$), and 40% pre-peak resistance ($V_{0.4}$) and their corresponding drifts, (Δ_{peak}), (Δ_u), and ($\Delta_{0.4}$). These values can be readily obtained for the monotonic test however for cyclic tests, a backbone curve encompassing the peak positive and negative cycles had to be determined first. Plotting the backbone curve allows the cyclic test to be analyzed like a monotonic test and thus enables the key parameters to be extracted. The backbone curves of the specimens subjected to cyclic loading are plotted in Figure 4.11. After the relevant design parameters are identified from the

backbone/monotonic curve, the walls' yield resistance and its corresponding drift, elastic stiffness and ductility can be obtained using Eq. (4.2a) [62]:

$$V_y = \left(\Delta_u - \sqrt{\Delta_u^2 - \frac{2A}{K_e}}\right) K_e \quad \textbf{(4.2a)}$$

$$K_e = \frac{V_{0.4}}{\Delta_{0.4}} \quad \textbf{(4.2b)}$$

$$\Delta_y = \frac{V_y}{K_e} \quad \textbf{(4.2c)}$$

$$\mu = \frac{\Delta_u}{\Delta_y} \quad \textbf{(4.2d)}$$

If $\Delta_u^2 < \frac{2A}{K_e}$, it is permitted to assume $V_y = 0.85V_{peak}$

where; V_y = Yield resistance according to the EEEP curve (kN)

Δ_y = Drift at which yield resistance was achieved (mm)

μ = Ductility ratio

Δ_u = Drift at which $V_{0.8}$ was achieved post peak load (mm)

$\Delta_{0.4}$ = Drift at which $V_{0.4}$ was achieved pre-peak load (mm)

$V_{0.4}$ = 40% of the peak load (kN)

A = Area below monotonic or backbone test curve up to Δ_u (kN.mm)

Due to the ductile performance of the walls tested herein, the deflection corresponding to $V_{0.8}$ was obtained at high drift levels. It was considered unreasonable to construct the EEEP curve

according to those drift levels as a building is expected to undergo realistic drift levels during a seismic event. This behaviour was observed in all specimens except the diagonally strapped wall (GD-10).

Several studies [64] suggested enforcing a limit equal to 2.0% of the total height of the wall to be consistent with building code requirements. The work conducted at McGill implemented a limit of 100 mm which corresponds to 4% storey drift. The rationale behind this choice is that the 2.5% drift limit imposed by the NBCC [9] is too conservative since the wall specimens would not reach its ultimate resistance at that drift level. A similar limit is imposed in this report and the procedure can be visualized by investigating Figure 4.10. If the deflection corresponding to $V_{0.8}$ is used according to the definition of ASTM E2126, then the EEEP would extend to a lateral drift equal to 225 mm, which in turn corresponds to a drift ratio of 9.375%. Hence, the EEEP curve was limited to a drift of 100 mm (blue line in Figure 4.10). The EEEP curves for the rest of the specimens are shown in Figure 4.12, while the calculated design parameters are displayed in Table 4.

The final parameter that was examined in this section is the energy dissipated by the wall under the EEEP curve and the backbone curve, as indicated in Table 5. This parameter is characterized by the area under the monotonic curve, which is represented by the light blue shaded region in Figure 4.10, and the area under backbone curve for cyclic tests. In addition, the design shear flow of each specimen is shown in the last column of Table 5 for comparisons with code approved walls. This value was obtained by dividing the yield resistance ($\boldsymbol{V_y}$) by the length of each wall (1,210 mm).

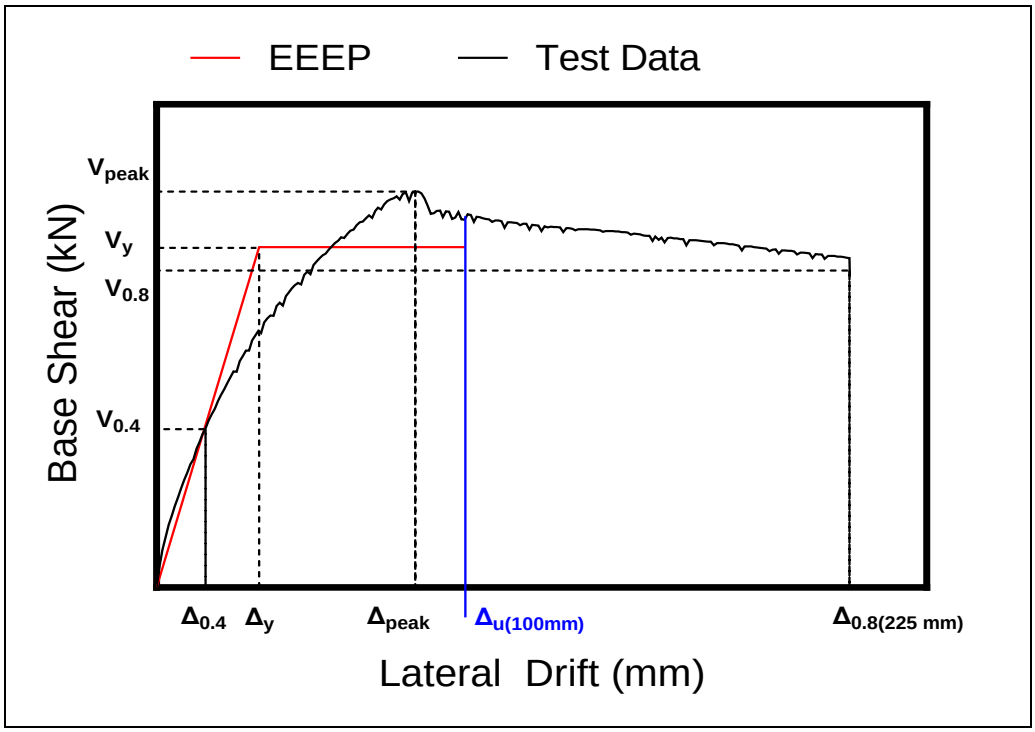


Figure 4.10: EEEP curve for monotonic test (GD-06).

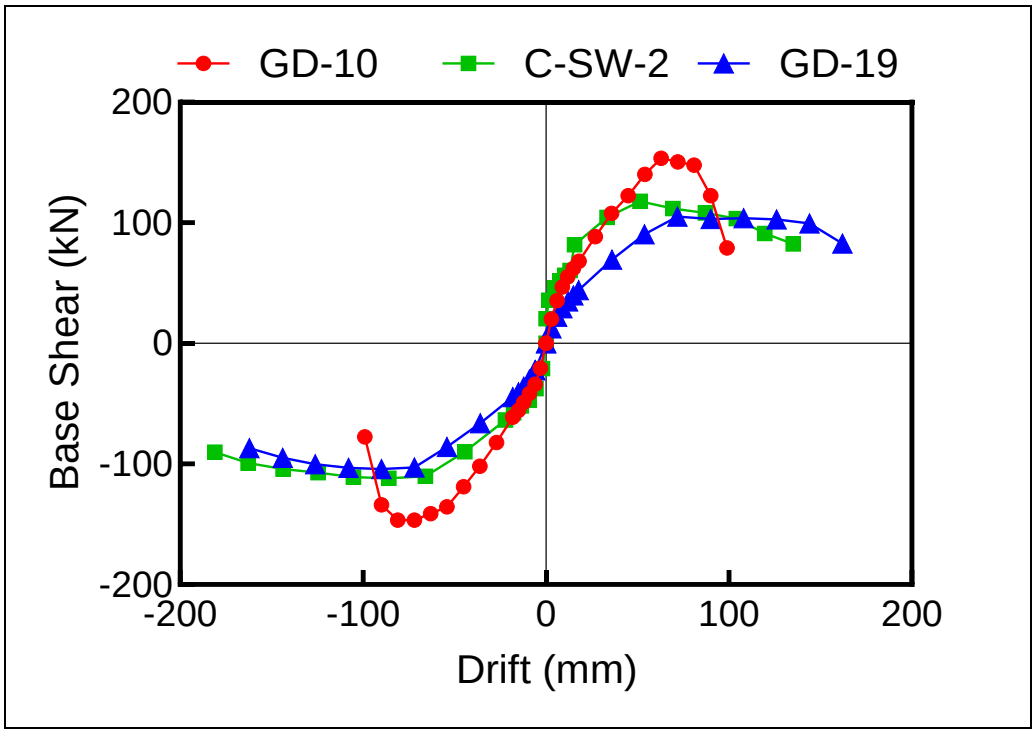


Figure 4.11: Backbone curves for the shear wall specimens.

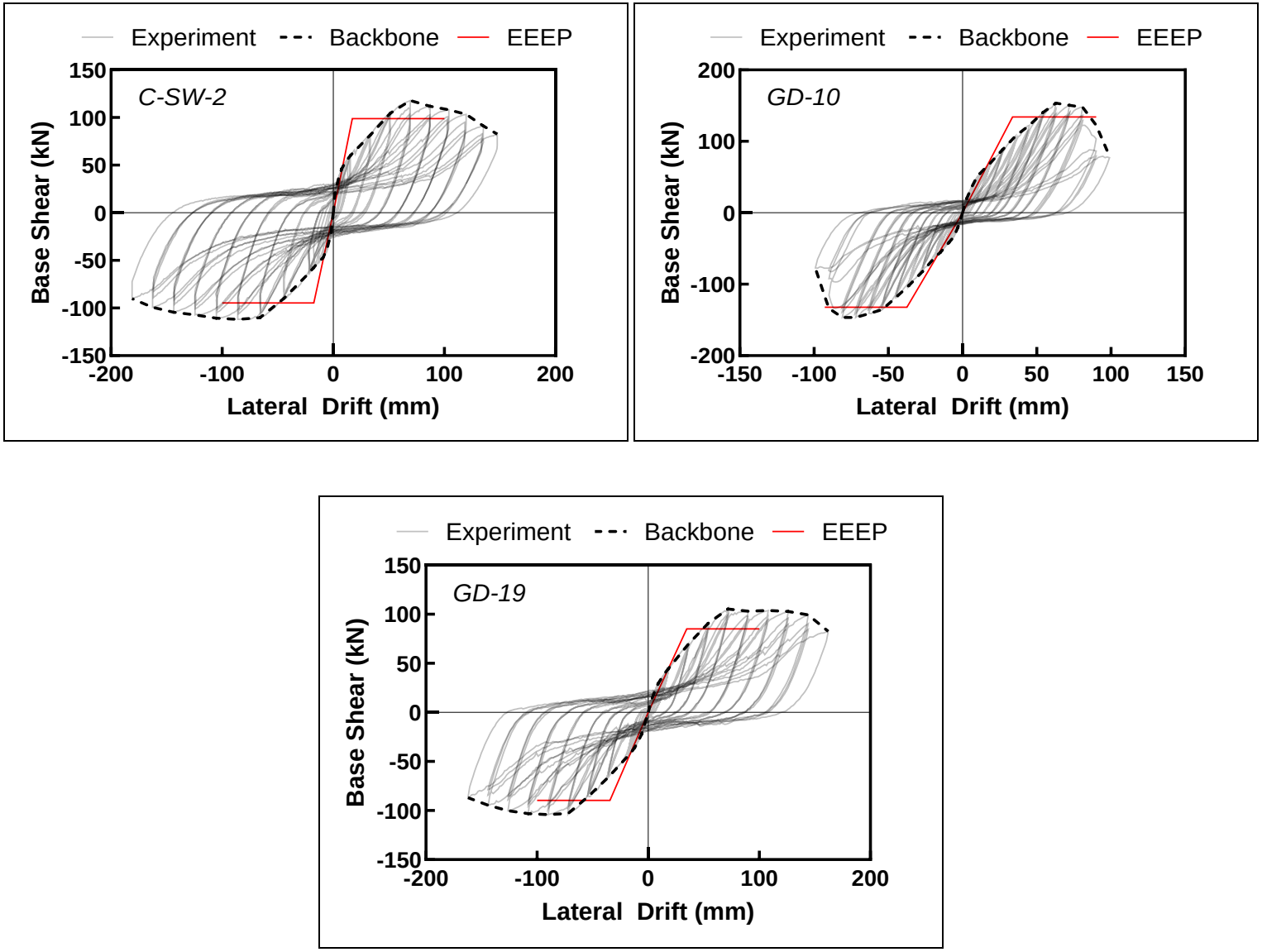


Figure 4.12: : EEEP curves for specimens C-SW-2, GD-10, and GD-19.

Table 4: EEEP design parameters

Specimen	$V_{peak}\ (kN)$	$V_y\ (kN)$	$\Delta_{peak}\ (mm)$	$\Delta_y\ (mm)$	$\Delta_u\ (mm)$	μ	$K_e\ (kN/mm)$	Drift at peak (%)	Drift at $V_{0.8}$ (%)
Positive Cycles									
GD-06	102.5	88.05	84	33.28	100	3.0	2.645	3.5	9.375
GD-19	105.29	85.23	71.96	34.76	100	2.88	2.45	3.5	6.667
C-SW-2	117.85	98.97	69.4	17.17	100	5.82	5.75	2.9	5.45
GD-10	153.5	134.225	63	33.75	90.01	2.67	3.977	2.6	3.75
Negative Cycles									
GD-19	104.1	89.63	71.99	34.31	100	2.9	2.6	4.5	6.75
C-SW-2	111.91	98.97	86	17.5	100	5.7	5.41	3.5	7.5
GD-10	146.5	132.33	72	37.5	92.67	2.47	3.53	2.6	3.86

Table 5: Energy dissipated and design shear flow values.

Specimen	$E_{EEEP}\ (J)$	$E_{Backbone}\ (J)$	$E_{TOTAL}\ (J)$	$V_n\ (kN/m)$
GD-06	7339.7	18678	18678	73
GD-19	14466.6	27265	166230	73.5
C-SW-2	17682.5	30746	225940	82.5
GD-10	19601	21100	115740	111

4.4 Comparison and Discussion of Results

Based on the results of the full-scale monotonic and cyclic tests for the proposed shear wall specimens, it can be observed that the shear resistance of all the proposed walls in this study are significantly higher than the values provided by the AISI S400 standard. For instance, if clause E2.3.1.1.3 of the standard is applied, which allows the use of two sheathings of the same material and fastener spacing on opposite sides of the wall, then the strongest shear wall according to table E2.3-1 would have a nominal shear resistance value equal to 46.6 kN/m. For the walls tested in this work, the weakest specimen (GD-6) had a yield shear resistance equal to 73 kN/m while the strongest specimen (GD-10) had a yield resistance equal to 111 kN/m, which is more than double the shear resistance of the walls listed in the standard. Moreover, the specimens could maintain this resistance at higher drifts (9% for specimen GD-06, 5.45% for specimen C-SW-2, and 3.75% for specimen GD-10). Hence, it can be concluded that one of the major objectives of this research, which is achieving higher strength and ductility, is achieved.

Re-examining Table 4, specimen GD-10 displayed the highest peak load as originally anticipated. The yielding of the strap braces, in conjunction with sheathing yielding and screw bearing deformations contributed significantly to the shear resistance of the system. On the other hand, the peak load of specimen C-SW-2 was 12% higher than specimen GD-19 due to the addition of an intermediate stud. Moreover, specimen C-SW-2 showed the highest initial stiffness overall, followed by specimen GD-10 and finally specimens GD-06/GD-19. Elastic stiffness is an important requirement for a lateral load resisting system in order to decrease storey drifts under wind and service loads. Alternatively, specimen GD-10 showed the poorest performance in terms of ductile

behaviour as its ductility factor was the lowest between all specimen (2.67), while the addition of an intermediate stud increased the ductility factor for the concentric-sheathed specimen from 4.62 to 7.67 (66% increase). The reason behind the inferior ductile performance of specimen GD-10 can be traced to the distinct failure mode experienced during the cyclic test of the specimen. As previously explained in Section 3.6.3, the hold-downs were subjected to plastic deformations at high displacements, which was reflected in a substantial decrease in the strength and stiffness of hysteresis loops and the system could not sustain any more load. Conversely, unlike specimen GD-10, both concentric-sheathed specimens displayed excellent ductile behaviour. For instance, the plastic deformation in the sheathing that occurred at lower displacement levels ($\delta \leq 72$) did not result in any degradation in the strength of the system, particularly due to the ability of the sheathing to redistribute stresses to other areas of the panel which were unaffected by inelastic deformations. Moreover, unlike specimen GD-10, the strength and stiffness deterioration of the specimens GD-19 and C-SW-2 following the buckling of the end studs was gradual and controlled, and the specimens were able to sustain inelastic load reversals for several extended cycles before terminating the test.

Inspecting the backbone curves (refer to Figure 4.11) would result in similar observations. There's a substantial difference between the peak points of specimen GD-10 when compared to the other two specimens, however the high peak is also followed by a steep descending branch, indicating poor ductility. Likewise, the backbone curves of specimen GD-19 and C-SW-2 extend to higher displacements, indicating better ductility and better energy dissipation.

The concentric-sheathed specimens' superior behaviour can also be confirmed by assessing the energy output of each system. For instance, according to Figure 4.7, specimen C-SW-2 dissipated 112.7% more energy when compared to specimen GD-10. Furthermore, the addition of the intermediate stud increased the energy dissipation capacity of the concentric-sheathed specimen by 36%, indicating a staggering increase in the ductility and dissipation capacity of the specimen at the low cost of adding an intermediate stud at both sides of the wall. The poor energy dissipation capacity of specimen GD-10 is also attributed to the failure of the hold-downs. It can be observed from Figure 4.7 that at drift levels below 80 mm, the energy dissipation capacity of specimen GD-10 is high when compared to the other two specimens. However after the hold-downs failed, the hysteresis loops of specimen GD-10 were characterized with a high degree of pinching that was reflected in low energy dissipation. Alternatively, if the specimen's dissipation capacity is compared using the energy output under the EEEP, then specimen GD-10 would have the best capacity. Nonetheless, the EEEP curves for the concentric-sheathed specimen had to be modified since they demonstrated very ductile behaviour, hence it is not recommended to compare the walls investigated herein using the energy output under the EEEP curves.

Similar conclusions can be made regarding the cyclic stiffness degradation of the specimen. At drift levels lower than 20 mm, the cyclic stiffness degradation of specimen GD-10 and C-SW-2 were almost identical, with the exception of the first cycle. This is attributed to the high elastic stiffness of both specimens as indicated in Table 4. For drift levels between 25 and 80 mm and as the sheathing is subjected to inelastic displacements, the cyclic stiffness of specimen GD-10 increases noticeably when compared to the concentric-sheathed specimens (GD-19 and C-SW-2). This increase is mainly attributed to the added stiffness brought upon by the bracing

members. Still, as the drift level approached 100 mm, there's a sudden drop in the cyclic stiffness of specimen GD-10 due to the failure of the hold-downs whereas the stiffness deterioration of specimens GD-19 and C-SW-2 was gradual and was sustained into higher drift levels (150 mm+).

To summarize, in the context of seismic design, the concentric-sheathed specimen displayed better performance when compared to the diagonally strapped specimen, even though the diagonally strapped specimen is capable of resisting much higher peak loads.

4.5 Connection Test Results

The results of the connection assemblies for screws in double shear are displayed in Figure 4.13 & Figure 4.14. Due to the growing bearing deformations (Figure 3.26), it can be observed that the response of the connection tests consists of pinched hysteresis loops that indicate acute strength and stiffness degradation. It can also be perceived that the strength degradation of the connection assemblies occurs at a displacement equal to 16 mm, suggesting that the fastener end distance doesn't have a major effect on the ultimate connection strength. The connection test results were analyzed in a similar manner to the shear walls and the key design parameters are listed in Table 6.

Table 6: Design parameters for the screw connection test.

Specimen	$P_{peak}\ (kN)$	$P_y\ (kN)$	$\Delta_{peak}\ (mm)$	$\Delta_y\ (mm)$	$\Delta_u\ (mm)$	μ	$K_e\ (kN/mm)$
Positive Cycles							
2-3	37.2	27.9	14.8	9.4	22.6	2.4	3.03
2-4	37.2	27.4	15.5	6.77	22.7	3.4	4.05
Negative Cycles							
2-3	38.4	27.1	16.1	7.9	21.02	2.7	3.02
2-4	38.7	28.1	15.08	6.5	21.5	3.3	2.7

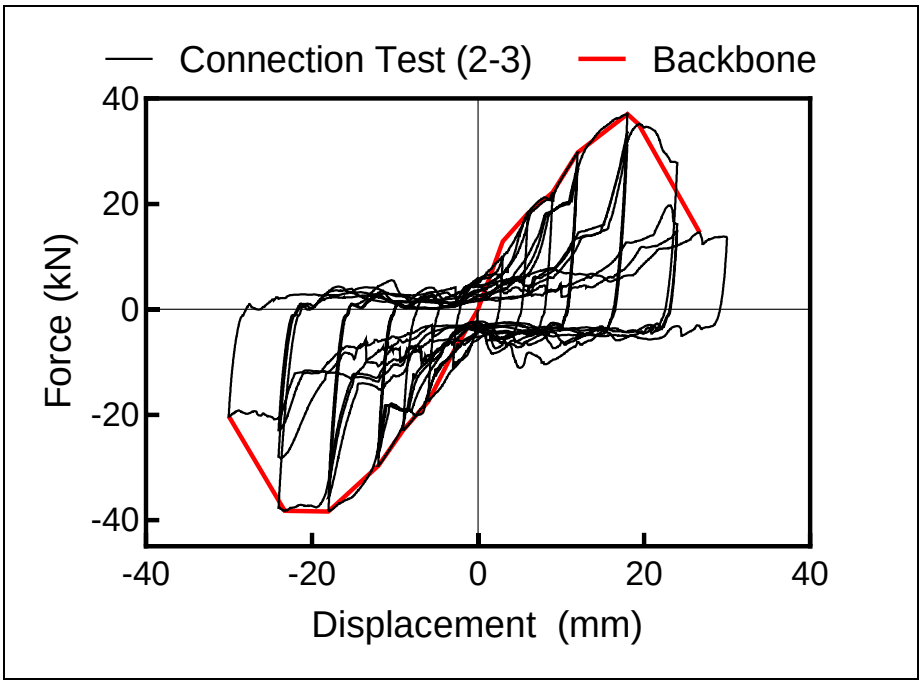


Figure 4.13: Screw connection test results (specimen 2-3)

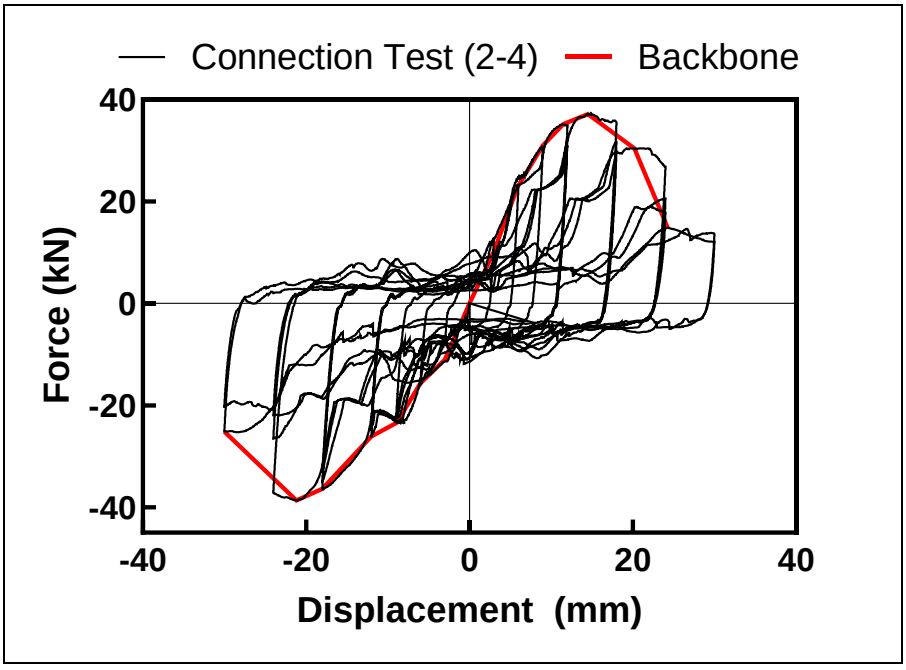


Figure 4.14: Screw connection test results (specimen 2-4)

For the purpose of validating the accuracy of the bolt bearing equation in predicting the ultimate strength of screws in double shear, the results of this section were compared with the results of

Eq. (2.6). Based on Table 6, the ultimate strength of one screw is **6.1 *kN*.** Alternatively, by applying the bolt bearing equations with a bearing factor and a modification factor equal to 3 and 1.33 respectively, the calculated ultimate strength is equal to **5.14 *kN*** (relative error equal to 17%). Hence, it can be concluded that the bolt bearing equation, at least in its current form, shows modest agreement with the connection test results discussed in this study.

4.6 Concluding Remarks

The preliminary testing program's results were analyzed in this chapter using the EEEP method and on a cycle-by-cycle basis. Accordingly, the following conclusions can be drawn:

1) The dominant failure mode in all specimens is the buckling of the end studs. This failure is undesirable since it compromises the gravity load bearing capacity of the system and prevents the sheathing from developing its full capacity.
2) All tested shear walls achieved substantially higher strengths and ductility than code approved shear walls.
3) The diagonally strapped specimen had the highest peak load, on the other hand it displayed the poorest ductility.
4) The addition of an intermediate stud to the concentric-sheathed specimen significantly increases the ductility, cyclic stiffness, and energy absorption capacity.
5) Overall, the concentric-sheathed specimen with an intermediate stud demonstrated the best seismic behaviour due to its high ductility and energy absorption capacity.
6) The bolt bearing equation showed acceptable agreement (17% relative error) with the connection test results for screws in double shear.

Chapter 5: Finite Element Modeling

5.1 Introduction

The monotonic and cyclic tests for the concentric-sheathed and the diagonally strapped walls offer valuable insight on the cyclic and collapse behaviour of such systems. Unfortunately, and due to the expensive nature of full-scale tests, the scope of building parameters that can be investigated is limited. The finite element method (FEM) has emerged as a valuable numerical tool for performing complex analyses of CFS shear walls and CFS structures in general [46]. For a numerical method such as FEM, an accurate model is essential in understanding the performance and failure modes of CFS shear walls. Additionally, FEM offers flexibility in conducting various parametric studies that cover a wide variety of building constraints and loading conditions that are too cumbersome to be achieved through laboratory testing. In this study, high fidelity shell finite element models of the shear walls were developed using the finite element software package ABAQUS [14].

Four main benchmark models were established: a pushover and a cyclic model for the concentric-sheathed wall (GD-6 and GD-19), a cyclic model for the concentric sheathed wall with an intermediate stud (C-SW-2), and finally, a cyclic model for the diagonally-braced walls (GD-10). The benchmark models were verified against the experimental results which involved quantifying properties such as ultimate wall capacity, elastic stiffness, hysteretic energy dissipation, and deformed shape. The validated models are then used to carry out various parametric studies with the aim of proposing efficient design alternatives.

In order to model the cold-formed steel shear wall specimen discussed in the previous chapter, ABAQUS generally offers two solvers: ABAQUS/Standard and ABAQUS/Explicit [65]. For non-linear problems, ABAQUS/Standard uses an iterative, implicit operator to advance the solution through time (Newton-Raphson being the most common procedure). Implicit methods require the solution algorithm to solve a set of coupled equations in order to achieve equilibrium. There are no limits on the time step in this method and the increment size is determined from accuracy and the convergence considerations. ABAQUS/Standard also has the capability of conducting general static analyses as well as transient dynamic analyses. In both cases and depending on the complexity and nonlinearity of the problem being modeled, the implicit solver might be considered computationally expensive. Alternatively, ABAQUS/Explicit uses an explicit integration technique, the central-difference method, to solve the dynamic equilibrium equations. The velocities and displacements are calculated in terms of quantities that are known at the beginning of the increment, and as a result no iterations are required. While the explicit dynamic procedure was originally developed to analyze high-speed dynamic events [14], by controlling the energy output, it can be successfully employed to solve quasi-static problems that involve complex post-buckling behaviour. The size of the time increment is limited however since the central-difference operator is conditionally stable. Thus, due to the solution technique, the explicit solver handles complex contact interactions and complex post-buckling problems with relative ease.

In the early phase of this research, models of specimens GD-06 and GD-19 were set up using the general static implicit solver. However due to the convergence problems that were encountered, the analysis of all specimens in this report were conducted using the explicit solver. The basic

solution strategy of the general static implicit solver, along with initial model details, are explained in the following sections.

5.2 Implicit Solution using ABAQUS/Standard

In a general static step, where velocities and accelerations of the system are neglected, the solution to a nonlinear stress/displacement problem in ABAQUS can be obtained by solving Eq. (5.1) [66], [67], [68]:

$$P - I = 0 \tag{5.1}$$

Where P is the vector of applied external forces (nodal, body and/or surface) on the node and I refers to the internal forces exerted on the nodes resulting from element stresses. Additionally, if the response of the structure is non-linear, the loading history is divided into increments [64] by gradually increasing the external force and calculating the displacements until an approximate static equilibrium is achieved. If the solution does not converge, the solver attempts another iteration such that the solution obtained at the end of the iteration is closer to equilibrium. However, in problems involving material and geometric non-linearities as well as complex contact interactions, the solution process might run into severe discontinuous iterations where there is a sudden change in stiffness (such as a loss of contact). The time step is then reduced, and iterations are carried out until the discontinuities are minimal and the convergence tolerance is satisfied. By default, this tolerance is set to 0.5% of an average force in the structure.

The default iterative numerical method employed by ABAQUS/Standard to solve Eq. (5.1) is the classical Newton-Raphson method. The method involves forming the structure's tangent stiffness

matrix, inverting it, and solving a set of non-linear coupled equations at the end of each iteration. As a result, there is a rather expensive computational cost per iteration. A major drawback of this method is that its prone to numerical difficulties if there is unstable behaviour in the structure being modelled and the tangent stiffness matrix cannot be inverted. Such instabilities that are encountered in modeling a CFS shear wall include the elastic buckling of the sheathing as the tension field forms, local buckling in the outer flanges of the built-up hat-section studs, and most importantly, softening in the global load-displacement response of the wall after the end stud undergoes flexural buckling.

When local instabilities exist within the structure, the strain energy gets transferred locally between parts of the model, which results in further numerical issues that prevent the solution from converging. Fortunately, for a variety of unstable problems, ABAQUS/Standard offers the option of dissipating the strain energy by applying artificial damping to the model (refer to Figure 5.1 [70]). The volume-proportional damping is added to the equilibrium equations as displayed in Eq. (5.2) [14]:

$$P - I - \underline{F_v} = 0 \quad \textbf{(5.2a)}$$

$$\underline{F_v} = c\underline{M^* v} \quad \textbf{(5.2b)}$$

in which M^* represents an artificial mass matrix with unit density, c is a damping factor, and v is a vector containing the nodal velocities per increment of time.

While the static solver supplemented with artificial damping provides a powerful tool to solve buckling problems, as proven by Schafer [44], caution should be exercised since addition of

viscous forces might change the physics of the problem being modeled. It is recommended to limit the stabilization energy output to a fraction of the internal energy of the model (about 5%) to obtain a quasi-static solution [14], [65].

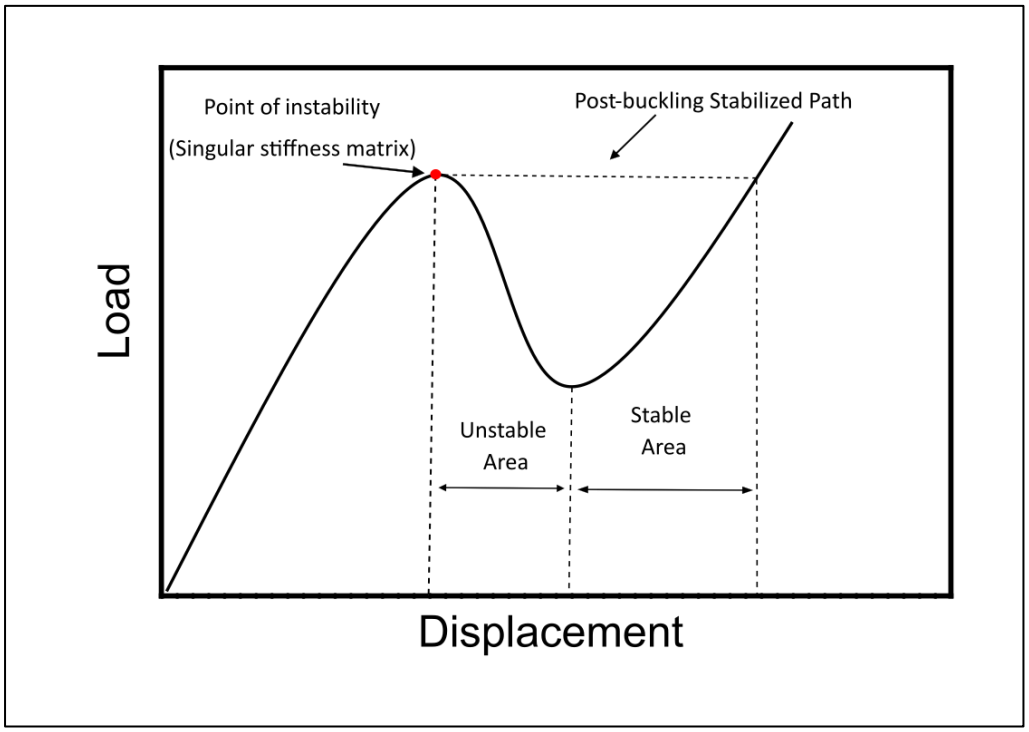


Figure 5.1: Automatic stabilization scheme when instabilities are encountered.

5.3 Initial Model Details

At earlier stages of this study, a model was setup for the purpose of validating the pushover and cyclic test of the concentric-sheathed wall. Since the displacement-controlled load in the experiments was applied at a rate such that inertial forces remained negligible, the initial models were analyzed with the general static implicit solver. Based on the recommendations of Schafer et al. [44], the model was constructed with quadratic shell elements (S8R) and material properties and nominal dimensions that are summarized in chapter 3. An elastic-perfectly plastic

constitutive material model was assigned to the shear wall parts. As shown in Figure 5.2, the initial model was able to capture the initial stiffness of the system and as well as the peak load with reasonable accuracy. The analysis, however, encountered several convergence issues and terminated at the point where the system reached its ultimate capacity. At high displacements, the solver reported negative eigenvalues and a severe cut back in the time increment (10^{-7} seconds). Negative eigenvalues signifies that the stiffness matrix is not positive definite which may physically translate to the initiation of buckling. The development of tension field due to the elastic shear buckling of the sheet and the flexural buckling of the end stud combined with the thin-wall nature of cold-formed steel members creates local and global instabilities which make it difficult to advance the solution past the point of global softening using the general static solver. Several approaches were employed to repair the convergence problems, including attempting different solution techniques such as Quasi-Newton method, switching to the dynamic implicit solver, simplifying the model by using rigid bodies, relaxing the convergence criteria, using different increment sizes, and addition of artificial damping to stabilize the model. Figure 5.3 & Figure 5.4 show the energy output of the monotonic and cyclic analyses carried out with artificial damping, respectively. For the monotonic model, the ratio of the stabilization energy to elastic strain energy is about 25%. On the other hand, the artificial stabilization energy calculated by the software to remove instabilities for the cyclic model is in orders of magnitude higher than the strain energy of the system, and both results contradict the recommendations of the ABAQUS manual that state that the viscous damping energy should be limited to a reasonable fraction (about 5%) of the total strain energy. All of the above reasons led to the decision of

employing the explicit solver to model the shear walls, specifically since a small-time increment is better suited for an explicit solution scheme.

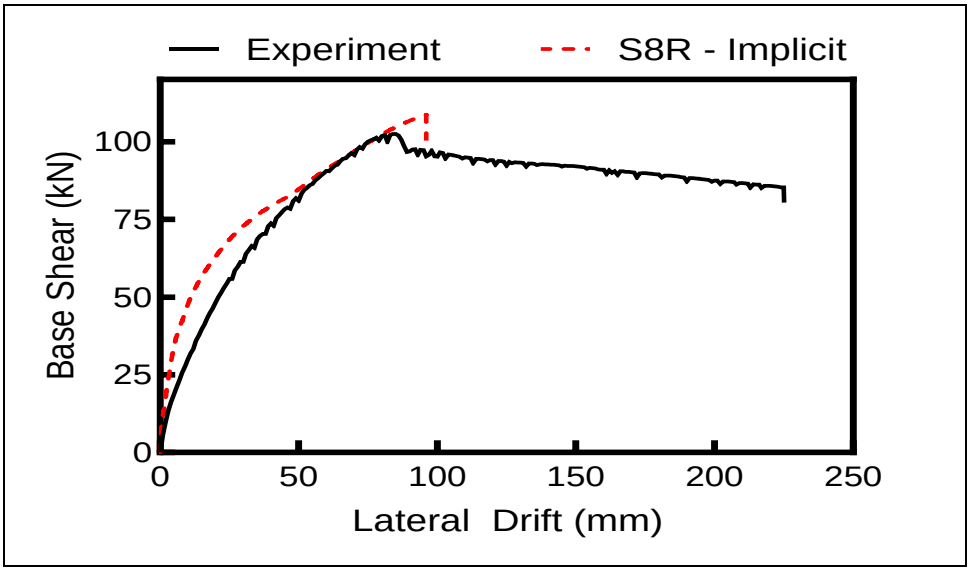


Figure 5.2: Experimental versus FEM results, general static step.

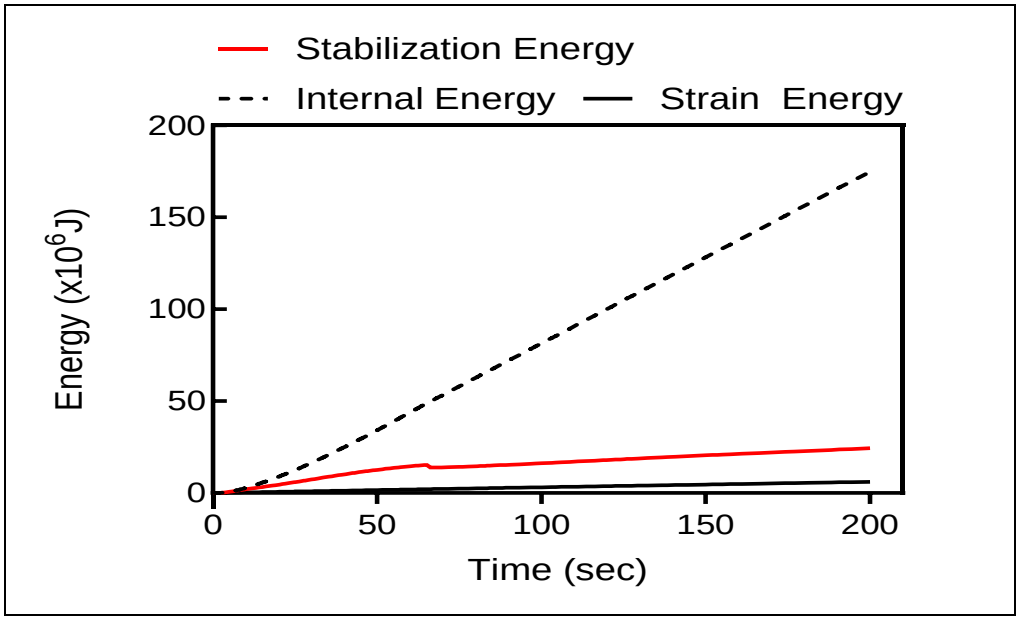


Figure 5.3: Energy output using the general static step with automatic stabilization (monotonic).

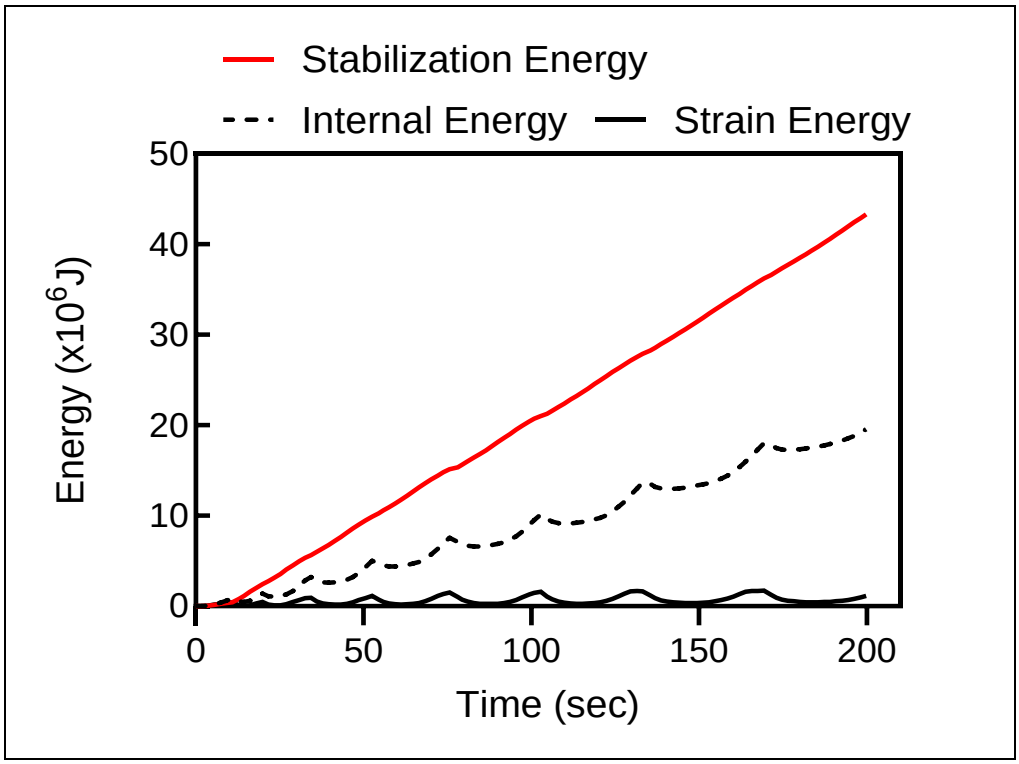


Figure 5.4: Energy output using the general static step with automatic stabilization (cyclic).

5.4 Finite Element Analysis using Explicit Dynamics

The basic difference between a static and a dynamic problem is the inclusion of D'Alembert's forces. Hence Eq. (5.1) can be re-written as:

$$P - I = \underline{M}\ddot{\underline{d}} \tag{5.3}$$

where $\underline{M}$ is the mass matrix and $\ddot{\underline{d}}$ is the acceleration vector. If the mass matrix was derived by placing the masses at the nodes, the result is a "lumped" mass matrix that is diagonal. Consequently, solving Eq. (5.3) for the acceleration becomes a trivial procedure since no coupled equations need to be solved.

The basic solution technique employed by ABAQUS/Explicit requires implementing an explicit integration rule in combination with a diagonal lumped mass matrix. Explicit integration methods are those that that solve for the kinematic state of the system using known values of displacements, velocities, and accelerations from previous increments [71]. Moreover, explicit methods do not require iterations nor inversion of the tangent stiffness matrix, thereby making explicit methods computationally attractive. The central difference rule is utilized by ABAQUS to carry out explicit dynamics. An essential property of the central difference rule, which is the stability limit, is discussed next.

5.4.1 Determining a Stable Time Step for Explicit Dynamics

As previously stated, implicit methods are unconditionally stable, meaning the time step can be increased without affecting the stability of the solution, although the accuracy might be compromised. In contrast, explicit methods are conditionally stable, indicating that the time step specified for the analysis should not exceed a critical time step otherwise the solution becomes numerically unstable or "unbounded" [66]. An unbounded solution is a diverging solution where the error continuously grows by orders of magnitude per time step. In addition, if the time step used in the analysis is too large, strains and subsequent stresses tend to localize, and the following solution is physically incorrect. In a time history analysis for instance, the response of a solution variable such as displacement will oscillate with increasing amplitudes. The stability limit for the central difference operator can be estimated in terms of the highest frequency of the structure using the Eq. (5.4):

$$\Delta t \leq \frac{2}{\omega_{max}} \tag{5.4}$$

In contrast if the specified time step is too small, the computations are unnecessarily expensive.

Recognizing that the highest frequency of the structure must be less than the highest frequency of any unassembled element of the mesh, the stability limit can be redefined as:

$$\Delta t_{\ stable} \approx \frac{L_e}{c_d} \tag{5.5}$$

in which L_e is the smallest characteristic length of the element, and c_d speed of the stress wave as it travels through a material. In turn, c_d is defined as:

$$c_d = \sqrt{\frac{E}{\rho}} \tag{5.6}$$

where E and ρ are the modulus of elasticity and density of the material, respectively. Physically, Eqs. (5.5) and (5.6) imply that the time step should be small enough such that information does not propagate more than the distance between nodes during a single time step.

Unless the stable time increment is specified by the user, ABAQUS initially determines the smallest stable time increment on an element basis. Hence the element-by-element stable time increment is controlled by the material properties and mesh size. Next, ABAQUS uses a global estimation algorithm to determine the stable time increment from the highest frequency of the model. Finally, the larger of the two values are used as the stable time increment in the analysis.

5.4.2 Obtaining a Quasi-static solution with ABAQUS/Explicit

Even though the explicit dynamic method was originally developed to model impact and blast dynamic events where inertia plays a significant role [14], the method has proven valuable in handling quasi-static problems that include severe nonlinearities and complex contact conditions, such as metal sheet forming [72]. All of the tests carried out on the CFS shear wall specimen discussed in the previous chapter were conducted under quasi-static conditions. Implementing the explicit dynamic procedure to quasi-static problems however requires special considerations, particularly in controlling the energy output. Moreover, it is impractical to simulate the aforementioned tests in their natural time scale as this would require an unnecessary number of small-time increments. Ideally, the main objective is to obtain a computationally cost-effective solution while maintaining negligible inertial effects. An approximate lower bound on the total time of a quasi-static simulation can be obtained by determining the structure's fundamental frequency. The fundamental frequency corresponds to the longest vibration period of the structure. Therefore, the loading has to be applied at a slower rate in order to avoid dynamic effects. The process consists of first performing a frequency analysis on the shear wall models to extract the frequency of the first mode. The period of the slowest mode is then calculated by taking the inverse the fundamental frequency, and the total simulation time is finally set to 10 to 50 times the natural period of the structure.

When performing quasi-static analyses with ABAQUS/Explicit, abrupt application of loads leads to a sudden upsurge in kinetic energy which in turn translates to noisy solutions that might be erroneous. To obtain a valid and efficient solution, the analysis requires the application of loads in a smooth manner such that a large change in acceleration between increments is prevented.

If the change in acceleration is smooth, then in turn the change in velocities and displacements is smooth as well. An accurate solution can be achieved by applying displacements to the structure (or velocities) using the built-in smooth step amplitude curve that's displayed in Figure 5.5. The smooth step amplitude curve automatically connects data pairs with curves whose first and second derivatives are zero at each data point. Admittedly, the smooth amplitude curve is rather efficient when performing cyclic analyses since the displacement loading only requires inputting the first and final data points of each cycle without generating any excessive stress waves due to discontinuity in the rate of the applied loading.

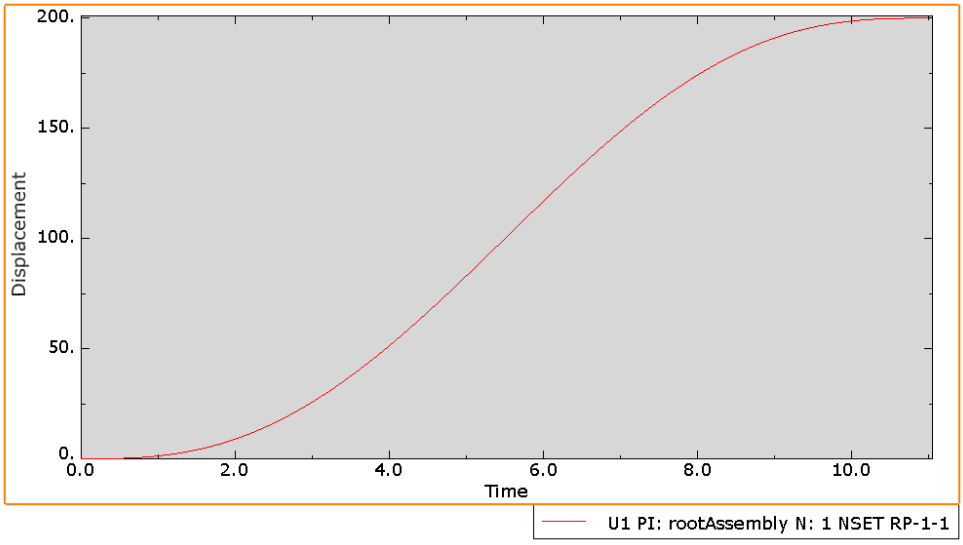


Figure 5.5: Displacement-controlled load amplitude definition using a smooth step curve.

5.4.3 Validating a Quasi-static solution with ABAQUS/Explicit

Rather than examining the stresses, strains, or deformed shape; the first step in post-processing a quasi-static simulation with the explicit solver is to validate that the inertia and energy outputs are within acceptable limits. This can be achieved by careful assessment of the energy balance equation, which states:

$$ALLIE + ALLKE + ALLVD + ALLFD - E_W = E_{TOTAL} \approx constant \quad \textbf{(5.7)}$$

where; $ALLIE$ = Total internal energy; $ALLIE = ALLSE + ALLPD + ALLCD + ALLAE$

$ALLSE$ = Stored elastic strain energy

$ALLPD$ = Energy due to plastic dissipation

$ALLCD$ = Energy dissipated by viscoelasticity

$ALLAE$ = Artificial strain energy

$ALLVD$ = Energy due to viscous dissipation

$ALLKE$ = Kinetic Energy

$ALLFD$ = Energy due to frictional dissipation

E_W = Work due to external forces

E_{TOTAL} = Total energy stored in the system.

In Eq. (5.7), ALLIE refers to the total internal energy of the system or the whole model; while ALLCD is the energy due to viscoelasticity and/or creep and is different from ALLVD. ALLVD on the other hand is the energy dissipated by bulk viscosity which is automatically introduced by ABAQUS to stabilize high frequency oscillations. ALLAE refers to artificial strain energy, and its purpose is to alleviate a pattern of non-physical deformation called hour-glassing that might be encountered in linear reduced-integration elements if the mesh is not refined adequately. Finally, ALLFD is the energy dissipated by frictional forces if friction was introduced to contact properties.

According to Eq. (5.7), to obtain a high quality quasi-static solution, the kinetic energy history must be first compared to the internal history energy. Moreover, it is recommended that the ratio of kinetic energy to internal energy remain limited to 5-10% throughout the loading history [73]. If that condition is satisfied, then the next step is to examine the kinetic energy history alone. Assuming a smooth loading has been applied to the model using the smooth-step amplitude, it is then expected that the resulting kinetic history output is smooth as well. If the kinetic energy history is noisy and shows fluctuations, the model might be experiencing severe plastic deformations at a high rate which may affect the caliber of the quasi-static solution. The last check in validating a quasi-static analysis involves evaluating the total energy output of the system and confirming that the artificial energies are only a fraction (5-10%) of the total internal energy of the system.

5.5 Explicit Finite Element Model Details

5.5.1 Element Selection and Mesh Details

Shell elements are generally recommended when the structure's thickness is significantly smaller than its other dimensions [14]. ABAQUS/Standard offers a shell library that is divided into three categories: thick, thin, and general-purpose shell elements, whereas ABAQUS/Explicit provides general purpose shell elements only. General purpose elements can be used for thick or thin shell applications (whether shear flexibility is accounted for or not). All the parts of the shear wall assemblies analyzed in this research (sheathing, studs, tracks, and hold-downs) were discretized using the S4R shell element. The S4R shell is a 4-noded, three-dimensional general purpose shell element with six degrees of freedom and linear shape functions. The element considers large

displacements and large rotations; and uses one point located at the center of the shell to form the element stiffness matrix. Reduced integration substantially decreases computational time and provides accurate results if the elements are not distorted or loaded in the plane of bending. However due to the reduced integration formulation, the element is prone to hour-glassing; which is a numerical instability caused by zero strains occurring at the single integration point of the element during its distortion [74], [75]. Hour-glassing, which is schematically shown in Figure 5.6, typically manifests as a geometrical pattern that takes a trapezoidal form or a "zig-zag" shape where individual elements are sternly deformed [65], [76], [77]. Several strategies can be used to overcome such spurious deformation modes. For instance, ABAQUS introduces artificial strain energy to limit the effects of hour-glassing in the form of "hour-glass control". Moreover, another strategy is to use a finer mesh or to distribute applied concentrated loads and boundary conditions over multiple nodes. Hence when linear reduced elements are used in the analysis, it is important to evaluate the output of artificial energy to verify that it is within acceptable limits of the total internal energy. For the work presented herein, the default hour-glass control options were sufficient in suppressing hour-glass mode.

Based on the preceding discussion, a fine mesh consisting of global seed size corresponding to 12 mm was assigned to the framing members and hold-downs, while a coarser mesh corresponding to a global seed size of 25 mm was assigned to the sheathing material, as displayed in Figure 5.7. The aspect ratio of the elements was kept as close to 1 as possible. According to Schafer [44], a coarse mesh can successfully capture global and distortional buckling modes of CFS members; however, a fine mesh is required to capture the local, global, and distortional buckling modes. Ideally, both the framing members and the steel sheathing are preferred to have

equivalent meshes, however since the stable time increment is greatly influenced by the mesh density, using an extremely fine mesh for the sheathing would result in an unnecessary small stable-time increment. As will be discussed in the following sections, the mesh density was sufficient in obtaining an economical solution and reproducing all significant buckling modes of the shear wall assembly.

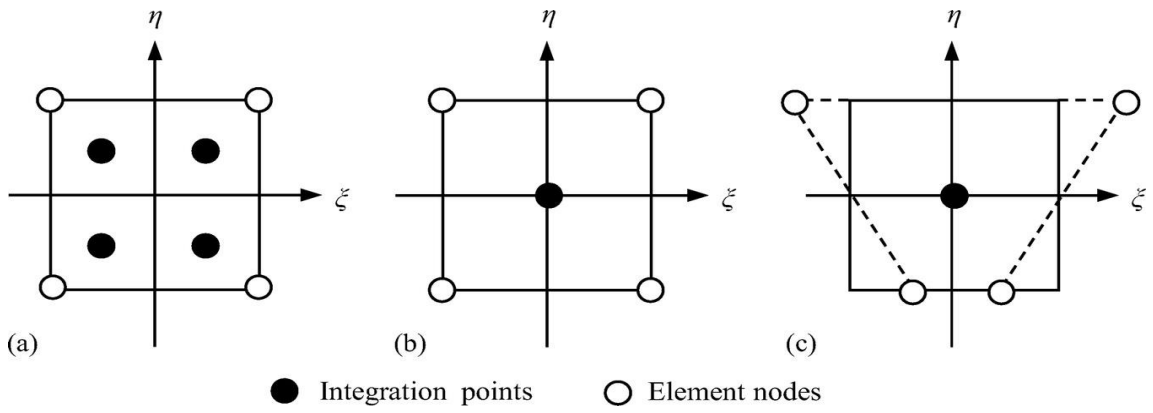


Figure 5.6: a) Fully integrated element; (b) Reduced integration element; (c) Hour-glass mode [77].

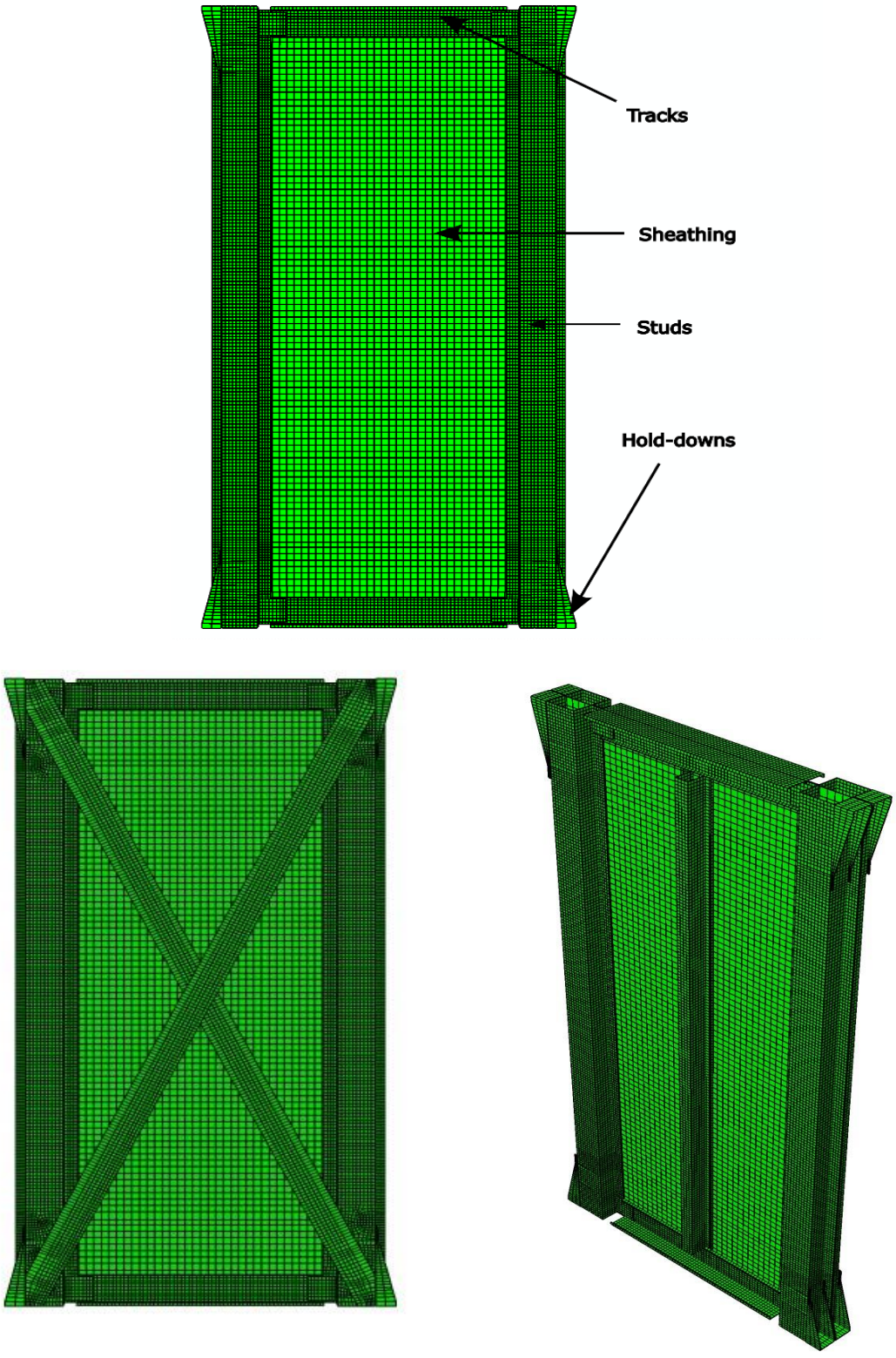


Figure 5.7: Discretized shear wall specimen.

5.5.2 Boundary Conditions

As previously described in chapter 3, the shear wall assemblies were rigidly connected to the hot-rolled steel testing frame through the hold-downs and tracks. The hold-downs were attached to the top control beam and the bottom base beam through M22 high strength hexagonal anchor bolts, while the tracks were connected to the beams using M12 anchor bolts. To simulate the laboratory conditions, the nodes at the location of the anchor bolts in the bottom tracks and the bottom of the hold-downs were fully fixed since no uplift was observed during the experiments. This allows the base shear force in the shear wall to be transferred directly to the foundation. The boundary condition at the base of the model is shown in Figure 5.8.

The loading model on the other hand is depicted in Figure 5.9. Nodes at the locations of the anchor bolts at the top tracks and hold-downs were tied to a reference point defined at the centroid of the top track using a kinematic coupling constraint. A displacement boundary condition was then assigned to the reference point using the smooth step amplitude to replicate the displacement-controlled loading of the control beam in the experiment. Application of the monotonic loading only requires the input of the final drift, while application of the cyclic loading requires the input of the peak drift values of each loading cycle. No vertical loads were applied to the reference point since the specimens were not subjected to gravity loads.

Finally, to simulate the out-of-plan support provided by the rigid test frame, all the nodes at the top and bottom of the shear wall that are not part of the boundary conditions or the kinematic constraint were restrained from moving in the out-of-plan direction (U3 and UR2).

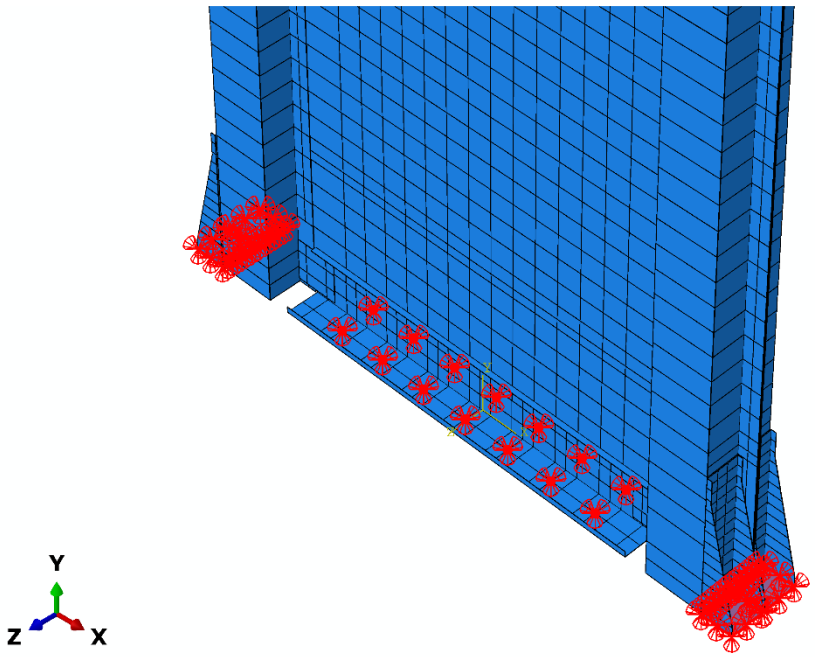


Figure 5.8: Boundary condition of shear wall models.

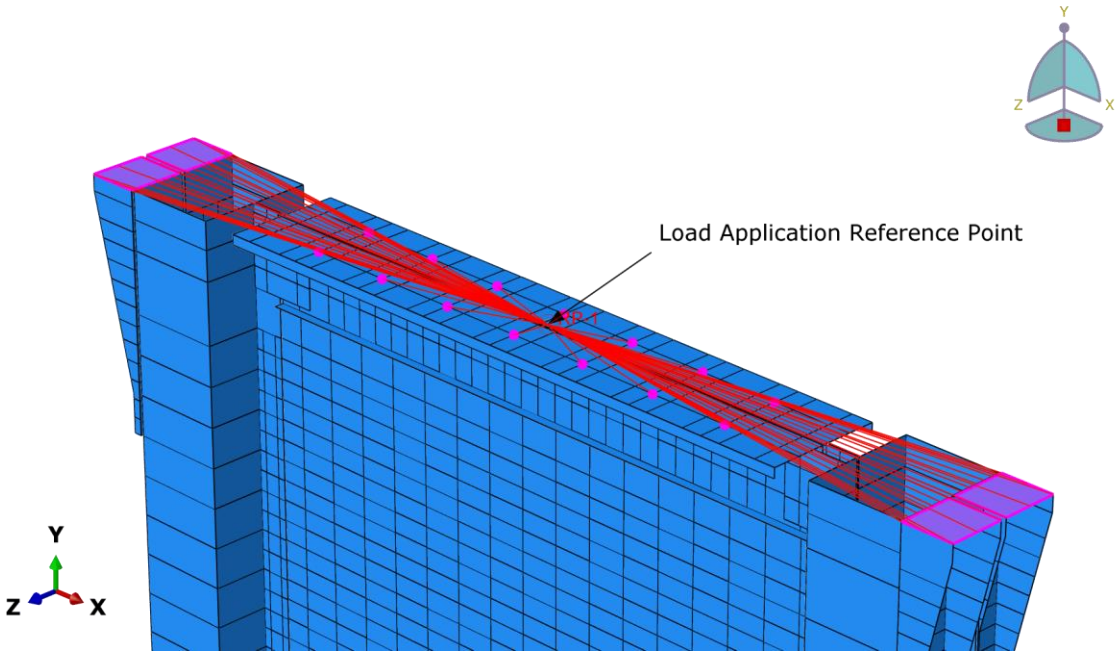


Figure 5.9: Loading model.

5.5.3 Material Properties and Constitutive Material Modelling

The components of the shear wall assemblies were modeled with the material properties obtained from the coupon tests that were stated in Chapter 3. The values of the mechanical properties were based on the average of three uniaxial tensile tests. These values represent the engineering stress and engineering strain, in which the stresses and strains are defined over a constant cross-sectional area and a constant specimen length [78]. The input of material properties in ABAQUS requires the mechanical properties to represent the true stress and strain values of the material, hence a simple conversion can be applied to the values of the coupon tests to obtain the true stress-strain diagram of each material [79]:

$$\sigma_{true} = \sigma_{eng}(1 + \varepsilon_{eng}) \quad \textbf{(5.8a)}$$

$$\varepsilon_{true} = \ln(1 + \varepsilon_{eng}) - \frac{\sigma_{true}}{E} \quad \textbf{(5.8b)}$$

Where σ_{true} and ε_{true} correspond to the true stress and strain, respectively, and E refers to the modulus of elasticity of the material. A sample of a conventional stress-strain curve and a true stress-strain curve for one of the coupon tests is shown in the Figure 5.10.

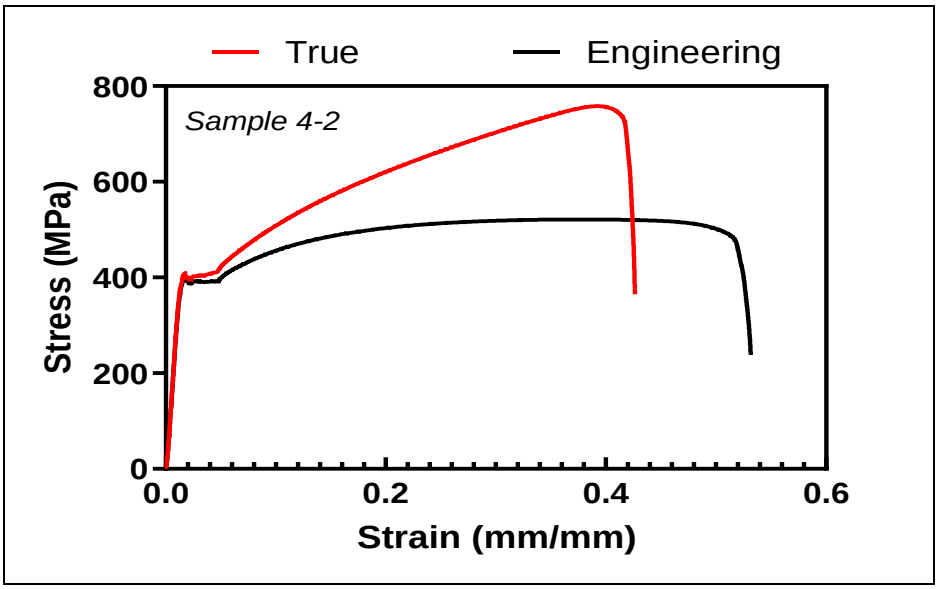


Figure 5.10: Conventional and true stress-strain diagram for sample 4-2.

All physical tests of the shear wall specimens were conducted at room temperature under a quasi-static displacement control loading protocol. Under such conditions, it is reasonable to assume that the constitutive material model that represents the cold-formed steel is independent of time and temperature effects. When the strain-rate of the material is not considered, the metal plasticity models that are available in ABAQUS are based on incremental relations. These relations apply the classical additive decomposition of strain [80], in which the total mechanical strain is postulated to be composed of an elastic, recoverable component and a non-recoverable, plastic component [66]:

$$\varepsilon = \varepsilon^{elastic} + \varepsilon^{plastic} \quad \textbf{(5.9)}$$

The mathematical formulation of classic metal plasticity models follows four main requirements: the yield criterion, the consistency rule, the flow rule, and finally, the hardening rule. The yield criterion relates the state of stress to the onset of yielding. The multi-axial Von Mises criteria is a

popular yield criterion used to describe the elastic and inelastic behaviour of non-voided ductile metals. The criterion states that yielding occurs once the stress in the material reaches or exceeds an effective or "Von Mises" stress, and that the effective stress is independent of the hydrostatic (mean) pressure. The Von Mises yield criterion can be geometrically interpreted as a cylinder in three-dimensional principal stress space with the axis lying along the line $\sigma_1 = \sigma_2 = \sigma_3$. Since the hydrostatic pressure doesn't affect yielding, even infinite, but equal principal stresses will not result in yielding of the material.

If the effective stress has been reached and the material is loaded beyond the yield point, the material undergoes plastic flow. If the flow obeys the associated flow rule, then the rule states that the increment of plastic strain is in a direction that is normal to the tangent to the yield surface at the load point. Another requirement, the consistency rule, also states that the load point must remain on the yield surface as the material deforms inelastically. Finally, the hardening rule describes how the yield criterion is modified when the material is loaded past its initial yield. The hardening rule dictates the evolution of the yield surface in stress space during plastic flow. The transformation of the yield surface might be a change in location or size, or a combination of both. Hardening refers to the mechanical property of some materials (such as metals) where the stress required to cause further plastic deformations increases. The plasticity models that are available in ABAQUS/Explicit are briefly discussed next.

There are several constitutive relations provided for modeling metal plasticity, these include: perfectly-plastic model, isotropic hardening model, Johnson-Cook isotropic hardening model, linear kinematic hardening model, and, combined non-linear isotropic/kinematic hardening

model. The perfectly-plastic model requires the least input, and it assumes that the yield stress does not change with plastic strain. As a result, the model does not consider material hardening nor softening. In the isotropic hardening model, which is shown in Figure 5.11, the yield surface expands or contracts uniformly in all directions in stress space as plastic strain takes place. The isotropic hardening model is nonlinear and allows the definition of the full plastic curve, as well as temperature effects and other user pre-defined fields. Hence by defining different plastic stress vs plastic strain pairs, the model is capable of modeling strain hardening followed by strain softening. The Johnson-Cook model is a variation of the isotropic hardening model that represent the material behaviour as a function of strains, strain rates, and temperature [81]. This particular model is suitable for modeling high-rate deformation of many metals, however, unlike the isotropic hardening model, the calibration process is more involved. Both the perfectly-plastic and isotropic hardening model were used in modeling the monotonic pushover test of the concentric-sheathed specimen GD-6, and both models were successful in obtaining good agreement with the test results up to the global softening point. However, the isotropic model provided better prediction for the post-yield behaviour of the specimen since the full range of stress and plastic strains were defined. On the other hand, in cases where cyclic loading is expected, stress and inelastic strain reversals typically result in strength and stiffness degradation, as was encountered in the cyclic tests discussed in Chapter 4. Under such conditions, modeling the Bauschinger effects becomes essential in representing the material behaviour. The Bauschinger effect is a material property in which an increase in the yield strength of a material in one direction results in a decrease of the yield strength in the opposite direction. This particular behaviour can be simulated using the linear kinematic hardening model. As

depicted in Figure 5.12, the basic concept in the linear kinematic hardening model is that the yield surface undergoes rigid body translation in stress space rather than uniform expansion. The model requires a bilinear representation of the stress strain curve where the slope of the plastic region controls the translation of the yield surface and is known as the constant hardening modulus. Due to its simplicity, the model is able to predict the first approximation of the behaviour of metals due to reversed loadings. As the load reversals of inelastic strain progress, a nonlinear component is required to better predict the shape of the cycles. For such cases, ABAQUS/Explicit offers a combined nonlinear kinematic/isotropic model. In this model, the evolution of the yield stress is separated into two components: an isotropic hardening component which dictates the uniform expansion or contraction of the yield surface, and a nonlinear kinematic hardening component which dictates the translation of the yield surface in the stress space due to plastic deformations. This model incorporates several hardening parameters as well as temperature and field variables, which result in better prediction of hysteresis cycles. The calibration process is more complex nonetheless and requires curve fitting of several material parameters that can be obtained from cyclic material test data. Due to the available test data, which consists of monotonic coupon tests and cyclic screw connection tests, and based on the preceding discussion, the linear kinematic hardening model was selected as the constitutive rule in modeling the structural parts of the shear wall specimens.

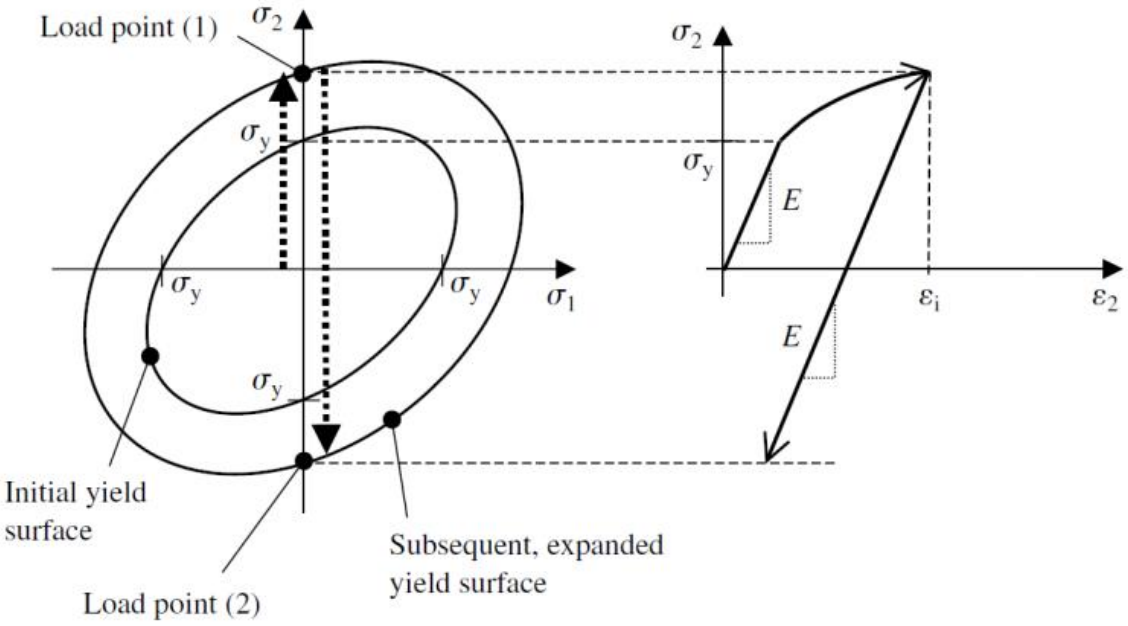


Figure 5.11: Isotropic hardening yield surface and resulting stress-strain curve [75].

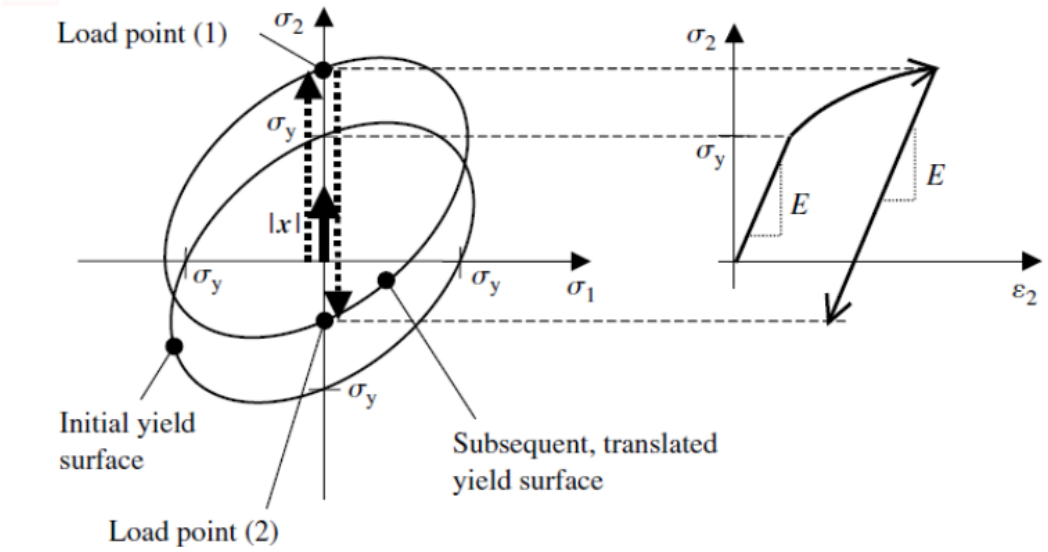


Figure 5.12: Kinematic hardening displaying the rigid body translation of the yield surface, the resulting stress-strain curve and the associated Bauschinger effect [80].

5.5.4 Screw Modelling

Since the performance of CFS shear walls is greatly influenced by the sheathing-to-framing connections [10], [12], [35], it was originally intended to model the screw connections using the Pinching4 user element (UEL) [47]. Unfortunately, the available Pinching4 user element is currently only compatible with the implicit solver (ABAQUS/Standard). An attempt was made to convert the user element (UEL) into a version compatible with the explicit solver (VUEL), however, as the code was too complex it was considered outside the scope of this project.

Consequently, to ensure that the screw modeling technique for the shear wall models is satisfactory, a model of the screw connection test that was discussed in Section 3.7 was created and verified against the experimental results prior to constructing the FE models of the shear walls. As shown in Figure 5.13, the built-up hat studs and sheathing were modelled using the S4R elements, with a fine mesh corresponding to 10 mm global seed. To replicate the rigidity provided by the connection plates, the nodes on the webs and flanges of the studs were fully fixed while the nodes on the sheathing in contact with the connection plates were only allowed to translate in the vertical direction. A displacement boundary condition was applied through a reference point that was coupled to the nodes on the top of the sheathing. Each screw in the experiment was modelled by two connector elements in series , and the “Slide-Plane + Align” connection types were assigned to each connector element. This connection type models each connector element as two in-plane shear springs whose ends are restricted from rotating. The plasticity of the connectors were defined using the kinematic hardening property by inputting force-relative displacement pairs that were obtained from screw connection test, which include the descending

branch of the screw. Since each screw was modeled by two connector elements, the force values were halved. The results are illustrated in Figure 5.14.

On the other hand, the M8 high-strength bolts were modeled as connector elements with BEAM Multi-Point Constraints (MPCs), which is comparable to providing a rigid beam between the nodes. Except at very high displacements in the cyclic tests (144 mm+), there was no damage observed in the bolts connecting the hold-downs to the studs nor the bolts connecting the straps to the studs, which justifies the choice of modelling such connections as rigid.

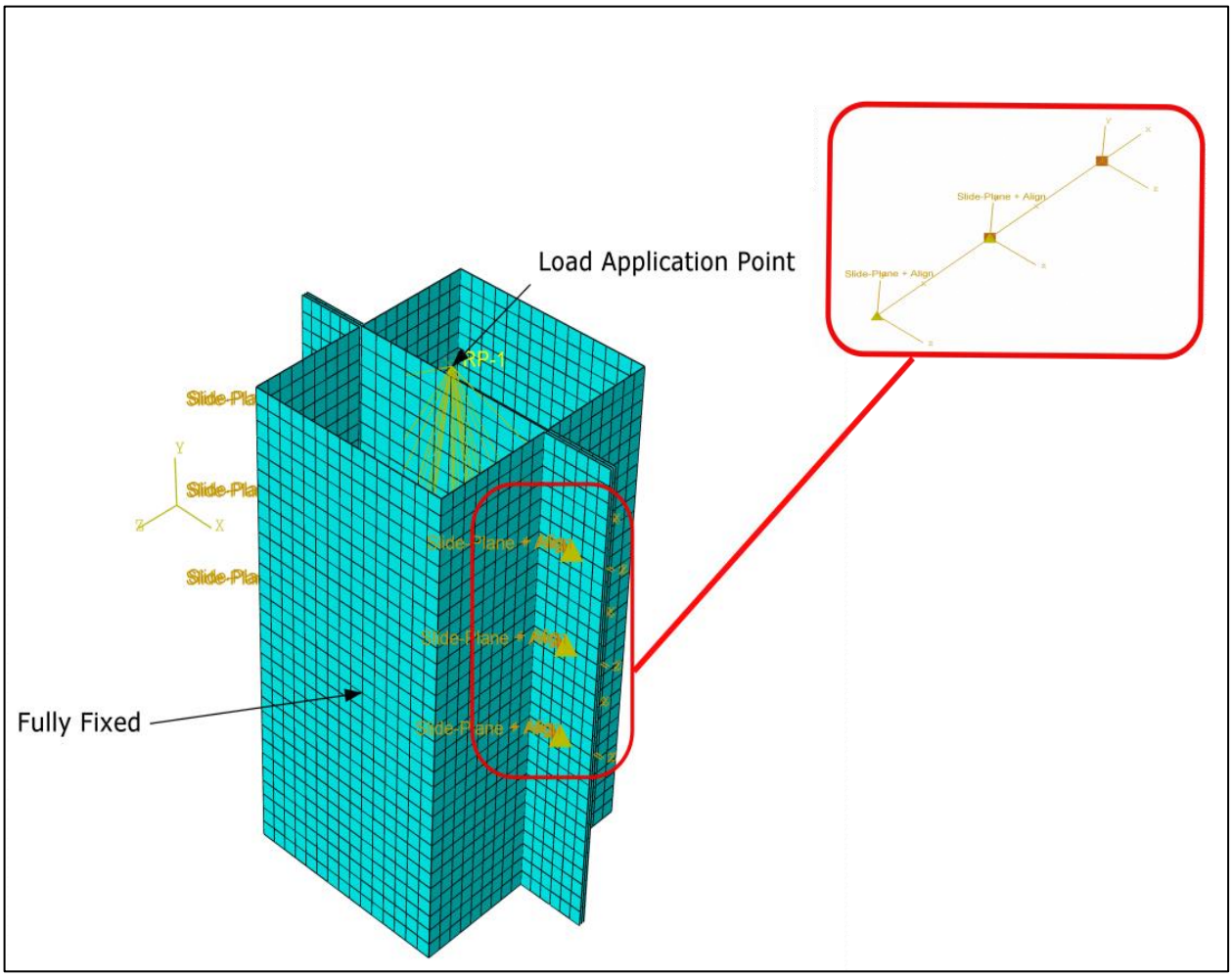


Figure 5.13: Screw connection test finite element model.

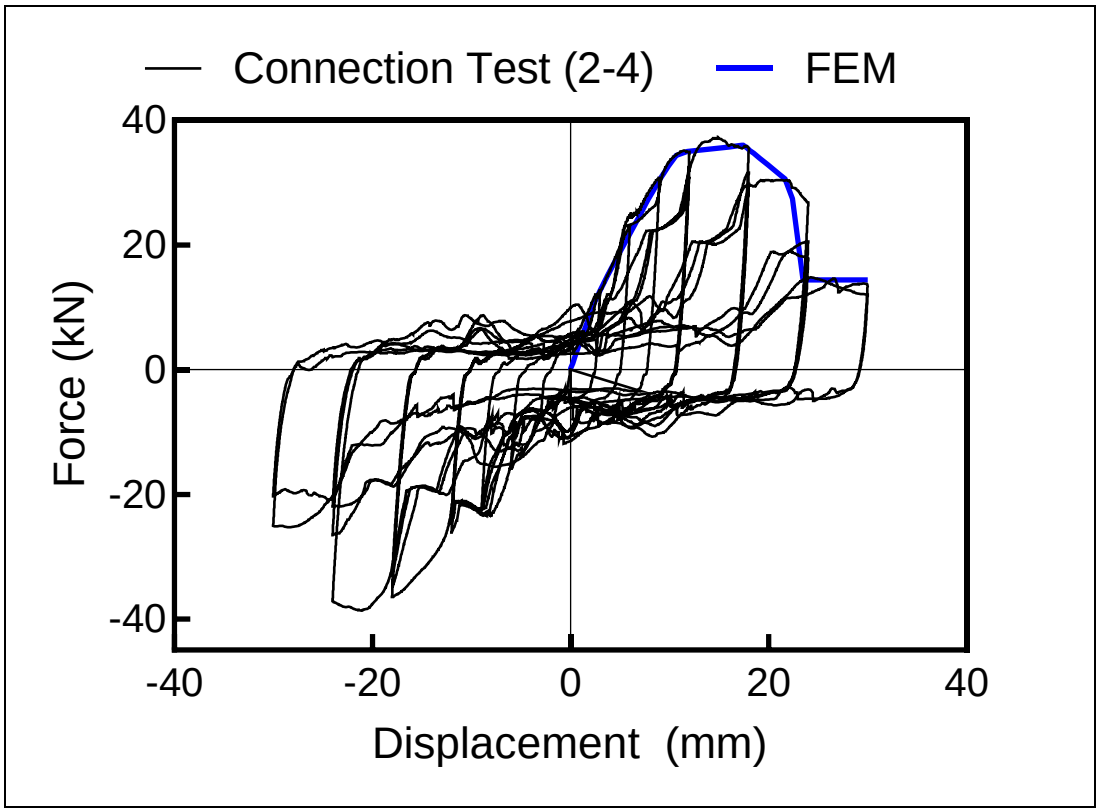


Figure 5.14: Results of the screw connection test finite element model.

It should be noted that screw connection test verification was performed for monotonic loading only. Even though the connector elements were assigned a kinematic hardening property, the extent of pinching that was encountered in the experiments was not replicated with good accuracy in the model. This is mainly attributed to two reasons: firstly, the kinematic hardening model for the screws only gives initial approximations of the behaviour of the connection assembly. Secondly, there is no damage definition in the model and as a result, any bearing damage in the experiment is not simulated accurately in the model. However, despite the previously mentioned limitations, and in the absence of a more robust model for the screws, it was decided that using a kinematic hardening model for the screw connections would provide the best available approximation.

5.5.5 Geometric Imperfections and Residual Stresses

Geometric imperfections refer to the variations of the physical structural member from the perfect geometry [82]. These imperfections might be a product of the manufacturing method, transportation of the structural members, or construction process. Imperfections in structural cold-formed steel members include warping, bowing, as well as local imperfections such as dents. Imperfections can be introduced to shell finite element models by specifying the node number and imperfections directly. Unfortunately, the local imperfections of the shear wall members were not measured prior to the monotonic or cyclic tests. Another approach is to define imperfections as a linear superposition of buckling eigenmodes. Several imperfections with varying scaling factors were attempted, incorporating global and local buckling of the studs as well as buckling of the sheathing. For the walls studied in this research, the inclusion of geometric imperfections of individual components had virtually no effect on the base shear-lateral drift response of the models. Therefore, it was reasonably assumed that the finite element models were imperfection insensitive.

Residual stresses on the other hand are stresses that are present in fabricated metallic structures due to effects of welding, uneven cooling of the member, and cold forming [83], [84]. Residual stresses, which typically include membrane and bending components, might affect the strength and buckling behaviour of cold-formed steel members. These stresses can be applied to the model as pre-defined field stresses before running the analysis. However, this also requires knowledge of the residual stresses' magnitude and pattern distribution, which were not measured prior to assembling and testing the specimens. In conclusion, the finite element

models of the shear wall specimen consider geometric and material non-linearity, and geometric imperfections and residual stresses are not considered.

5.6 Verification of Benchmark Finite Element Models

The modelling protocol that was outlined in Section 5.5 is used to establish benchmark high fidelity shell finite element models of the shear wall specimen and validate them against the experimental results. The benchmark models include a monotonic pushover model for the concentric-sheathed specimen (GD-06), two cyclic models for the concentric sheathed specimens (GD-19 & C-SW-2), and finally, a cyclic model for the diagonally strapped model (GD-19).

The main properties and parameters of the shear wall that were used to compare the results of the monotonic numerical analysis include elastic stiffness, peak load, drift at which the peak load is attained, and the deformed shape of the shear walls at different stages of loading. For the cyclic models, the same properties were assessed in addition to the total amount of energy dissipated during different increments of cyclic loading and analysis of the shape and pinching of isolated hysteresis loops.

Special attention is given to the energy output of the numerical models, particularly to satisfy the energy balance equation. Hence, for each benchmark model, frequency analyses and the subsequent loading rates are first introduced, followed by an assessment of the energy output. Then, the base shear versus drift curve is presented and compared with the experimental results. The deformed shape of each model is evaluated next at different loading stages to validate that the finite element models are capable of reproducing the failure modes that were observed

during the experiments. Finally, the energy dissipation capacity of each model is discussed along with the sources of error.

5.6.1 Monotonic Finite Element Analysis of Specimen GD-06.

As stated in Section 5.5, the stable time increment is controlled by the material properties, the mesh density, and the frequency of the model. Therefore to determine a suitable loading rate, a frequency analysis was conducted on all models prior to performing the monotonic/cyclic displacement-controlled analysis. The frequency of specimen GD-06 along with its first mode, which corresponds to out-of-plan buckling of the sheathing, are shown in Figure 5.15. Thereafter, the total simulation time was set to 50 times the period of the first mode. To replicate the quasi-static load application of the experiment, a 225 mm displacement was applied to the reference point (refer to Figure 5.9) over a time period of 11 seconds using the smooth amplitude function. Moreover, a model of the frame without the sheathing was also analyzed to determine the contribution of the sheathing to the overall response. The history of different types of energy is evaluated first.

From Figure 5.16, it is evident that the internal and external energies of the system are exact since both graphs overlap. In addition, the kinetic energy output (red graph in Figure 5.16) is quite insignificant implying that inertial effects did not alter the simulation. This confirms that the analysis has been conducted under quasi-static conditions. Finally, while the other forms of artificial energies are slightly higher than the kinetic energy, they are still negligible when compared to the internal energy output, indicating that the mesh density and default control settings were sufficient in limiting the effects of hourglass modes.

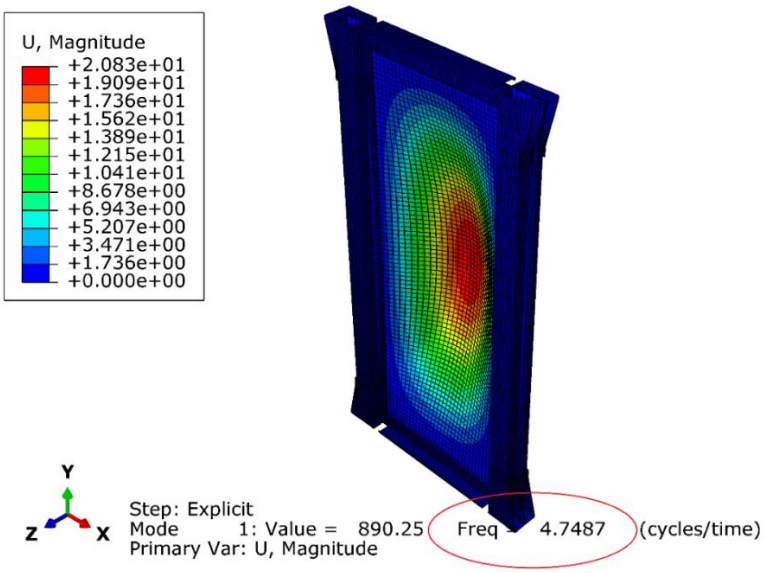


Figure 5.15: Frequency analysis for specimen GD-06.

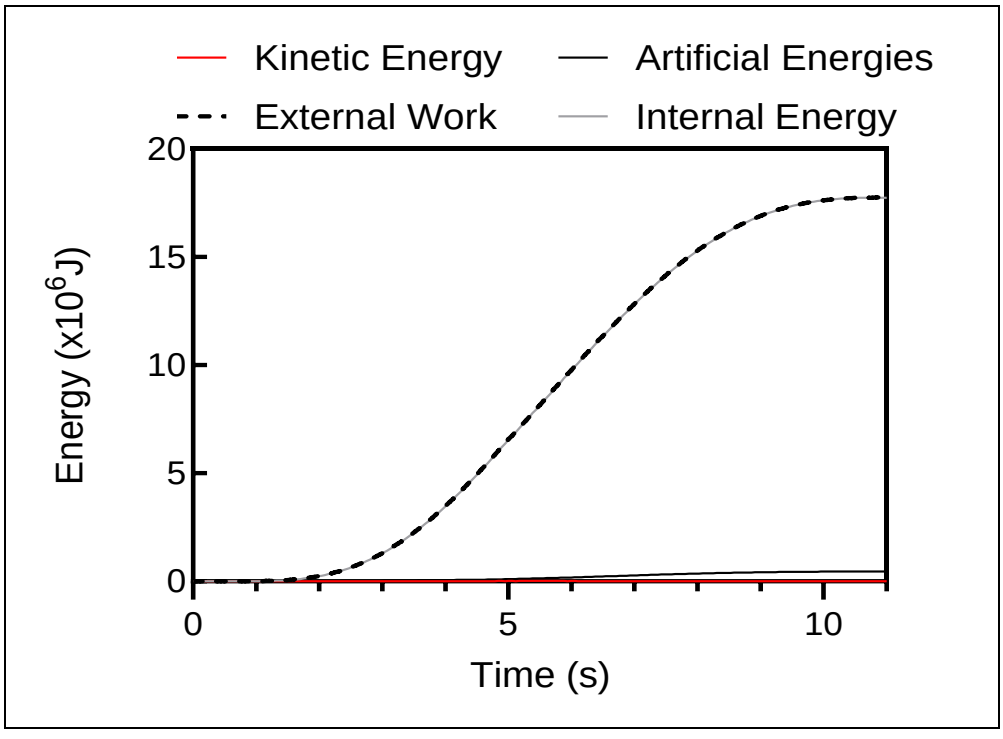


Figure 5.16: Energy history output for specimen GD-06.

The independent history of kinetic energy is examined next. It is anticipated that a smooth application of the load would result in a smooth kinetic energy output. The kinetic energy versus time curve presented in Figure 5.17 below indicates that there are two instances where there is an abrupt upsurge in kinetic energy with some noisy output in between. Re-examination of the deformed shape of the model demonstrated that the formation of the tension field and the initiation of buckling in the end stud resulted in a sudden and rapid increase of kinetic energy. After the stud has buckled and the tension field has stabilized, the kinetic energy varied smoothly with time, as illustrated by the descending branch of the graph.

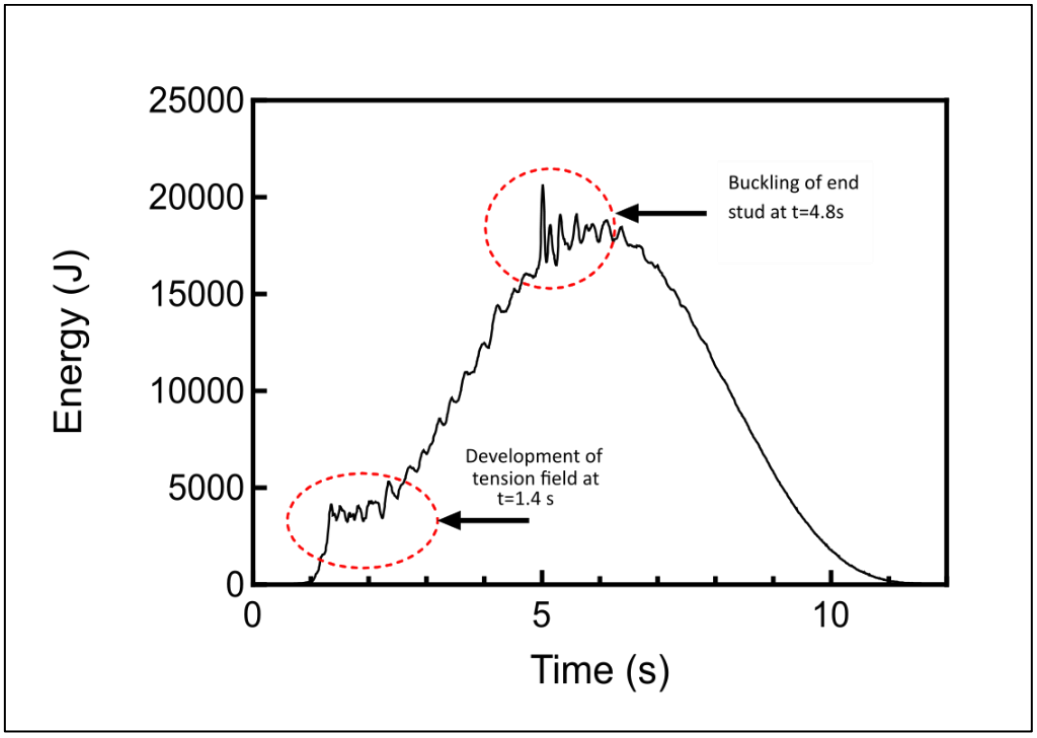


Figure 5.17: Kinetic energy history output for the monotonic simulation.

Finally, the base shear versus drift plots are assessed. As displayed in Figure 5.18, there is good agreement between the finite element model and experimental results. The model predicts the

strength and drifts at peak load accurately as there is a minor difference between the experimental and numerical values (0.25%). In addition, the model was able to reproduce most of the failure modes that were discussed in chapter 3, specifically the shear buckling of the sheathing and flexural buckling in the end studs (refer to Figure 5.19). Conversely, the model marginally overestimates the initial stiffness of the specimen. This was a common observation in all models and can be attributed to the following. The bolt holes in the specimen were pre-drilled with hole sizes that were slightly larger than the bolt's diameter. As a result, the bolts were not compactly bearing against the base beam nor to the control beam when the shear wall was first assembled. The specimens required the application of the displacement-controlled load in order for the bolted members to be firmly connected to the test frame. Consequently, the "slip" of the bolts was reflected in the elastic portion of the experimental graphs where the model's response is noticeably stiffer than the experiment. In addition, the model is somewhat slow in predicting the post-yield degradation that was exhibited by the specimen. However this can be attributed to the constitutive material model in which the monotonic simulation employed the isotropic hardening model. A finite element model of the bare frame was also developed and analyzed, and the response of the frame without the sheathing is included in Figure 5.18. The bare frame's response distinctly displays that the thin cold-formed steel sheet significantly increased the stiffness and strength of the shear wall.

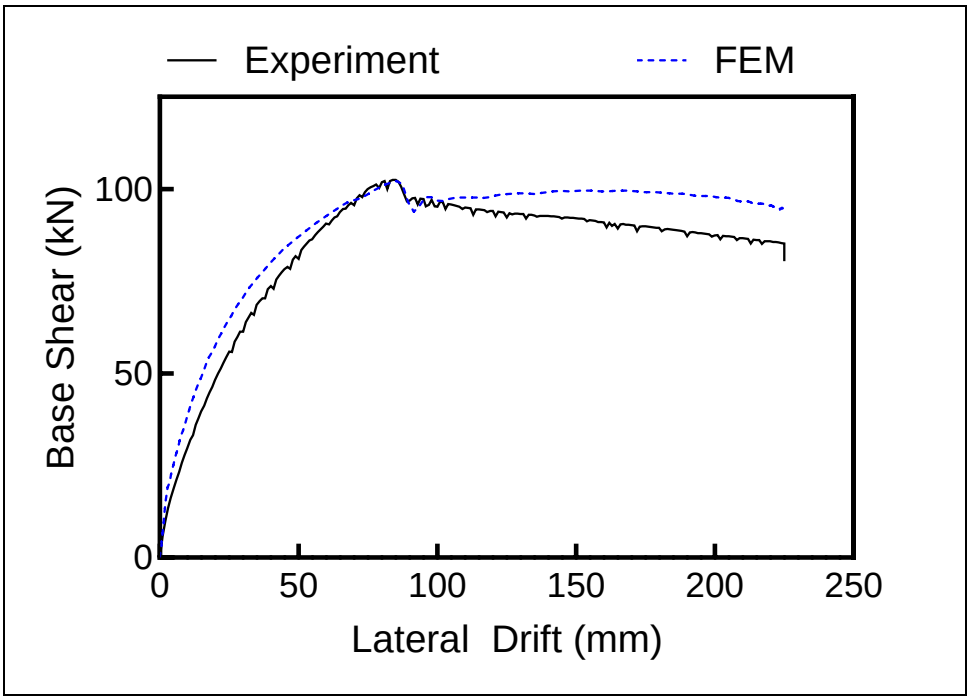


Figure 5.18: Comparison between FEM and experimental results for specimen GD-06.

The verification of the mass scaling factor is examined before moving on to the cyclic analyses. In order to accelerate the computational time of the models, a constant mass scaling factor equal to 625 was applied to the whole model. Since there are limits to how much the solution time can be accelerated while still obtaining a quasi-static solution, a trial-and-error approach was adopted. Starting with an unrealistic and high mass scaling factor, the simulation was carried out several times while successively decreasing the mass scaling factor. The base shear versus drift curve for each attempt is then plotted along with the kinetic energy output, and the quality of each solution is assessed until an optimal factor was obtained at which the inertial effects remained negligible. According to Figure 5.20, it can be concluded that the quality of the solution decays rapidly with increasing scaling factor.

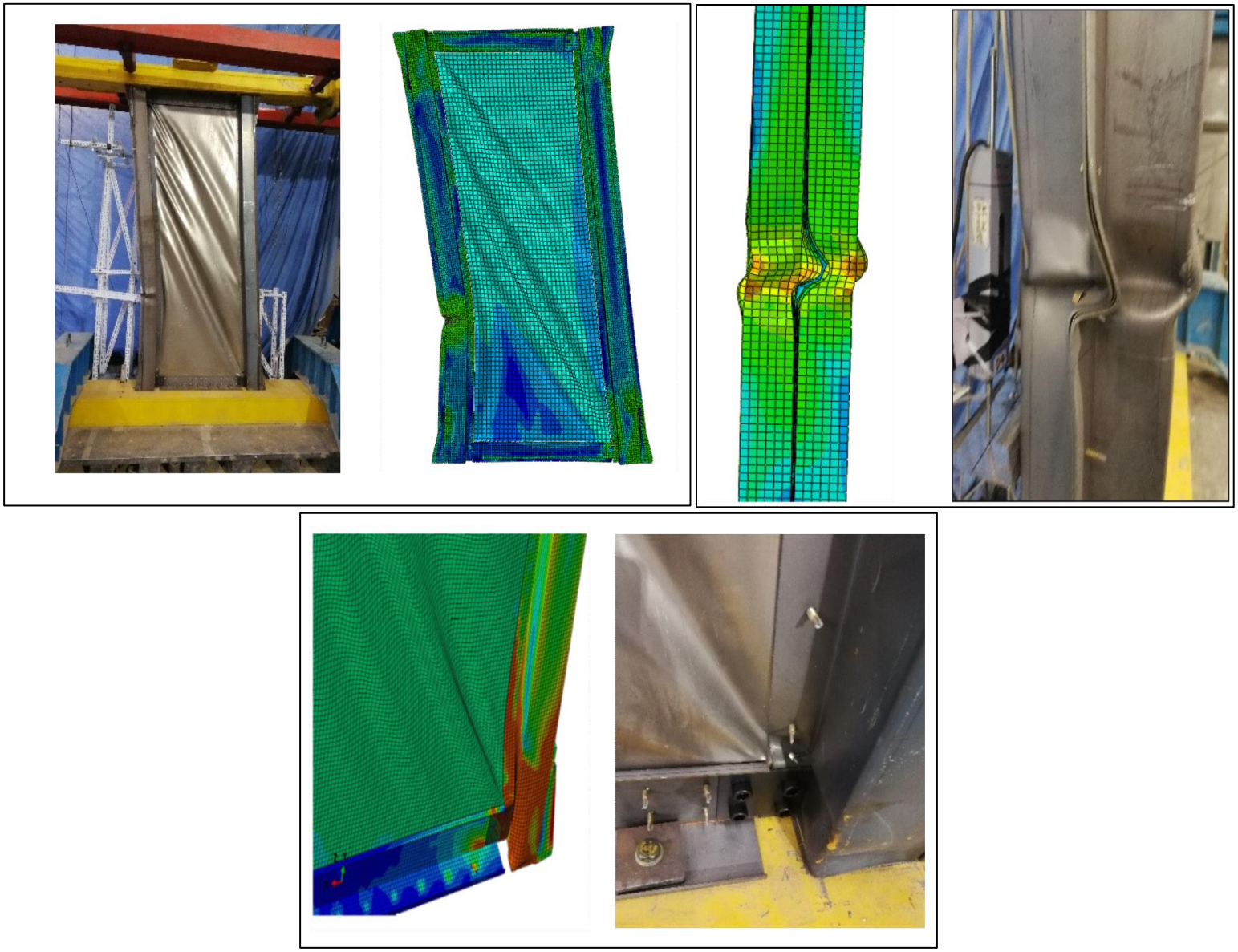


Figure 5.19: Comparison between failure modes in the experiment and the numerical model for specimen GD-06.

The graphs with the scaling factors of 40000 and 62500 are also good examples of cases where the analysis time step exceeds the critical time step and the solution becomes unbounded. Due to the unrealistic and high scaling factors, the solution becomes unstable and oscillates with increasing amplitudes. The unstable behaviour is also reflected in the energy output of each simulation. By inspection, Figure 5.21 indicates that at a scaling factor of 40000 and 62500, the kinetic-to-internal energy ratio is significant and thus the dynamic effects in the simulation are more dominant. On the other hand, while a mass scaling factor of 2500 results in an acceptable kinetic energy output, by re-examining Figure 5.20, the quality of the quasi-static solution starts to diminish which is reflected in the noisy base shear versus drift plot. Hence, all the finite element models included in this study employed a constant mass scaling factor equal to 625, which in turn translates to a speed up factor on the stable time increment equal to 25.

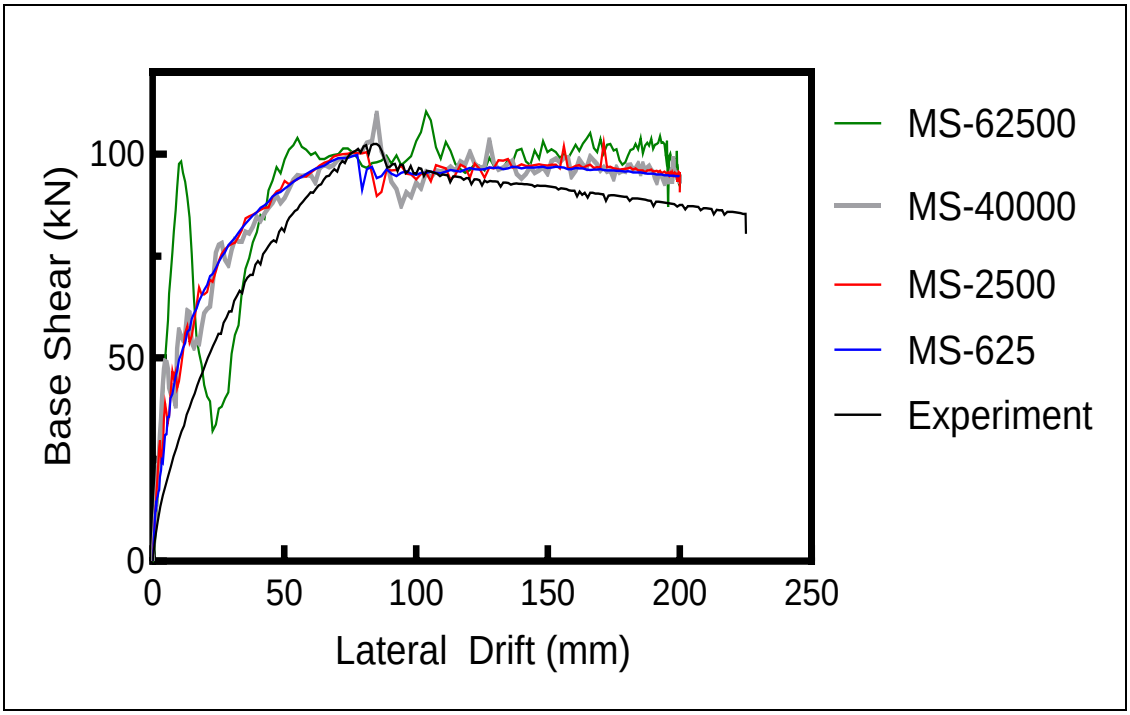


Figure 5.20: Base shear vs drift results with varying mass scaling factors.

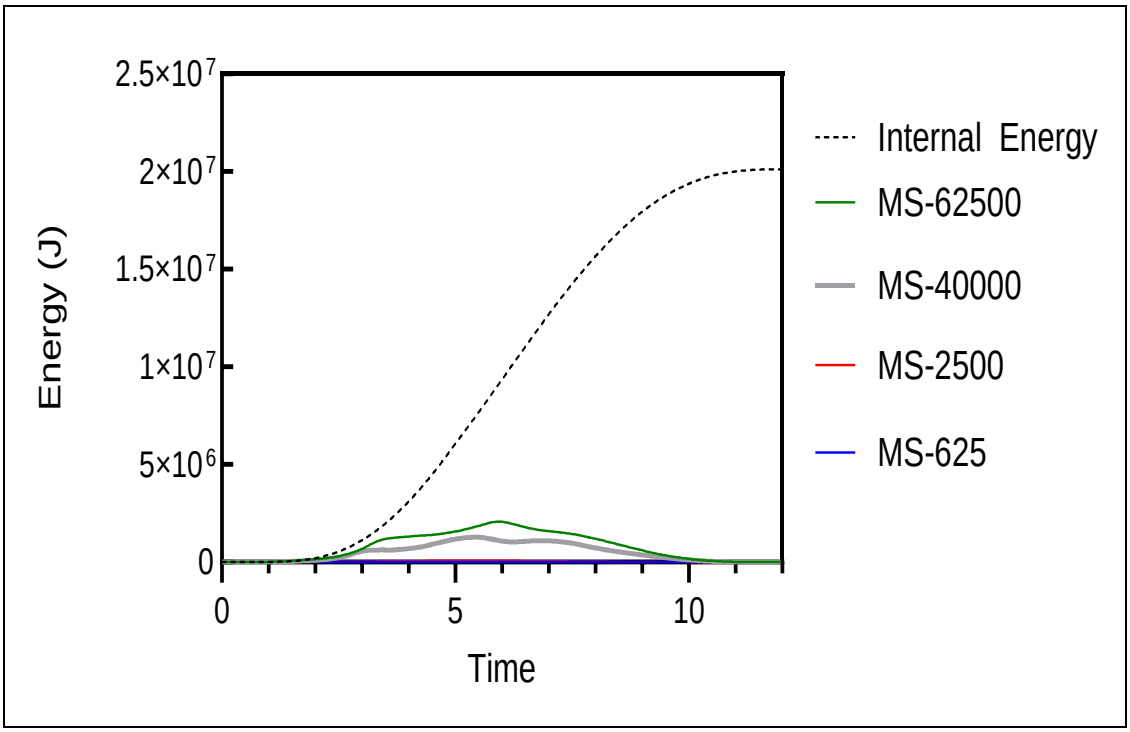


Figure 5.21: Kinetic energy history output for different mass scaling values.

5.6.2 Cyclic Finite Element Analysis of Specimens GD-19 & C-SW-2.

A significant distinction that the benchmark cyclic models offer is the energy dissipation capacity and the hysteretic behaviour of the specimens under cyclic loadings. The deformed shape corresponding to the fundamental frequency of specimen C-SW-2 is shown in Figure 5.22. The noticeably higher frequency indicates that this model is stiffer than model for specimen GD-06/GD-19, which is consistent with the experimental investigation described in Chapter 4. A higher frequency results in a smaller period which subsequently leads to a shorter loading rate. Thus, to be conservative, the loading rate for each cycle for both models was determined by multiplying the natural period of specimen GD-19 by 25 (5 seconds). The displacement applied to the reference point at the top of the wall followed the loading protocol previously discussed

in Figure 3.9, however the post-yield cycles were repeated once rather than three times to save computational time and to develop stable hysteresis loops.

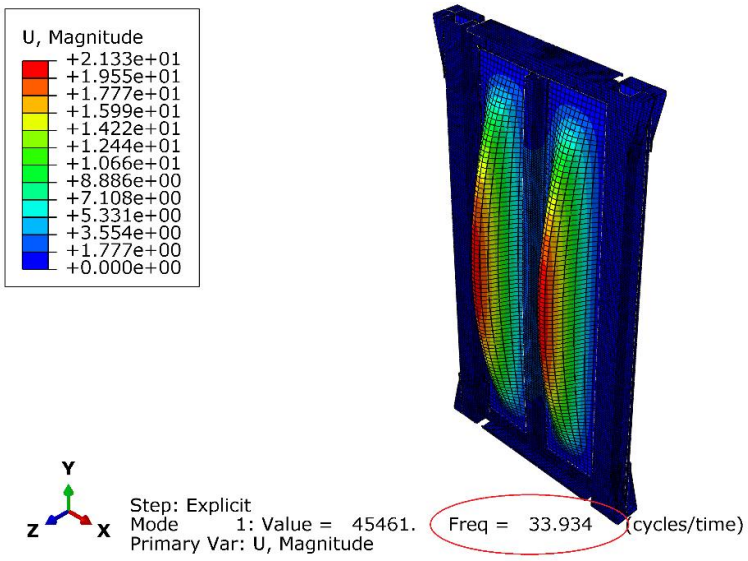


Figure 5.22: Frequency analysis for specimen C-SW-2.

The energy output for specimen C-SW-2 is shown in Figure 5.23. By inspection, it can be observed that the kinetic and artificial energies represent a very small fraction of the internal energy and can be considered as negligible. Accordingly, Figure 5.23 confirms that the cyclic analysis has been carried out under quasi-static conditions. The energy output for specimen GD-19 follows the same trend and is not discussed here. The folds in the internal energy and external work are due to the loss of elastic and plastic energy during load reversals.

The base shear versus drift curves for specimens GD-19 and C-SW-2 are shown in Figure 5.24 & Figure 5.25, respectively. Similar deductions to the monotonic analysis can be drawn from the hysteresis curves. There is excellent agreement in terms of peak load as the difference between numerical and experimental results for specimen GD-19 and specimen C-SW-2 is 5% and 11.75%

respectively. The peak loads in the finite element models were also attained at a drift level which matches the experimental observations ($\delta = 72$ mm).

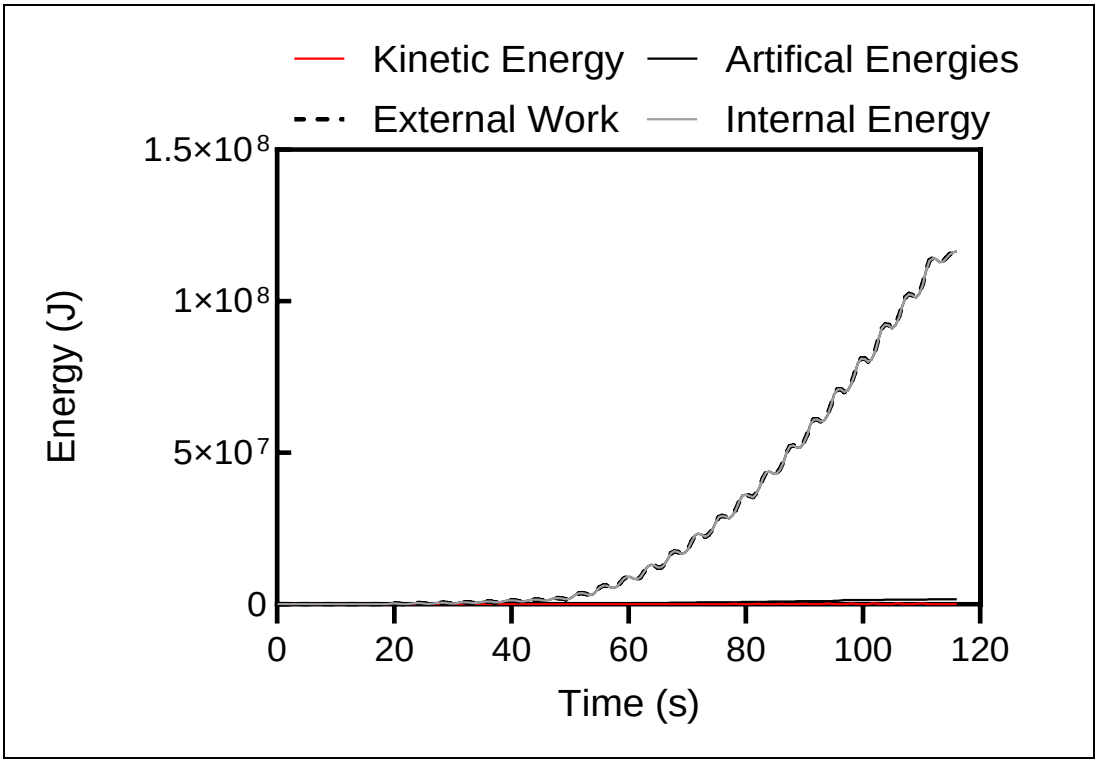


Figure 5.23: Energy output for specimen C-SW-2.

Additionally, the models show good correlation with the experimental results with regards to the unloading and reloading stiffness, especially at drift levels between the yield drift and 108 mm. The deformed shapes of both models also resemble the failure modes that were encountered in the experiments (Figure 5.26 & Figure 5.27). Specifically, the pattern and number of buckle waves in the sheet and the location at which buckling occurs in the studs correlate strongly to the tension field configuration and stud failure location observed in the experiments. In contrast, the models overestimate the initial stiffness and the total dissipated energy in both specimens. For specimen C-SW-2 particularly, the unloading stiffness is overestimated at drift levels exceeding 108 mm, and the model is slow in predicting the strength degradation of the system. Also, since

the models do not incorporate damage initiation, damage evolution, or element removal, any failure modes associated with tearing of the sheet or studs were not produced by the models.

The isolated hysteresis loops along with the total dissipated energy comparisons for specimens GD-19 and C-SW-2 are shown in Figure 5.28 and Figure 5.29, respectively. To gain further insight on the quality of the numerical simulation, the comparisons are carried out at different stages of the loading history. Plots (a) of Figure 5.28 and Figure 5.29 represent the elastic stage, plots (b) represent the stage before any cracks or ruptures occurred, and finally, plots (c) represent the stage after the rupturing of the studs was observed. There is poor agreement in the elastic stage for both models since the numerical solution overestimates the elastic stiffness of the walls. This behaviour is mainly attributed to the slip of the specimen at the beginning of the experiment where the anchor bolts were not compactly connected to the test frame. For the cycles corresponding to drifts between the yield drift and 108 mm, the model predicts the unloading and reloading stiffness with good accuracy and there is a minor overestimation of energy dissipated per cycle. Conversely, at drift levels exceeding 108mm, the models overpredict the energy dissipated per cycle although the loading and unloading stiffness for both specimens correlates reasonably well with the experimental results. One explanation for this behaviour is the tearing of the sheathing and the studs due to load reversals. These phenomena were not produced by the models since damage and element deletion were not incorporated in the numerical analyses and hence the strength and stiffness degradation is not simulated correctly. Similarly, geometric imperfections and residual stresses were also not considered which most likely resulted in a stiffer response. The same conclusions can be drawn by inspecting plot (d) of Figure 5.28 and Figure 5.29, which compares the cumulative energy dissipated by the model and

the experiment. There is good agreement in terms of total energy dissipated up until a drift level of 100 mm. Afterwards, the models overestimate the total energy dissipated, specifically due to the loss of stiffness caused by the tearing of the members.

Another reason for the discrepancy between the numerical and experimental results can be justified by the choice of material model for the screws and the cold-formed steel members. While the kinematic hardening model is simple to implement since it does not require a complex calibration process, a more robust hardening model is required to replicate the severe level of pinching associated with the shear wall specimens. Moreover, as stated in Section 5.5.4, it is anticipated that employing the pinching4 material model for the screws would result in more accurate representation of the hysteresis curves.

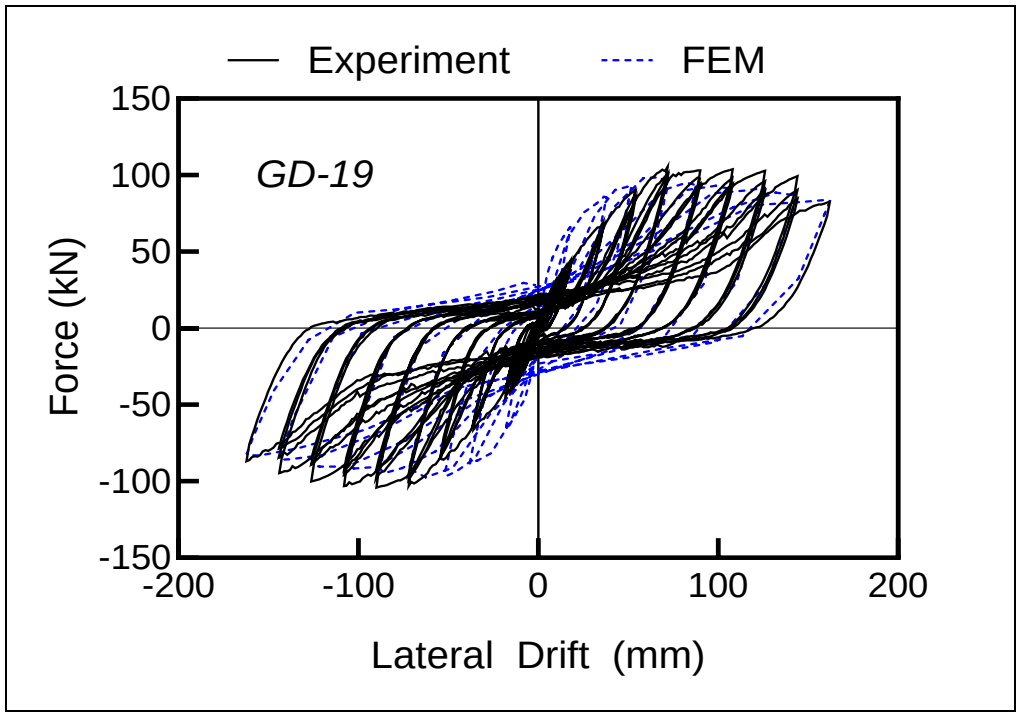


Figure 5.24: Comparison between FEM and experimental results for specimen GD-19.

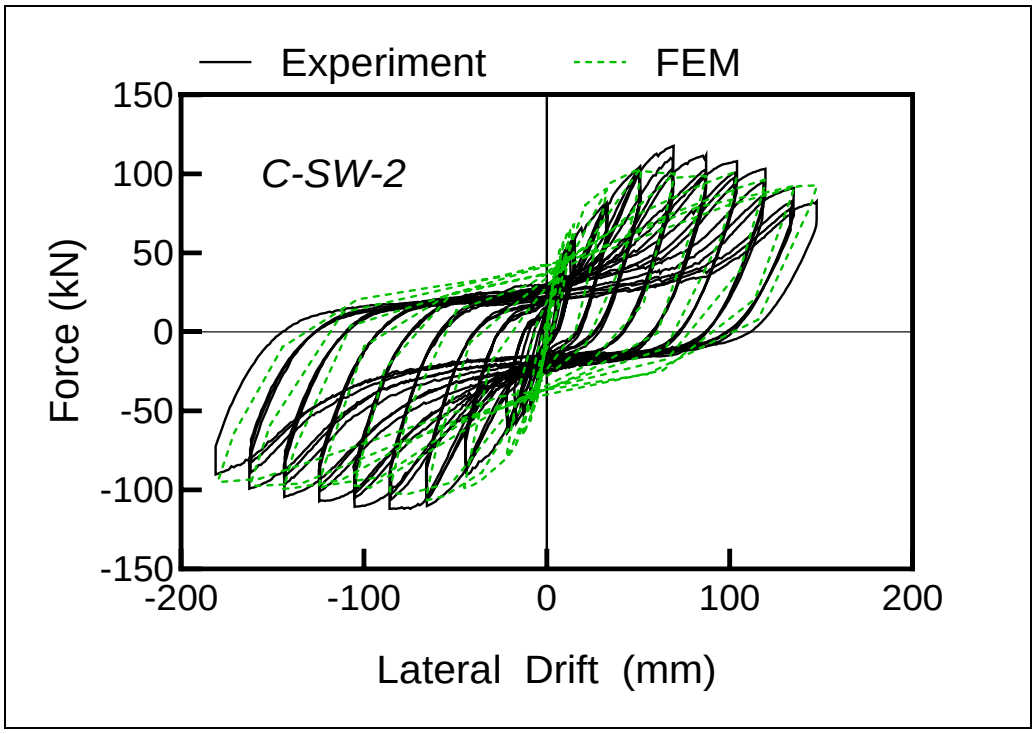


Figure 5.25: Comparison between FEM and experimental results for specimen C-SW-2.

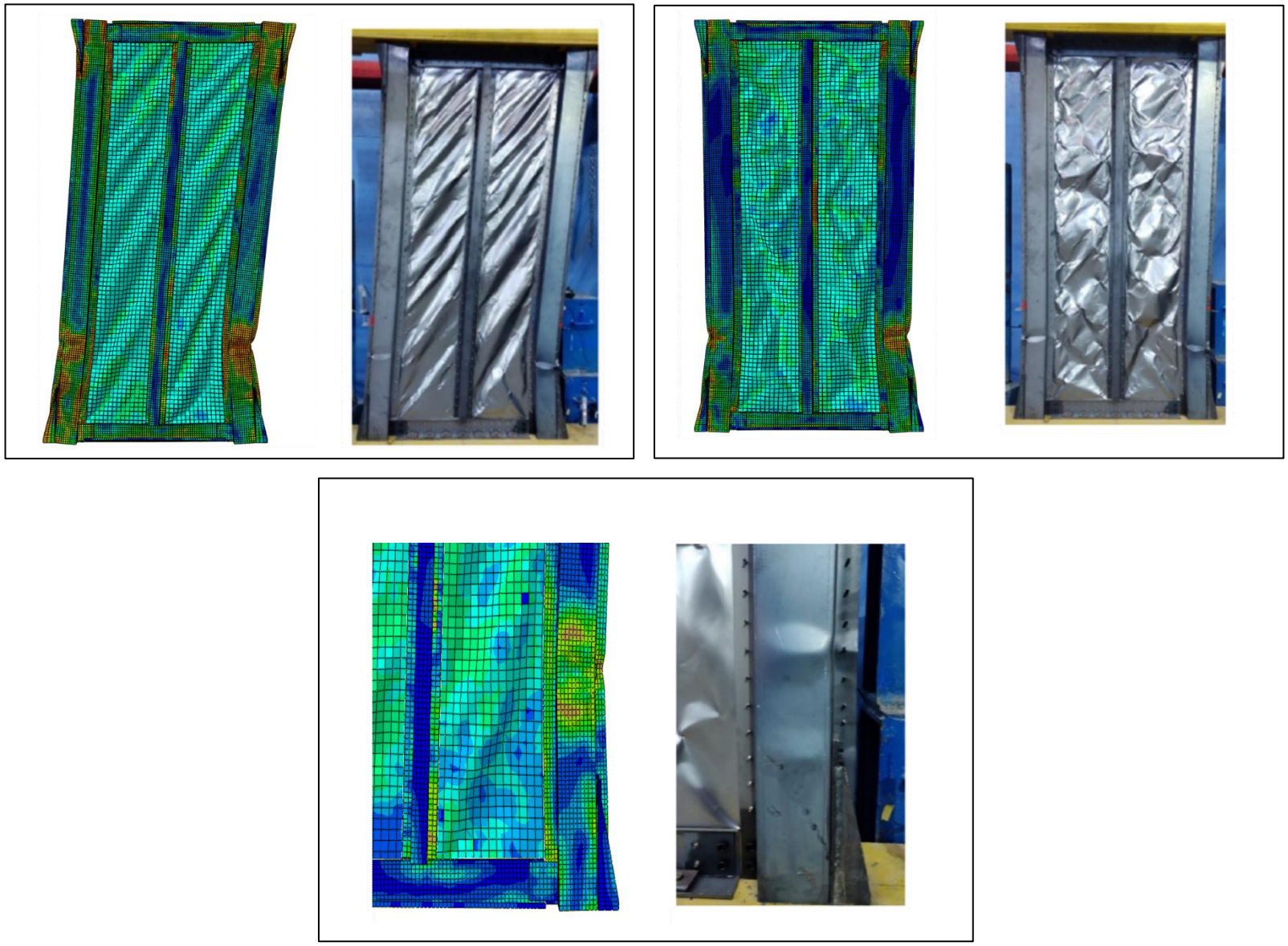
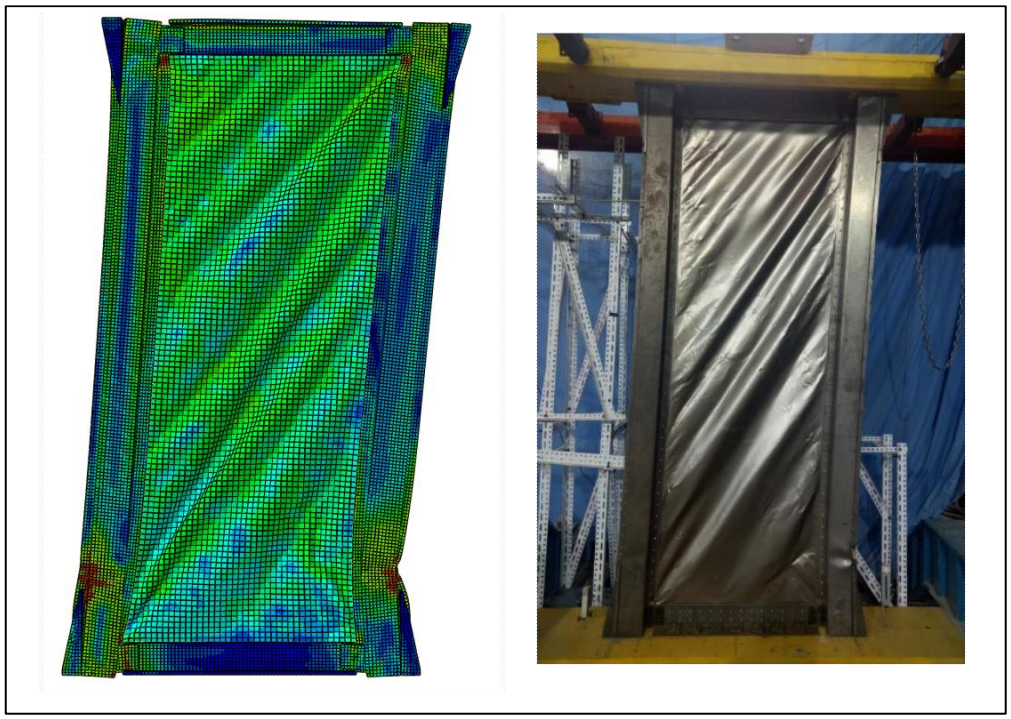


Figure 5.26: Failure modes comparison between the FEM model and experiment for specimen C-SW-2.



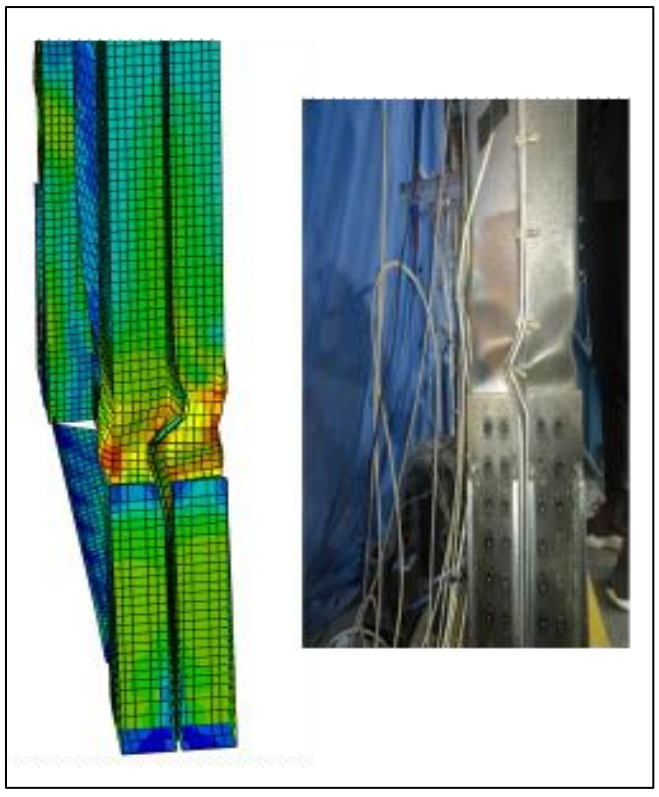


Figure 5.27: : Failure modes comparison between the FEM model and experiment for specimen C-SW-2.

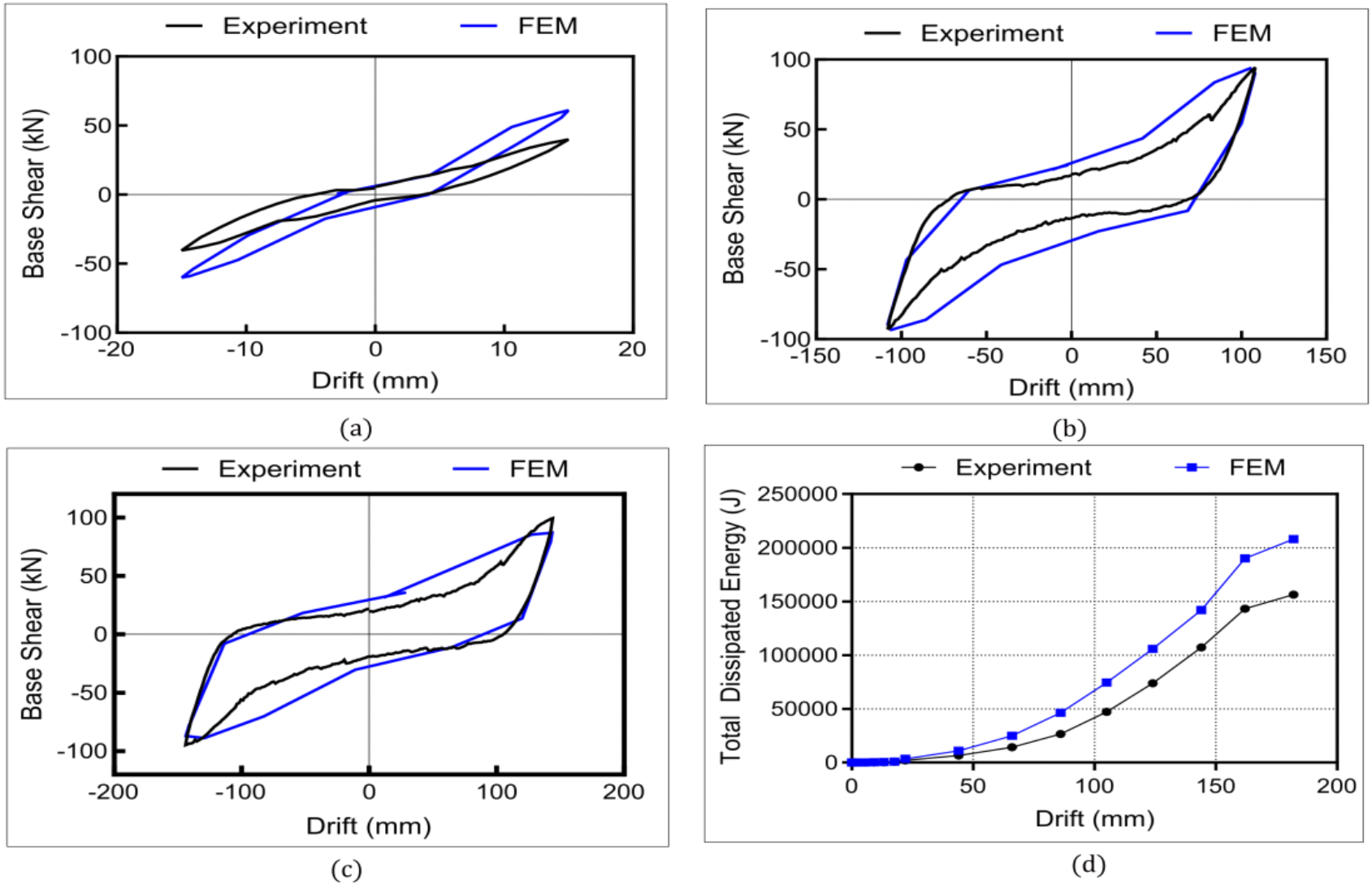


Figure 5.28: Cyclic energy output comparisons between the experimental and numerical results for specimen GD-19. (a) The elastic stage; (b) pre-stud tearing stage; (c) post-stud tearing stage; (d) cumulative energy dissipated.

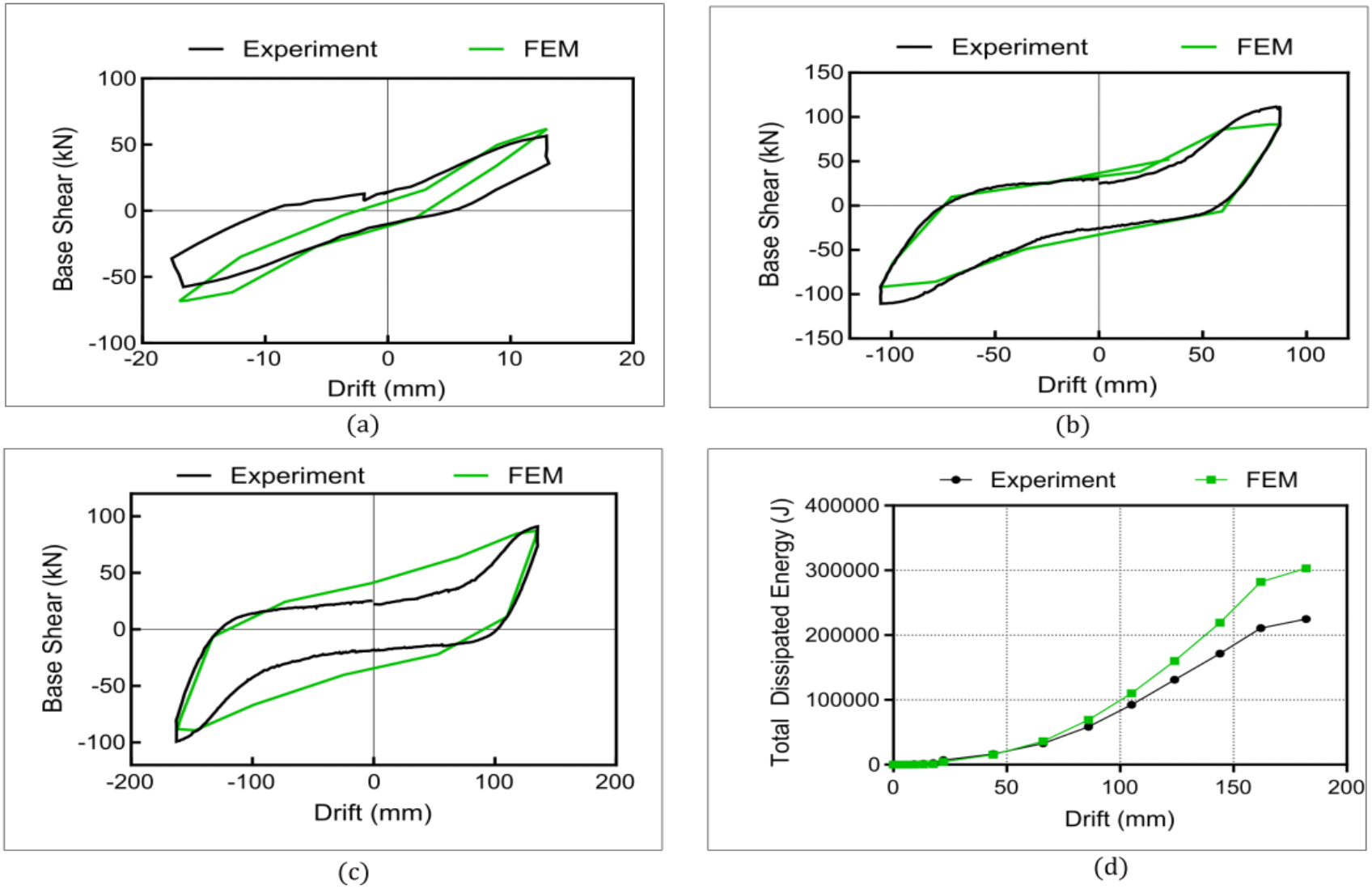


Figure 5.29: Cyclic energy output comparisons between the experimental and numerical results for specimen C-SW-2. (a) The elastic stage; (b) pre-stud tearing stage; (c) post-stud tearing stage; (d) cumulative energy dissipated.

5.6.3 Cyclic Finite Element Analysis of Specimen GD-10.

The final section of this chapter is concerned with verifying the finite element model of the diagonally strapped specimen (GD-10). Determination of the loading rate, validating the quasi-static behaviour of the model, as well as applying the displacement load followed the same procedure as the concentric-sheathed specimens mentioned in previous sections. Using the natural period of the specimen as a lower bound, it was determined that a loading rate of 4 seconds per cycle produces a smooth quasi-static simulation. Regarding the cyclic displacement-controlled load, the model was subjected to the same loading protocol as the experiment however the loading cycles post-yield were applied once to save computation time. The comparisons are carried out using the same parameters that were discussed in Section 5.6.2.

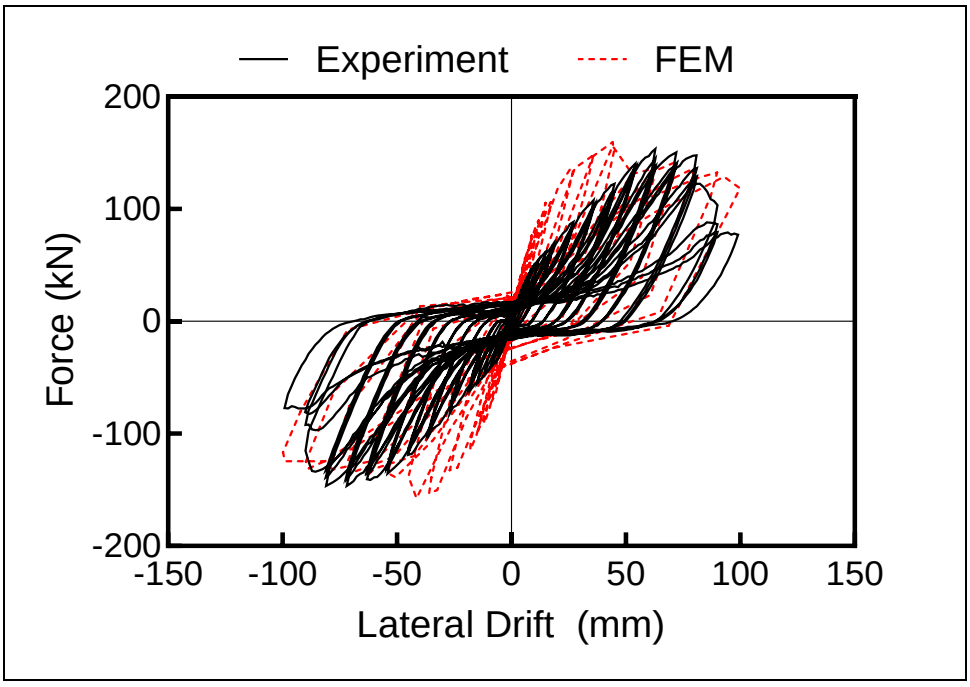


Figure 5.30: Comparison between FEM and experimental results for specimen GD-10.

Based on the numerical and experimental hysteresis curves shown in Figure 5.30, the model simulates the overall behaviour of specimen GD-10 with modest accuracy. Even though the

capacity of the system is accurately estimated (4% error), the model is too rapid in predicting the drift at which the peak load occurs and the elastic stiffness is yet again overestimated for comparable reasons as the concentric-sheathed specimens. While the model was effective in reproducing several failure modes of the system (refer to Figure 5.31), specifically the pattern of buckles observed in the straps, studs, and sheet, it failed to capture an important phenomenon which was the failure of the hold-downs. As discussed in Chapter 3, a unique failure mode in the form of plastic bending was observed in the hold-downs. The hold-down failure was reflected in a sharp drop in the strength and stiffness of the specimen. The finite element model was not able to replicate this specific behaviour which in turn led to errors in emulating the sharp strength degradation of the specimen as well as overestimation of the total dissipated energy.

Similar deductions can be made when examining isolated hysteresis loops of the model. Figure 5.32 displays comparisons of isolated hysteresis loops at three stages, the elastic stage, pre-hold-own failure stage, and post-hold-down failure stage. The sources of error that were encountered in the previous models are also applicable herein. In the elastic stage, the model overpredicts elastic stiffness of the shear wall. Furthermore, prior to the hold-down failure, there is reasonable agreement in terms of reloading stiffness, however the model is slow in simulating the reloading stiffness. Finally, for high displacement and after the hold-downs have failed, there is poor agreement between the model and experimental results. For all cases however, the pinching produced by the model is not as pronounced as the experimental observations, which is reflected in a high error when comparing the energy dissipated (44%). A summary of the input parameters, experimental results, and numerical results are displayed in Table 7 & Table 8.

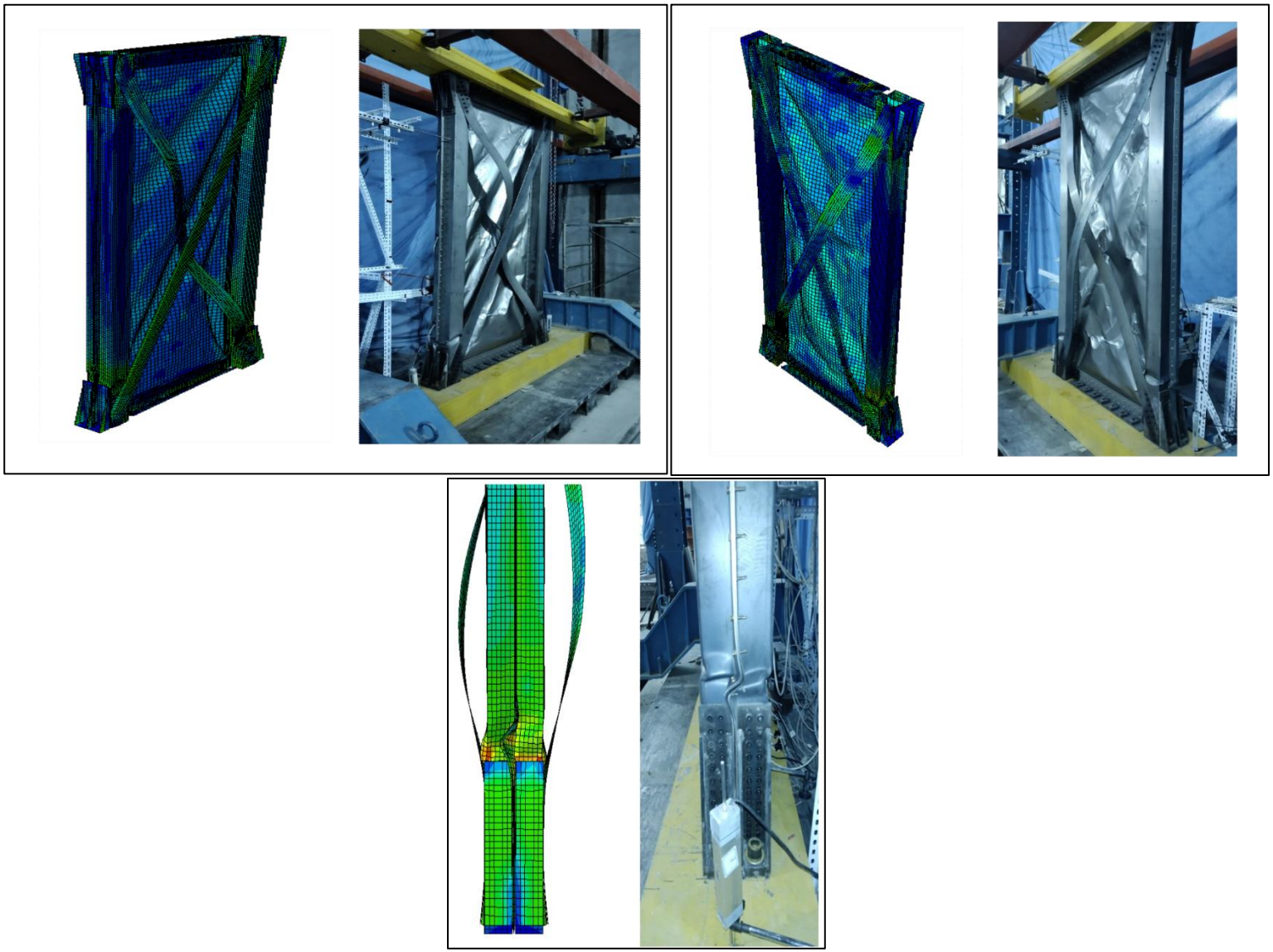


Figure 5.31: Failure modes comparison between the FEM model and experiment for specimen GD-10.

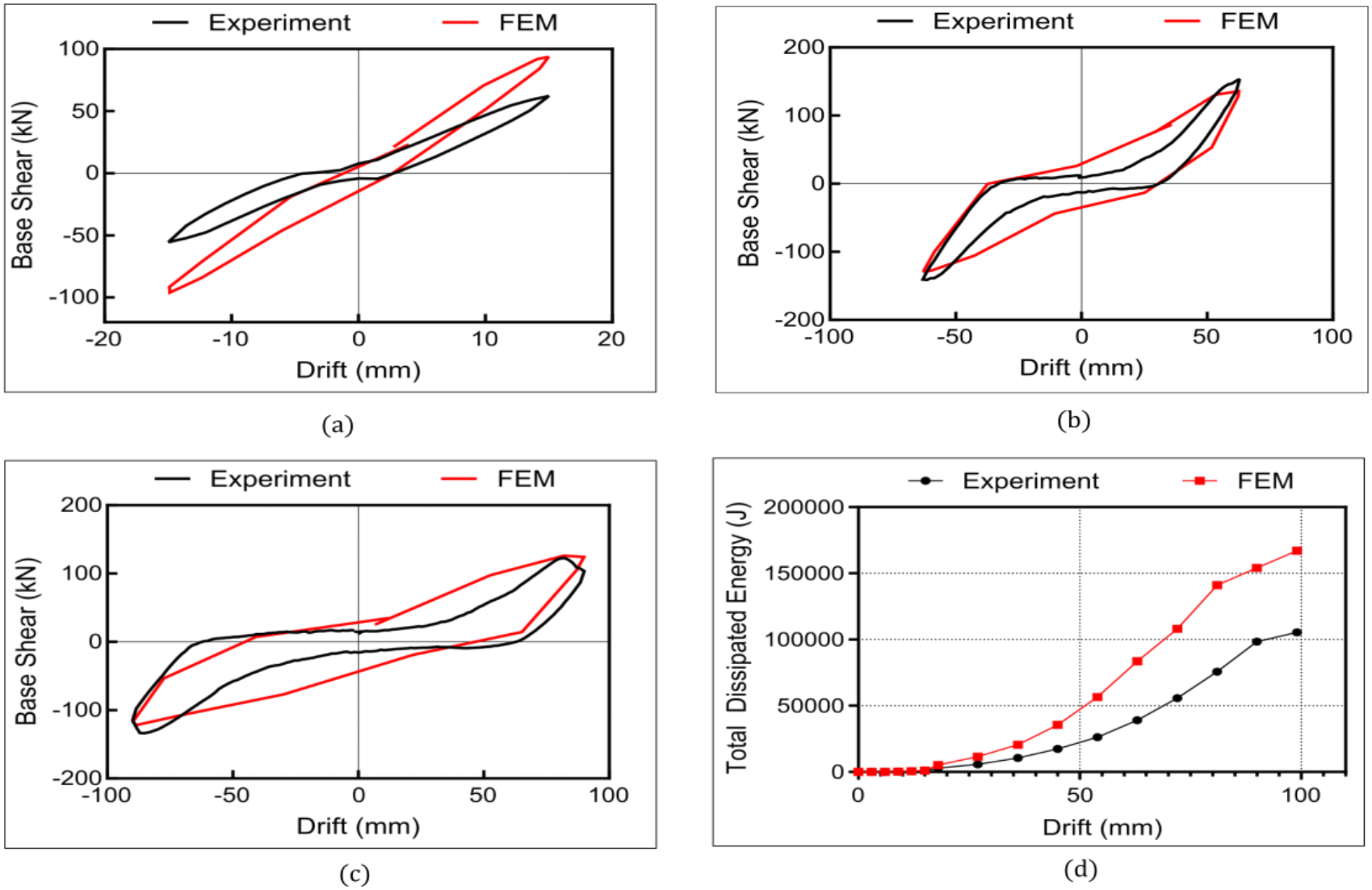


Figure 5.32: Cyclic energy output comparisons between the experimental and numerical results for specimen GD-10.

Table 7: Summary of input parameters for the explicit numerical analyses.

Specimen	Number of elements (S4R)	Frequency (Hz)	Loading rate (s)	Δt_{stable} (s)
GD-06	35904	4.75	11	$1.5e10^{-5}$
GD-19	35904	4.75	5	$1.5e10^{-5}$
C-SW-2	43648	33.93	5	$2.2e10^{-5}$
GD-10	39136	12.7	4	$1.65e10^{-5}$

Table 8: Summary of experimental and numerical results.

Specimen	V_{peak} (Exp.)	V_{peak} (FEM)	% Error	Drift at peak (Exp.)	Drift at peak (FEM)	Total Energy (Exp.)	Total Energy (FEM)	% Error
GD-06	102.5	102.2	0.25%	85	85	18678	20080	7.5%
GD-19	105.29	100	5%	72	72	166230	208000	25%
C-SW-2	117.85	104	11.75%	72	72	225940	301000	33%
GD-10	153.5	159	4%	63	45	115740	167000	44%

- **Force is expressed in kilo-Newtons, drifts in mm, and energy in Joules.**

5.7 Concluding Remarks

The verification of the benchmark finite element models was discussed in this chapter. In order to overcome convergence issues, the explicit solver was employed to model the shear wall specimens. Furthermore, to ensure that every simulation was conducted under quasi-static conditions, the energy balance equation was satisfied for each benchmark model. Based on the preceding discussions, the following conclusions can be stated:

1) The models of the concentric-sheathed specimen displayed good agreement with the experiments in terms of peak load, drift at peak loads, energy dissipation capacity and failure modes.

2) The model of the diagonally strapped specimen on the other hand showed modest correlation with the experimental results.
3) The solution accuracy decays at higher displacements, this is attributed to the tearing and fracture in the studs that were encountered in the experiments but not simulated by the finite element models.
4) For the diagonally-strapped specimen, the failure of the hold-downs was not reproduced by the finite element models which results in overestimation of the dissipated energy.
5) It is anticipated that a more robust kinematic hardening mode, such as the pinching4 material model for the screws, would result in better approximations of the hysteresis loops.

Chapter 6: Parametric Study

6.1 Introduction

This chapter describes the parametric study that was carried out on the benchmark models that were validated in Chapter 5. It was identified in the experimental investigation that the premature buckling of the studs restricted the sheathing from reaching its full capacity. Accordingly, one of the main objectives of this chapter is to come up with economical design alternatives that maximizes the efficiency of the structural system by preventing the buckling of the end studs. This can be achieved by investigating the sensitivity of several building and specimen parameters on the overall behaviour of the cold-formed steel shear walls.

Generally speaking, a substantial number of parameters that influence the behaviour of CFS shear wall exist, and a comprehensive study involving each parameter would be cumbersome [85]. Subsequently, the study discussed herein shall focus on the following parameters: framing thickness, sheathing thickness, strap thickness, screw spacing, aspect ratio, and finally, different construction details such as placing the hold-downs on both sides of the stud. The same modelling assumptions, geometry, and boundary conditions that were established in Chapter 5 are applied, with the exception of the parameters being investigated. Moreover, all the parametric studies are conducted using the material properties that were discussed in Chapter 3. The results of the parametric analyses are reported in the form of base shear-drift plots and total energy dissipated for cyclic models, as well as patterns of the formation of the tension field. Finally, since it showed modest correlation with the experimental results, parametric studies on the diagonally strapped specimen (GD-10) are limited to monotonic loading only.

6.2 Framing Thickness

The first parameter to be investigated is the thickness of the framing members since it relates directly to the strength and stiffness of the studs. To adhere to common engineering practice, the range of sizes that were investigated were retrieved from the specifications published by the Canadian Sheet Steel Building Institute (CSSBI) [86]. Therefore, the effect of framing thickness on the behaviour of the three tested specimens was investigated using models with framing thicknesses of 4.2 mm, 3.43 mm, 3.05 mm, 1.81 mm, and 1.5 mm. For models of specimen C-SW-2, the thickness of the intermediate stud is maintained constant at 1.5 mm. The results are compared with the benchmark models as illustrated in Figure 6.1 through Figure 6.3

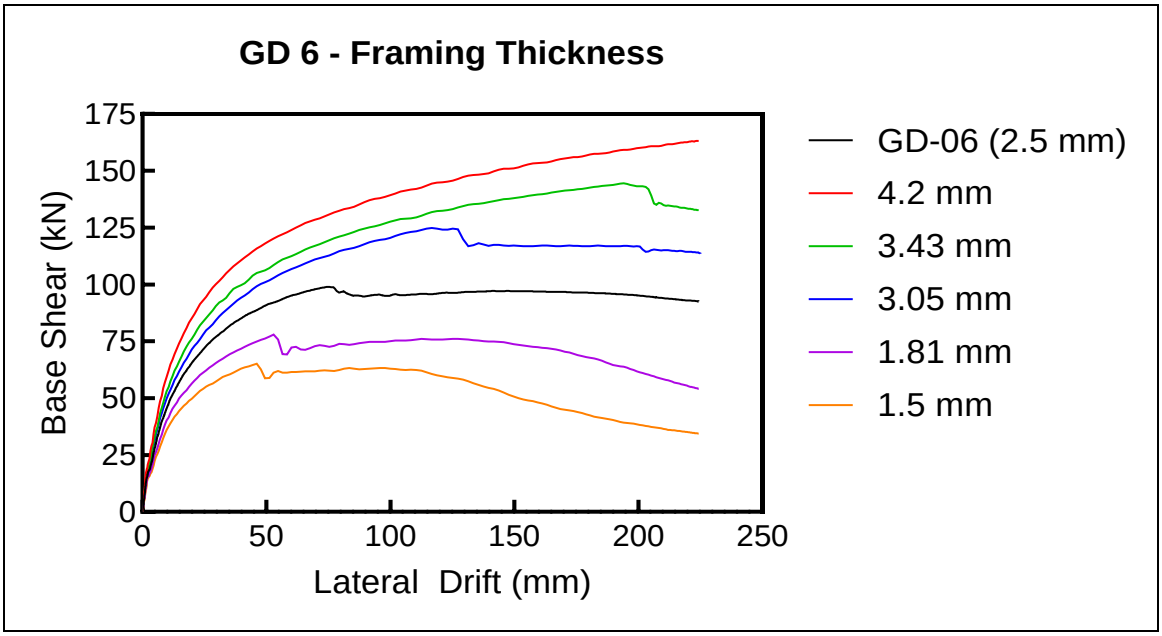


Figure 6.1: Comparison between different framing sizes for specimen GD-06.

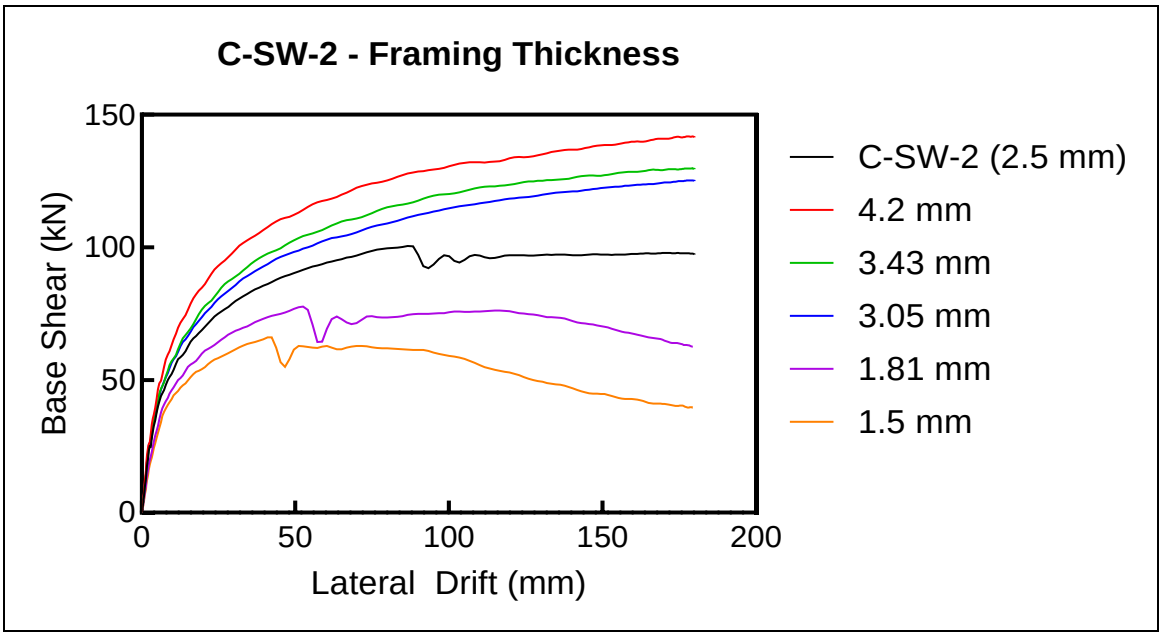


Figure 6.2: Comparison between different framing sizes for specimen C-SW-2.

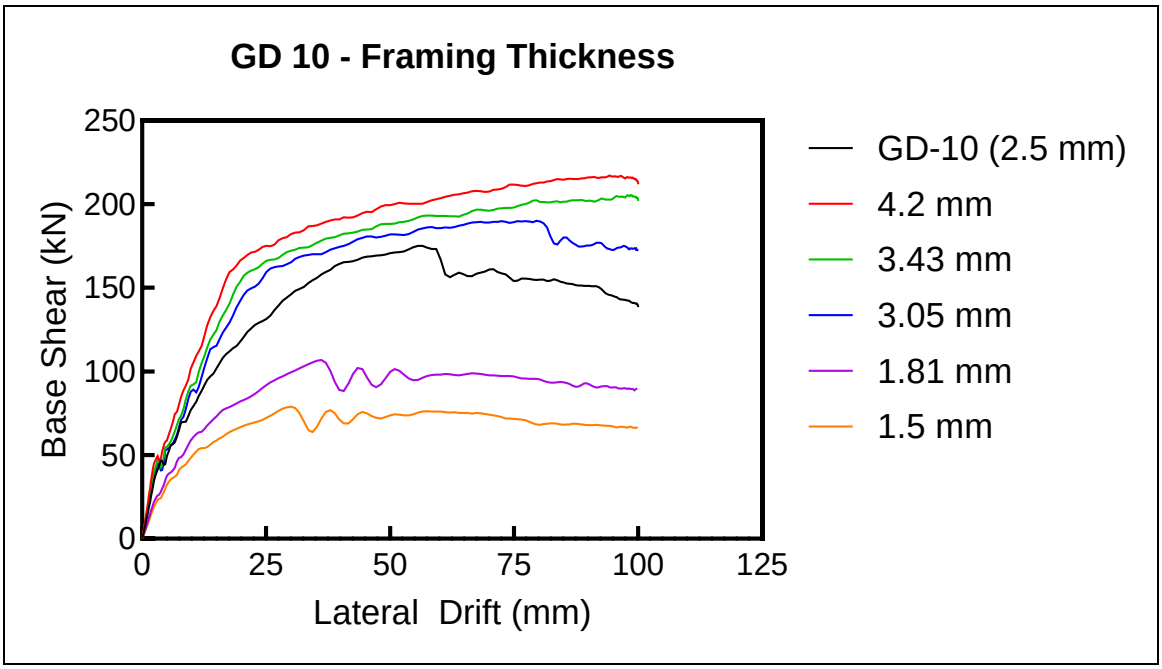


Figure 6.3: Comparison between different framing sizes for specimen GD-10.

It can be observed from the figures that the elastic stiffness and ultimate resistance of the walls increase as the framing thickness increases. In addition, as the thickness of the framing members increase, the global softening point on the base shear-drift plot occurs at higher drifts which

signifies that the end studs are capable of withstanding higher loads before undergoing flexural buckling. This behaviour was expected however and can be explained by re-analyzing the load-bearing mechanism of the walls. As stated in Chapter 3, the load-bearing mechanism of the shear walls is a combination of tension field action and portal frame action. Increasing the thickness of the framing members increases the axial and flexural rigidity of the studs which in turn allows the studs to bear higher loads caused by the inclined tension field action. Furthermore, the increased stiffness of the framing members provides improved anchorage for the sheathing and allows for a more uniform tension field to develop thereby increasing the load bearing capacity of the sheathing. Additionally, at a certain stud thickness, the load-deformation graphs show no obvious softening point at high drifts. Further examination of the deformed shapes of the model indicates that as the framing members get thicker, the end stud buckling failure mode is eliminated and the dominant failure mode is the inelastic shear buckling of the sheet. This particular phenomenon occurred at stud thickness equal to 4.2 mm for specimen GD-06, 3.43 mm for specimen GD-10, and 3.05 mm for specimen C-SW-2. It is worth noting that for specimen C-SW-2, the intermediate stud acts as a stiffener which reduces the load on the end stud, confirming the superior performance of the specimen. Figure 6.4 shows a sample of the deformed shape of specimen GD-06 using framing member with varying thicknesses.

To gain further insight on the effects of the framing thickness, the moment of inertia of the studs was plotted against the peak load of each model. As displayed in Figure 6.5, the relationship between the moment of inertia and peak load can be approximated as linear. While more simulations are needed to confirm this assumption, Figure 6.5 shows the potential of performing dimensional analysis to determine the trend of varying the thickness of the framing members.

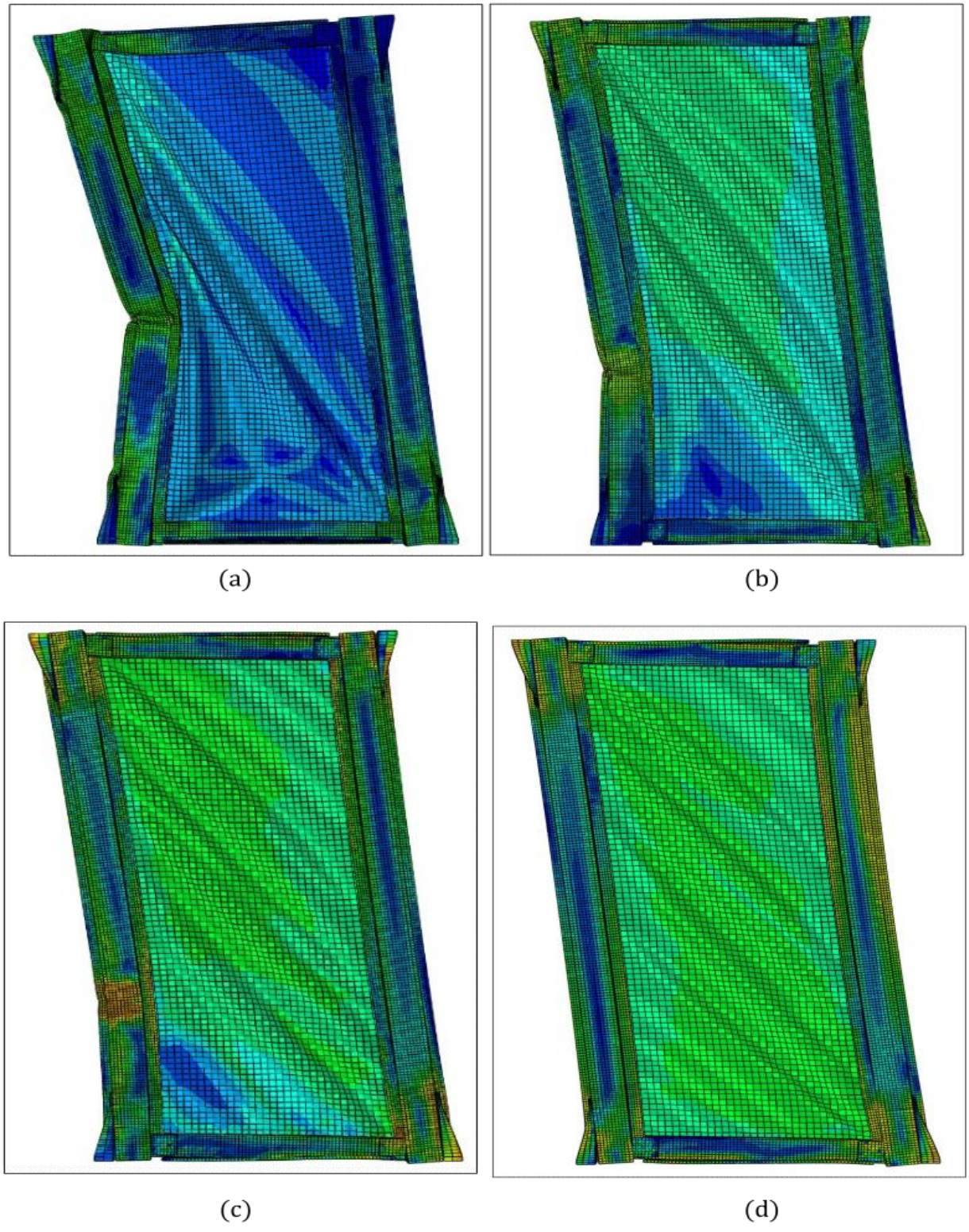


Figure 6.4: Deformed shape of specimen GD-06 using different framing thicknesses. (a) 1.5 mm; (b) 3.05 mm (c) 3.43 mm; (d) 4.2 mm.

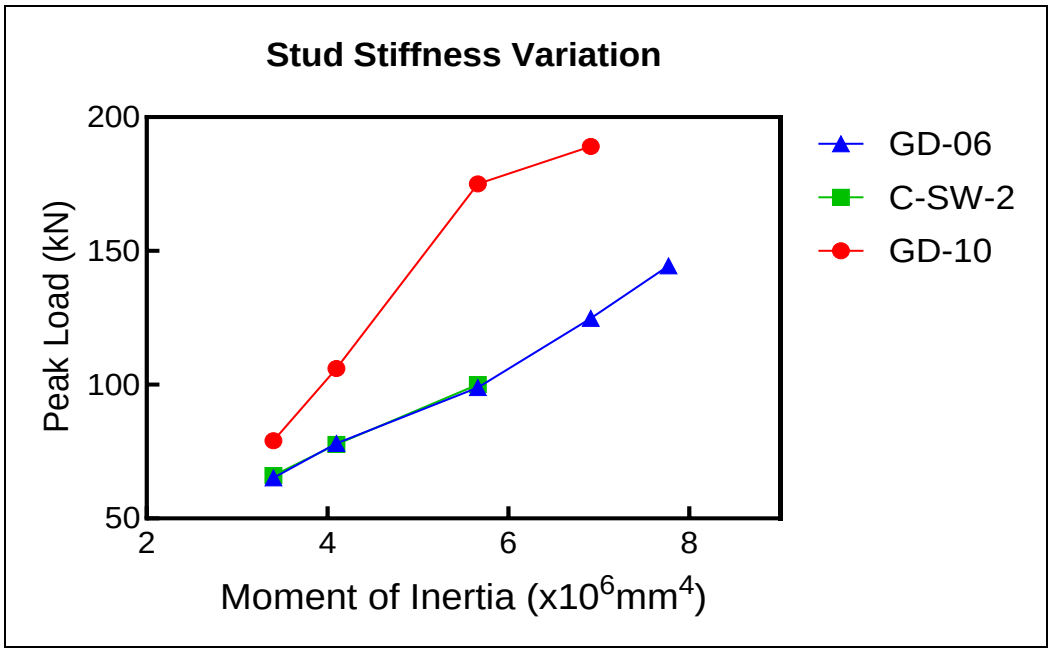


Figure 6.5: Variation of peak load vs. moment of inertia (major axis bending).

6.3 Sheathing Thickness

To evaluate the influence of sheathing thickness on the behaviour of the shear walls, six models were established with the following sheathing thicknesses: 1.37, 1.09, 0.65, 0.5, 0.43, and 0.36 (mm), whereas the framing thickness was kept constant at 2.5 (mm). The main objective was to observe the effect of varying the sheathing thickness on various structural properties such as the elastic stiffness, drift at peak load and peak load. The results are displayed in Figure 6.6 through Figure 6.8. While increasing the thickness of the infill panel increases the elastic stiffness and peak load of the shear walls, it can be inferred that using thicker sheathing decreases the ductility of the system as the end studs buckle at lower drifts. Recall from Eq. (2.3), the "pull-in" inclined tension field forces are a function of the thickness of the panels, the angle of inclination, and the yield strength of the sheathing material (at least in the elastic region). Hence while using thicker panels would increase the shear resistance of the wall, it also translates to higher forces on the

end studs that lead to premature buckling which is not beneficial in the context of seismic design. On the other hand, for specimens GD-06 and C-SW-2, models with thinner sheathings (0.43 mm and 0.36 mm) showed no softening behaviour on the global base shear versus drift plots which was reflected in the formation of a uniform tension field across the panel. This behaviour wasn't observed in models of specimen GD-10 however, since the added forces from the strap bracing resulted in stud buckling regardless of the thickness of the sheathing. A sample of the deformed shape of specimen C-SW-2 with varying sheathing thicknesses is shown in Figure 6.9.

The peak resistance of each model was plotted against the thickness to determine the trend of varying the sheet thickness. Figure 6.10 indicates that the relationship between sheathing thickness and the peak load is linear for specimen GD-10 and can be assumed as exponential for specimen GD-06. For specimen C-SW-2, the trend follows a linear path when sheathing thickness of 0.8 or higher is used.

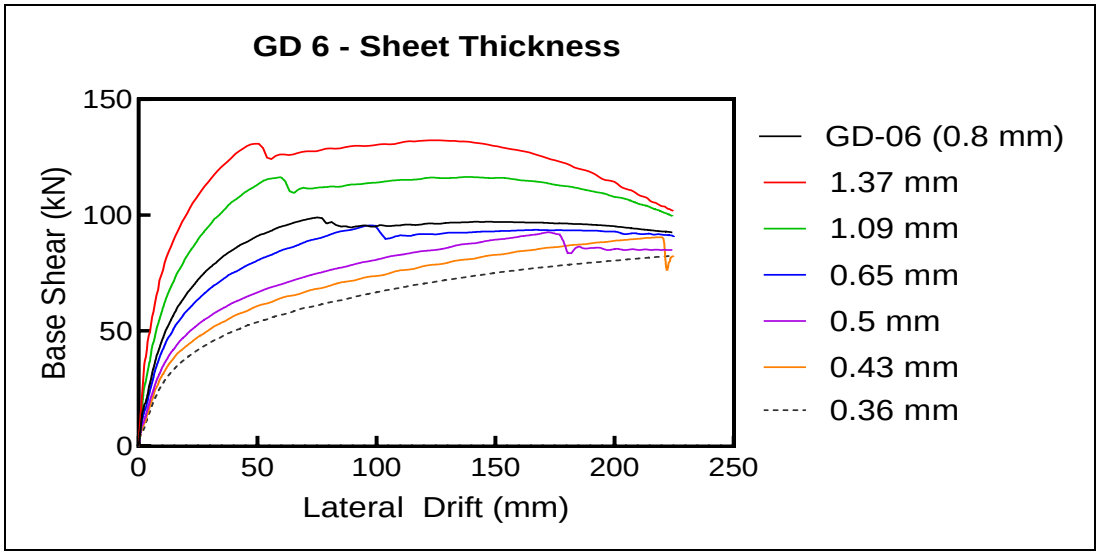


Figure 6.6: Comparison between different sheathing sizes for specimen GD-06.

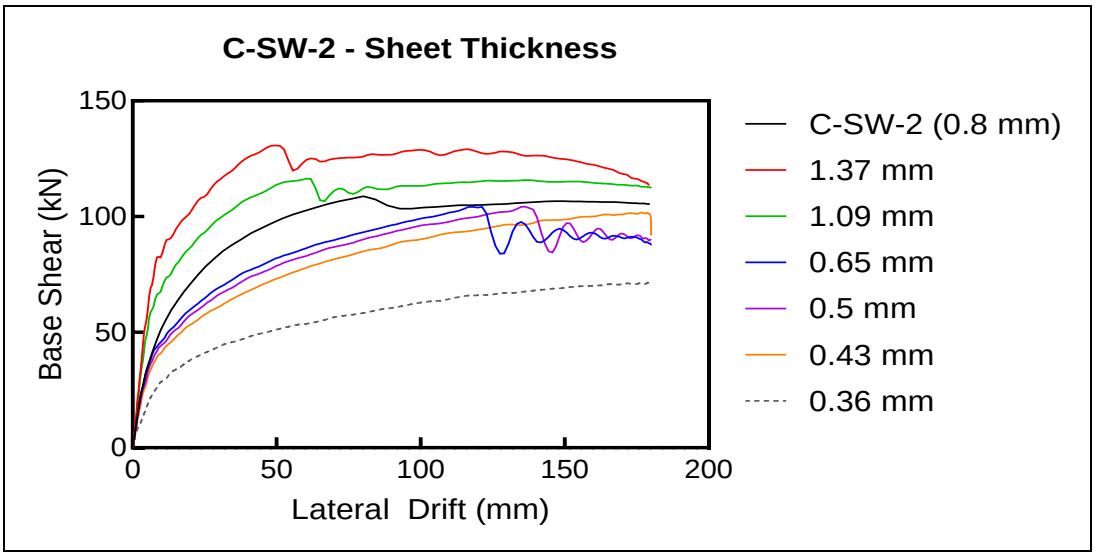


Figure 6.7: Comparison between different sheathing sizes for specimen C-SW-2.

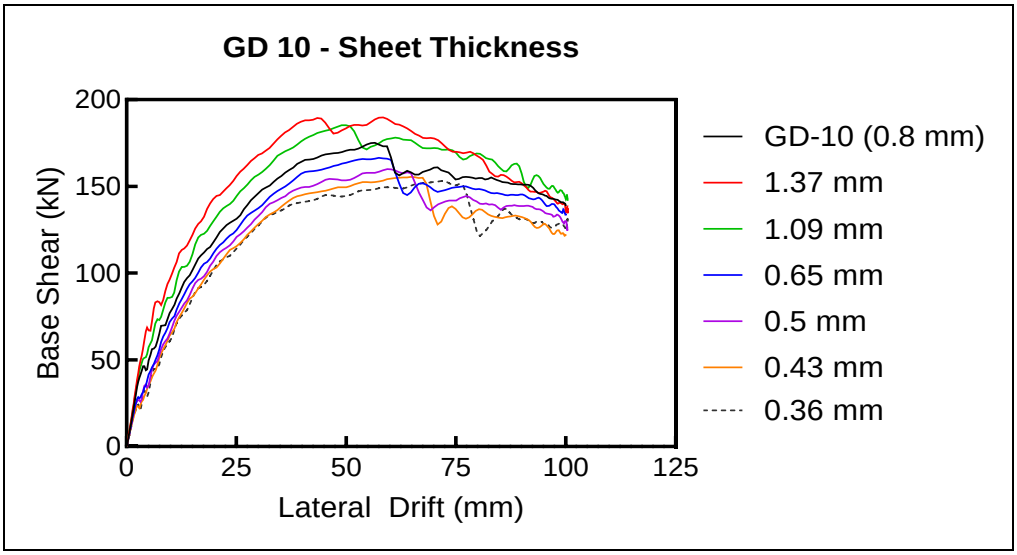


Figure 6.8: Comparison between different sheathing sizes for specimen GD-10.

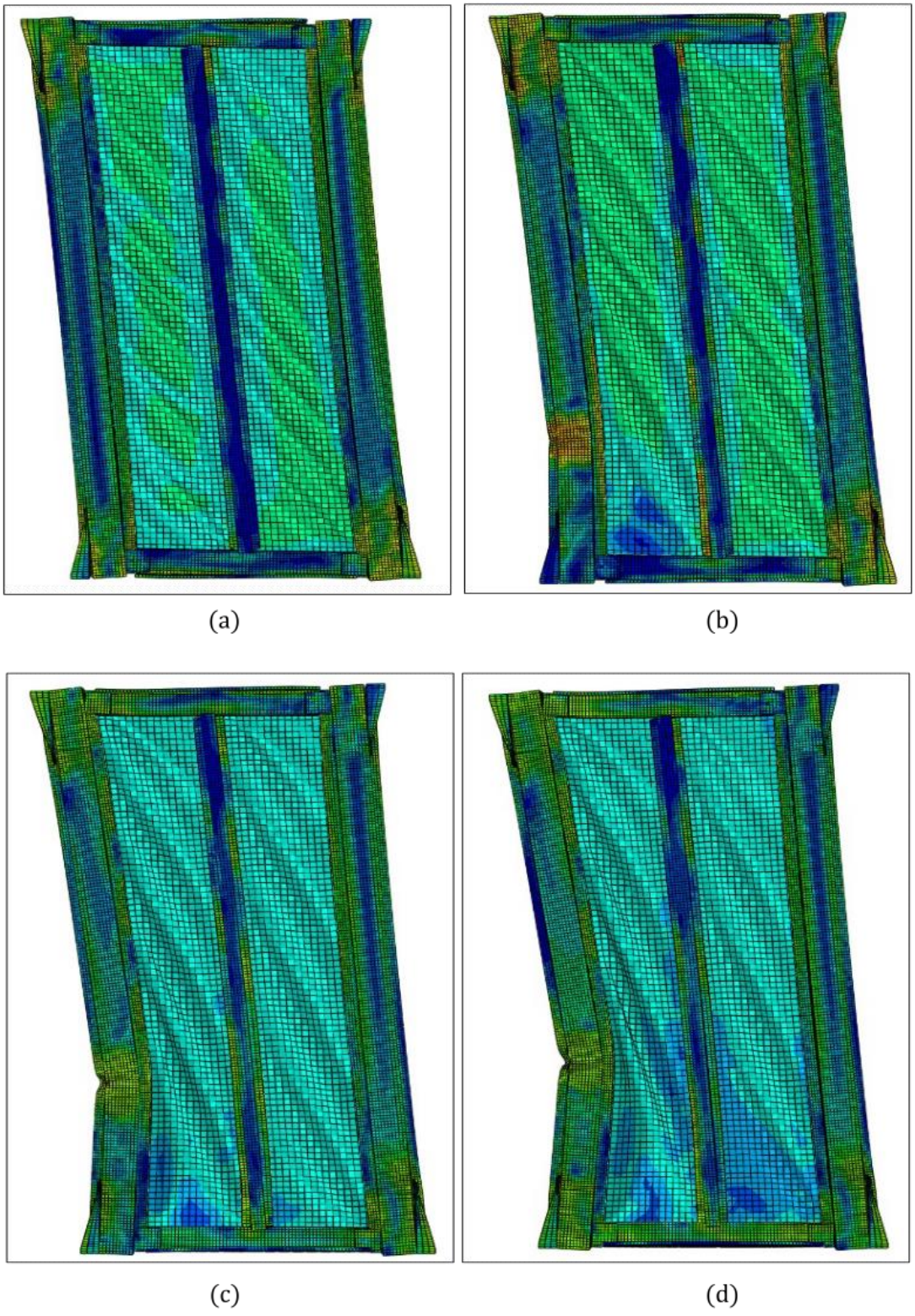


Figure 6.9: Deformed shape of specimen C-SW-2 using different sheathing thicknesses. (a) 0.43 mm; (b) 0.65 mm (c) 1.09 mm; (d) 1.37 mm.

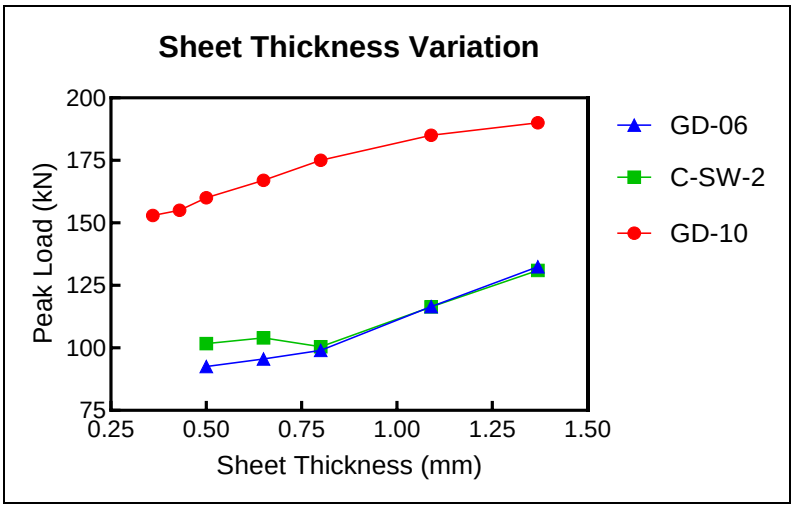


Figure 6.10: Variation of peak load vs. sheathing thickness.

It is evident from the results of sections 6.2 and 6.3 that the thickness of the framing members and the thickness of the sheathing have a major influence on the behaviour of the walls. Simply increasing the thickness of the stud to eliminate the buckling failure mode would result in an uneconomical design. Alternatively, using a very thin sheet (≤ 0.43 mm) significantly decreases the shear resistance of the wall which would lead to a design that is not efficient. Also, for walls with thin sheets, the screw connection failure is most likely the primary failure mode. If a non-dimensional parameter β is defined such that $\beta = (t_{sheathing} / t_{studs})$, then the ratio of sheathing thickness to framing thickness at which stud buckling is prevented can be obtained. As displayed in Figure 6.11, when the ratio is limited to $\beta < 0.2$, a uniform tension field forms across the panel and the sheathing can attain its full capacity. This behaviour is also consistent with capacity-based design as the main inelastic fuse of the system in this case is the sheathing rather than the studs. It should be emphasized that this ratio is applicable only for shear wall configurations similar to specimen GD-06, since for specimen C-SW-2 and GD-10, the intermediate stud and strap bracing also influence the development of the tension field. The effect of strap bracing is investigated in the following section.

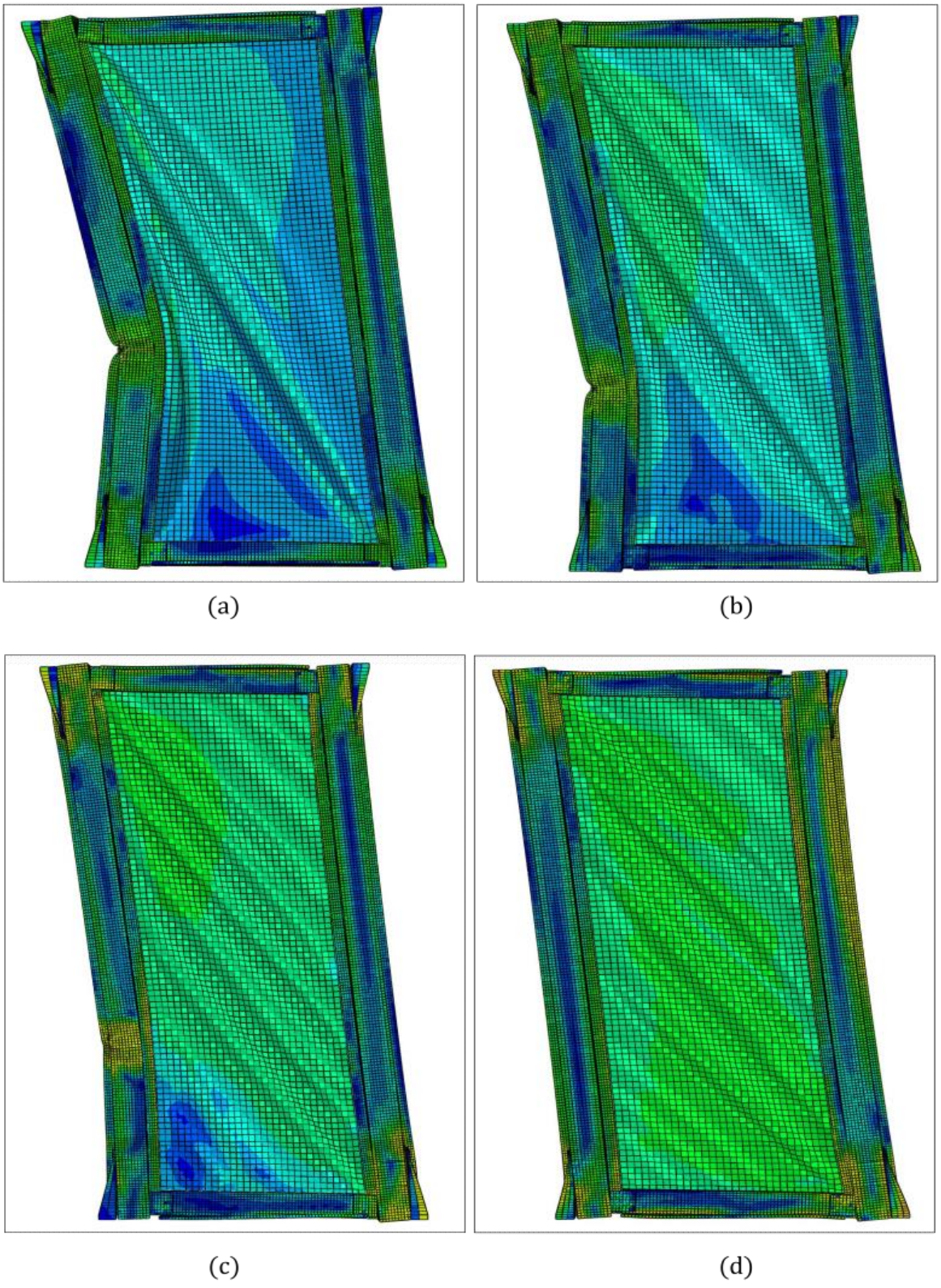


Figure 6.11: Development of tension field under different framing to sheathing ratios. (a) β = 0.55; (b) β = 0.32 (benchmark); (c) β = 0.2; (d) β = 0.19.

6.4 Strap Thickness

The same range of thicknesses that were assessed in section 6.2 are used in this section to determine the effect of changing the thickness of the strap bracing on specimen GD-10, whereas the framing and sheathing thicknesses remain as 2.5 mm and 0.8 mm, respectively. The results, which are displayed in Figure 6.12, indicate a similar pattern to that of Section 6.3.

Increasing the strap thickness increases the peak load and elastic stiffness, however it decreases the ductility of the system as the global softening point occurs at lower drifts. This behaviour can also be explained by inspecting the mechanics of the diagonally strapped wall. The system mainly resists lateral loads by a combination of tension field action and strap yielding in tension. As previously stated, the inclined tension field forces can be resolved into horizontal pull in forces and vertical compression forces (or vertical tension forces in the opposite stud). Likewise, the inclined force of the strap can be resolved into vertical forces and horizontal forces. The horizontal force is transferred to the beam while the vertical component is transferred to the end studs in the form of a compression axial force. Since the straps are attached to both sides of the wall, the compression forces on the studs are relatively large. Additionally, studying the relationship of strap thickness to the peak load (Figure 6.13) illustrates a logarithmic trend. When straps thicker than 2.5 mm are used, the increase in peak load is very insignificant since the end studs cannot sustain the increased loads transferred from the brace.

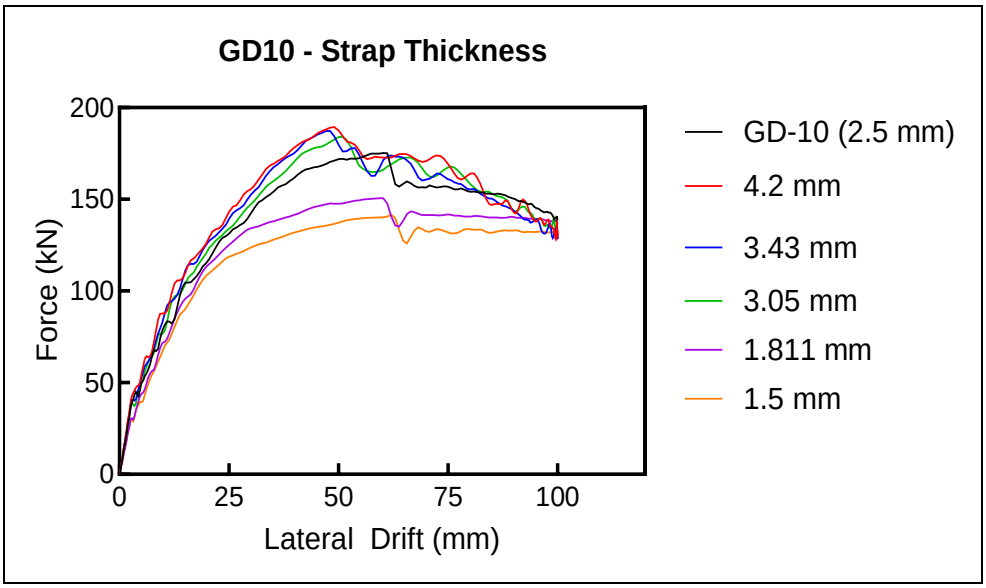


Figure 6.12: Comparison between different bracing sizes for specimen GD-10.

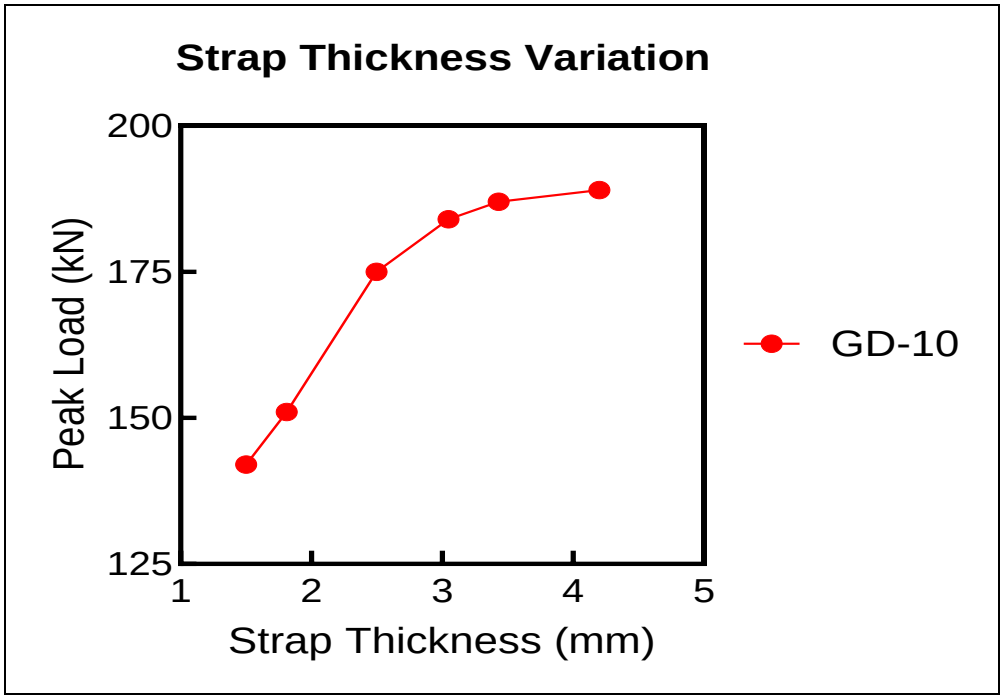


Figure 6.13: Variation of peak load vs. bracing thickness.

6.5 Screw Spacing

To study the influence of screw layout on the lateral resistance and ductility of the shear walls, models with varying perimeter screw spacings were subjected to monotonic displacement loads.

Four screw spacings were assessed: 25, 75, 100, and 150 (mm). The results are displayed in Figure 6.14 through Figure 6.16.

As expected, decreasing the screw spacing increases the peak load as well as elastic stiffness of the shear wall specimens. This behaviour was also observed in previous CFS shear wall research [6], [11], [12]. Decreasing the spacing of the screws increases the total number of screw around the perimeter of the wall and thereby increases the sheathing bearing deformations which contributes significantly to the total lateral resistance of the walls. Another significant observation can be made by assessing Figure 6.14, as the screw spacing is decreased, the ductility of the system also decreases. For instance, when a screw spacing of 75 mm is used, the peak load occurs at a drift equal to 3.8% of the total height of the wall. Conversley, when the screw spacing is increased to 100 mm, the peak load occurs at a drift equal to 4% of the height. Decreasing the screw spacing provides better anchorage for the sheathing and as a result increases the stresses in the studs in the form of added axial forces and bending moment, which in turn explains why the studs have buckled at lower drifts.

The results of Section 6.2 to Section 6.5 for each specimen are summarized in Table 9 through Table 12. The results are displayed in terms of peak load, elastic stiffness, and drift at peak load. Also for the following tables, the percent different of various parameters is calculated with respect to the benchmark models discussed in the previous chapter.

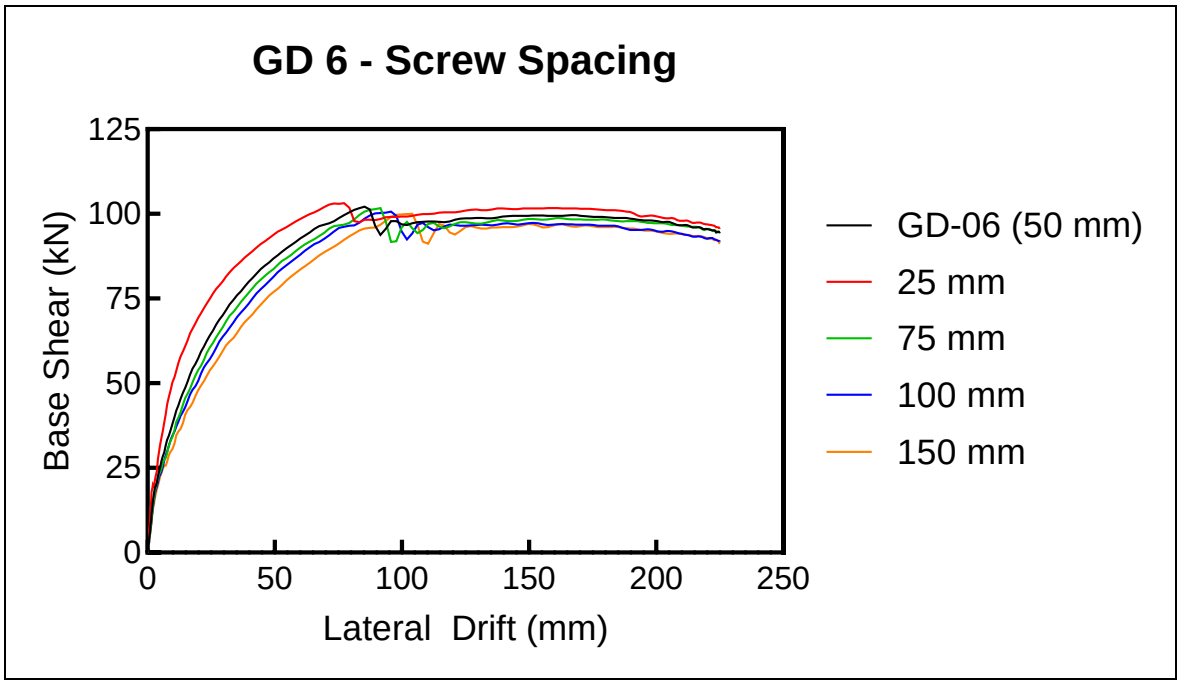


Figure 6.14: FEM results using different screw spacing for specimen GD-06.

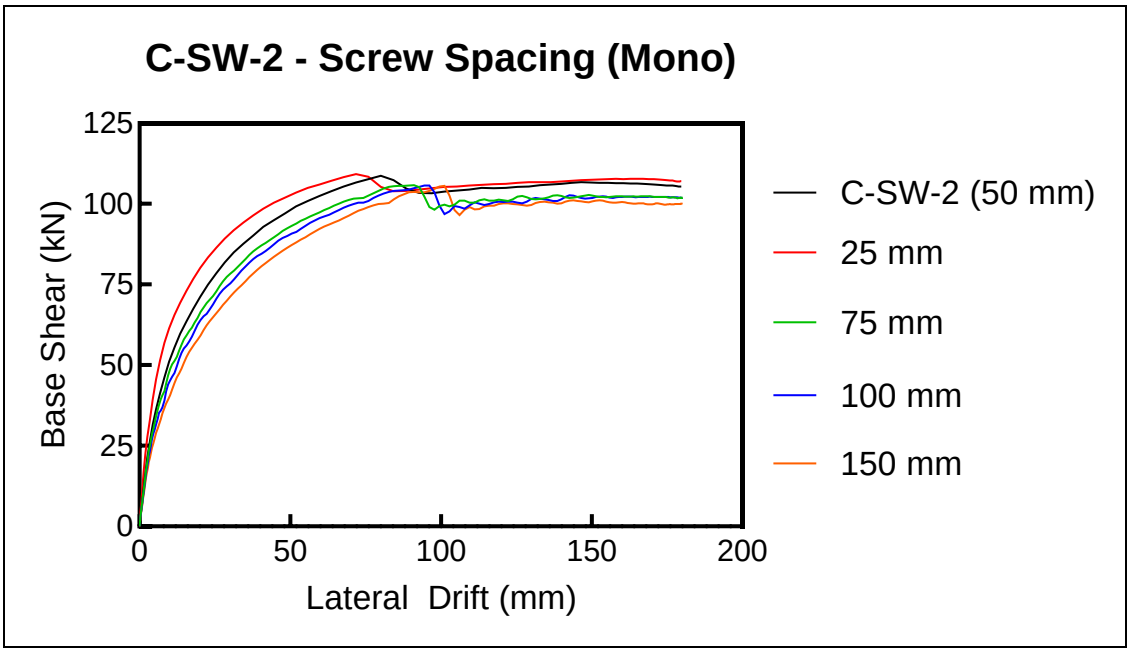


Figure 6.15: FEM results using different screw spacing for specimen C-SW-2.

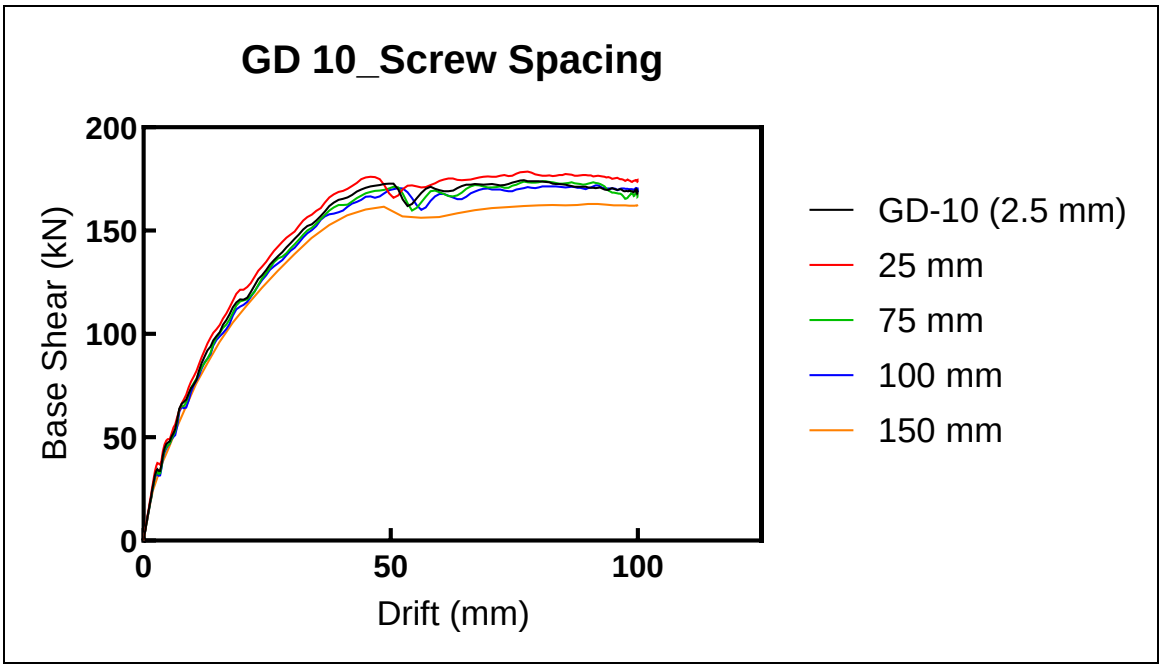


Figure 6.16: FEM results using different screw spacing for specimen GD-10.

Table 9: Effects of varying the thickness of the framing members.

Stud Thickness (mm)	V_{peak} (kN)	% Difference	K_e (kN/mm)	% Difference	Drift at peak (%)
GD-06					
4.2	163	65	5.7	11.7	9.375
3.43	144.5	46	5.1	0	8.1
3.05	125	26	5	2	5.2
1.811	78	21	4.5	11.8	2.2
1.5	65	34	4.15	18.6	1.875
C-SW-2					
4.2	142	42	7.6	4.1	7.5
3.43	130	30	6.5	11	7.5
3.05	125	25	6.4	12	7.2
1.811	77.6	22.4	6.1	16.5	2.1
1.5	66.1	34	6.1	16.5	1.6
GD-10					
4.2	215	23	10.75	35	4.1
3.43	205	17	9.65	21	4.1
3.05	189	8	8.8	10.7	2.7
1.811	106	39	6.4	19.5	1.5
1.5	79	55	6.4	19.5	1.25

Table 10: Effects of varying the thickness of the sheathing.

Sheet Thickness (mm)	$V_{peak}\ (kN)$	% Difference	$K_e\ (kN/mm)$	% Difference	Drift at peak (%)
GD-06					
1.37	132.4	33.8	10.3	102	2.1
1.09	116.5	17.7	6.95	36	2.5
0.65	95.6	3.4	4.37	14	3.75
0.5	92.6	6.5	3.2	37	7.2
0.43	90	9.1	2.75	46	9.375
0.36	82	17.2	2.3	55	9.375
C-SW-2					
1.37	131	31	12.2	67.1	2.0
1.09	116.4	16.4	10.8	48	2.7
0.65	104	4	5.85	19.8	5
0.5	101.7	1.7	5.175	29	5.8
0.43	100.5	0.5	4.4	39.76	7.5
0.36	72	28	2.74	62.5	7.5
GD-10					
1.37	190	8.5	12.2	53.5	1.8
1.09	185	5.7	9.74	22.5	2.1
0.65	167	4.5	7.4	7	2.625
0.5	160	8.6	6.7	15.7	2.7
0.43	155	11.5	6.5	18	2.9
0.36	153	12.5	6.1	23.2	3.25

Table 11: Effects of varying the spacing of the screws.

Sheet Thickness (mm)	V_{peak} (kN)	% Difference	K_e (kN/mm)	% Difference	Drift at peak (%)
GD-06					
25	107	4.65	4.27	15.4	3.9
75	102	0.43	3.1	16.2	3.8
100	100.6	1.5	3.0	19	4
150	100	2.1	2.7	27	4.4
C-SW-2					
25	110	1.2	6.25	9.1	2.9
75	105.7	2.7	4.9	12	3.66
100	105.5	2.7	4.75	14.1	3.75
150	105.6	2.7	4.13	14	3.77
GD-10					
25	178	2.4	8.125	4.9	1.9
75	173	0.22	7.6	1.9	2.1
100	171	1.35	7.3	4.6	2.25
150	162	6.5	7.15	4.8	2.0

Table 12: Effects of varying the thickness of the bracing straps.

Strap Thickness (mm)	V_{peak} (kN)	% Difference	K_e (kN/mm)	% Difference	Drift at peak (%)
GD-10					
4.2	189	8.2	9.45	21.5	2.04
3.43	187	7	8.9	14.1	1.95
3.05	184	5.2	8.6	10.25	2.125
1.811	151	14	7.3	6.4	2.5
1.5	142	19.1	7.3	6.4	2.5

6.6 Aspect Ratio

The influence of the aspect ratio (width/height) of the wall is investigated in this section. Six models were set up having aspect ratios of 0.25, 0.286, 0.333, 0.4, 0.666, and 1. To be consistent with typical building parameters, the height of the models were fixed at 2,400 mm while the width of the wall was altered. Hence an aspect ratio of 0.25 represents a relatively narrow shear wall while an aspect ratio of 1 corresponds to a wide shear wall. It is predicted that the aspect ratio will have a significant effect on the strength and stiffness of the system, since changing the aspect ratio of the wall changes inclination of the tension field. Also, this particular parametric study is limited to the concentric-sheathe specimen (GD-06) only. The effects of the variation of the aspect ratio are displayed in Figure 6.17, while the deformed shapes of walls with different aspect ratios are displayed in Figure 6.18.

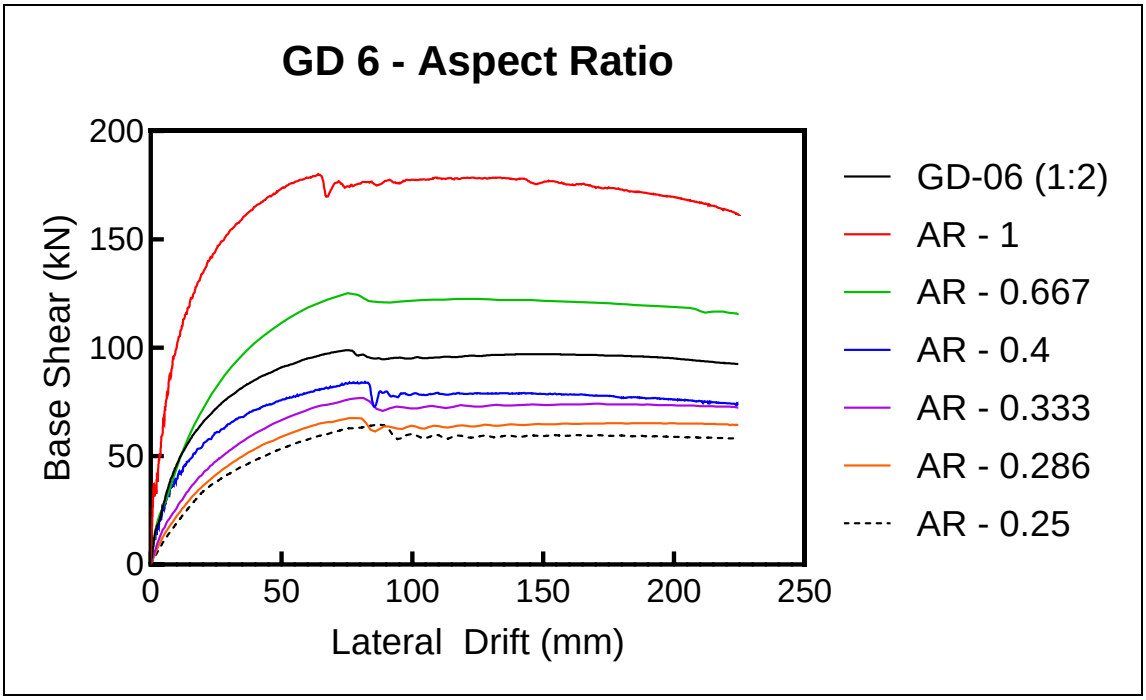


Figure 6.17: Effect of aspect ratio on the behaviour of specimen GD-06.

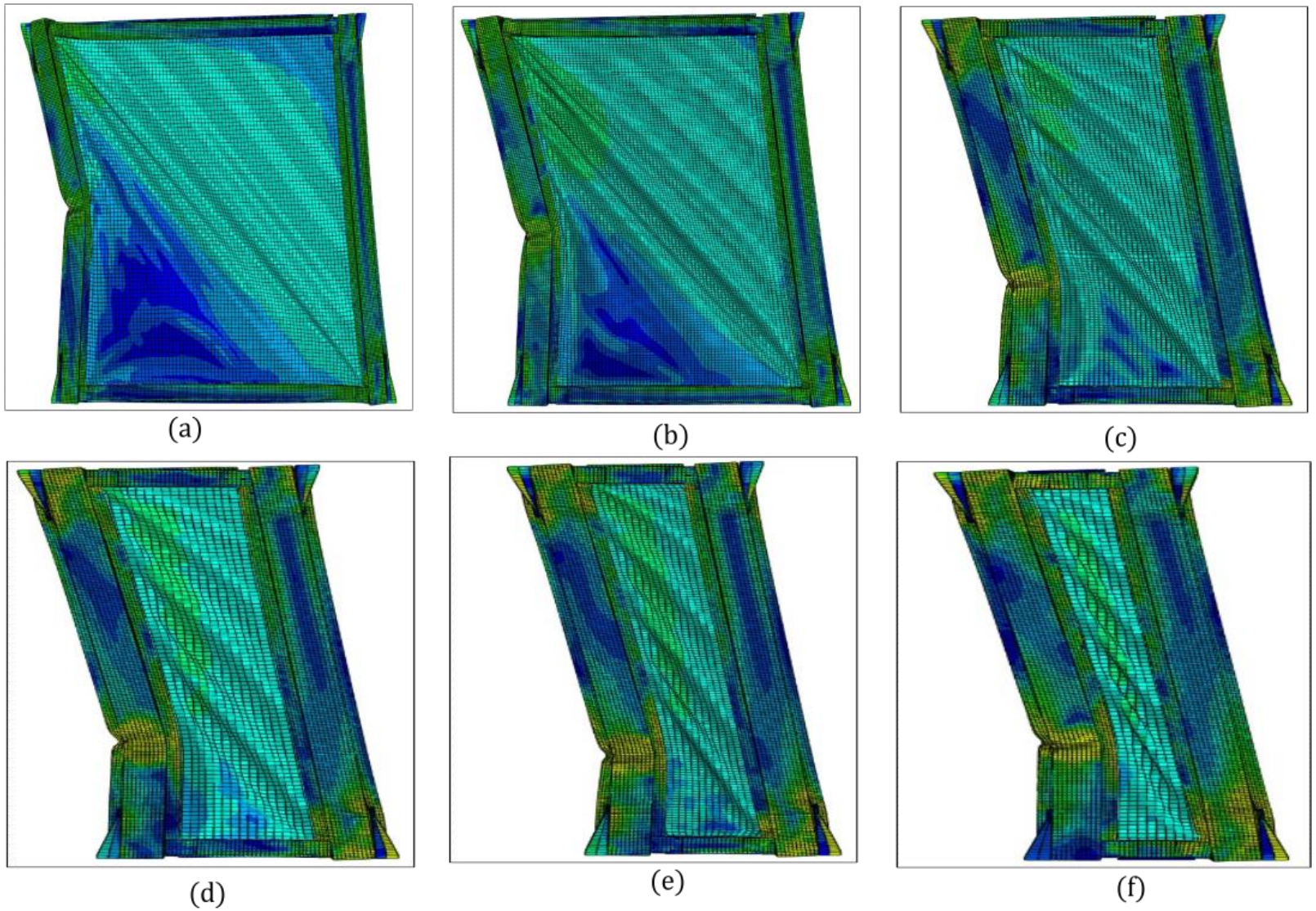


Figure 6.18: Deformed shapes of the concentric-sheathed wall with different aspect ratios (width/height). (a) 1;(b) 0.667;(c) 0.4;(d) 0.333;(e) 0.286;(f) 0.25.

The findings indicate that walls with a higher aspect ratio performed substantially better than walls with lower aspect ratios. For instance, when the aspect ratio is increased from 0.5 (benchmark) to 0.666, the peak load increases by 22%. On the other hand, decreasing the aspect ratio to 0.4 decreases the peak load by 18%. The inclination of the tension field is steeper in narrow walls which reduces the tension field contribution to shear resistance and as a result bending deformations become the governing factor. Conversely, the inclination of the tension field in wider walls is more shallow (gentle incline) hence the behaviour of such walls are dominated by shear deformations, which leads to higher attained peak loads. The results of this section are summarized in Table 13.

Table 13: Summary of varying the aspect ratio for specimen GD-06.

Aspect Ratio	$V_{peak}\ (kN)$	% Difference	$K_e\ (kN/mm)$	% Difference
GD-06				
1	180	75.6	13.1	157
0.666	125	22	4.35	64.15
0.4	84	18	3.9	47.2
0.333	77	24.8	2.4	9.4
0.286	68	33.7	2.1	20.7
0.25	65	36.5	1.75	34

Based on the results of Section 6.5 and Section 6.6, and in an attempt to reduce the forces on the studs, two new configurations are proposed with slight modifications to the original specimen. For the first configuration, the width of the wall was increased by moving the studs to the outer parameter of the wall and attaching the sheet to the inner flanges only. As for the second configuration, the distance between the studs remained the same, however the portion of the sheet that was connected to the outer flanges was removed. By incorporating these minor

modifications, the following advantages are achieved. First, attaching the sheathing to one flange reduces the transferred forces on the studs and allows the sheathing to develop its full capacity, thus following capacity design principles. Second, by moving the studs to the out perimeter of the wall, the aspect ratio of the wall increases to 0.6375 from 0.5 (benchmark). Increasing the aspect ratio is anticipated to increase the shear resistance of the wall using the same amount of sheathing material. Last, for the narrow configuration, while the aspect ratio is reduced to 0.37, the configuration uses less material which results in a more economical design. The same parametric study is repeated by varying the screw spacing and analyzing the wide and narrow configurations of specimens GD-19 and C-SW-2 under monotonic and cyclic loads.

As displayed in Figure 6.19 through Figure 6.22, when the sheathing is attached to one flange of the studs, varying the screw spacing along the perimeter of the wall has a noticeable effect of the monotonic and cyclic response of the shear walls. Moreover, the harmonic response in the figures are due to the noise in the solution caused by the buckling of the studs. By inspecting plots (a) of the following figures, it can be concluded that increasing the screw spacing decreases the ultimate resistance of the wall specimens. As expected, the wide configurations exhibited improved elastic stiffness, increased peak load, and higher energy dissipation capacity, mainly due to the higher aspect ratio. Interestingly, for the narrow configurations, while the elastic stiffness decreased, the peak load was higher than the benchmark specimens (except when spacing was increased to 150), indicating that the sheathing is developing its full capacity. Furthermore, the best energy dissipation capacity was obtained when the screw spacing was increased to 75 mm rather than 25 mm. The results of this section are summarized in Table 14.

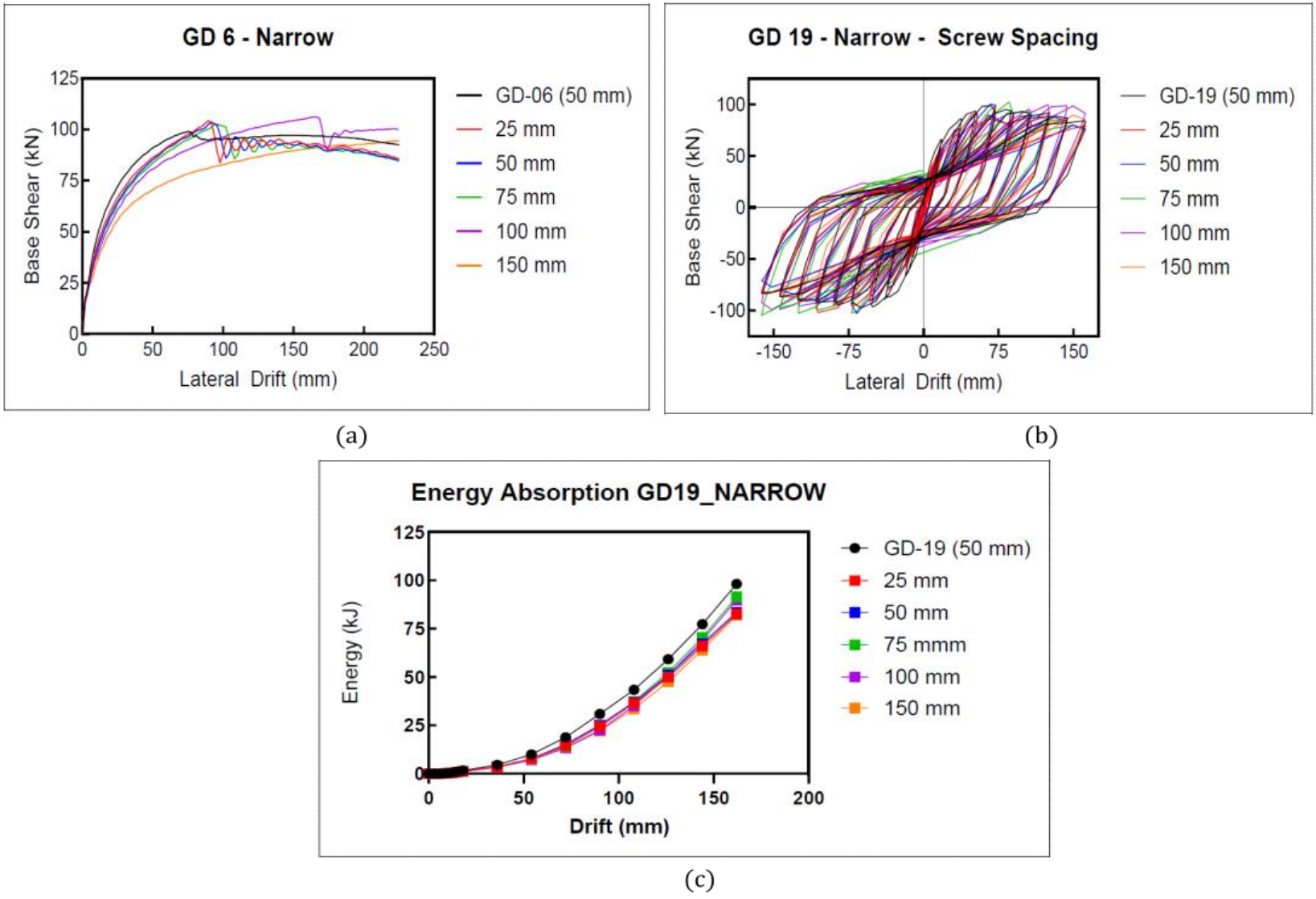


Figure 6.19: Influence on varying the screw spacing for the narrow configuration of specimen GD-19. (a) Monotonic; (b) Cyclic; (c) Energy absorption.

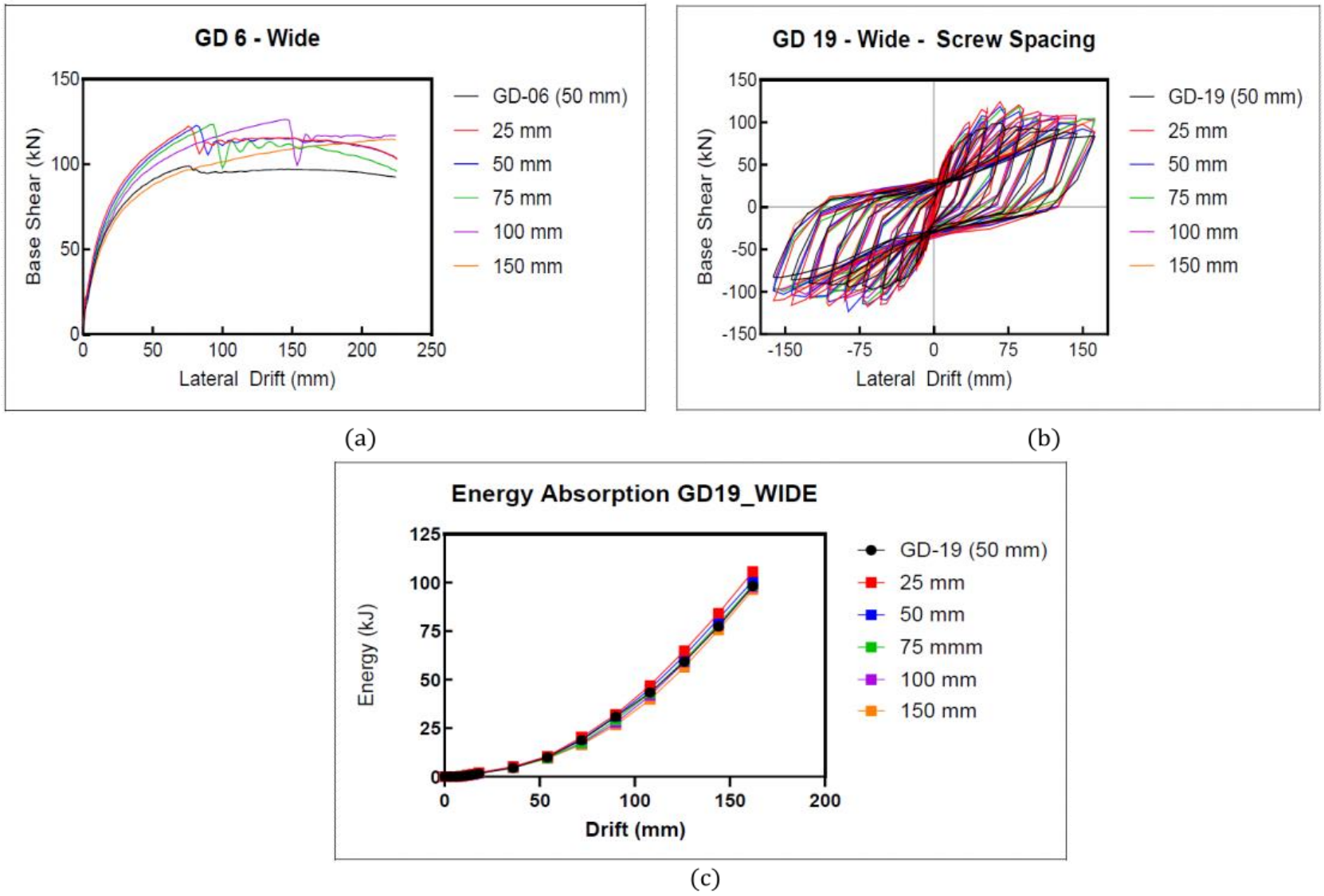
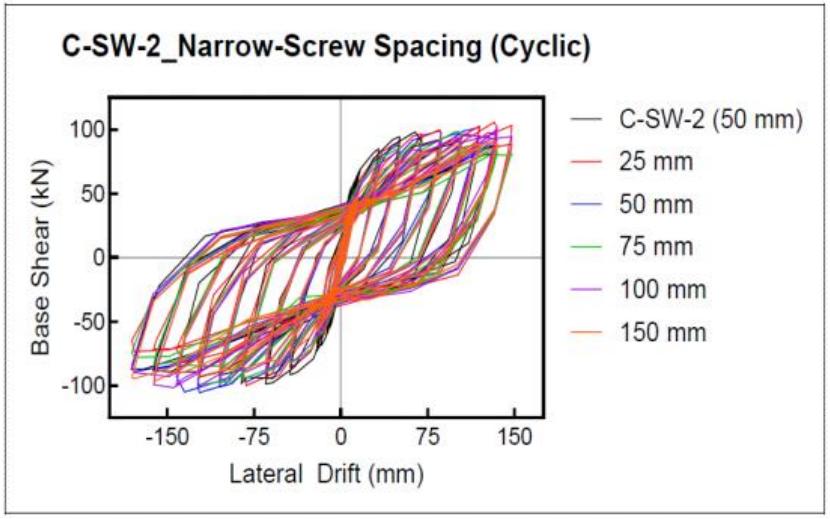


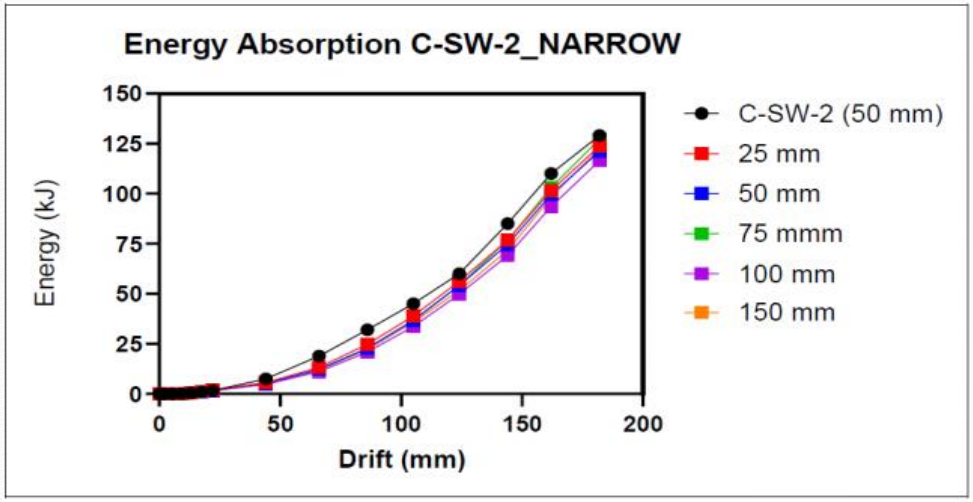
Figure 6.20: Influence on varying the screw spacing for the wide configuration of specimen GD-19. (a) Monotonic; (b) Cyclic; (c) Energy absorption.



(a)

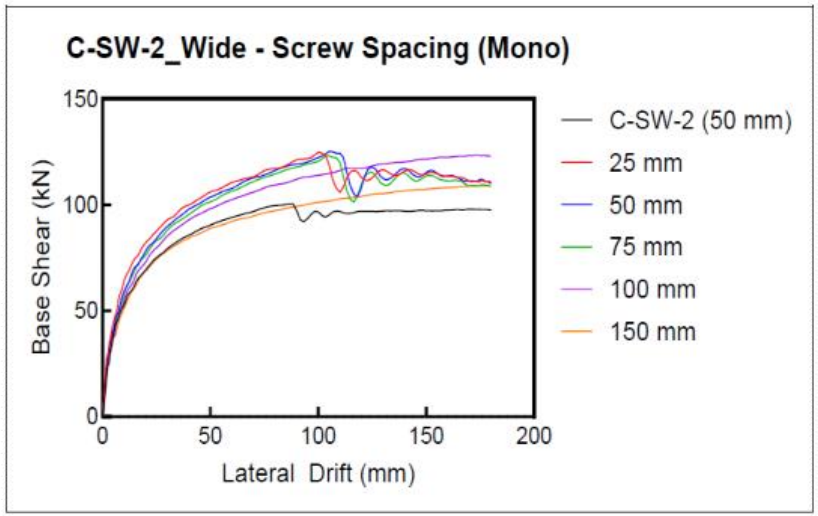


(b)

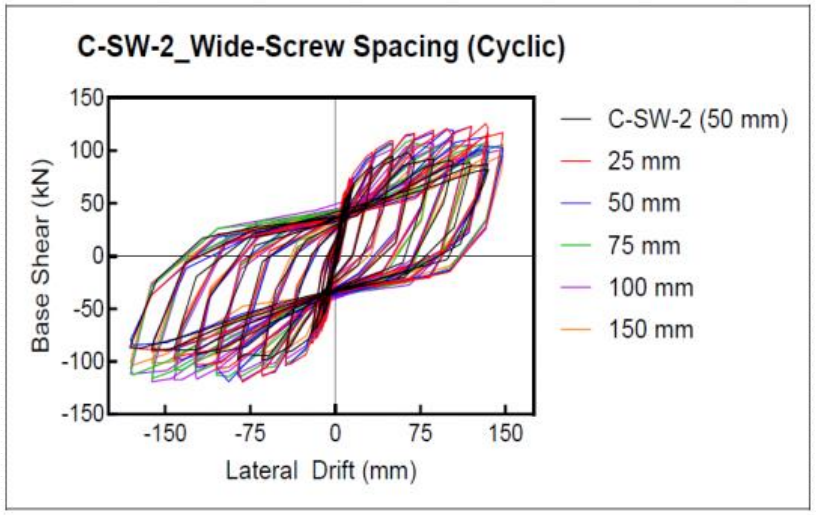


(c)

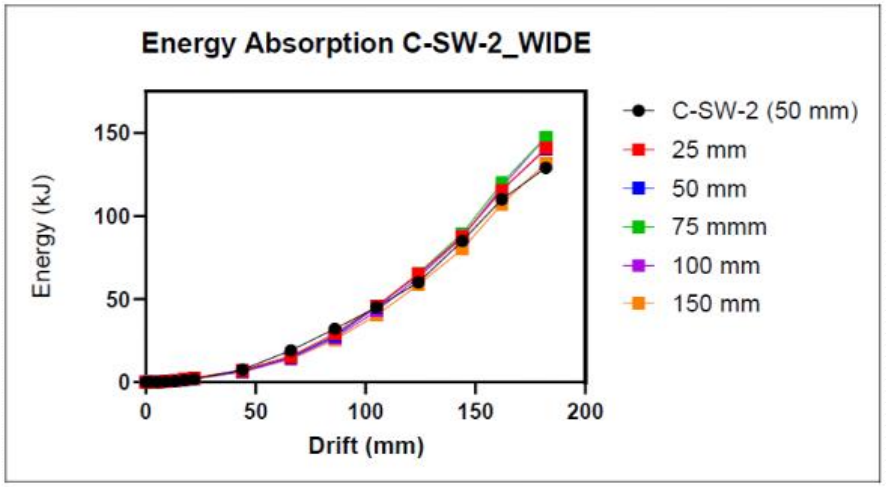
Figure 6.21: Influence on varying the screw spacing for the narrow configuration of specimen C-SW-2. (a) Monotonic; (b) Cyclic; (c) Energy absorption.



(a)



(b)



(c)

Figure 6.22: Influence on varying the screw spacing for the wide configuration of specimen C-SW-2. (a) Monotonic; (b) Cyclic; (c) Energy absorption.

Table 14: Summary of varying the screw spacing for the wide and narrow configurations of specimen GD-19 & C-SW-2.

Screw Spacing (mm)	V_{peak} (kN)	% Difference	K_e (kN/mm)	% Difference	Drift at peak (%)	Energy (kJ)	% Difference
GD19_Narrow							
25	104.27	5.32	4.30	15.19	3.70	82.67	15.64
50	103.60	4.64	3.90	23.08	3.80	83.54	14.76
75	102.60	3.64	3.70	27.02	4.00	91.55	6.58
100	106.04	7.11	3.20	36.88	6.90	89.90	8.27
150	94.44	4.60	3.20	36.88	9.38	81.98	16.35
C-SW-2_Narrow							
25	105.31	4.79	6.50	12.16	4.60	123.82	4.02
50	105.95	5.43	5.40	27.03	4.90	121.15	6.09
75	104.13	3.61	5.70	22.97	5.05	127.23	1.37
100	104.21	3.69	4.90	33.78	5.67	116.62	9.60
150	101.73	1.22	4.20	43.24	7.37	122.53	5.02
GD-19_Wide							
25	122.50	23.74	5.90	16.37	3.13	105.61	7.77
50	123.00	24.24	5.15	1.58	3.38	100.92	2.98
75	123.50	24.75	4.94	2.56	3.81	98.55	0.56
100	126.38	27.65	4.43	12.62	6.01	97.76	0.24
150	114.76	15.92	4.10	19.13	9.30	96.34	1.69
C-SW-2_Wide							
25	124.84	24.22	7.68	3.78	4.20	140.86	9.19
50	125.18	24.56	6.67	9.86	4.37	140.15	8.64
75	123.13	22.52	6.50	12.16	4.40	147.57	14.40
100	123.48	22.87	5.80	21.62	6.87	147.53	14.36
150	109.16	8.62	5.20	29.73	7.35	131.90	2.25

6.7 Construction Details

In this section, different construction details are implemented in the models. The aim is not to perform a direct comparison with the benchmark models but rather monitor the performance of each model to improve the efficiency of the specimen and come up with economic design alternatives. The construction details include stiffening the studs, placing the hold-downs on both sides of the studs, using a corrugated sheet as the infill panel, and assessing the sheathing connections of a wall model with multiple panels.

6.7.1 Sigma-Stiffened Studs

The concept of improving the local buckling and axial strength of a CFS section by setting intermediate or edge stiffeners has been studied extensively in the literature [87]. This strategy is applied to specimen GD-19 with the focus on enhancing the performance of the wall without increasing the cost. The webs and top flange of the hat sections were stiffened at intermediate locations as displayed in Figure 6.23.

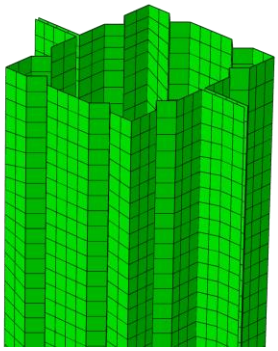


Figure 6.23: Sigma-stiffened end studs.

The model with stiffened studs exhibited a similar response to the benchmark model, in terms of deformed shape and failure modes. However, as illustrated in Figure 6.24, the energy dissipation capacity as well as the peak load increases considerably when the studs are stiffened (17% and 28% respectively). In addition, the deformed shape of the sigma-stiffened model is shown in Figure 6.25. Thus, it is recommended that future research consider implementing stiffened end-studs in shear wall assemblies since they improve the performance significantly.

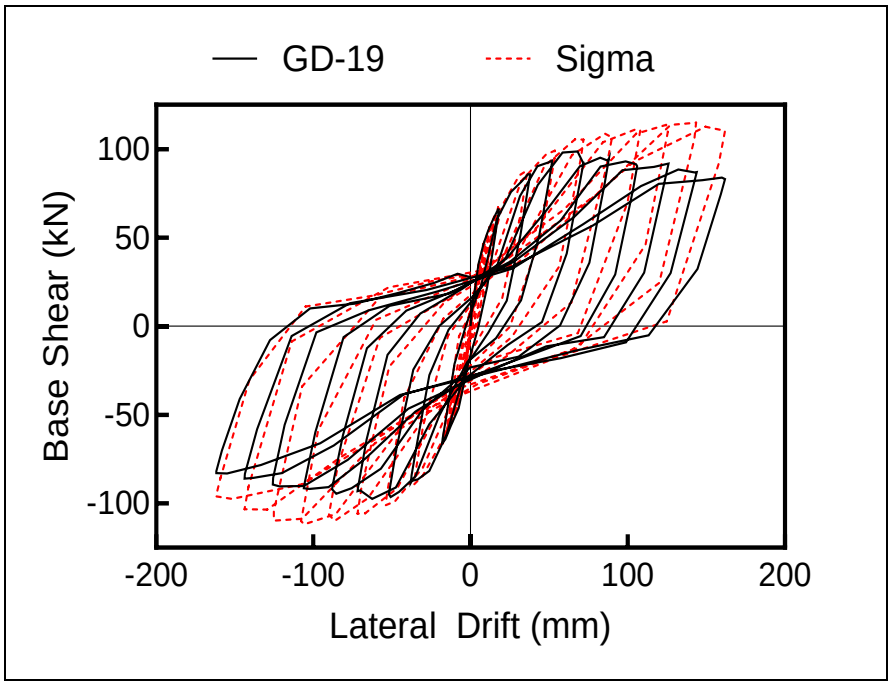


Figure 6.24: Cyclic analysis using sigma-stiffened studs.

6.7.2 Hold-down Placement

A model was constructed with the hold-downs attached to both sides of the studs (fully clamped boundary condition). The main aim was to reduce eccentricity associated with the placement of hold-downs on one side of the end studs. As displayed in Figure 6.26, the deflected shape of the studs slightly resembles the deformed shape of a column with fixed boundaries on both ends.

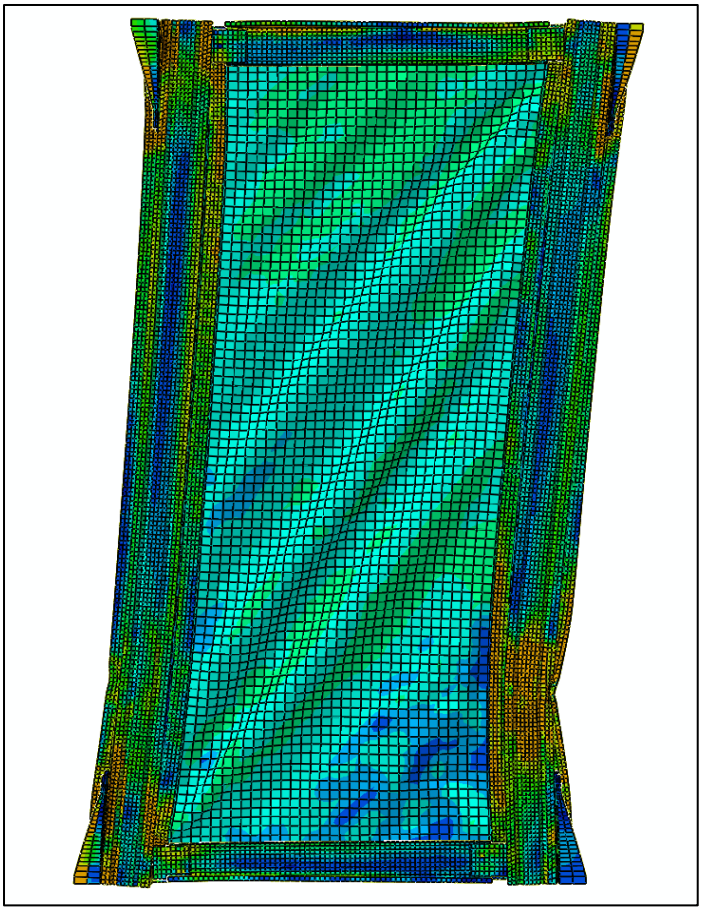


Figure 6.25: Deformed shape of the shear wall model with sigma-stiffened studs.

Also, placing the hold-downs on both sides resulted in a higher concentration of stresses at the face of the hold-downs and led to the development of a slightly more pronounced tension field, indicating an increase in the rigidity of the frame. Fortunately, there is a substantial increase in the peak load (20%), energy dissipated (62%) and stiffness of the system (168%) (Figure 6.27). Even though the issue of the end-stud buckling is not entirely resolved, the high capacities and drifts dissipated by the system shows potential.

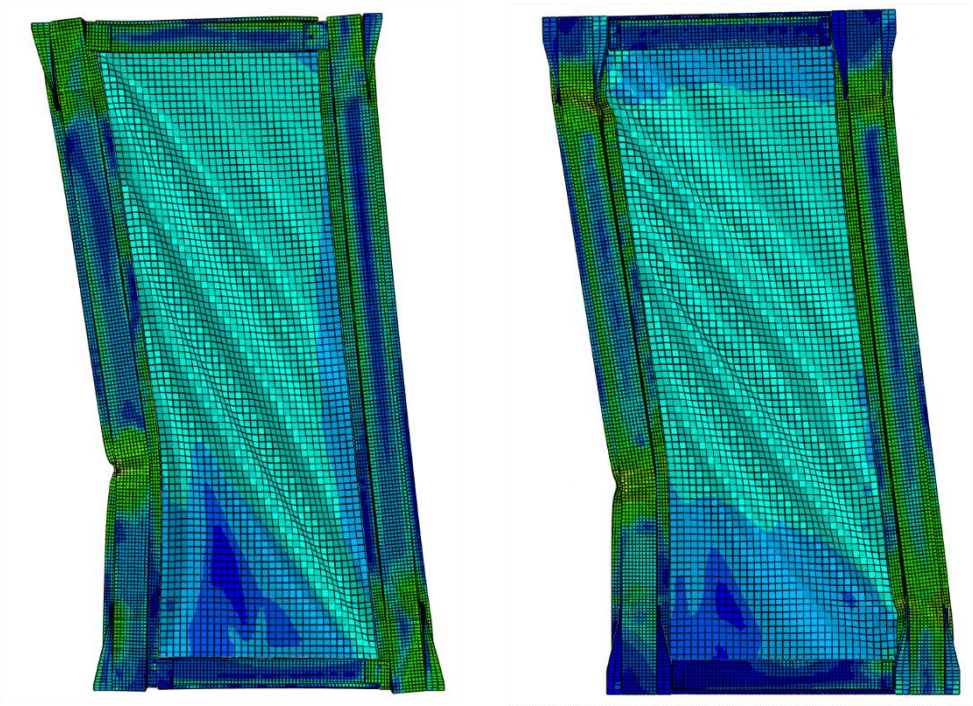


Figure 6.26: Deformed shape comparison between benchmark model (left) and model with studs clamped from both sides (right).

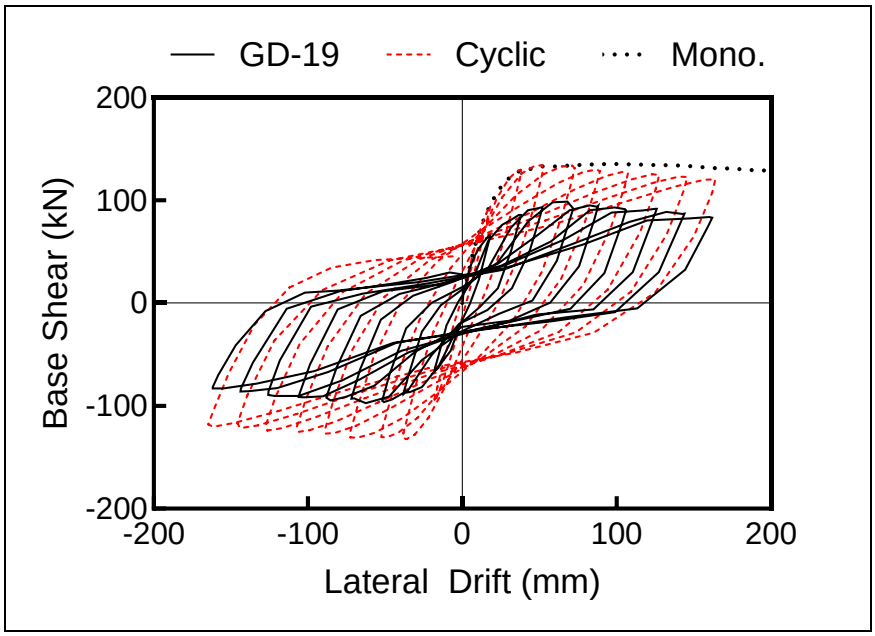


Figure 6.27: Cyclic analysis using hold-downs on both sides of the studs.

6.7.3 Corrugated Sheathing

In this section, the use of a corrugated sheathing as the infill panel is explored. The sheathing geometry were retrieved from [88] and displayed in Figure 6.28. Several design modifications had to be incorporated. Because of the corrugated profile of the sheathing, the screw spacing was increased to 75 mm and confining the sheathing between built-up framing members was not feasible. Due to that, two models were compared where the corrugated sheathing was attached to one side and both sides of the frame. As presented in Figure 6.29, when two sheathings are used, the attained peak load is almost doubled. The system in the elastic region is characterized by a stiff response, followed by a sudden loss of strength as the sheathing buckles (Figure 6.30). Hence while there is a gain in strength when two sheathings are used, the moderate ductility and low post-peak resistance of the system make it relatively unattractive for seismic design.

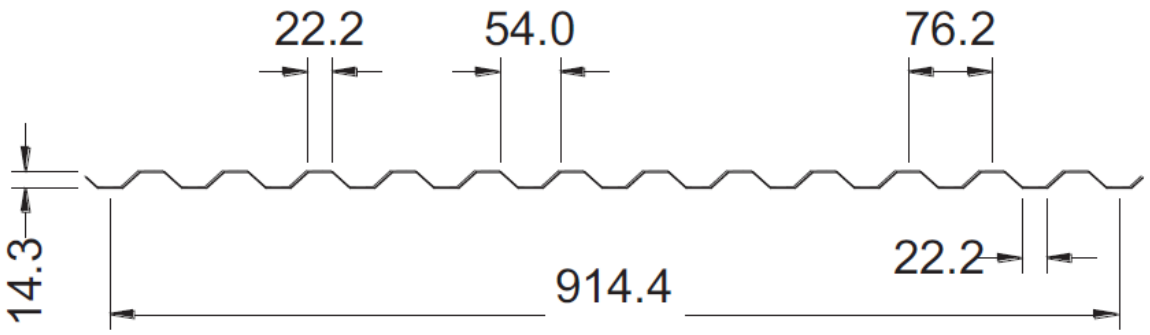


Figure 6.28: Profile of steel deck [88].

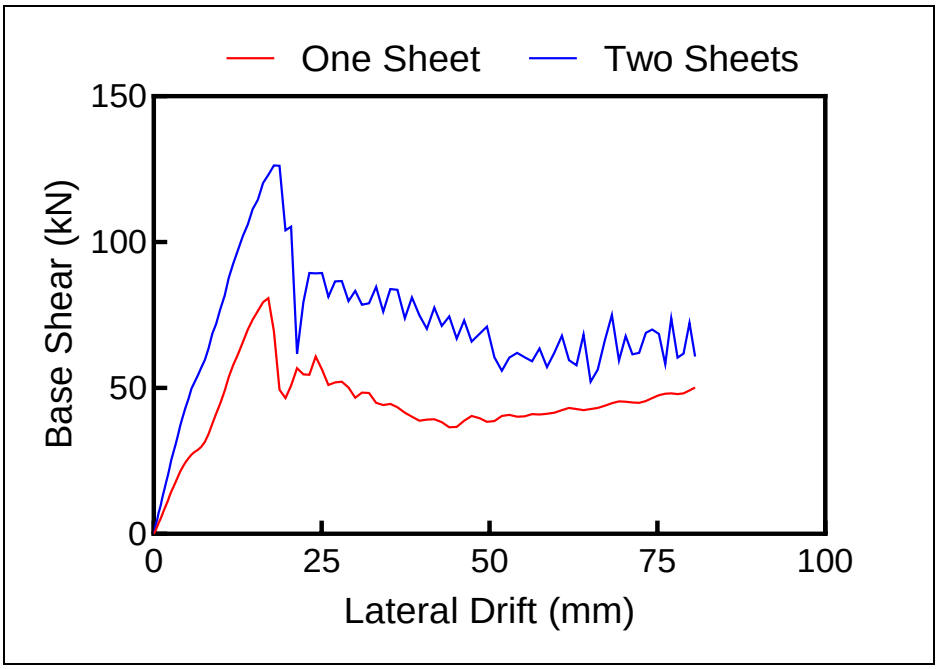


Figure 6.29: Monotonic analysis using corrugated sheathing as infill panel.

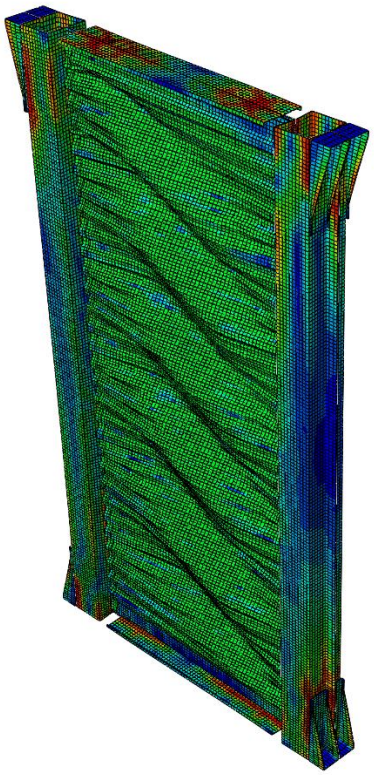


Figure 6.30: Deformed shape of wall models with corrugated sheathing.

6.7.4 Walls with Multiple Panels

A model spanning two bays was analyzed to assess the influence of the type of mid-span sheathing connections on the response of the wall. The model was first analyzed where the sheathing connections were discontinued at midspan, hence each bay contained a separate panel. The second analysis involved overlapping the sheathings at mid-span over the length of the stud. Figure 6.31 displays the results of the monotonic analysis and denotes that there is a 10% increase in peak load when the mid-span sheathing connections are continuous. Assessing the stress contours of both models (Figure 6.32) implies that when continuous mid-span sheathing connections are used, the system behaves in a manner similar to specimen C-SW-2 where the intermediate stud acts as a stiffener. The tension fields bounding the mid-span stud are approximately equal since the stress in the stud is negligible.

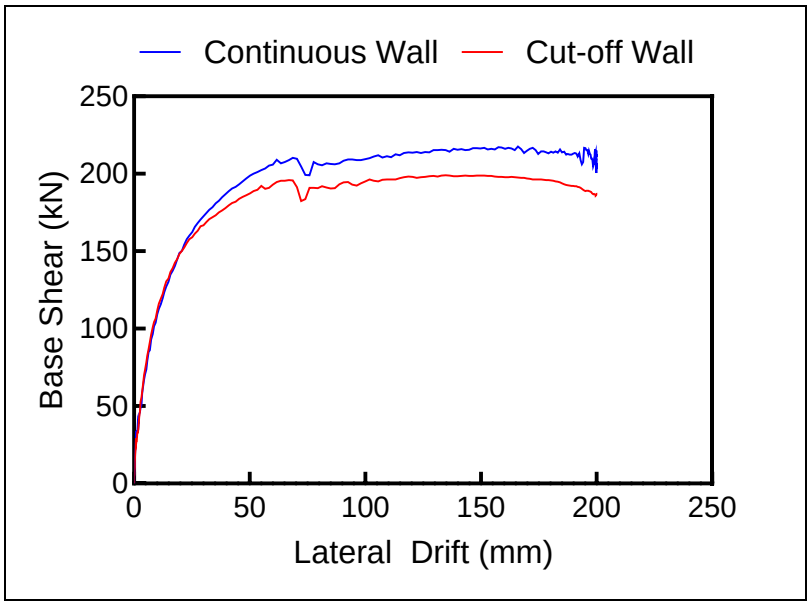
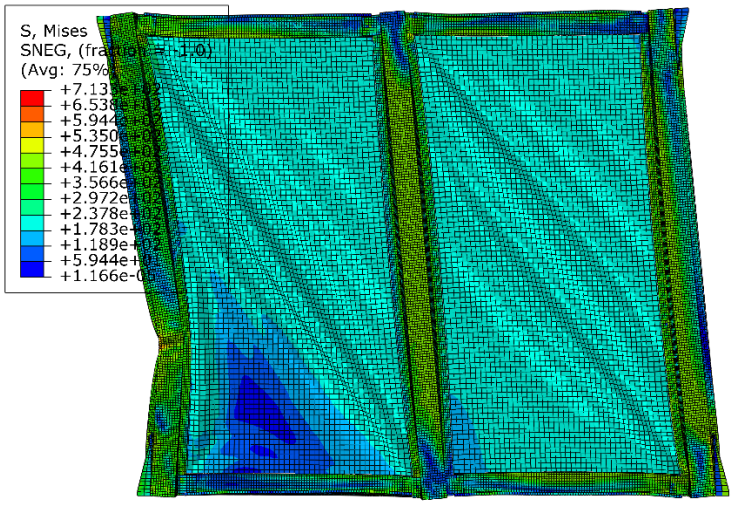
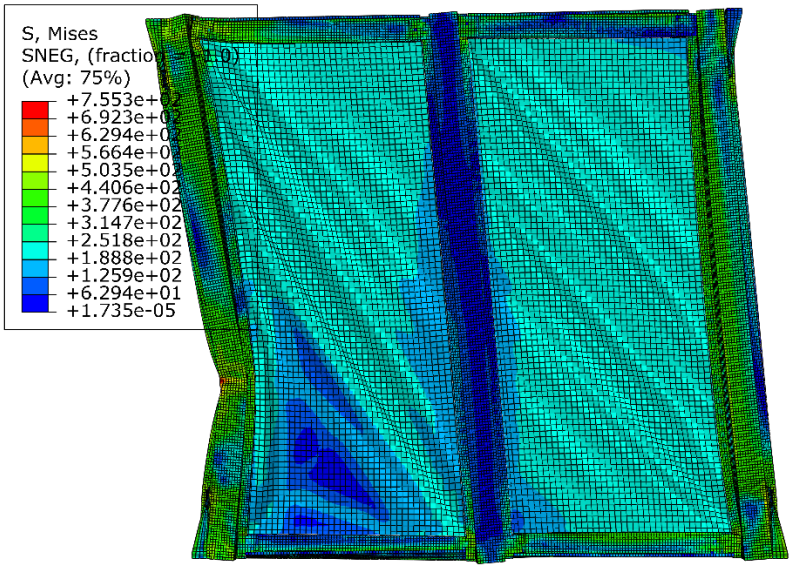


Figure 6.31: Monotonic analyses of multi-panel walls with different mid-span sheathing connections.



(a)



(b)

Figure 6.32: Stress contour plots for the multi-panel walls. (a) Cut-off wall; (b) continuous wall.

6.8 Concluding Remarks

An extensive parametric study was reported in this chapter. The parameters of interest include: stud thickness, sheathing thickness, strap thickness, aspect ratio, screw spacing, and various construction details. Based on the analyses, the following conclusions can be stated:

1) Increasing the studs' thickness increases the elastic stiffness, ductility, and ultimate resistance of the shear walls.
2) On the other hand, increasing the thickness of the sheathing or strap increases the elastic stiffness and resistance of the wall, however, decreases the ductility.
3) A non-dimension parameter β was defined such that $\beta = (t_{sheathing} / t_{studs})$, if the ratio is limited to $\beta < 0.2$, then the stud buckling failure mode is eliminated and a uniform tension field develops across the length of the panel.
4) Decreasing the screw spacing increases the elastic stiffness and ultimate resistance of the walls, however, decreases the ductility.
5) Increasing the aspect ratio (width/height) of specimen GD-06 changes the inclination tension field. In turn, this increases the shear resistance of the wall.
6) To reduce the forces on the studs, two configurations were proposed where the sheathing is attached to the inner flange of the built-up studs.
7) By implementing these simple changes, the behaviour of the wall is improved without any increase in the cost.
8) Stiffening the end-studs and placing the hold-downs on both sides of the studs considerably increase the ultimate load and energy dissipation capacity of the shear wall.

9) Attaching corrugated sheathings to the outside of the frame from both sides increases the ultimate resistance of the system, however, decreases the ductility considerably.

10) If multiple span shear walls are to be used, it is recommended to use continuous mid-span sheathing connections.

Chapter 7: Design Procedure

7.1 Introduction

Shell finite element models provide a powerful method to analyze and model the behaviour of complex structures, unfortunately, they are not feasible as a design tool due to their complexity and unavailability. Engineers require simplified and expeditious methods to assess and design such structures with commercial software that are readily available in their workplace.

In this chapter, an analytical method is proposed to predict the monotonic response of the concentric-sheathed specimen (GD-06) up to the yield level. Furthermore, a simplified, hand-based method to determine the force and moment demand of the studs at the yield level is presented as well. Both methods, which rely on factors derived from the numerical analyses of Chapter 6, consider semi-rigid frame behaviour and are based on partial tension field theory [27]. The uniqueness of the proposed method lies in the implementation of semi-rigid joints to model the stud-to-hold-down connections.

The general behaviour of the concentric-sheathed CFS shear wall is first introduced, followed by a comparison of the design methods available in the literature and codes. Then, using specimen GD-06 as a benchmark, a detailed derivation of the proposed design framework including the relevant graphs and equations is explained. The chapter concludes with a numerical example that illustrates the pertinency of the proposed method on CFS shear walls with different height-to-width aspect ratios.

7.2 General Behaviour of Concentric-Sheathed CFS Shear Wall

When concentric-sheathed CFS shear walls are acted upon by lateral loads, the forces are resisted by the steel sheathing in combination with sway action from the boundary frame. Since the sheathing is typically very thin and slender, it buckles in compression as soon as the lateral load is applied and develops an inclined tension field. The tension field produces inclined forces that are transferred to the framing members through the self-tapping screws around the wall's perimeter. Ideally, if the framing members are designed to possess sufficient strength and stiffness to resist these tension pull-in forces, then the sheathing would realize its full capacity through yielding and bearing deformations at the location of the screws. In such a case a uniform tension field would develop in the steel sheathing, as discussed in Section 6.3. Regrettably for the walls examined herein, the end stud on the compression side buckled prematurely which caused the tension field to form partially in the sheathing. Consequently, the sheathing pull-in forces are also acting over a limited height of the stud. This behaviour is schematically shown in Figure 7.1, where the area bounded by the red lines corresponds to width of the effective tension band. The length and height of the partial field are denoted by L_{PTF} and H_{PTF}, respectively. The resulting inclined forces on the frame due to the partial tension field is also illustrated in Figure 7.1. The sheathing pull-in forces, which are inclined at an angle α (where α is measured from the vertical), can be resolved into a vertical and horizontal component that act on the stud in conjunction with forces from frame sway action. Thus the demand on the boundary studs can be reasonably considered to be a combination of sheathing pull-in forces and portal frame sway action, which is shown in Figure 7.2 and Figure 7.3 for the compression and tension studs, respectively.

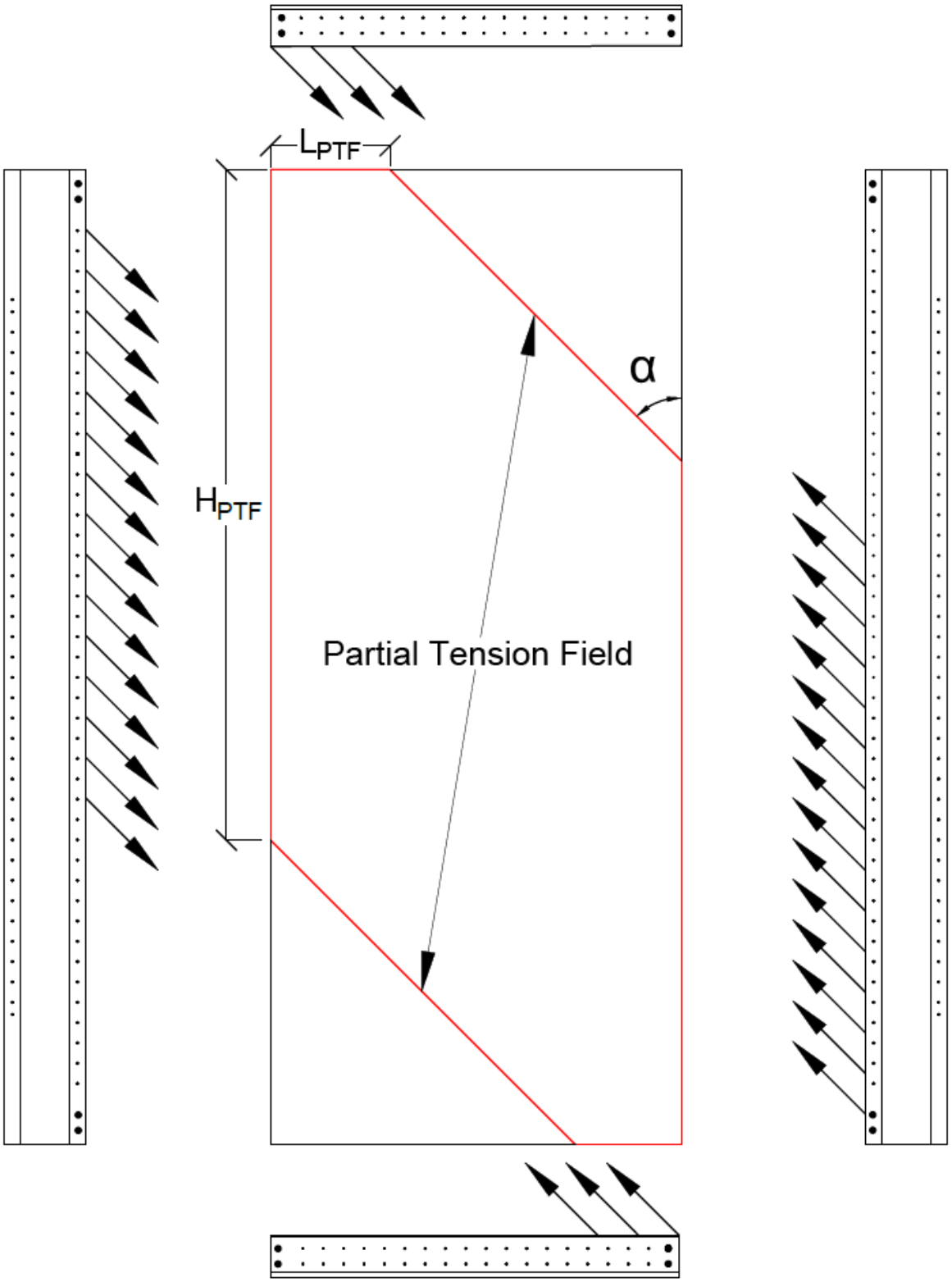


Figure 7.1: Force break-down on the boundary frame due to partial tension field action.

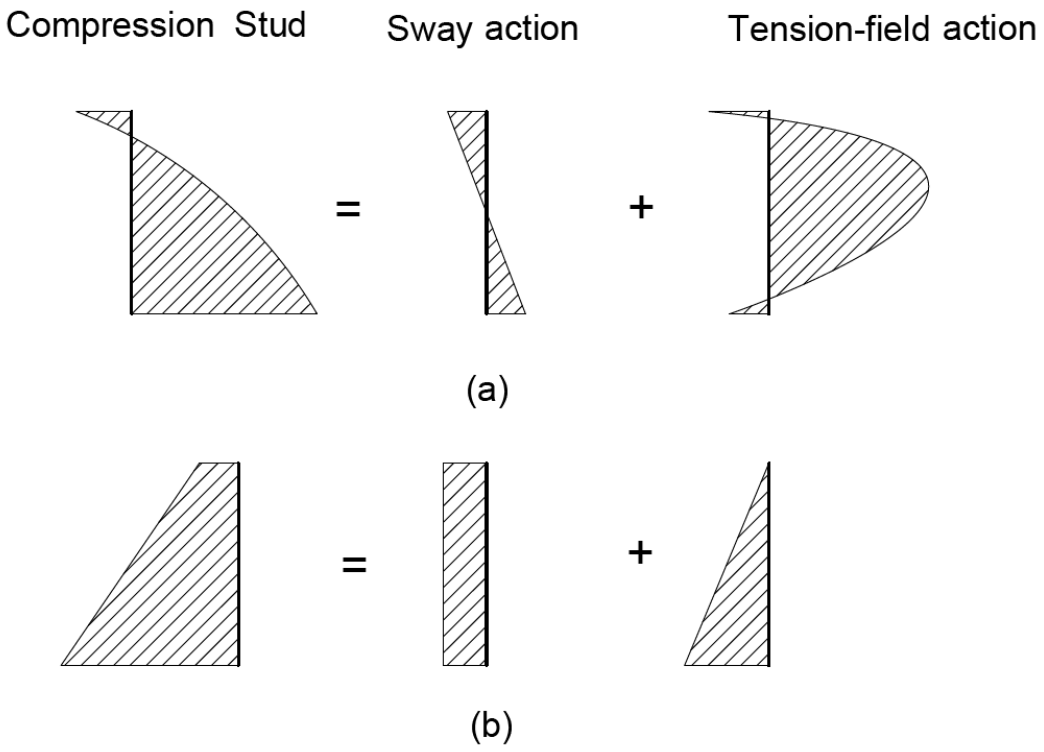


Figure 7.2: Schematic moment diagram (a) and axial force diagram (b) for the compression stud of the CFS shear wall.

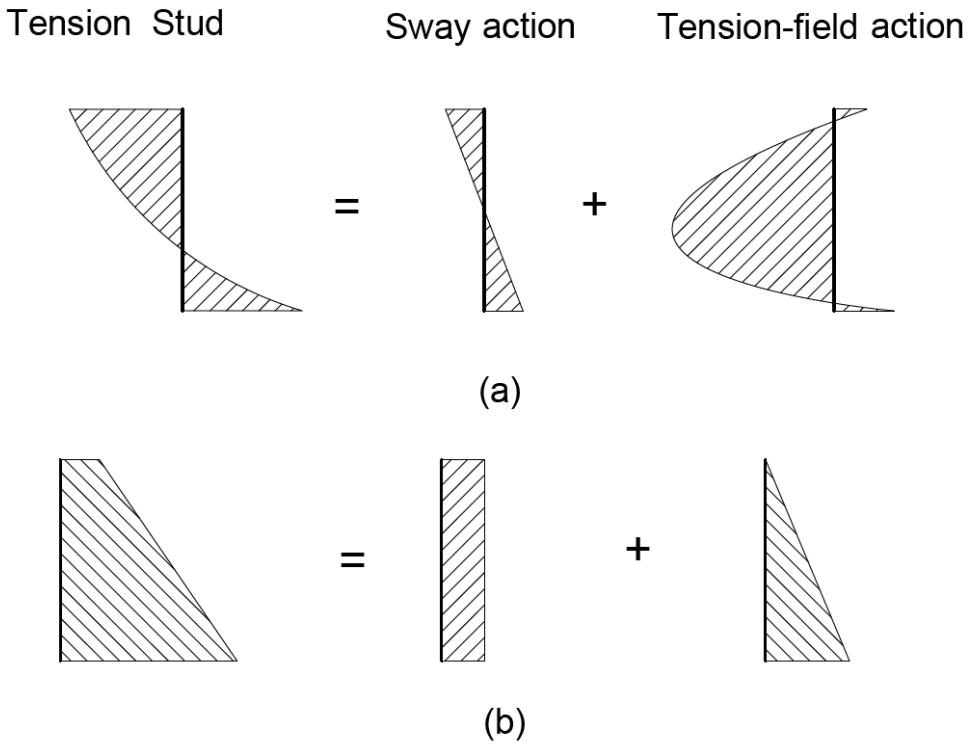


Figure 7.3: Schematic moment diagram (a) and axial force diagram (b) for the tension stud of the CFS shear wall, gravity loads excluded.

7.3 Prediction of Shear Wall Capacity

In this section, the lateral resistance of the concentric-sheathed shear wall (GD-06) is approximated using several methods which are available in the literature and design codes. While the majority of these methods are based on assumptions and conditions that might not be applicable to the shear wall investigated herein, the objective of this section is to highlight the challenges and lack of design provisions with respect to concentric-sheathed high-capacity CFS shear walls. Consequently, three methods are assessed: 1) the effective strip method [8], 2) the modified strip method [11], [12], and 3) the special plate shear wall method [25]. Detailed sample calculations can be found in Appendix A.

7.3.1 Effective Strip Method [8]:

According to the effective strip method, the nominal capacity of a CFS shear wall can be determined from the following expression:

$$V_n = min\begin{cases} 1.33P_n cos\alpha \\ 1.33F_y w_e t_{sh} cos\alpha \end{cases} \quad \textbf{(7.1)}$$

where P_n is the individual screw capacity calculated according to chapter J4 from CSA 136 [43], w_e is the width of the effective strip as per section E2.3.1.1.1 from AISI S400-20 [10], and α is the angle given by the wall's aspect ratio. In Eq. (7.1), the first expression refers to the sheathing-to-framing screw capacity and the second equation refers to the sheathing yield capacity. Substituting the appropriate values, the capacity of specimen GD-06 is $\boldsymbol{68\ kN}$**.** According to Table 4, the tested capacity of the specimen is $\boldsymbol{102.5\ kN}$. It's evident that the effective strip method greatly underestimates the shear resistance of the shear wall. Nevertheless such a result was expected. The effective strip method is based on shear walls having the sheathing connected on

one side of the frame. Furthermore, the method is empirically calibrated on parameters (wall aspect ratio, and member thicknesses) that are not applicable to the shear wall configurations investigated in this study. Finally, the individual screw capacity P_n is based on screws fastening two layers of steel, which is inconsistent for the walls assessed in this study.

7.3.2 Modified Effective Strip Method [11], [12]:

A preliminary design method to calculate the shear resistance of centre-sheathed, higher capacity CFS shear walls was proposed by [11] & [12]. The modified effective strip method (MESM) was based on experimental observations where the authors detected bearing damage in all the screws of the CFS shear wall. As a result, the MESM assumes that all the screws participate in the shear resistance of the wall rather than the screws that lie within the effective strip, as explained in Eq. (2.5). A major distinction between this method and the original effective strip method is the screw nominal capacity. In the MESM, the screw's capacity is based on the bearing strength of bolted connections in double shear, as described in Eq. (2.6).

Applying the preceding equations and ignoring the contribution of high-strength bolts at the corners of the sheathing, the shear capacity of specimen GD-06 is $\mathbf{250.47}\ \boldsymbol{kN}$. This value is more than twice the value obtained from experimental results. While at first glance it might seem that the MESM overestimates the shear resistance of the wall, it should be considered that according to the results of Chapter 3, the studs buckled prematurely which prevented the sheathing from achieving its full capacity. Hence assuming that all the screws around the wall's perimeter participated in the lateral resistance of the wall may not be a valid assumption for the case of the concentric-sheathed specimen. Moreover, the boundary frame of the shear wall specimens in

[11] & [12] consist of back-to-back channel sections, while the shear wall specimens examined in this research are bound by built-up hat sections.

7.3.3 Steel Plate Shear Walls [25]:

For a steel plate shear wall, the factored shear resistance of the infill plate can be expressed as [25]:

$$V_r = 0.5F_y wLsin2\alpha \quad \textbf{(7.2)}$$

where w the thickness of the wall; L is the centre-to-centre distance between the columns; F_y is the yield stress, and α is the angle of inclination and can be obtained from Eq. (2.2). Substituting the appropriate values, the shear resistance of specimen GD-06 is $\boldsymbol{V_r = 68.1\ kN}$, which is yet again significantly lower than the experimental value. Similar to the previous methods, this result is also expected since Eq. (7.2) was derived using plastic analysis with the postulation that a uniform tension field forms in the infill plate. Yet as proven by Figure 3.13 and **Figure 3.14**, the buckling of the studs prevented the tension field from developing uniformly within the sheathing. Also, the angle of inclination in Eq. (2.2) was formulated with the assumption that the boundary condition for the columns is fully fixed. This assumption is reasonable for a steel plate shear wall where the framing members are fully welded although this assumption might not be reasonable for CFS framing members that employ discrete fasteners. Finally, Eq. (7.2) does not include the effects of the portal frame action, which may have resulted in a lower predicted capacity.

7.3.4 Concluding Remarks

Based on the brief exercise presented in this section, several design considerations can be obtained. The major contribution to the shear strength of the CFS shear wall is derived from the

tension field action in the sheathing. However unlike hot-rolled steel shear walls, the tension field forms partially across the sheathing. Therefore the first challenge lies in determining the height and length of the partial tension field. In addition, if the strip model is to be used to represent the tension field action in the sheathing, then the angle of inclination needs to be determined accurately. The effective strip method and the MESM both assumed that the inclination of the tension field is equal to the angle given by the wall's aspect ratio, while in steel plate shear walls the angle of inclination was derived from the principle of least work. Hence the next challenge consists of determining an expression for the inclination angle of the partial tension field. Finally, the MESM has been re-calibrated in [6] to include a provision that accounts for the frame contribution to the total shear strength of the shear wall. Assuming that this concept holds true for the walls studied in this research (that is, the shear resistance is a combination of tension field action and portal frame action), then the last challenge is to determine the extent of contribution of the frame. These design challenges, which will be addressed in the following sections, are summarized below:

1) Determine an expression for the angle of inclination of the tension field.
2) Determine the height and length of the partial tension field.
3) Determine the ratio of frame contribution to the total shear resistance of the wall.

7.4 Derivation of the Analytical Model

7.4.1 Introduction

In this section, an analytical method which is based on the strip model representation of the tension field action in the sheathing is proposed. Historically, strip models have been successfully

employed in modeling hot-rolled steel plate shear walls [19], [20], [31]. The model accounts for inelasticity in the sheathing and assumes that the framing members remain elastic, thus satisfying capacity design principles. Moreover, to obtain a more realistic response of the specimen, semi-rigid rotational behaviour of the stud-to-hold connections are accounted for. The analytical model was set up and analyzed on SAP 2000 [89], however it can be analyzed using any software package that conducts structural analysis of plane frames.

The original strip model by Thorburn et. al [19] represents the fully developed tension field action in the buckled infill plate as a series of inclined, pin-ended strips. The same basic concept is applied here with some modifications to account for the dimensions of the partial tension field. In order to formulate a strip model for the CFS shear wall, the angle of inclination (α), length and width of the partial tension field (L_{PTF} and H_{PTF}) must be determined first. Hence, using the finite element benchmark model of specimen GD-06, the procedure to determine the angle of inclination and the width of the effective tension band is established. Afterwards, the details and results of the analytical model are discussed. The results are compared with the experimental data and shell finite element simulations presented in Chapter 5 in terms of monotonic global response and axial force/bending moment demand on the boundary studs. It should also be noted that all the analyses presented in the following sections are conducted at the yield drift level, which is defined as per Eq. (4.2a).

7.4.2 Inclination Angle (α):

An expression for the angle of inclination of the partial tension field is formulated in this section. Unfortunately, the angle of inclination was not measured during the experimental investigation

of this study, henceforth the proposed equation is based on the numerical analyses previously discussed in Chapter 5 & Chapter 6. The first step involves identifying the shell elements within the sheathing that contain principal stresses that exceed the yield stress. To do so, a vector plot of the principal stresses at the yield drift was extracted, as displayed in Figure 7.4. Then, the principal stresses of the elements within the tension field were acquired in order to calculate the principal angle of each shell element using the basic relation displayed in Eq. (7.3). Finally, the average value of the principal angle of the shell elements was established as the angle of inclination for the tension field.

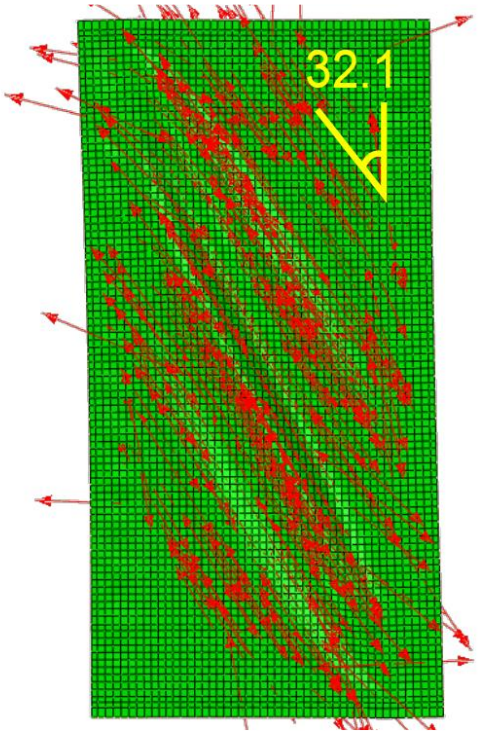


Figure 7.4: Vector plot displaying the direction of the principal stresses at the yield drift for the numerical model of specimen GD-06.

$$\tan 2\theta_p = \frac{2\tau_{xy}}{\sigma_x - \sigma_y} \qquad \textbf{(7.3)}$$

For the purpose of obtaining the variation between the angle of inclination and the aspect ratio of the shear wall, the same procedure was repeated for shear walls with varying aspect ratios

that were discussed in Section 6.6. The graph, which is displayed in Figure 7.5, indicates that the inclination angle increases as the aspect ratio increases. This observation also matches the results of Section 6.6, where wider walls displayed higher peak loads since they are dominated by shear-deformations due to the high inclination angle. Furthermore, Eq. (7.4) displays the expression of the angle of inclination as a function of the aspect ratio of the shear wall, which was obtained through nonlinear regression.

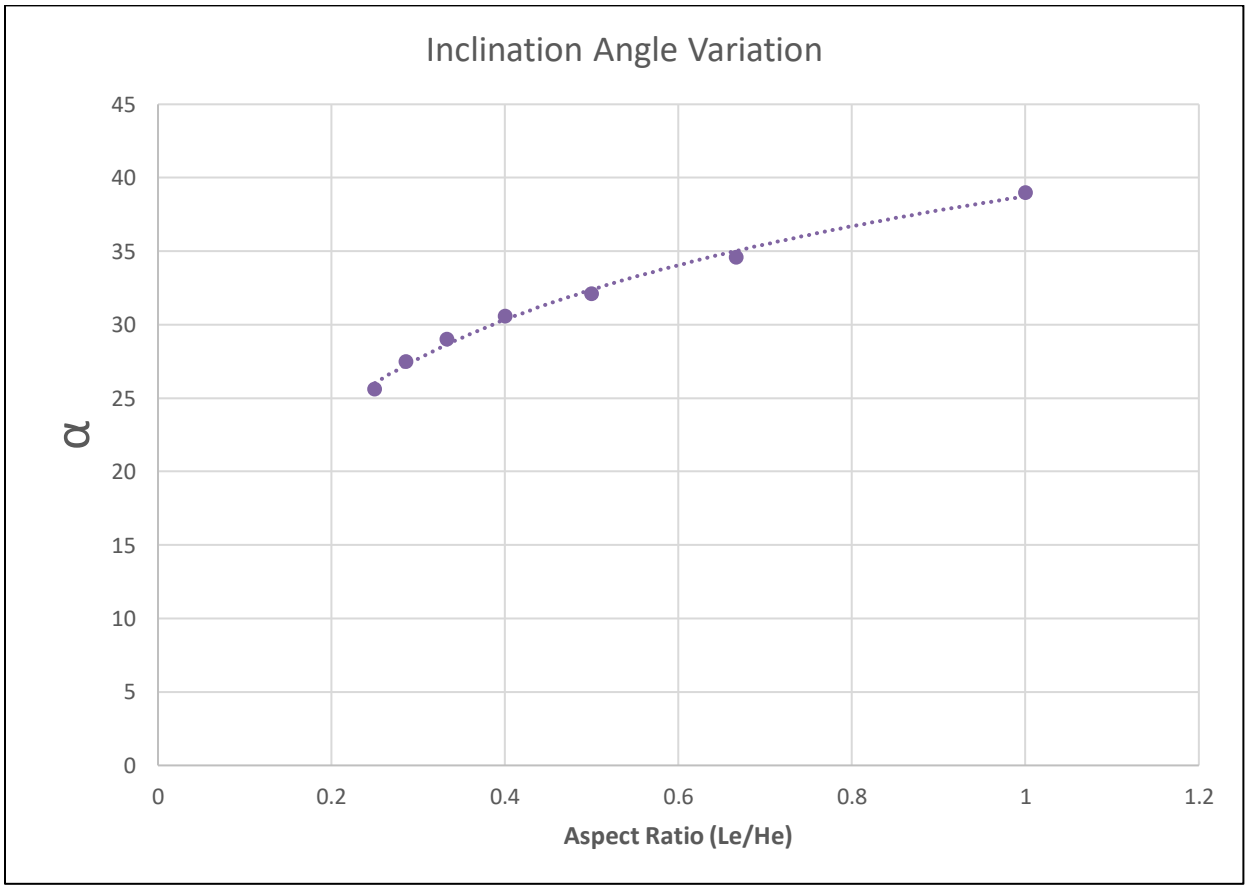


Figure 7.5: Variation of the angle of inclination (α) with the aspect ratio (L_e/H_e)

$$\alpha = 9.2 \ln\left(\frac{L_e}{H_e}\right) + 38.75 \quad \textbf{(7.4)}$$

where L_e and H_e are the center-to-center width and height, respectively.

7.4.3 Height and Length of the Partial Tension Field:

A similar approach was undertaken to determine the dimensions of the partial tension field. At the yield drift, the shell elements that displayed a stress in excess of the yield stress were assumed to participate in tension field action. The height of the tension field was then approximated from the principal stress contours, as shown in Figure 7.6. The height of the partial tension field (H_{PTF}) was then divided by the height of the stud to determine a calibration coefficient (γ). Hence the calibration coefficient (γ) can be thought of as the percent of the sheathing height that participates in tension field action.

The process was then carried out on shear wall models with varying aspect ratios, and the variation of the γ coefficient was plotted against the aspect ratios which is shown in Figure 7.7. The γ coefficient is then defined in terms of the aspect ratios as illustrated in Eq. (7.5). Lastly, if the angle of inclination and the height of the tension field is known, then the length of the tension field can be calculated from the geometry of the panel.

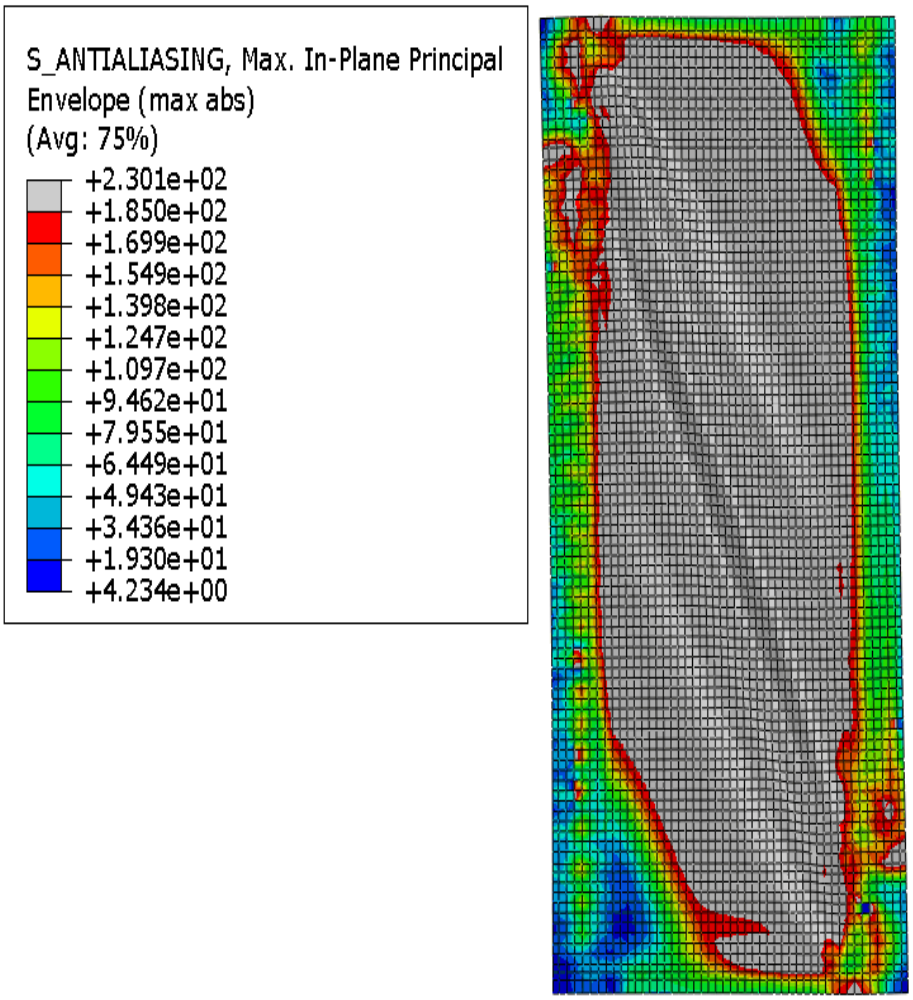


Figure 7.6: Determination of the height of the tension field from the principal stress contours (F_y = *185 kPa*).

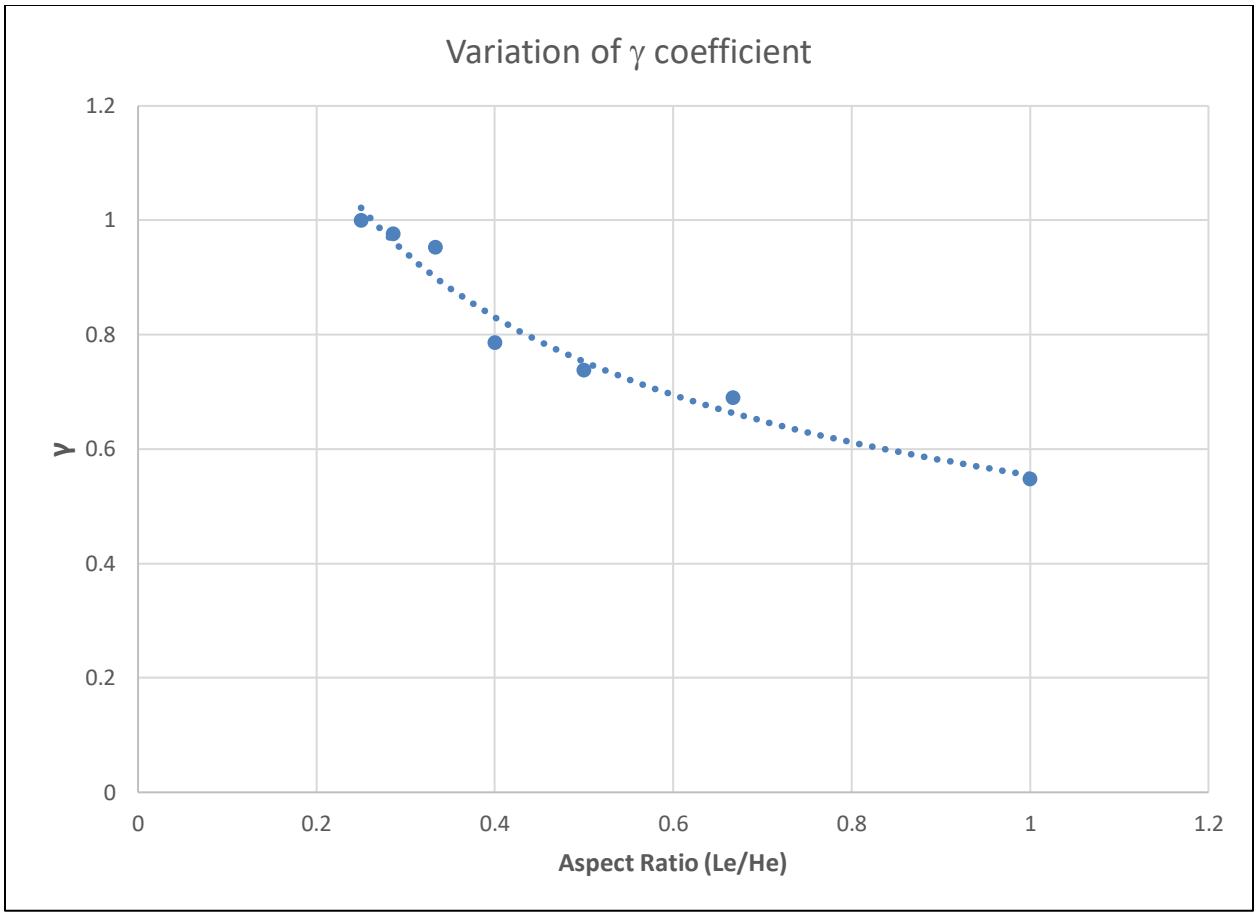


Figure 7.7: Variation of the γ coefficient with the aspect ratio (L_e/H_e).

$$\gamma = 0.55\left(\frac{L_e}{H_e}\right)^{-0.44} \quad \textbf{(7.5)}$$

7.4.4 Equivalent Strip Area

The analytical model involves converting the effective tension band into parallel pin-ended strip oriented at the same angle as the tension field. The strips are assigned an area equal to the width of the tension band multiplied by the sheathing thickness ($t_{sheathing}$). As schematically shown in Figure 7.8, a minimum of ten strips is employed in this study to represent the sheathing. The choice of ten strips is based on the recommendations of the original strip model [19] where ten strips was the minimum number of strips required to produce credible moment and axial force

diagrams on the framing members [26]. Referring to Figure 7.8, the strip area A_s for a tension band of height, H_{PTF}, and length , L_{PTF}, having n strips is:

$$A_s = \left[\frac{L_{PTF}\cos\alpha + H_{PTF}\sin\alpha}{n}\right] t_{sheathing} \quad \textbf{(7.6)}$$

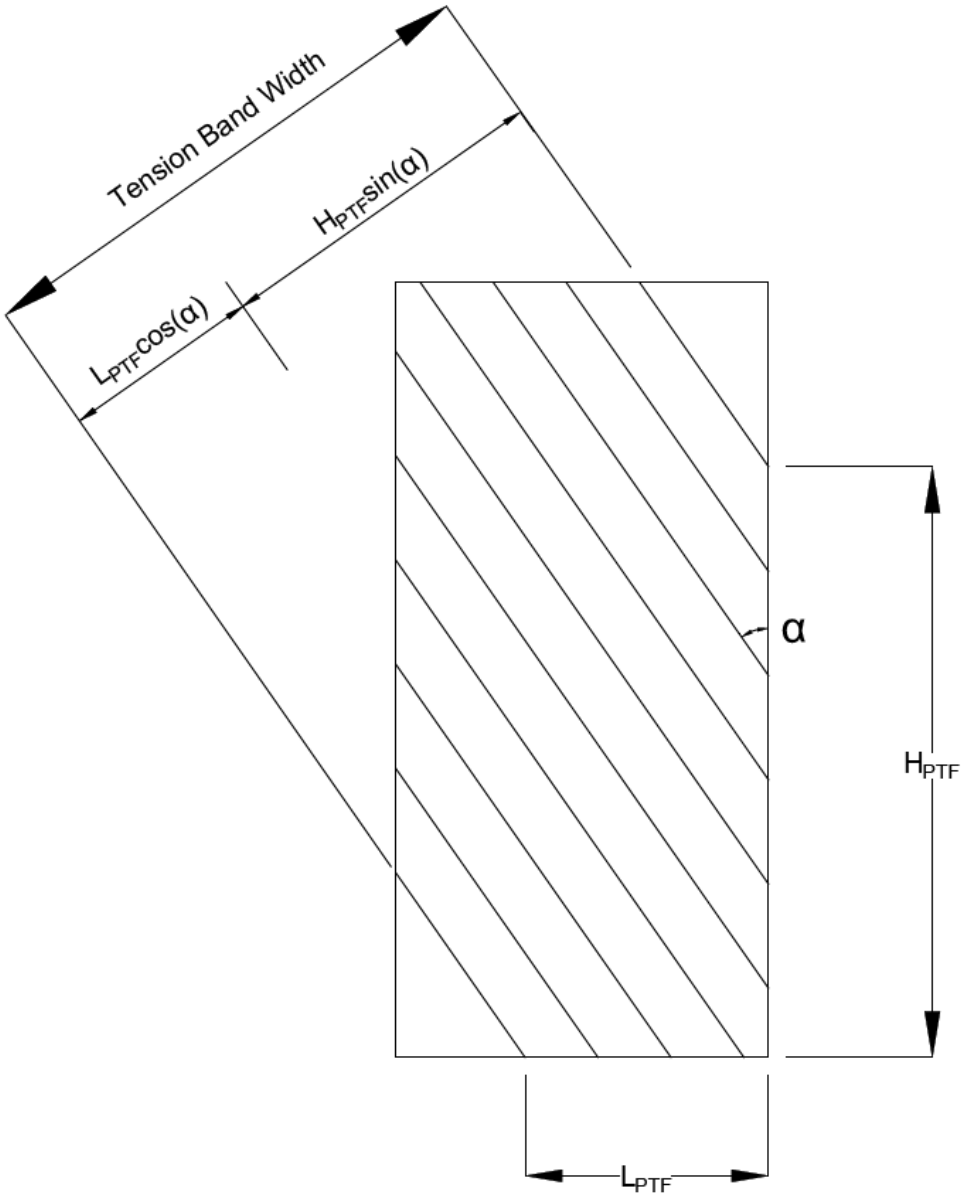


Figure 7.8: Strip model for monotonic analysis of concentric-sheathed CFS shear walls.

7.4.5 Analytical Model Details

The shear wall was modelled and analyzed on SAP 2000 [89] as a 2D frame, for the purpose of engineering practice. Although prior to the discussion of the model's details and results, the following dimensions are defined. As displayed in Figure 7.9, the notations o, e, and c, refer to overall, effective or center-to-center, and clear dimension respectively. The properties of the built-up framing members were first input using the section designer utility. The boundary frame was then defined as linear elastic frame elements using the effective dimensions, although to maintain the (2:1) aspect ratio of the wall, rigid frame elements were defined at the locations of the hold-downs and connector plates. The rigid diaphragm effect at the top of the wall was considered by constraining the horizontal displacements of the top tracks using rigid body constraints. Then, using Eq. (7.4) through Eq. (7.6), the sheathing was modelled as a series of inclined truss elements parallel to the tension field. To account for the inelastic behaviour in the sheathing, axial hinges were assigned at the ends of each strip, replicating the bearing deformations at the location of the screws. The hinges were modelled as having a bi-linear elastic-plastic stress vs. strain curves whose load bearing capacity dropped to zero once the ultimate stress is reached.

The shear wall was assigned a fully fixed boundary condition at the bottom two corners simulating the rigid connection of the hold-downs to the foundation. Furthermore, the connection of the studs to the hold-downs was modelled as partially fixed by incorporating a rotational spring at the stud-to-hold-down joint, as schematically illustrated in Figure 7.10. This was achieved by assigning a major moment release with a rotational stiffness at the top and bottom of each stud. The rotational stiffness value was numerically calibrated through a trial-

and-error approach where the end-fixity factor was assumed and the stiffness value was back calculated from Eq. (2.8). Based on the calibration process, the recommended value for the end-fixity factor at the top and bottom of the studs are 0.2 and 0.3, respectively. The analytical model was then subjected to a displacement time history where non-linear geometric effects were considered.

To verify the accuracy of the analytical model, the axial force and bending moment diagrams of the studs were extracted from the ABAQUS models at the yield level. Each stud was first isolated and the sum of nodal forces and moments along the cross-sectional height of the studs were acquired using the free body cut tool. Also, the global storey shear vs drift comparison between the analytical model, experimental data, and shell finite element model are compared in Figure 7.11, while comparisons on internal frame forces are shown in Figure 7.12 & Figure 7.13

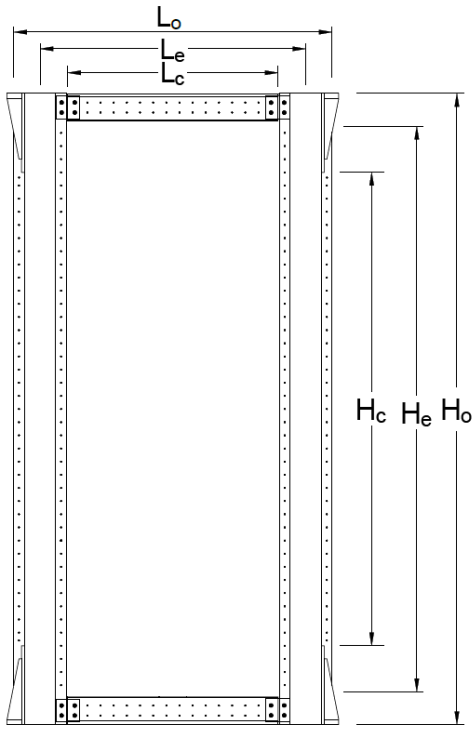


Figure 7.9: Definition of different dimensions.

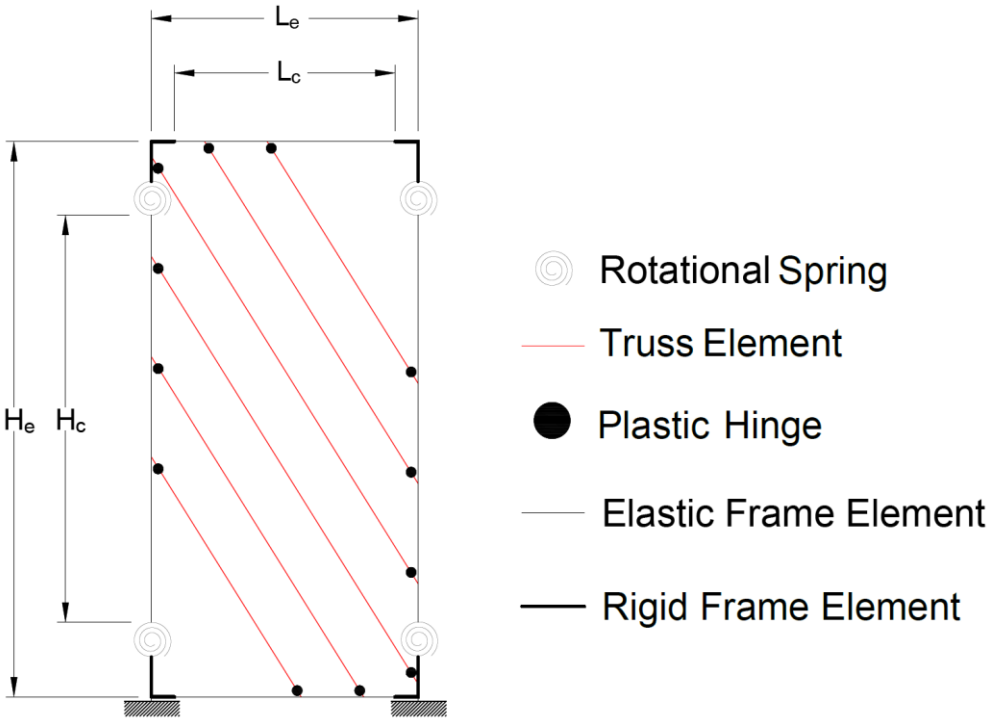


Figure 7.10: Schematic of the analytical model.

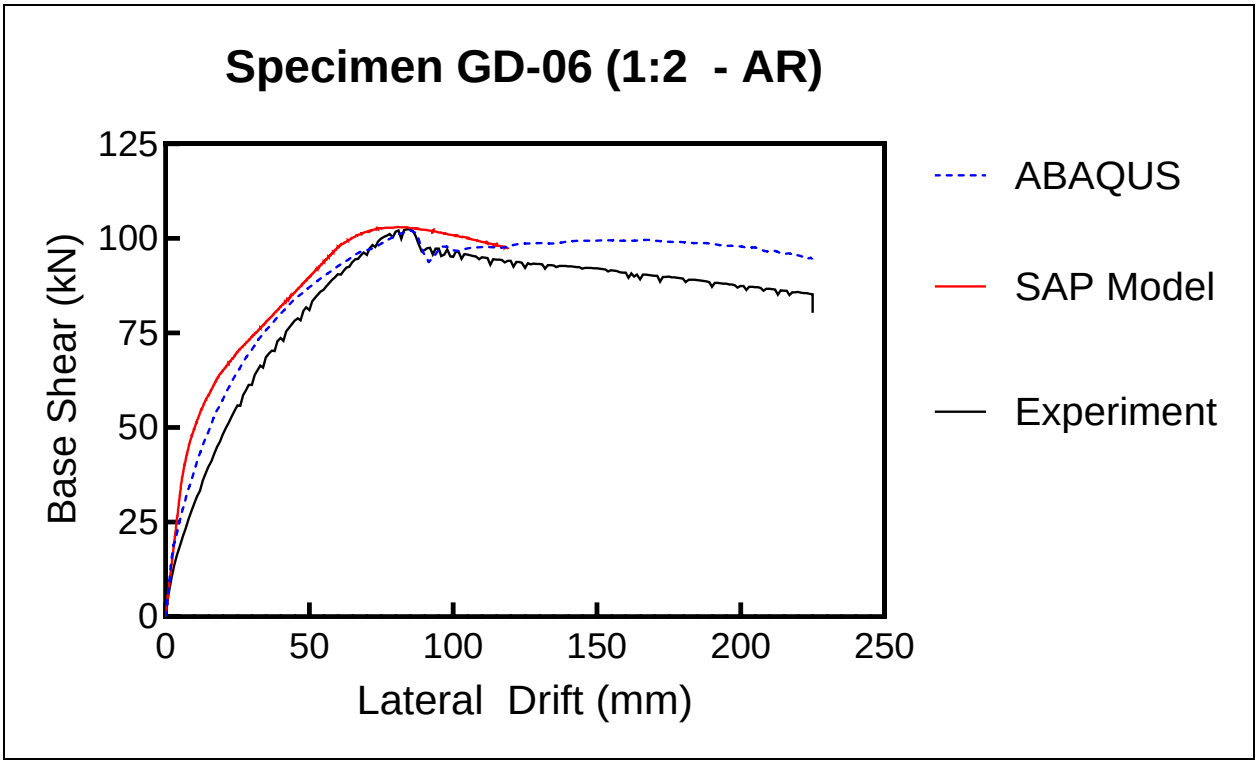
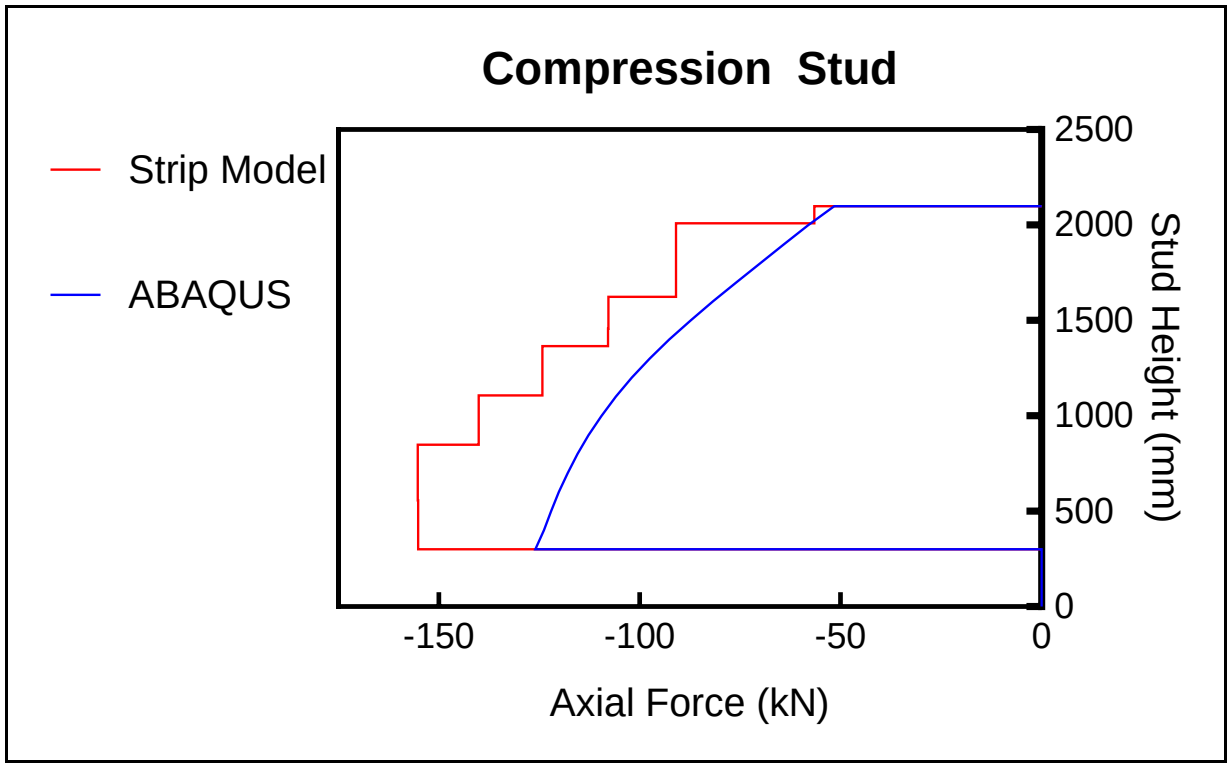
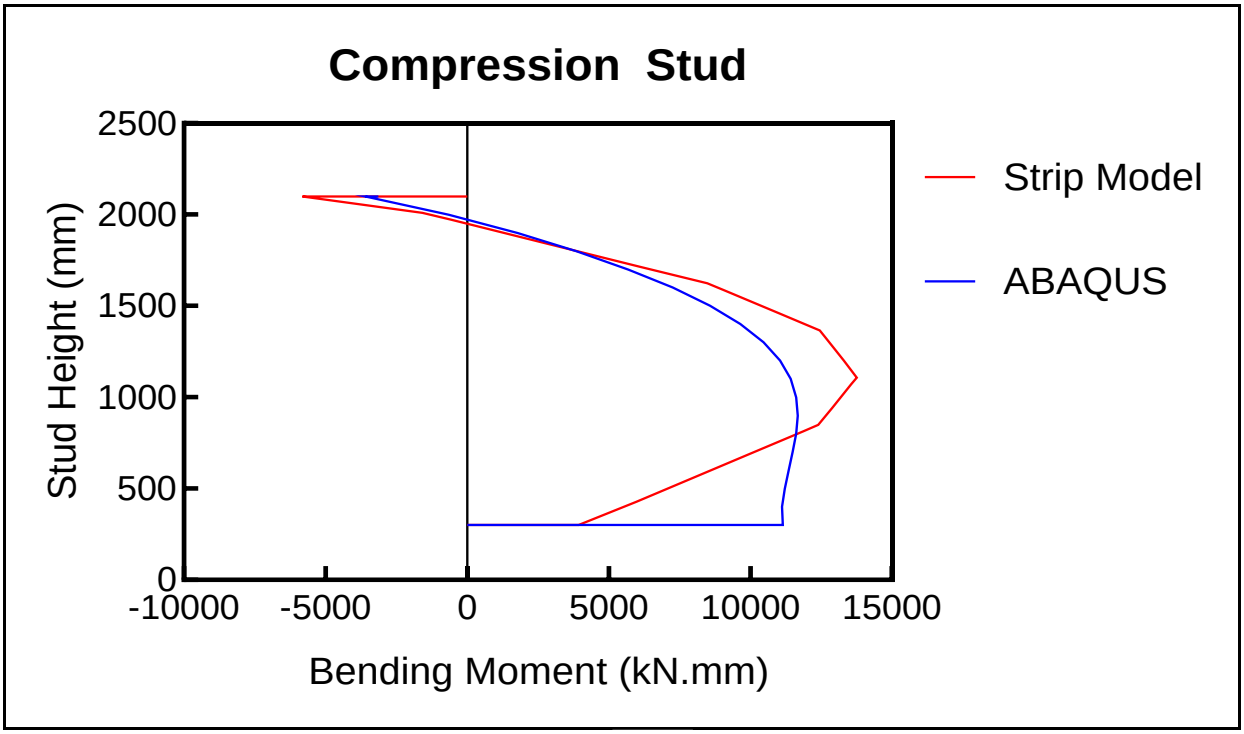


Figure 7.11: Base shear vs drift curves of the experimental data vs the ABAQUS shell model and the Analytical strip model.

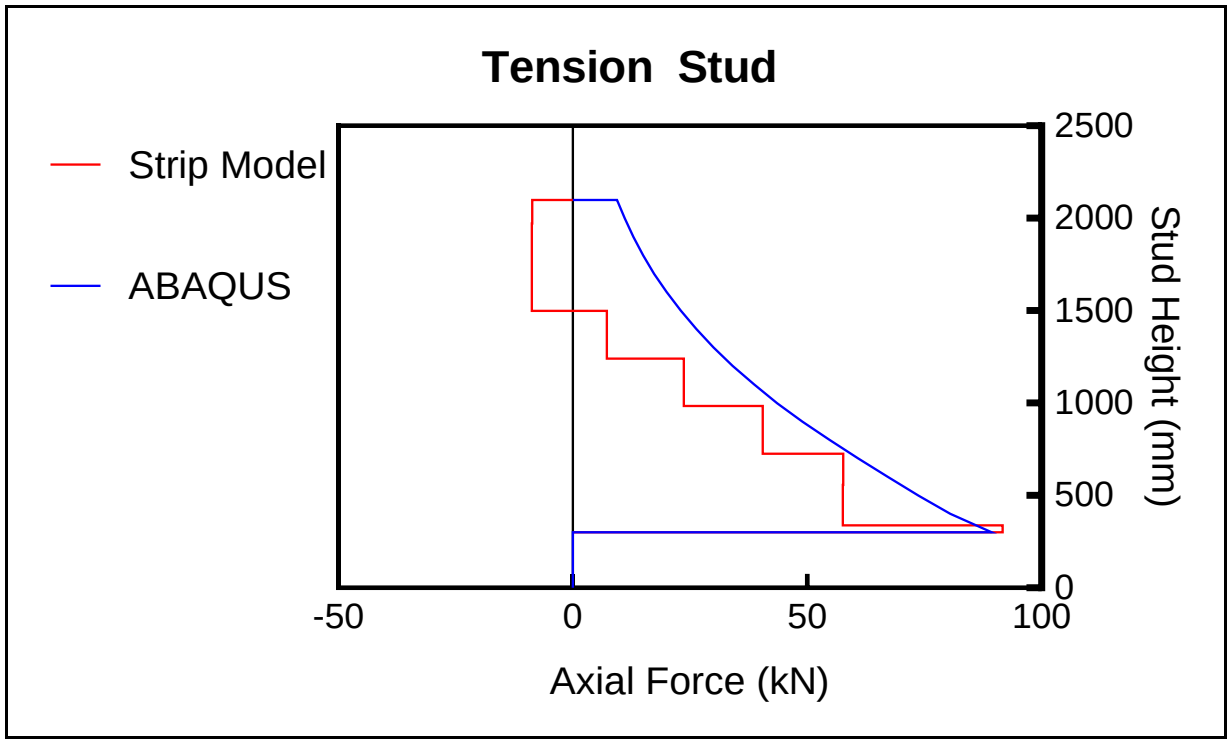


(a)

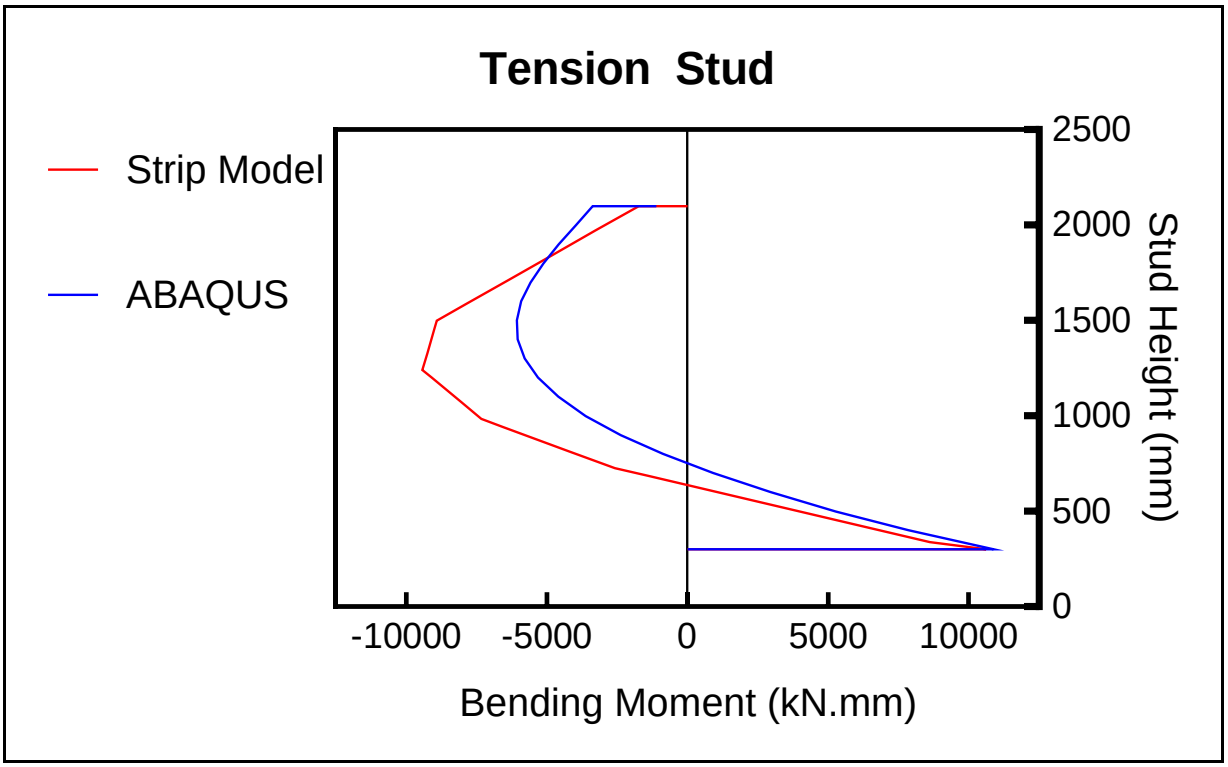


(b)

Figure 7.12: Comparison between axial force diagram (a) and bending moment diagram (b) for the compression stud.



(a)



(b)

Figure 7.13: Comparison between axial force diagram (a) and bending moment diagram (b) for the tension stud.

7.4.6 Discussion of Analytical Model Results

The comparison of the base shear vs drift in Figure 7.11 indicate that up to the yield level, the analytical model implemented in SAP 2000 shows good agreement with the experimental data and shell finite element results. The elastic stiffness of the analytical model is slightly over predicted however the peak load is approximated accurately. By modelling the sheathing as a series of pin-ended strips, any slip exhibited by the screws is not considered by the analytical model, unlike the shell FEM model and the experiment, which in turn might have contributed to the stiffer initial response of the analytical model. Furthermore, at a drift of 120 mm plastic hinges have formed in both ends of each strip, which in turn lead to convergence issues for the solver and the analysis had to be terminated.

Assessing the curves in Figure 7.12 & Figure 7.13 confirm that the load bearing mechanism of the shear wall is indeed a combination of frame sway action and tension field action, which is reflected in the particular shapes of the axial force and bending moment diagrams. The axial force diagrams also correlated well with the shell finite element model results, albeit with some overprediction in the compression stud. The axial force diagram for the analytical model is stepped due to the discretization of the steel sheathing into pin-ended strips. Also, there exists some minor differences in the moment diagrams of the analytical model and the finite element model.

Recall from Section 7.4.3 that the strip model represents the shell elements in the sheathing that have been loaded beyond their yield stress. As a result, the strip model does not consider the pull-in effects of the elements that are not included in the partial tension field. While their effects

are not significant, these elements contribute to the forces on the studs in the finite element model which explains the inconsistencies between the strip and shell model. Examining Figure 7.12 (b) reveals that the moment diagram of the shell model gradually decreases after attaining peak bending moment value while in the analytical model there is a steep gradient. The same phenomenon is present in the tension stud. From Figure 7.13 (b), the bending moment of the tension studs at mid-height is substantially higher than that demonstrated by the finite element model. Despite these discrepancies, the results of this section suggest that the analytical model can be used as a design tool for higher capacity CFS shear walls.

7.5 Simplified Analysis

While the analytical model has shown good correlation with the shell finite element models as discussed in the previous section, the analytical model is still moderately time consuming. In this section, a simplified, hand-based method to determine the forces on the studs is proposed. The motivation behind this method is not to develop a comprehensive closed-form solution, but rather to offer an expeditious, preliminary method to determine the stud axial force and bending moment demand for the purpose of sizing the studs in the early design phase.

The simplified procedure involves determining the forces on the studs through the concept of superposition. That is achieved by establishing and analyzing two separate models: an isolated elastic model of each stud subjected to the inclined sheathing pull-in forces; and an elastic model of the bare frame subjected to a fraction of the yield load, as illustrated in Figure 7.16. By incorporating rotational springs in both models, semi-rigid behaviour can be considered. The remaining challenge is to quantify the frame contribution.

The overall behaviour of the bare frame was examined in Chapter 5 by constructing and analyzing a finite element model of the frame without the steel sheathing. The graph is repeated in Figure 7.14, along with the EEEP design curves of each model. If a factor (η) is defined such that $\eta = (P_{FRAME}/P_{WALL})$, where ($P_{WALL}$) and ($P_{FRAME}$) are measured at the yield drift of the wall as displayed in the figure below, then the fraction of yield load that is resisted by the frame can be calculated by multiplying the yield load by η. The frame contribution factor was then calculated for shear walls with different aspect ratios as shown in Figure 7.15. Examining the trend in the curve reveals that frame contribution increases as the aspect ratio of the shear wall decreases, which is attributed to the fact that slender walls are dominated by bending deformations. Moreover, an expression to compute η in terms of the aspect ratio is derived in Eq. (7.7).

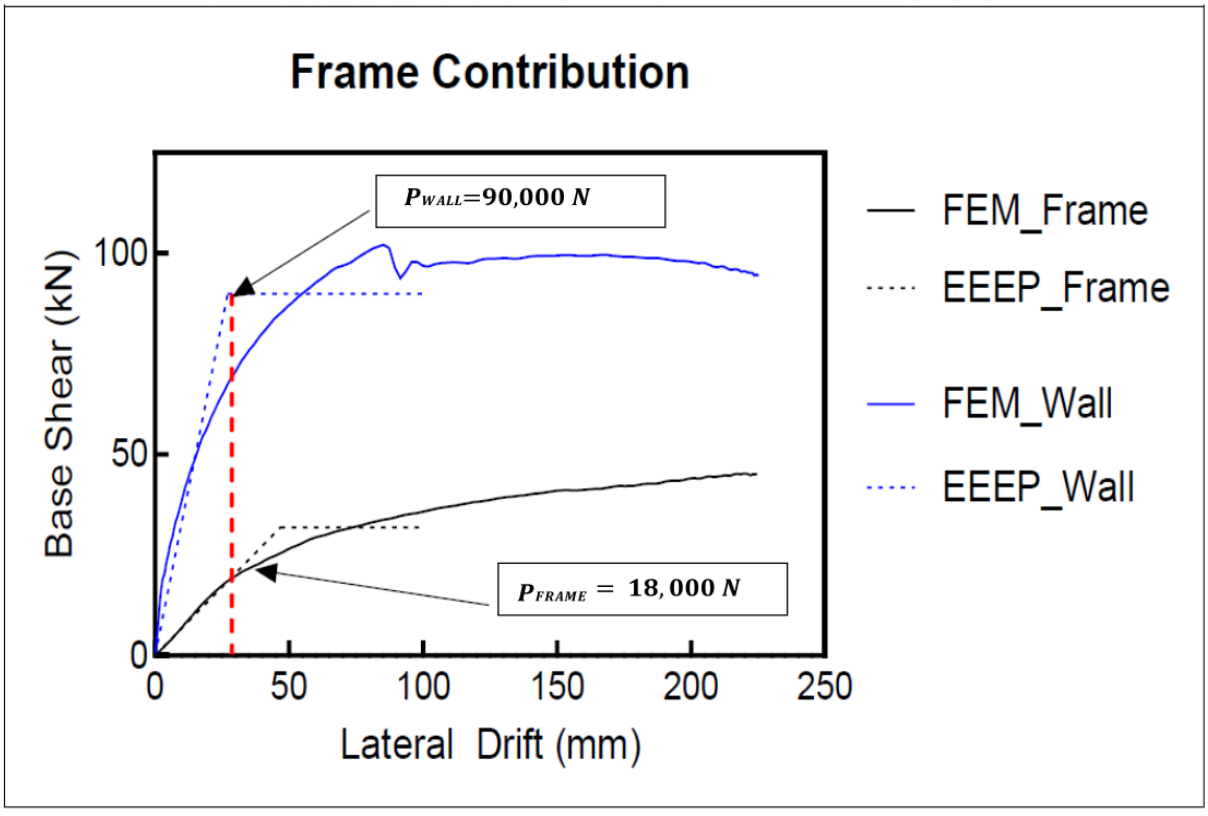


Figure 7.14: Determination of frame contribution coefficient (η)

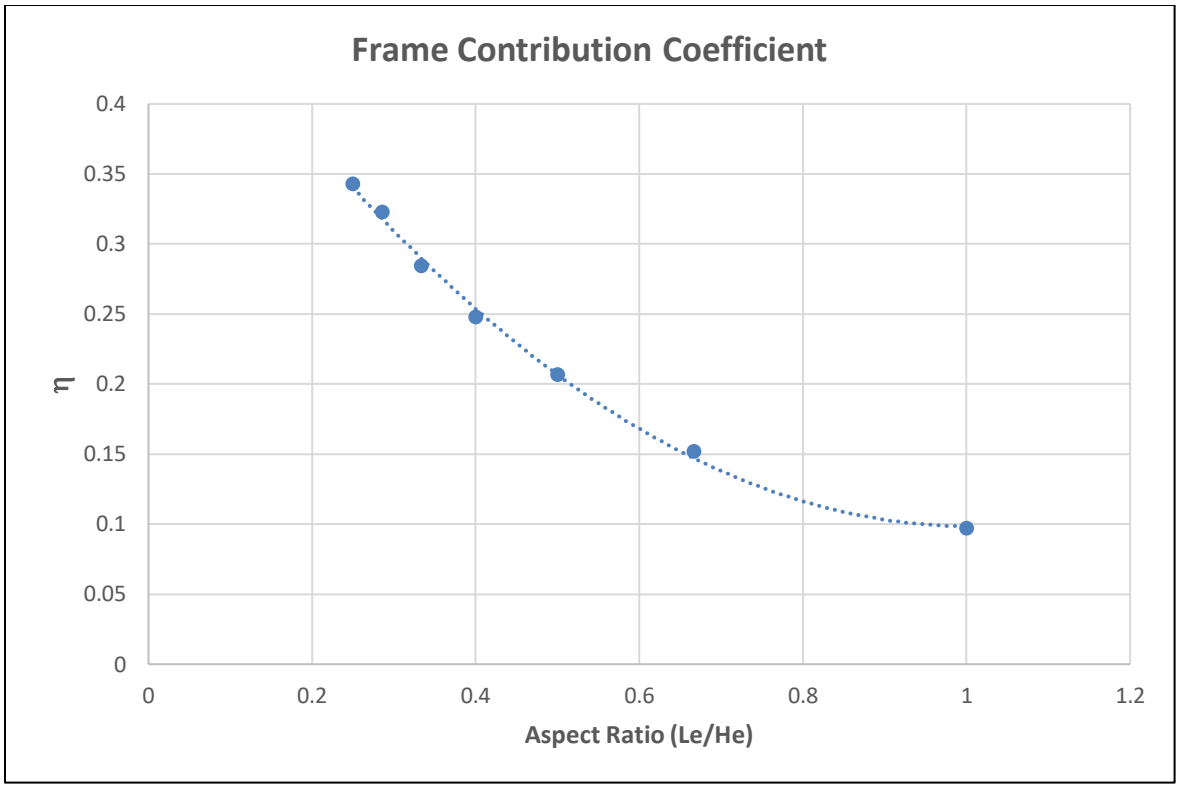


Figure 7.15: Variation of frame contribution coefficient (η) with the aspect ratio.

$$\eta = 0.42(\frac{L_e}{H_e})^2 - 0.85\left(\frac{L_e}{H_e}\right) + 0.53 \quad \textbf{(7.7)}$$

If the aspect ratio and material properties of the shear wall are known (Section 7.4), then the sheathing forces can be established from Eq. (2.3) and the semi-rigid structures formulae tabulated in Appendix B. The free body diagrams of the wall's components subjected to sheathing forces is schematically shown in Figure 7.17. Conversely, if the force resisted by portal frame action is known, then the moment distribution method for semi-rigid frames which was discussed in Section 2.6 can be employed to analyze the bare frame. Finally, the axial forces and bending moments of each stud can be super-imposed to obtain the demand of each stud. The procedure can be easily programed into an excel sheet to expediate calculations.

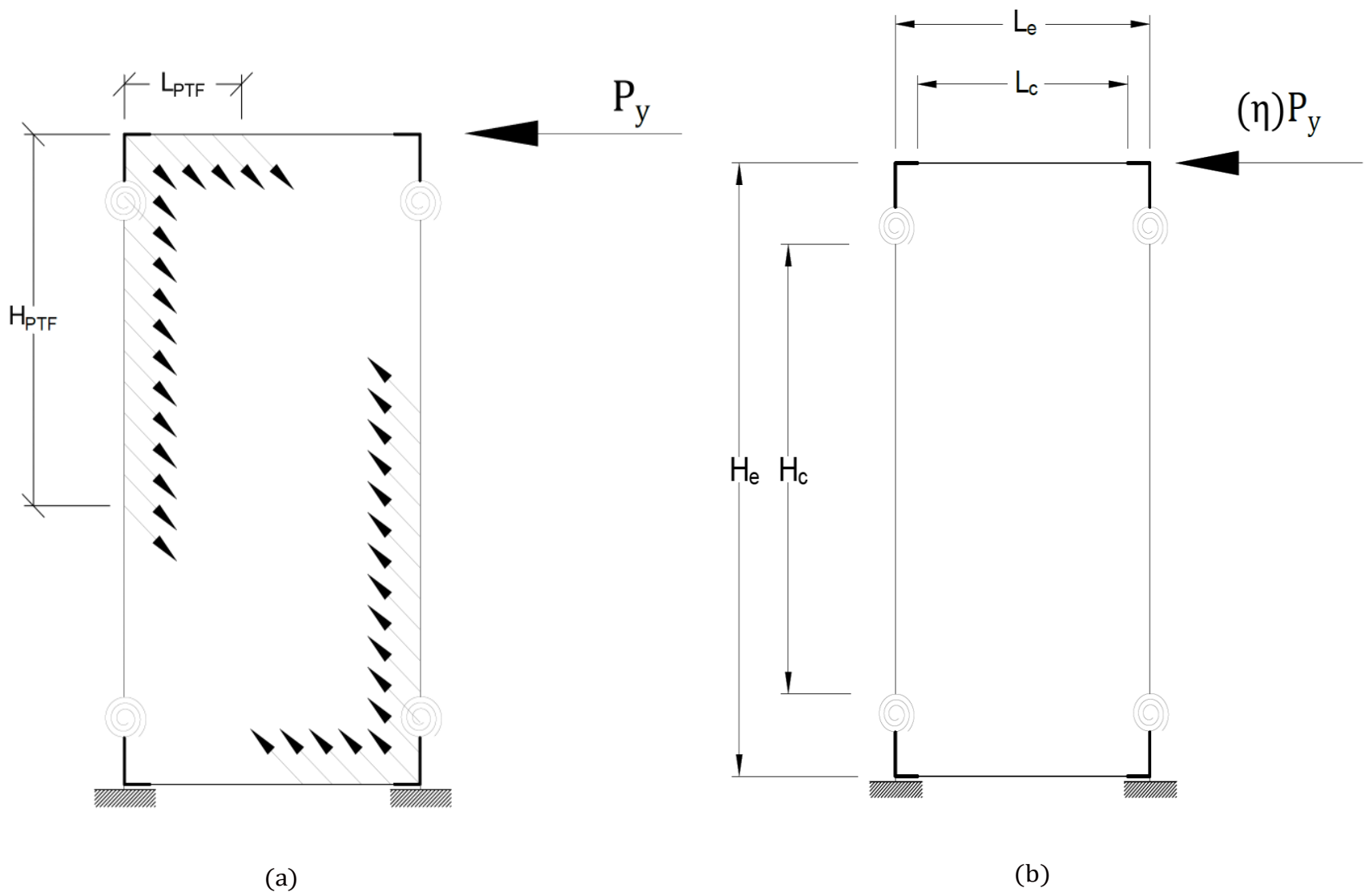


Figure 7.16: (a) Elastic model of the shear wall displaying the sheathing forces; (b) elastic model of the bare frame subjected to a fraction of the yield load.

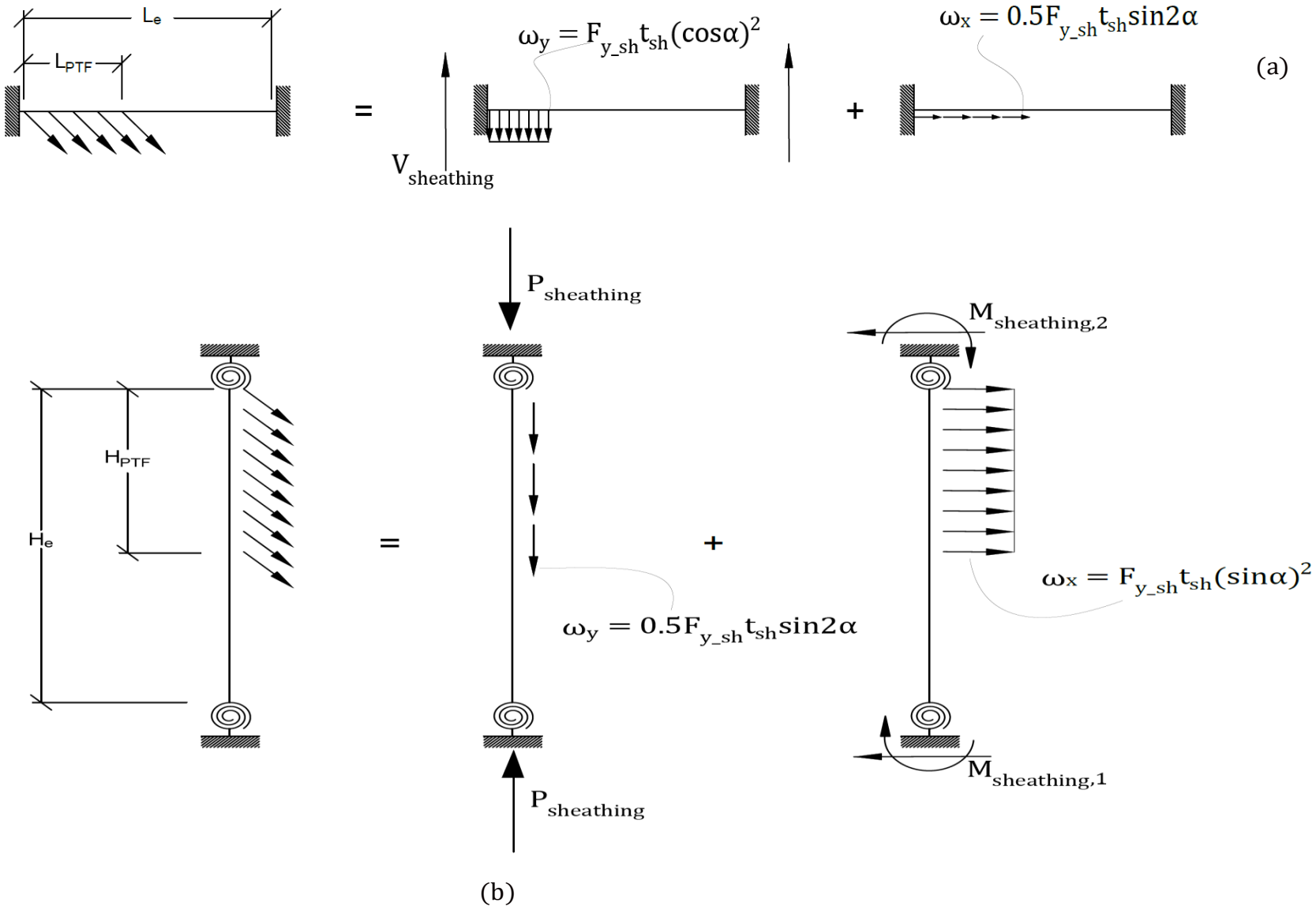
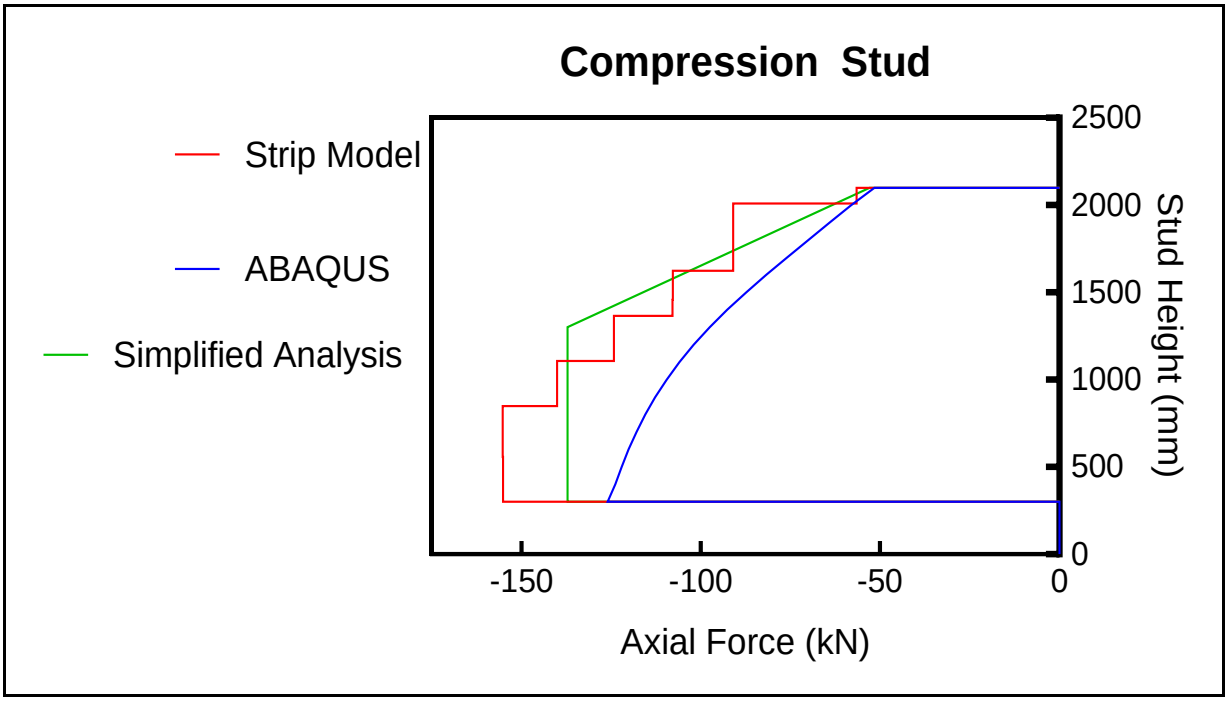
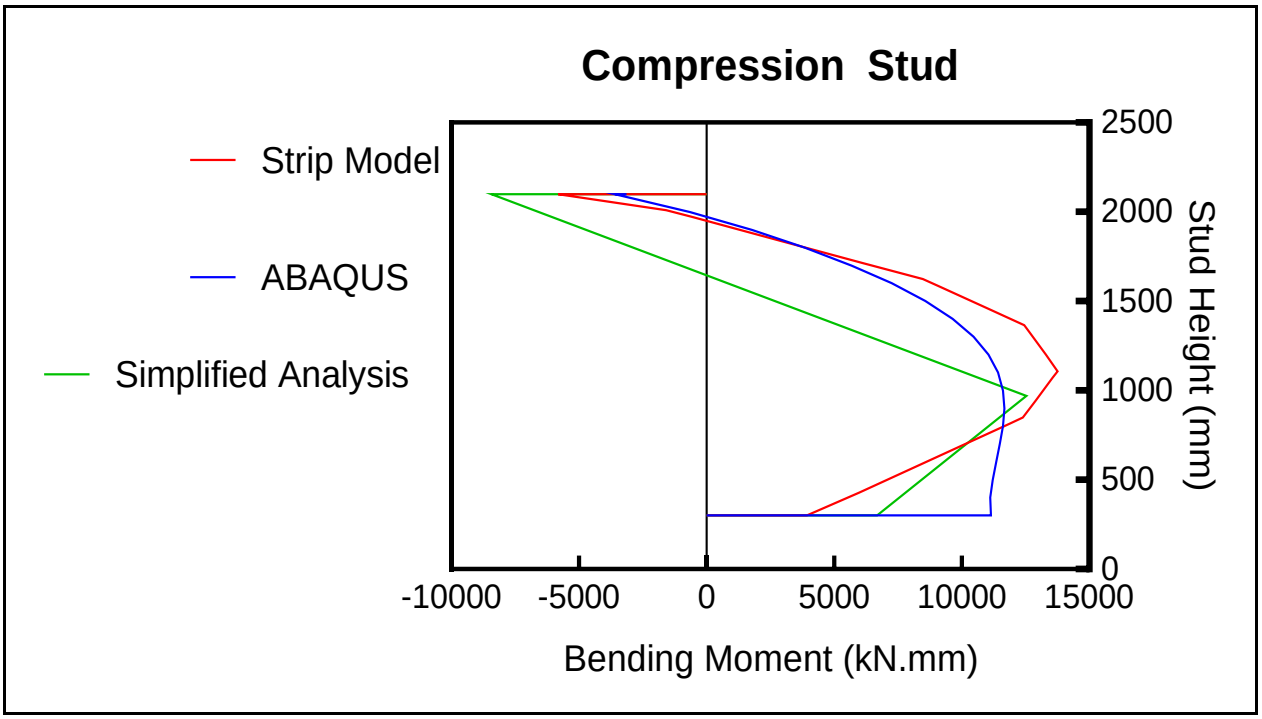


Figure 7.17: Free body diagrams of shear wall components subjected to sheathing yielding forces, (a) Track; (b) Studs.

The simplified method is applied on specimen GD-06 and the results are compared with the analytical and finite element analyses as shown in Figure 7.18, Figure 7.19 and Table 16. The curves indicate that the simplified procedure predicts the axial forces and bending moments on the studs with good accuracy. There is excellent agreement in terms of maximum force and moment for the compression stud, although the method overestimates the negative moment at the top of the compression stud. Using the principle of superposition, the bending moments due to the portal frame action and sheathing pull-in forces are in the same direction at the top of the compression stud, which explains why the value was larger than the finite element results. On the other hand, there is good agreement in terms of bending moments for the tension stud yet the simplified method marginally underestimates the axial load. However the undervaluing of the forces in the tension studs is highly unlikely to be substantial since the design forces would be determined based on the stresses occurring in the opposite compression stud.

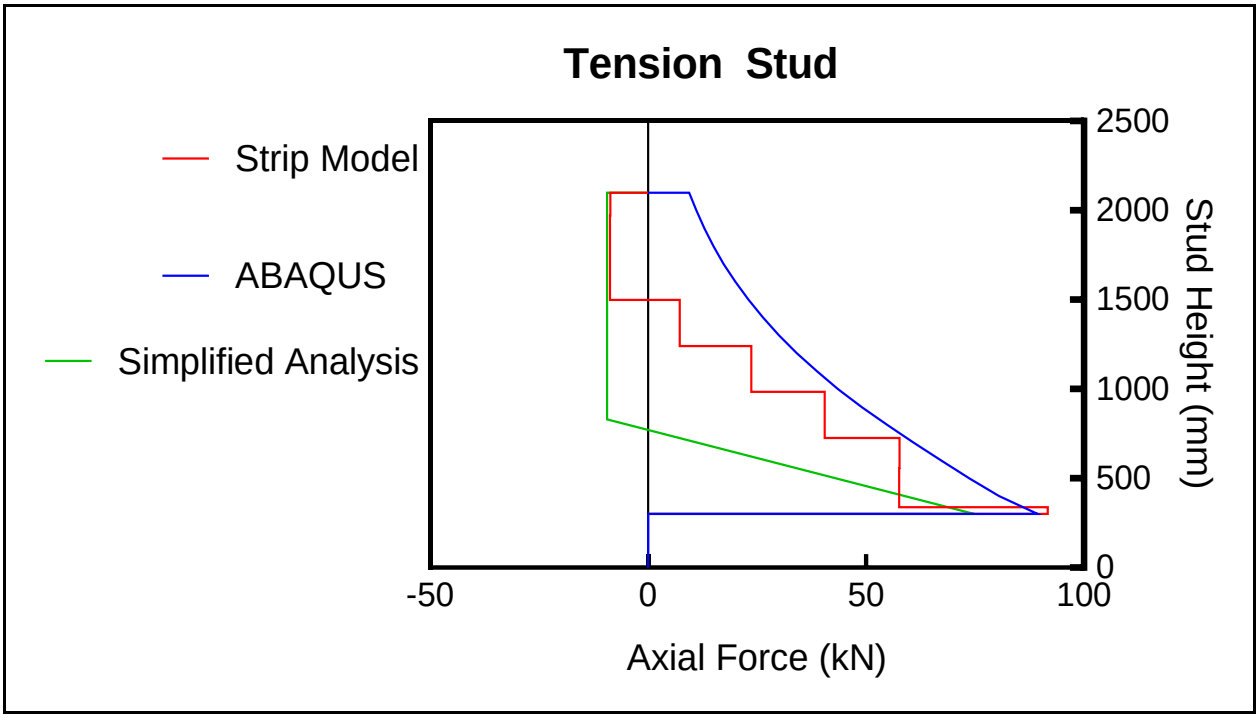


(a)

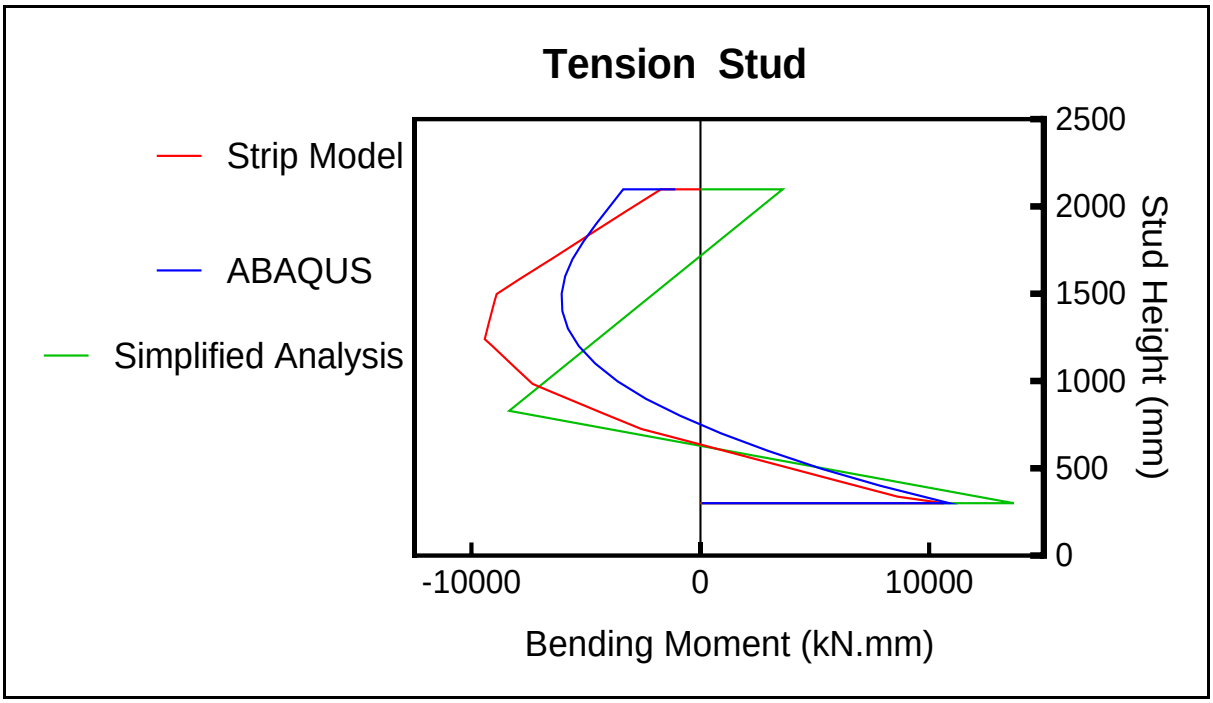


(b)

Figure 7.18: Comparison between axial force diagram (a) and bending moment diagram (b) for the compression stud.



(a)



(b)

Figure 7.19: Comparison between axial force diagram (a) and bending moment diagram (b) for the tension stud.

Table 15: Comparison of results (force values in *kN*, bending moment values in *kN.mm*)

Method	P_{MAX}	% Error	$+M_{MAX}$	% Error	$-M_{MAX}$	% Error
Compression Stud						
ABAQUS	-126	-	11672	-	-3588	-
Analytical	-155	23	13750	17.8	-5805	61.8
Simplified	-137	8.7	12583	7.8	-8407	133.3
Tension Stud						
ABAQUS	90	-	10888	-	-6067	-
Analytical	91.76	1.9	10617	2.5	-9422	55.2
Simplified	75	16.667	13696	25.7	-8358	37.76

It should be noted that even though the proposed methods in this chapter give accurate approximations regarding the monotonic response of the shear wall and the internal forces in the framing members, the overall behaviour of the system is not consistent with capacity design principals. Assuming the built-up studs were designed to possess sufficient strength and stiffness,

then, theoretically speaking, a uniform tension field would have developed across the full height of the sheathing prior to the buckling of the studs. In this case, the proposed design procedure will have to be modified in order to consider the change in the behaviour of the system. Firstly, since the tension field forms across the total height of the sheathing, then determining the γ coefficient is unnecessary and the equivalent strip area can be calculated from the center-to-center height and length of the panel. Secondly, since there is added resistance by the sheathing due to the full tension field, then the frame contribution coefficient η needs to be recalculated using the same method discussed in section 7.5. Lastly, with regards to the simplified procedure, the sheathing pull-in forces that are shown in Figure 7.17 must be modified to act on the total height and length of the studs and tracks, to reflect the formation of a uniform tension field across the sheathing.

7.6 Summary

In this chapter, an analytical and simplified method were proposed to predict the axial force and bending moment demand on the studs of the CFS shear walls at the yield drift. The analytical method involves converting the steel sheathing into a series of pin-ended strips oriented parallel to the tension field, while the simplified method consists of applying the principle of superposition to determine the demand on the studs. For convenience, both methods are broken down into a step-by-step procedure below. An illustrative example is solved to highlight the pertinence of both methods on walls with different aspect ratios.

7.6.1 Analytical Method

If the design load, aspect ratio, and material properties of the shear wall is known, then the computational procedure of the analytical method can be summarized as follows:

1) Determine the inclination angle (α) from Eq. (7.4).
2) Determine the height of the partial tension field (H_{PTF}) from Eq. (7.5).
3) Based on the geometry of the panel and steps 1 & 2, determine the length of the partial tension field (L_{PTF}).
4) Determine the equivalent area of steel of the strip model using Eq. (7.6).
5) Using a plane frame analysis software (such as SAP 2000), define the boundary frame using the effective (center-to-center) dimensions shown in Figure 7.9.
6) Using Eq. (2.8), define rotational springs in the boundary frame studs. In the absence of experimental results for the fixity factor, this study recommends using a value of 0.2 and 0.3 and the top and bottom of the wall respectively.
7) Represent the partial tension field in the sheathing as a series of discrete, pin-ended elastic frame elements oriented at an angle equal to α.
8) Define plasticity in the model by assigning plastic hinges at the ends of each strip.
9) Using body constraints (or an equivalent modelling technique), define the top track as rigid to simulate the effects of the rigid diaphragm provided by the slab.
10) Run the analysis using non-linear time history for displacement control or nonlinear static for force-control.
11) Obtain the design base shear vs storey drift curve and frame force/moment diagrams.

7.6.2 Simplified Method

The computational procedure of the simplified, hand-based method is summarized below:

1) Determine the angle of inclination, height and length of the partial tension field similar to steps 1 through 3 of the previous method.
2) Establish an isolated model of each stud subjected to inclined forces as per Figure 7.17.
3) Determine the bending moments and axial forces due to sheathing pull-in forces using Table B.1.
4) Determine the frame contribution factor (η) using Eq. (7.7).
5) Set up a model of the bare frame subjected to the yield load multiplied by the frame contribution factor (η).
6) Determine the bending moments and axial forces of the frame using the procedure of moment-distribution for semi-rigid frames.
7) Using the principle of superposition, obtain the force and moment demand for each stud.

7.6.3 Numerical Example:

The plan of a typical, one-storey cold-formed steel-framed office buildings is displayed in Figure 7.20. For this example, diaphragms are permitted to be idealized as rigid. The uniform wind load is denoted as W_{wind} as shown in the figure below. Use the analytical and simplified method to determine the overall storey shear vs drift of the shear wall on grid B and plot the axial force and bending moment diagrams of the shear wall studs. Assume the fixity factor is 0.3 and 0.2 and the bottom and top of the stud, respectively. The dimensions of the shear wall are displayed in Figure 7.21 and the relevant material properties are listed below:

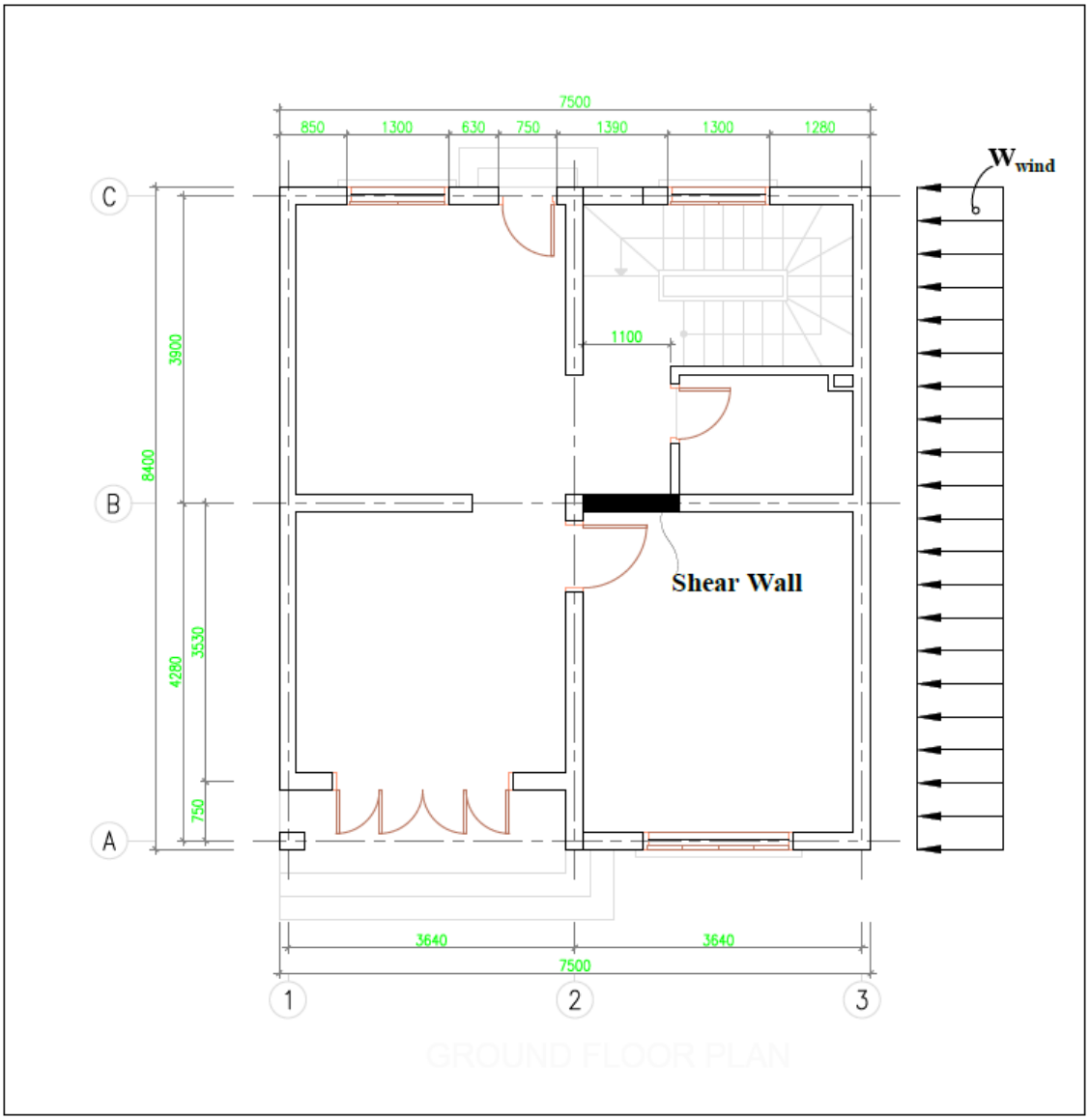


Figure 7.20: Layout of a typical office building.

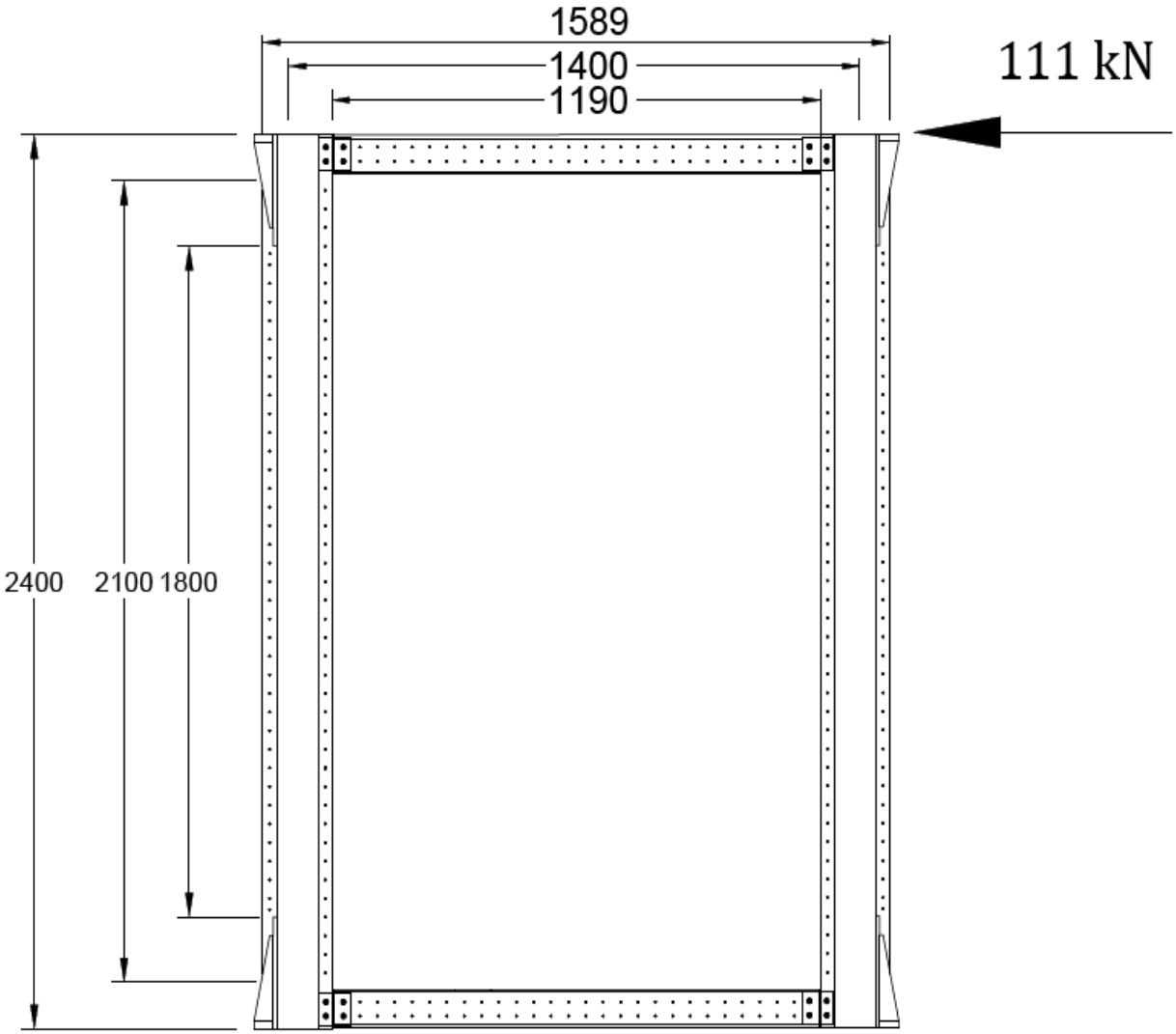


Figure 7.21: Shear wall elevation.

- $E_{FRAME} = 181572\ MPa$
- $I_{studs} = 5663490\ mm^4$
- $I_{trakcs} = 1258126\ mm^4$
- $r_{bottom} = 0.3$
- $P_y = 111{,}000\ N$
- $F_y = 167\ MPa$
- $t_{sheathing} = 0.8\ mm$
- $r_{top} = 0.2$

Analytical Method:

Step 1: Determine the angle of inclination (Eq. (7.4)):

$$\alpha = 9.2 \ln\left(\frac{L_e}{H_e}\right) + 38.75 = 9.2 \times \ln\left(\frac{1400}{2100}\right) + 38.75 = \mathbf{35}°$$

Step 2: Determine the height of the partial tension field (Eq. (7.5)):

$$\gamma = 0.55\left(\frac{L_e}{H_e}\right)^{-0.44} = 0.55\left(\frac{1400}{2100}\right)^{-0.44} = 0.66; \rightarrow H_{PTF} = 0.66 \times 2100 = \mathbf{1390}$$

Step 3: Based on Step 1 & 2, determine the length of the partial tension field, the geometry of the panel is shown below:

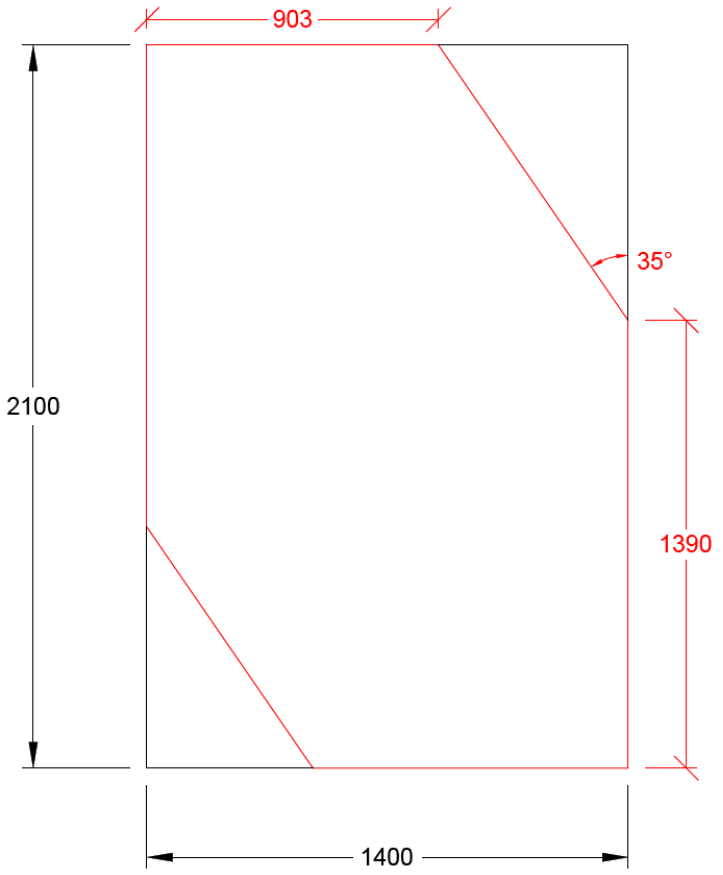


Figure 7.22: Geometry of the panel showing the width of the partial tension field.

Step 4: Determine the equivalent area of steel (Eq.(7.6)), assume 10 strips:

$$A_s = \left[\frac{L_{PTF}\cos\alpha + H_{PTF}\sin\alpha}{n}\right] t_{sheathing} = \left[\frac{903\cos 35 + 1390\sin 35}{10}\right] \times 0.8 = 123\ mm^2$$

Using this information, an analytical model based on the strip representation of the sheathing can be analyzed using SAP or any adequate plane frame analysis software. The SAP 2000 output is compared with the finite element analysis results in Figure 7.23:

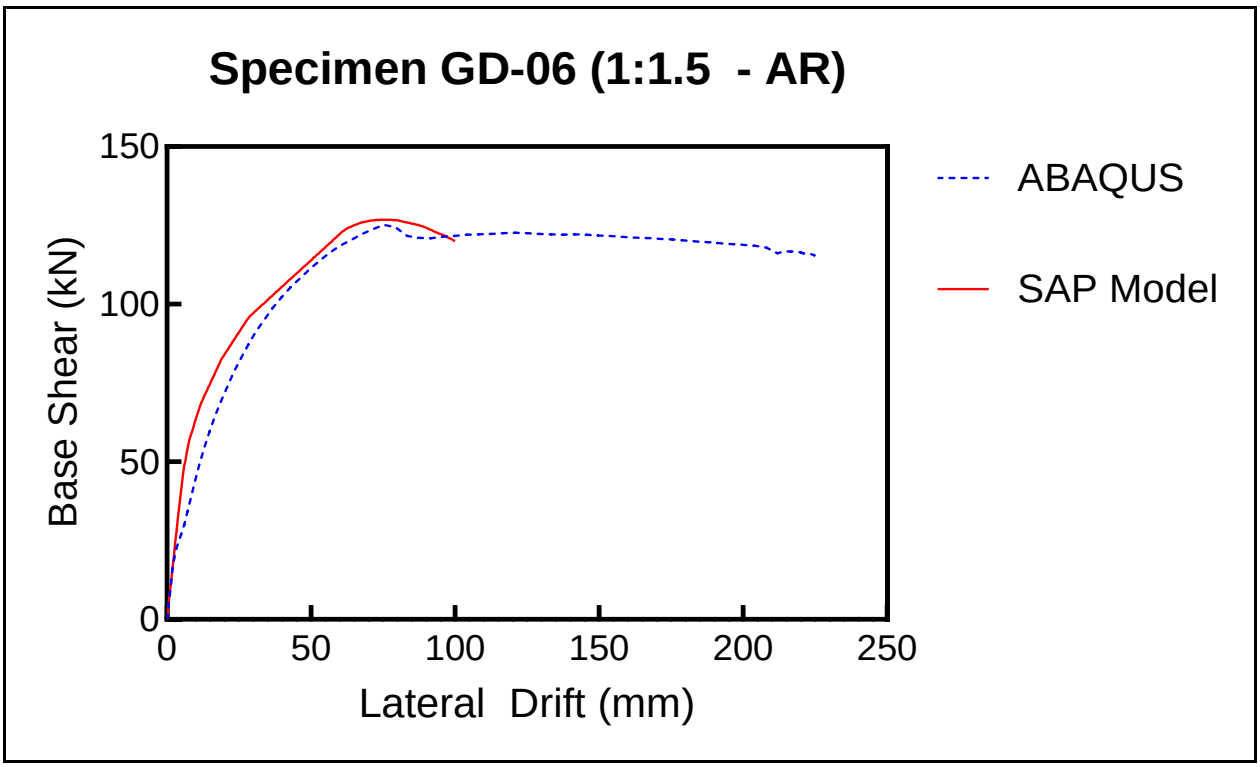


Figure 7.23: Results of the analytical model compared with ABAQUS shell finite element model.

Similar to the results of Section 7.4.6, the analytical models correlates well with the shell finite element results up to the yield drift level. The analytical model slightly overestimates the elastic stiffness of the shear wall, which is attributed to the fact that the analytical model does not

consider the slip in the screws. Moreover, plastic hinges form in all the strips at a drift of 100 mm, which explains why the analysis have been terminated at that particular drift level.

Simplified Method:

Step 1: Determine the angle of inclination, height and length of the partial tension field:

Similar to the analytical procedure, $\boldsymbol{\alpha = 35°, H_{PTF} = 1390;\ L_{PTF} = 903}$.

Step 2: Determine the sheathing forces as per Figure 7.17:

- $\omega_{x,stud} = F_{y_sh}\, t_{sh}\, (sin\, \alpha)^2 = 44\ N/mm$
- $\omega_{y,stud} = 0.5 F_{y_sh}\, t_{sh}\, sin\, 2\alpha = 63\ N/mm$
- $\omega_{y,track} = F_{y_sh}\, t_{sh}\, (cos\, \alpha)^2 = 89.5\ N/mm$

Step 3: Using Table 18 for members with semi-rigid connections subjected to partial distributed loadings, calculate the bending moments and axial forces due to the sheathing pull in effects (refer to the notation on Figure 7.17 & Table 18). A sample for the compression stud is shown below:

- $\boldsymbol{M_{sh,2}} = \frac{r_1}{4-r_1 r_2}\left(\frac{H^2}{60}\right)(n-m)\{w_a(2+r_2)[3(n-m)^3 + 15m(n^2+m^2)] + 10w_a(4-r_2)(n+2m) - 30w_a[(n+m)^2+2m^2] + w_b(2+r_2)[3(m-n)^3 + 15n(m^2+n^2)] + 10w_b(4-r_2)(m+2n) - 30w_b[(m+n)^2+2n^2]\}$
- $\boldsymbol{M_{sh,2}} = \frac{0.2}{4-0.2*0.3}\left(\frac{1800^2}{60}\right)(0.69-0)\{44(2+0.3)[3(0.69-0)^3 + 15*0(0.69^2+0^2)] + 10*44(4-0.3)(0.69+2*0) - 30*44[(0.69+0)^2+2(0)^2] + 44(2+0.3)[3(0-$

$0.69)^3 + 15 * (0.69)(0^2 + 0.69^2)] + 10 * 44(4 - 0.3)(0 + 2 * 0.69) - 30 * 44[(0 + 0.69)^2 + 2(0.69)^2]\}$

- $\boldsymbol{M_{sh,2} = -3483\ kN.mm}$
- $\boldsymbol{M_{sh,1}} = \frac{r_2}{4 - r_1 r_2}\left(\frac{H^2}{60}\right)(n-m)\{w_a(2+r_1)[3(n-m)^3 + 15m(n^2+m^2)] - 20w_a(1 - r_1)(n+2m) - 15r_1 w_a[(n+m)^2 + 2m^2] + w_b(2+r_1)[3(m-n)^3 + 15n(m^2+n^2)] - 20w_b(1-r_1)(m+2n) - 15r_1 w_b[(m+n)^2 + 2n^2]\}$
- $\boldsymbol{M_{sh,1}} = \frac{0.3}{4 - 0.2 * 0.3}\left(\frac{1800^2}{60}\right)(0.69 - 0)\{44(2 + 0.2)[3(0.69 - 0)^3 + 15 * 0(0.69^2 + 0^2)] - 20 * 44(1 - 0.2)(0.69 + 2 * 0) - 15 * 0.2 * 44[(0.69 + 0)^2 + 2(0)^2] + 44(2 + 0.2)[3(0^2 - 0.69^2)^3 + 15 * (0.69)(0^2 + 0.69^2)] - 20 * 44(1 - 0.2)(0 + 2 * 0.69) - 150.2 * 44[(0 + 0.69)^2 + 2(0.69)^2]\}$
- $\boldsymbol{M_{sh,1} = -2556\ kN.mm}$
- $\boldsymbol{M_{max}} = \frac{[(\frac{\omega_{x,stud} * H_{PTF}}{2*H})(2*H - H_{PTF})]^2}{2 * \omega_{x,stud}} - \frac{(M_{sh,1} + M_{sh,2})}{2}$
- $\boldsymbol{M_{max}} = \frac{\left[\left(\frac{44*1240}{2*1800}\right)(2*1800 - 1240)\right]^2}{2*44} - \frac{(6409)}{2} = \boldsymbol{11503\ kN.mm}$
- $\boldsymbol{X_{max}} = \left(\frac{H_{PTF}}{2*H}\right)(2 * H - H_{PTF}) = \boldsymbol{813\ mm}\ (from\ the\ top).$

Similarly, solving for the shears in the tracks assuming the end conditions are fixed due to the restraint by the rigid diaphragm:

- $\boldsymbol{V_{sh,1} = 50\ kN}$
- $\boldsymbol{V_{sh,2} = 21\ \ kN}$

Step 3: Determine the frame contribution factor from Eq.(7.7):

$$\eta = 0.42(\frac{1400}{2100})^2 - 0.85\left(\frac{1400}{2100}\right) + 0.53 = 0.15$$

Step 4: Establish a bare frame model as displayed Figure 7.24 in subjected to (0.15*111,000 = 16,650 N):

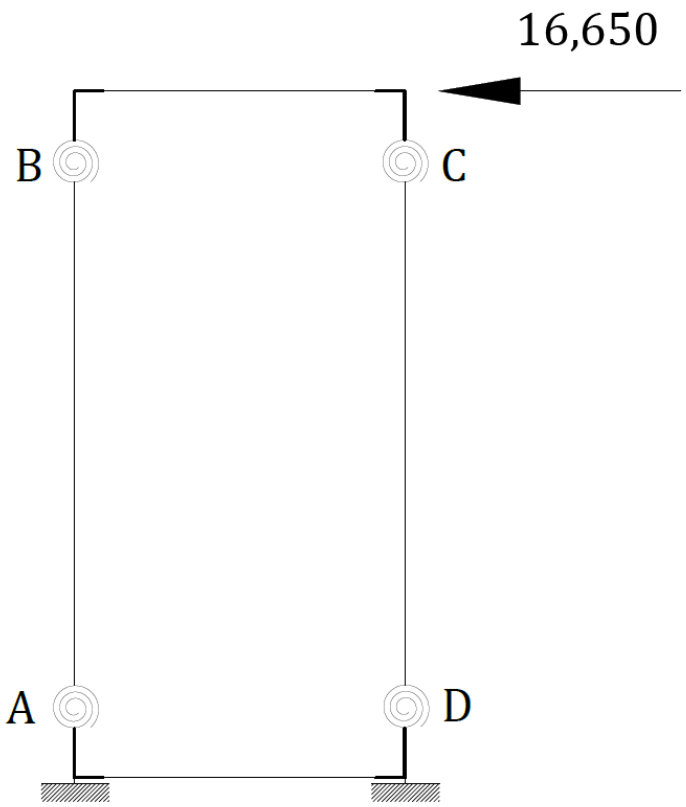


Figure 7.24: Bare frame model subjected to a fraction of the yield design load.

Step 5: Determine the moments and axial forces in the bare frame using the moment distribution method for semi-rigid frames:

- The stiffness factor for a semi-rigid member with two different end fixity factors can be obtained as (from Eq.(2.9) & Eq. (2.11)):

- $K_{BA} = K_{CD} = \left(\frac{3r_{top}}{4-r_{top}r_{bottom}}\right)\left(\frac{4EI_{stud}}{H_c}\right) = \left(\frac{3*0.2}{4-0.2*0.3}\right)\left(\frac{4*181572*5663490}{1800}\right) = 347997024$

- The stiffness factor for the track with rigid connections at both ends:
  - $K_{BC} = K_{CB} = \left(\frac{4EI_{track}}{L_c}\right) = \left(\frac{4*181572*1258126}{1190}\right) = 767867073$
- Carry-over factor from top to bottom of the studs: $CO_{stud} = \frac{0.3}{2} = 0.15$
  - $(DF)_{BA} = (DF)_{CD} = \frac{3479970242}{347997024+767867072.5} = 0.311$
  - $(DF)_{BC} = (DF)_{CB} = \frac{767867072.5}{347997024+767867072.5} = 0.689$
- For a semi-rigid member, the moments at the end of the member due to lateral sway can be defined as:
  - $(M)_{BA} = (M)_{CD} = \left[\frac{r_{top}(2+r_{bottom})}{4-r_{top}r_{bottom}}\right]\left(\frac{6EI_{stud}}{{H_c}^2}\right) = \left[\frac{0.2(2+0.3)}{4-0.2*0.3}\right]\left(\frac{6*181572*5663490}{1800^2}\right) = 222331\ N.mm$

    Similarly;

  - $(M)_{AB} = (M)_{DC} = 318997\ N.mm$
  - $\therefore\ (M)_{AB}/(M)_{BA} = 1.434$
  - Assume $(M)_{BA} = 100\ N.mm$ and carry out classical moment distribution for sway frames after applying the modification factors. The procedure is tabulated in Table 16. The free-body diagram of member AB is also shown in Figure 7.25.

Table 16: Moment distribution for the bare frame (bending moments unit are in *N.mm*).

Joint	A	B		C		D
Member	AB	BA	BC	CB	CD	DC
DF	0	0.311863	0.688137	0.688137	0.311863	0
FEM	143.4783	100	0	0	100	143.4783
Dist.	0	-31.1863	-68.8137	-68.8137	-31.1863	0
FEM	-4.67795	0	-34.4068	-34.4068	0	-4.67795
Dist.	0	10.73023	23.67661	23.67661	10.73023	0
FEM	1.609534	0	11.8383	11.8383	0	1.609534
Dist.	0	-3.69193	-8.14637	-8.14637	-3.69193	0
FEM	-0.55379	0	-4.07319	-4.07319	0	-0.55379
Dist.	0	1.270277	2.802909	2.802909	1.270277	0
FEM	0.190542	0	1.401454	1.401454	0	0.190542
Dist.	0	-0.43706	-0.96439	-0.96439	-0.43706	0
FEM	-0.06556	0	-0.4822	-0.4822	0	-0.06556
Dist.	0	0.150379	0.331817	0.331817	0.150379	0
FEM	0.022557	0	0.165908	0.165908	0	0.022557
Dist.	0	-0.05174	-0.11417	-0.11417	-0.05174	0
FEM	-0.00776	0	-0.05708	-0.05708	0	-0.00776
Dist.	0	0.017802	0.039281	0.039281	0.017802	0
∑	139.9958	76.80163	-76.8016	-76.8016	76.80163	139.9958

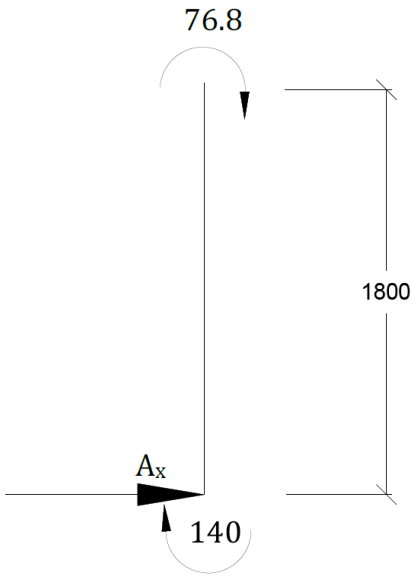
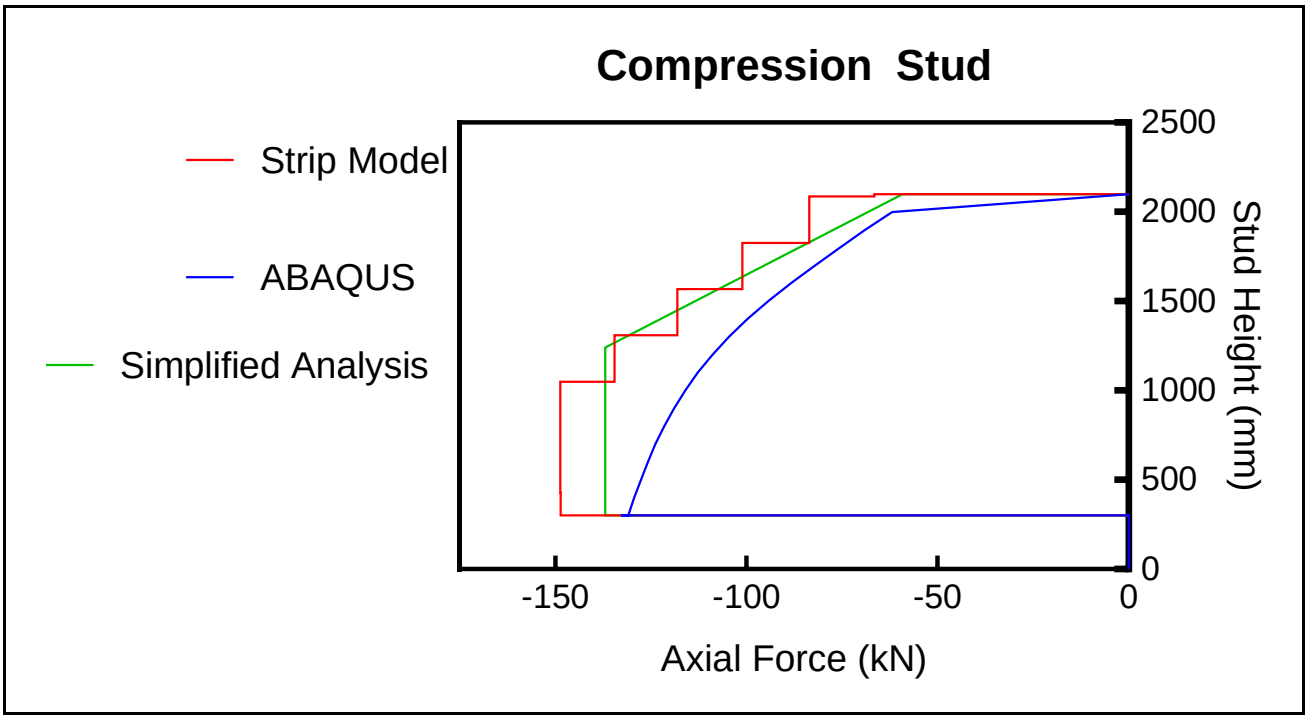


Figure 7.25: Free-body diagram of member AB.

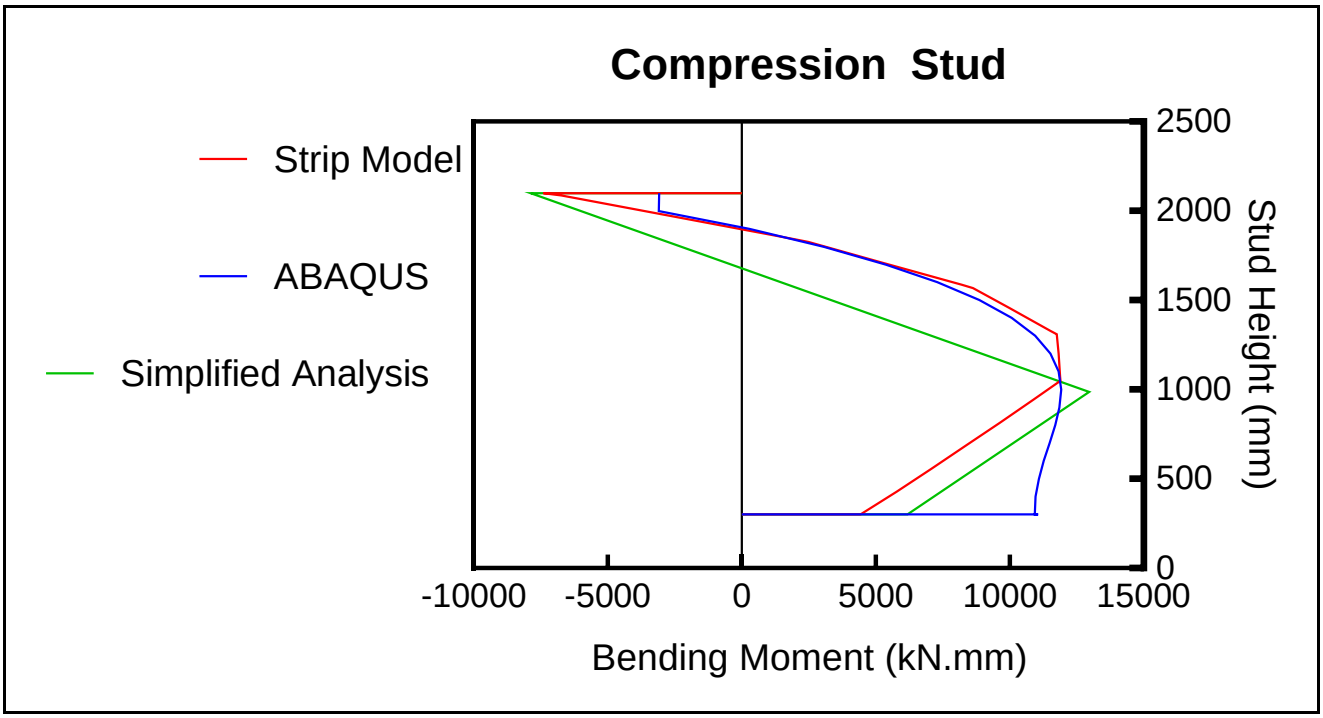
- Summing forces in Figure 7.25:
  - $\sum M_B = 0 \rightarrow A_x = D_x = \frac{140+76.8}{1800} = 0.120444$
  - $\sum F_x = 0 \rightarrow \mu = \frac{16650}{0.120444+0.120444} = 69119.25$
- Recalculate the moments after multiplying by the proportionality factor μ:
  - $(M)_{AB} = (M)_{DC} = 9676.5\ kN.mm$
  - $(M)_{BA} = (M)_{CD} = 5309\ kN.mm$
  - $A_x = D_x = 8.325\ kN$
  - $V_c = D_y = -8.9\ kN$
  - $V_B = A_y = 8.9\ kN$

Step 6: Using the principle of superposition, obtain the force and moment demand for each stud.

The results are compared with the finite element and analytical model results and displayed in Figure 7.26 & Figure 7.27:

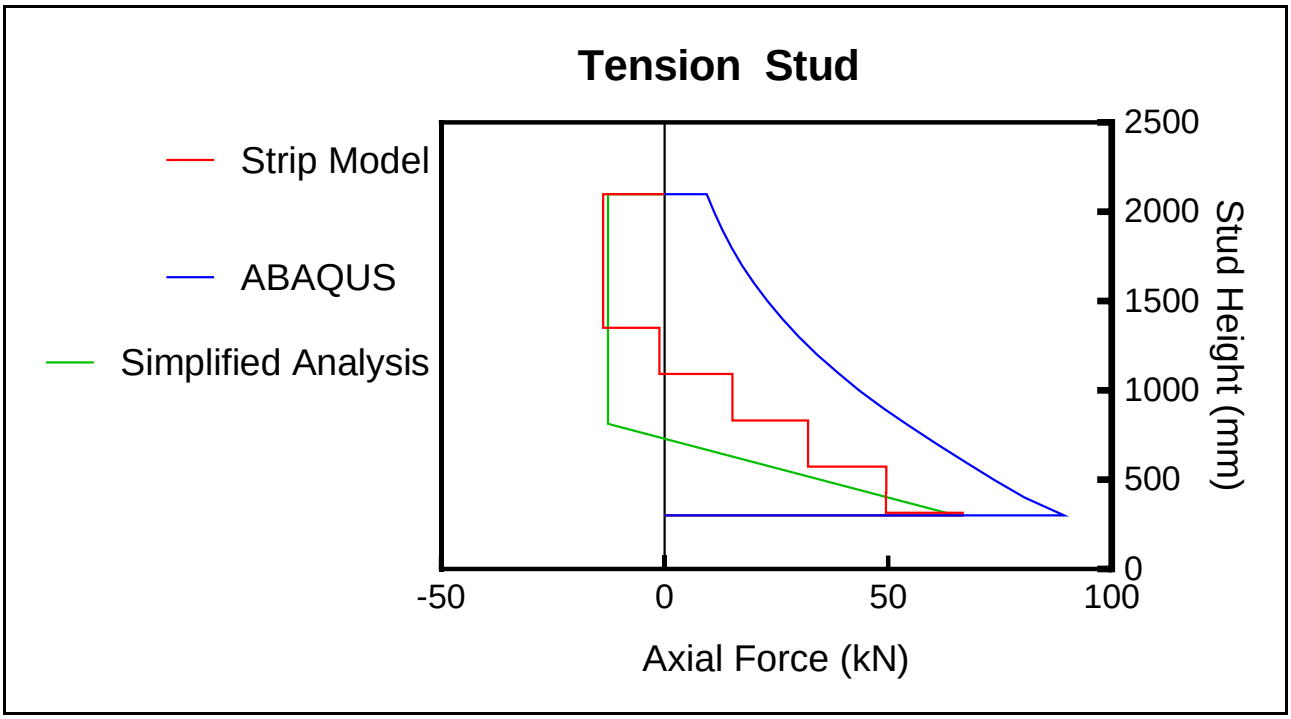


(a)

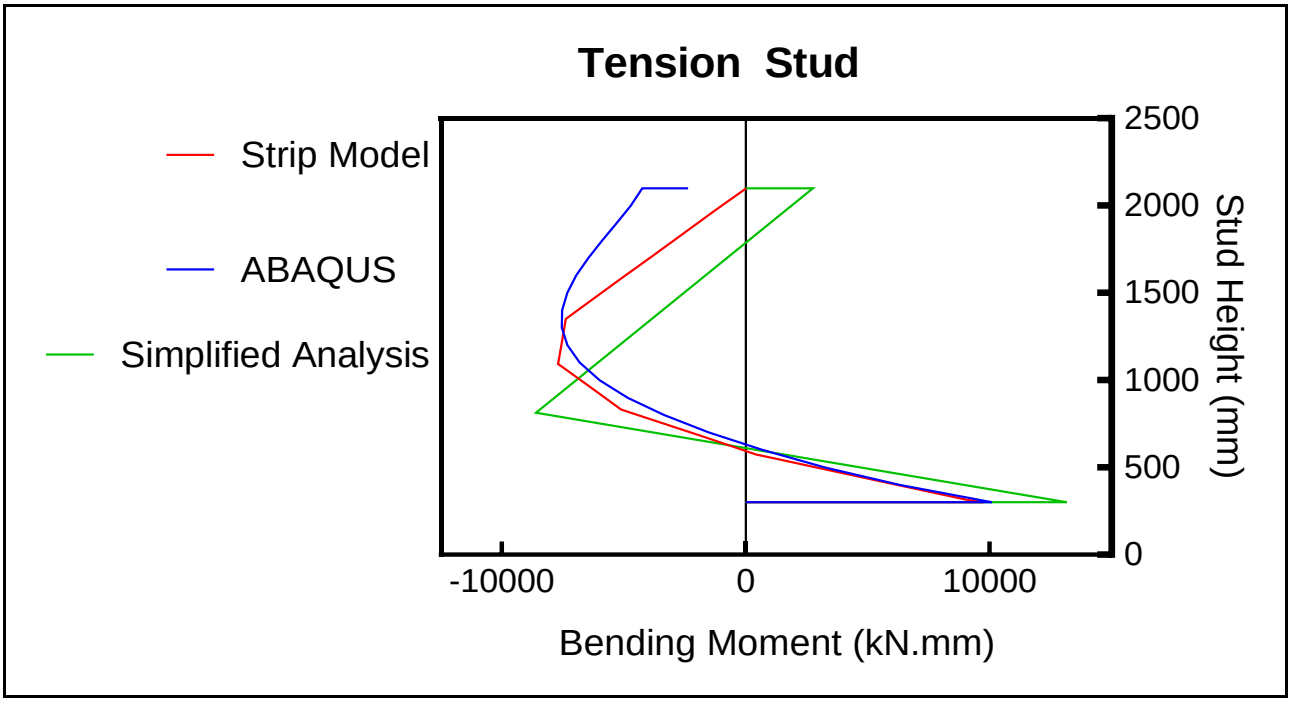


(b)

Figure 7.26: Comparison between axial force diagram (a) and bending moment diagram (b) for the compression stud.



(a)



(b)

Figure 7.27: Comparison between axial force diagram (a) and bending moment diagram (b) for the tension stud.

Table 17: Comparison of results (force values in *kN*, bending moment values in *kN.mm*)

Method	P_{MAX}	% Error	$+M_{MAX}$	% Error	$-M_{MAX}$	% Error
Compression Stud						
ABAQUS	-133	-	11824	-	-3100	-
Analytical	-149	12	11918	0.8	-7393	138.5
Simplified	-137	2.9	12961	9.6	-7864	153.6
Tension Stud						
ABAQUS	89.5	-	10090	-	-7535	-
Analytical	66.77	25	10174	0.83	-8593	14
Simplified	65.2	27.2	13159	30.4	-7687	2

Similar to the results of Section 7.5, the simplified analysis predicts the axial force and bending moments in the compression stud quite accurately however underestimates the axial force in the tension stud. The model of the sheathing pull-in forces that's displayed in Figure 7.17 only considers the elements that participate in the tension field action. In reality, the portion of the sheathing that's not included in the partial tension field induce stresses on the stud that are not considered in this method. Moreover, the shear transferred to the stud from the top track acts in an opposite direction to the axial tensile forces, which resulted in the incorrect estimation of the axial forces in the tension studs.

Chapter 8: Conclusions and Recommendations

8.1 Conclusions

In this research project, three innovative, higher-capacity cold-formed steel shear wall configurations were proposed and investigated. A concentrically-sheathed shear wall with built-up hat section studs, a concentrically-sheathed shear wall with an intermediate stud and built-up hat section studs, and a diagonally strapped concentric sheathed shear wall with built-up hat section studs. The preliminary testing program was conducted in collaboration with Chongqing University and consisted of monotonic and cyclic testing for the shear wall specimen, coupon material tests and cyclic loading tests for connection assemblies in double shear. High-fidelity shell finite element models were established for each specimen and validated against the experimental results. Due to severe convergence issues, the explicit solver was employed to carry out the numerical analyses of the shear wall specimen. The calibrated numerical models were then used to conduct an extensive parametric study, where several factors such as screw spacing and aspect ratio were assessed. Finally, using numerically calibrated expression derived from the parametric analyses, two preliminary design methods to determine the axial force and bending moment demand on the boundary studs are proposed. An analytical method that's based on the strip model formulation, and a simplified, hand-based analysis method.

Based on the results and observations of this study, the main conclusions can be summarized as follows:

1) The major failure mode that was encountered in all shear wall specimens was the buckling of the end studs. This type of failure is undesirable as it prevents the sheathing, the main energy dissipating element, from reaching its full capacity.
2) The tested specimens attained higher loads (almost double) and drifts than the shear walls approved in the standards.
3) The diagonally-strapped specimen displayed the highest shear resistance, conversely it displayed the poorest ductility.
4) The addition of an intermediate stud to the concentric-sheathed specimen significantly increased the ductility, cyclic stiffness, and energy absorption capacity of the shear wall and as a result, the concentric-sheathed specimen with an intermediate stud demonstrated the best seismic behaviour.
5) The bolt bearing equation (Eq. (2.7)) showed acceptable agreement with the connection test results for screws in double shear.
6) The finite element models correlated well with the experimental results in terms of peak load, energy dissipation capacity and failure modes for the concentric-sheathed specimens. Unfortunately, the diagonally-strapped model displayed poor agreement with the experimental results, particularly due to the screw modelling technique and the unique failure mode (failure of the hold-down) encountered in the experiment.
7) Regarding the parametric analysis, a non-dimensional parameter β was defined such that $\beta = (t_{sheathing} / t_{studs})$. If the ratio is limited to $\beta < 0.2$, then the stud buckling failure mode is eliminated and a uniform tension field develops across the height of the panel.

8) To reduce the forces on the studs, two configurations were proposed where the sheathing is attached to the inner flange of the built-up studs. Through implementing these changes, the performance of the wall can be improved without increasing the cost.
9) The results of the analytical and simplified design method demonstrated strong correlation with the shell finite element results, indicating that both methods can be used for preliminary design purposes.

8.2 Recommendations for Future Work

The research on higher-capacity cold-formed steel shear walls is still in its early phases. The work presented in this report supplied additional data for the concentric-sheathed wall configuration. Still, there are many aspects that can be explored in order to advance the field of CFS shear walls:

- Perhaps the most critical challenge that was faced in this research was the premature buckling of the studs. Seeing how this phenomenon was also encountered in other testing program, future research should explore different construction and design strategies to alleviate this problem.
- The effects of gravity loads were not included in the testing program. In actual engineering applications, the shear wall is expected to resist lateral loads in conjunction with gravity loads. The addition of gravity loads will contribute to the axial forces on the studs on the compression side. Hence, it is recommended for future research to consider gravity loads when testing higher-capacity CFS shear walls.
- The bolt-bearing equation (Eq. (2.7)) was compared to a limited number of tests in this research. Since the screw capacity is a major contributor to the shear resistance

of the shear walls, further testing is recommended in order to substantiate the accuracy of the equation.

- Another challenge that was faced in this research was the numerical modelling of the screw connections. The screw connection tests revealed that the screw's behaviour is characterized by hysteresis loops that are severely pinched. The pinching4 material model is able to replicate the level of pinching and strength degradation, however it is currently only compatible with the implicit solver. Future works could look into converting the pinching4 material model into a version compatible with the explicit solver since the explicit solver handles complex buckling problems, a phenomenon commonly encountered when modelling CFS structures, with relative ease.

References

[1] Y. Xinmei, "Research on the Seismic Performance of Multi-storey Cold-formed Steel-Steel Plate Shear Wall Structure," PhD dissertation, Chang'an University, Xi'an, China, 2021.

[2] G. Alshamsi, L. Xu, S. Yu, Y. Xinmei and Z. Yuxuan, "Effects of Connector Modelling on Explicit Shell Finite Element Models of Cold-formed Steel Shear Walls," in *The Fourteenth International Conference on Computational Structures Technology*, Montpellier, France, 2022.

[3] G. Alshamsi, L. Xu, Y. Shi, Y. Xinmei and Z. Yuxuan , "Experimental & Numerical Investigation of an Innovative, High Capacity Cold-Formed Steel Shear Wall," in *Cold-Formed Steel Research Consortuim Colloquium*, 2022.

[4] W. Yu and R. A. Laboube, Cold-Formed Steel Design, 4th ed., New Jersey: John Wiley & Sons, Inc., 2010.

[5] R. Serette, J. Encalada, G. Hall, B. Matchen, N. Hoang and A. Williams, "Additional Shear Wall Values for Light Wegith Steel Framing," Santa Clara, CA, 1997.

[6] J. C. Wu, "Performance of Centre-sheathed Cold-formed Steel Framed Shear Walls Phase 2," Master's Thesis, Department of Civil Engineering and Applied Mechanics, McGill University, Montreal, Quebec, 2019.

[7] AISI-D113-19, "Cold-Formed Steel Shear Wall Design Guide," Washington, DC, USA, 2019.

[8] N. Yanagi and C. Yu, "Effective Strip Method for the Design of Cold-Formed Steel Framed Shear Wall with Steel Sheet Sheathing," *Journal of Structural Engineering,* vol. 140, no. 4, April 2014.

[9] National Research Council of Canada, "National Building Code of Canada," Ottawa, ON, Canada, 2020.

[10] AISI-S400, "North American Standard for Seismic Design of Cold-Formed Steel Structural Systems," American Iron and Steel Institute, Washington, USA, 2020.

[11] V. Santos and C. Rogers, "Higher Capacity Cold-Formed Steel Sheathed and Framed Shear Walls for Mid-rise Buildings: Part 1," Montreal, Quebec, Canada, 2017.

[12] V. Briere and C. Rogers, "Higher Capacity Cold-Formed Steel Sheathed and Framed Shear Walls for Mid-rise Buildings: Part 2," Montreal, Quebec, Canada, 2017.

[13] R. Rizk and C. Rogers, "Higher Strength Cold-Formed Steel Framed / Steel Shear Walls for Mid-Rise Construction," McGill University, Quebec, Canada, 2017.

[14] ABAQUS (2022), "Analysis User's Manual," Dassault Systemes, Inc., 2022.

[15] R. Park, "Evaluation of Ductility of Structures and Structural Assemblages from Laboratory Testing," *Bulletin of the New Zealand National Society for Earthquake Engineering ,* vol. 22, no. 3, pp. 155-166, 1989.

[16] D. J. Webster, "The Inelastic Seismic Response of Steel Plate Shear Wall Web Plates and their Interaction with the Vertical Boundary Members," PhD Thesis, Department of Civil and Environmental Engineering, University of Washington, Seattle, Washington, 2013.

[17] A. Astaneh-Asl, "Seismic Behaviour and Design of Steel Shear Walls," Structural Steel Education Council, California, 2001.

[18] X. Qian and A. Astaneh-Asl, "Development of a High-Performance Steel Plate Shear Wall System with an Innovative Gusset Plate Moment Connection," Report Number: UCB/CEE-STEEL-2017/01, University of California at Berkeley, Berkeley, California, 2017.

[19] L. J. Thornburn, G. L. Kulak and C. J. Montgomery, "Analysis of Steel Plate Shear Walls," Edmonton, Alberta, 1983.

[20] P. A. Timler and G. L. Kulak, "Experimental Study of Steel Plate Shear Walls," The University of Alberta, Edmonton, Alberta, 1983.

[21] E. W. Tromposch and G. L. Kulak, "Cyclic and Static Behaviour of Thin Panel Steel Plate Shear Walls," The University of Alberta, Edmonton, Alberta, 1987.

[22] J. W. Berman, "Seismic Behaviour of Code Designed Steel Plate Shear Walls," *Engineering Structures,* vol. 33, no. 1, pp. 230-244, 2011.

[23] K.-C. Tsai, C.-H. Li, C.-H. Lin, C.-Y. Tsai and Y.-J. Yu, "Cyclic Tests of Four Two-Story Narrow Steel Plate Shear Walls - Part 1: Analytical Studies and Specimen Design," *Earthquake Engineering and Structural Dynamics,* vol. 39, no. 7, pp. 775-799, 2010.

[24] J. W. Berman, "Capacity Design of Vertical Boundary Elements in Steel Plate Shear Walls," *Engineering Journal,* vol. 45, pp. 57-72, 2008.

[25] J. Berman and M. Bruneau, "Plastic Analysis and Design of Steel Plate Shear Walls," *Journal of Structural Engineering,* vol. 129, no. 11, 2003.

[26] M. Bruneau, C.-M. Uang and R. Sabelli, Ductile Design of Steel Structures, McGraw Hill, 2011.

[27] H. Wagner, "Flat Sheet Metal Girders with Very Thin Metal Webs, Part I - General Theories and Assumptions," National Advisory Commitee for Aeronautics, Technical Memorandum No. 604, 1931.

[28] Canadian Standards Association S16:19, "Design of Steel Structures," CSA Group, Mississauga, ON, Canada, 2019.

[29] ANSI/AISC 341-16, "Seismic Provisions for Structural Steel Buildings," American Institute for Steel Construction, Chicago, Illinois, 2016.

[30] M. R. Behbahanifard, G. Y. Grondin and A. E. Elwi, "Experimental and Numerical Investigation of Steel Plate Shear Wall," Univeristy of Alberta, Edmonton, Calgary, 2003.

[31] R. G. Driver, G. L. Kulak, D. J. L. Kennedy and A. E. Elwi, "Cyclic Test of Four-Story Steel Plate Shear Wall," *Journal of Structural Engineering,* vol. 124, no. 2, pp. 111-221, 1998.

[32] AISI Lateral Standard, "Standard for Cold-Formed Steel Framing - Later Design, 2004 edition," American Iron and Steel Institute, Washington, DC, 2004 .

[33] C. Yu, H. Vora, T. Dainard, J. Tucker and P. Veetvkuri, "Steel Sheet Sheathing Options for Cold-Formed Steel Framed Shear Wall Assemblies Providing Shear Resistance," University of Texas, Denton, Texas, 2007.

[34] N. Balh and C. A. Rogers, "Development of Canadian Seismic Design Provisions for Steel Sheathed Shear Walls," Montreal, Quebec, Canada, 2010.

[35] C. Ong-Tone and C. A. Rogers, "Tests and Evaluation of Cold-Formed Steel Frame/Steel Sheathed Shear Walls",," Montreal, Quebec, Canada, 2009.

[36] J. Ellis, "Shear Resistance of Cold-Formed Steel Framed Shear Wall Assemblies using CUREE Test Protocol," Simpson Strong-Tie Co., Inc., 2007.

[37] Federal Emergency Managment Agency, "Qualitative of Building Seismic Performance Factors," Applied Technology Council, Redwood City, California, 2009.

[38] AISI S213-07, "North American Standard for Cold-Formed Steel Framing - Lateral Design," American Iron and Steel Institute , Washington, USA, 2007.

[39] I. Shamim, "Seismic Design of Lateral Force Resisting Cold-Formed Steel Framed (CFS) Structures," PhD Thesis, McGill University, Montreal, 2012.

[40] I. Shamim and C. A. Rogers, "Numerical Evaluation: AISI S400 Steel-Sheathed CFS Framed Shear Wall Seismic Design Method," *Thin-Walled Structures,* pp. 48-59, 2015.

[41] L. Xu and J. Martinez, "Strength and Stiffness Determination of Shear Wall Panels in Cold-Formed Steel Framing," *Thin-Walled Structures,* no. 44, pp. 1084-1095, 2006.

[42] G. Brandt, "Rapid Determination of Ultimate Strength of Eccentrically Loaded Bolt Groups," *Engineering Journal,* vol. 19, pp. 94-100, 1982.

[43] CSA S136 (R2021), "North American Specification for the Design of Cold-formed Steel Structural Members," CSA Group, Toronto, Ontario, Canada, 2016.

[44] B. W. Schafer, Z. Li and C. D. Moen, "Computational Modeling of Cold-Formed Steel," *Thin-Walled Structures,* vol. 48, no. 10-11, pp. 752-762, 2010.

[45] ADINA R&D Inc., "ADINA Theory and Modeling Guide," Watertown, MA, USA, 2008.

[46] N. Usefi, P. Sharafi and H. Ronagh, "Numerical Models for Lateral Behaviour Analysis of Cold-Formed Steel Framed Walls: State of the Art, Evaluation and Challenges," *Thin-Walled Structures ,* pp. 252-285, 2019.

[47] C. Ding, "Monotonic and Cyclic Simulation of Screw-Fastened Connections for Cold-Formed Steel Framing," Blacksburg, VA, 2015.

[48] F. Mckenna, "OpenSees: A Framework for Earthquake Engineering Simulation," *Computing in Science and Engineering,* vol. 13, no. 4, pp. 58-66, 2011.

[49] L. N. Lowes, N. Mitra and A. Altoontash, "A Beam-Column Joint Model for Simulating the Earthquake Response of Reinforced Concrete Frames," 2003.

[50] H. H. Ngo, "Numerical and Experimental Studies of Wood Sheathed Cold-Formed Steel Framed Shear Walls," Baltimore, Maryland, 2014.

[51] P. Lui, K. D. Peterman and B. W. Schafer, "Test Report on Cold-formed Steel Shear Walls," Structural Stability Research Council, Grapevine, Texas, (2012).

[52] Z. Zhang and B. Schafer, "Simulation of Steel Sheathed Cold-Formed Steel Framed Shear Walls," in *Proceedings of the Annual Stability Conference Structural Stability Research*, Missouri, USA, 2019.

[53] I. Rouaz, N. Bourahla and S. Kechidi, "Numerical Evaluations of Shear Strength of CFS Shear Wall Panels for Different Height-to-width Ratios," *Journal of Materials and Engineering Structures,* pp. 399-417, 2018.

[54] W.-F. Chen, Practical Analysis for Semi-rigid Frame Design, London: World Scientific, 2000.

[55] G. R. Monforton and T. Wu, "Matrix Analysis of Semi-Rigid Connected Frames," *Journal of the Structural Division,* vol. 89, no. 6, 1963.

[56] H. Cross, "Analysis of Continuous Frames by Distributing Fixed-End Moments," *Transactions of the American Societ of Civil Engineers,* vol. 96, no. 1, 1930.

[57] R. C. Hibbeler, Structural Analysis, Pearson Education, Inc., 2018.

[58] JGJ 227-2011, "Technical Specification for Low-Rise Cold-Formed Thin-Walled Steel Buildings," Ministry of Housing and Urban-Rural Development, Beijing, 2011 .

[59] GB/T 228.1-2010, "Metallic Materials-Tensile Testing-Part 1: Method of Test at Room Temperature," Standardization Administration of China, Beijing, 2010 .

[60] JGJ 101-15, "Specification of Testing Methods for Earthquake Resistant Building," Ministry of Housing and Urban-Rural Development , Beijing, 2015.

[61] G. C. Foliente, "Issues in Seismic Performance Testing and Evaluation of Timber Structural Systems," in *International Wood Engineering Conference*, New Orleans, LA, 1996.

[62] ASTM, "Standard Test Methods for Cyclic (Reversed) Load Test for Shear Resistance of Vertical Elements of the Lateral Force Resisting Systems for Buildings," West Conshohocken, PA, 2019.

[63] X. Liu, W. Zhang, C. Yu, Y. Li, Z. Jiang and S. Yu, "Experimental Study on Cold-formed Steel Shear Walls with Different Corrugated Steel Sheathings.," *Journal of Constructional Steel Research,* vol. 199, 2022.

[64] D. A. Graham, D. M. Carradine, D. A. Bender and J. D. Dolan, "Performance of Log Shear Walls Subjected to Monotonic and Reverse-Cyclic Loading," *Journal of Structural Engineering,* vol. 136, pp. 37-45, 2010.

[65] R. J. Boulbes, Troubleshooting Finite-Element Modeling with ABAQUS: With Applications in Structural Engineering Analysis, Cham, Switzerland: Springer International Publishing, 2020.

[66] R. D. Cook, D. S. Malkus, M. E. Plesha and R. J. Witt, Concepts and Applications of Finite Element Analysis, Toronto: John Wiley & Sons, 1989.

[67] L. L. Daryl, A First Course in the Finite Element Method, Toronto, Ontario: Thomson, 2007.

[68] S. R. Wu and L. Gu, Introduction to the Explicit Finite Element Method for Nonlinear Transient Dynamics, New Jersey: John Wiley & Sons, 2012.

[69] E. Ellobody, R. Feng and B. Young, Finite Element Analysis and Design of Metal Structures, Waltham, MA: Buttworth-Heinemann, 2014.

[70] N. Blind and R. Ostlund, "Analysis of an Engine Frame Subjected to Large Imbalance Loads," Department of Applied Physics and Mechanical Engineering, Lulea University of Technology, Lulea, Sweden, 2009.

[71] B. J. Mac Donald, Practical Stress Analysis with Finite Elements, Dublin, Ireland: Glasnevin Publishing, 2011.

[72] K. Cai and H. Yuan, "Testing, Numerical and Analytical Modelling of Self-drilling Screw Connections Between Thin Steel Sheets in Shear," *Thin-Walled Structures,* vol. 182, 2023.

[73] H. El Jisr, A. Elkady and D. G. Lignos, "Hysteretic Behaviour of Moment-Resisting Frames Considering Slab Restraint and Framing Action," *Journal of Structural Engineering,* vol. 146, no. 8, 2020.

[74] T. Belytschko and J. S.-J. Ong, "Hourglass Control in Linear and Nonlinear Problems," *Computer Methods in Applied Mechanics and Engineering,* vol. 43, pp. 251-276, 1984.

[75] J. R. Stewart, A. S. Gullerud and M. W. Heinstein, "Solution Verification for Explicit Transient Dynamics Problems in the Presence of Hourglass and Contact Forces," *Computer Methods in Applied Mechanics and Engineering,* vol. 195, no. 13-16, pp. 1499-1516, 2006.

[76] O.-P. Jacquotte and J. T. Oden, "Analysis of Hourglass Instabilities and Control in Underintegrated Finite Element Methods," *Computer Methods in Applied Mechanics and Engineering,* vol. 44, no. 3, pp. 339-363, 1984.

[77] N. Ravichandran, K. Muraleetharan, L. M. Taylor and K. D. Mish, "Uniform Gradient Element Formulation with Hourglass Control Scheme for Solving Fully Coupled Finite-Element Equations for Saturated Soils," *International Journal of Geomechanics ,* vol. 16, no. 1, 2016.

[78] R. C. Hibbeler, Mechanics of Materials, New Jersey: Pearson Prentice Hall, 2014.

[79] A. R. Badr, H. H. Elanwar and S. A. Mourad, "Numerical and Experimental Investigation on Cold-formed Walls Sheathed by Fiber Cement Board," *Journal of Construction Steel Research,* vol. 158, pp. 366-380, 2019.

[80] F. Dunne and N. Petrinic, Introduction to Computational Plasticity, Oxford: Oxford University Press, 2005.

[81] M. Daoud, J. Chatelain and A. Bouzid, "Effect of Rake Angle on Johnson-Cook Material Constants and their Impact on Cutting Process Parameters of AI2024-T3 Alloy Machine Simulation," *The International Journal of Advanced Manufacturing Technology,* vol. 81, pp. 1987-1999, 2015.

[82] B. Schafer and T. Pekoz, "Geometric Imperfections and Residual Stresses for Use in the Analytical Modeling of Cold-Formed Steel Members," in *13th International Specialty Conference on Cold-Formed Steel Structures*, Missouri, 1996.

[83] C. Souto, A. Menghini, A. Diaz, J. M. Manso, A. Jesus and C. A. Castiglioni, "Determination of Manufacturing Residual Stresses in Cold-Formed Thin-Walled Steel Profiles," *Thin-Walled Structures,* vol. 180, 2022.

[84] H. Liu, W. Wang, L. Deng and Y. He, "Inelastic Buckling Analysis of Cold-formed Steel Members with Residual Stresses Based on CFSM," *Structures,* vol. 56, 2023.

[85] M. H. Kharrazi, "Rational Method for Analysis and Design of Steel Plate Walls," PhD Thesis, Department of Civil Engineering, University of British Columbia, Vancouver, 2005.

[86] CSSBI, "Sheet Steel Facts 10," Canadian Sheet Steel Building Institute, Cambridge, Ontario, 2012.

[87] Z. He, S. Peng, X. Zhou, Z. Li, G. Yang and Z. Zhang, "Design Recommendations of Cold-Formed Steel Built-up Sections Under Concentric and Eccentric Compression," *Journal of Constructional Steel Research,* vol. 212, 2024.

[88] CSSBI, "Design of Steel Deck Diaphragms," Canadian Steel Sheet Building Institute, Cambridge, Ontario, 2019.

[89] Computers & Structures, Inc., "CSI Analysis Reference Manual," Berkeley, California, USA, 2016.

[90] W. Chen and E. M. Lui, Handbook of Structural Engineering, Boca Raton, Florida: CRC Press, 2005.

Appendices

Appendix A: Sample Calculations

This section details the calculations involved in estimating the nominal shear resistance of the specimen GD-06 using the methods that were presented in Chapter 7.

A.1 Effective Strip Method [8]:

$$V_n = min\begin{cases} 1.33P_n cos\alpha \\ 1.33F_y w_e t_{sh} cos\alpha \end{cases} \quad \text{(A.1)}$$

where;

- P_n = Nominal shear strength [resistance] of screw connections within the effective strip width, w_e on the steel sheathing
- $\alpha = arctan(h/w)$
  - h = Shear wall height
  - w = Shear wall length
- t_{sh}= Design thickness of steel sheathing
- F_y= Yield stress of steel sheathing
- $w_e = w_{max}$ when λ ≤ 0.0819 (A.2a)

  = ρw_{max} when λ > 0.0819 (A.2b)

where;

  - w_{max}= $w/\sin\alpha$ (A.3)
  - ρ = $\frac{1-0.55(\lambda-0.08)^{0.12}}{\lambda^{0.12}}$ (A.4)
  - λ = $1.736\ \frac{\alpha_1\alpha_2}{a\beta_1\beta_2\beta_3^2}$ (A.5a)

    where;

- $\alpha_1 = \frac{F_{ush}}{310.3}$ (A.5b)
- $\alpha_2 = \frac{F_{uf}}{310.3}$ (A.5c)
- $\beta_1 = \frac{t_{sh}}{0.457}$ (A.5d)
- $\beta_2 = \frac{t_f}{0.457}$ (A.5e)
- $\beta_3 = \frac{s}{152.4}$ (A.5f)
- F_{ush} = Tensile strength of steel sheet sheathing
- F_{uf} = Minimum tensile strength of framing materials
- t_{sh} = Design thickness of steel sheet sheathing
- t_f = Minimum design thicknesses of framing materials
- a = Wall aspect ratio
- s = screw spacing

Step 1: Determine the effective width of the strip:

$a = (2400)/(1210) = 1.9$

$\alpha = arctan(a) = arctan(1.9) = 63.2°$

$W_{max} = w/sin\alpha = (1210)/sin(63.2) = 1{,}355.6\ mm$

$\alpha_1 = \frac{293.33}{310.3} = 0.945$

$\alpha_2 = \frac{530}{310.3} = 1.708$

$\beta_1 = \frac{0.8}{0.457} = 1.75$

$\beta_2 = \frac{2.5}{0.457} = 5.47$

$\beta_3 = \frac{50}{152.4} = 0.328$

$\lambda = 1.736\ \frac{(0.945)(1.708)}{(1.9)(1.75)(5.47)(0.328)} = 0.304$

$\lambda = 0.304 > 0.0819; therefore \;\; W_{max} = \rho w_{max}$

$\rho = \frac{1-0.55(0.304-0.08)^{0.12}}{0.304^{0.12}} = 0.6234$

$\boldsymbol{W_{max} = (0.6234)(1355.6) = 845\ mm}$

Step 2: Determine the nominal shear capacity of individual connections:

a) Shear strength limited by tilting and bearing **(CSA S-136 [43] section J4.3.1)***:*

$\frac{t_2}{t_1} = \frac{0.8}{2.5} = 0.32 \leq 1.0$; t_1 is the thickness of the member in contact with the screw head; t_2 is the thickness of the member not in contact with the screw head or washer.

$$P_{nv} = minimum \begin{cases} 4.2(t_2^3 d)^{\frac{1}{2}} F_u = 4.2(0.8^3 \times 5.5)^{\frac{1}{2}} \times 293.33 = \mathbf{2.067}\ kN \\ 2.7 t_1 d F_{u1} = 2.7 \times 2.5 \times 5.5 \times 530 = 19.676\ kN \\ 2.7 t_2 d F_{u2} = 2.7 \times 0.8 \times 5.5 \times 293.33 = 3.5\ kN \end{cases}$$

b) Connection shear limited by shear in screw*:*

$P_{nv} = 8.36\ kN$ (ST 5.5 Beita Brand screws)

c) Connection Shear limited by end distance:

$$P_{ns} = teF_u \qquad \text{(A.6)}$$

where; $e = \frac{w_f}{2cos\alpha}$ (A.7)

$e = \frac{50}{2cos63.2^\circ} = 55.5; P_{ns} = (2.5) \times (55.5) \times (530) = 74\ kN$

Finally, the shear wall resistance can be calculated as the minimum of the nominal capacity of the fasteners within the effective strip (figure 2) or the sheathing yield capacity as follows:

$$\therefore V_n = min\begin{cases} 1.33P_n cos\alpha = 1.33 \times 56.4 \times 2{,}067 \times cos63.2° = 70\ kN \\ 1.33F_y w_e t_{sh} cos\alpha = 1.33 \times 167 \times 845 \times 0.8 \times cos63.2° = \mathbf{68\ kN} \end{cases}$$

Where in the equation above, the term P_n (connection capacity) is calculated from the following expression:

$$\left(\frac{W_e}{2s\ sin\alpha} P_{ns,s} + \frac{W_e}{2s\ cos\alpha}\ P_{ns,t} + P_{ns,t\&s}\right) \times 2 \qquad \text{(A.8)}$$

The connection capacity is doubled since the tracks contain two rows of screws and the studs contain two columns of screws.

A.2 Modified Effective Strip Method [11], [12]:

The modified strip method (MESM) assumes that all the screws participate in the shear resistance of the walls and that each screw's capacity is now based on the double shear bolt connection bearing resistance [43]. The shear resistance of a wall using the MESM can be computed as:

$$S_{n(MESM)} = (\frac{n}{2} P_{nb} cos\alpha)/w \qquad \text{(A.9)}$$

$$P_{nb} = C m_f d t F_u \qquad \text{(A.10)}$$

where;

- n = total number of screws of the wall
- P_{nb} = screw fastener's nominal bearing capacity
- a = angle given by the wall's aspect ratio
- w = width of the wall
- C = bearing factor, determined from **Table J3.3.1-1** [43].
- m_f = modification factor for type of bearing connection, **Table J3.3.1-2** [43].

$$P_{nb} = 3.0 \times 1.33 \times 5.5 \times 0.8 \times 293.33 = \mathbf{5,144\ N}$$

$$S_{n(MESM)} = \frac{\frac{216}{2} \times 5144 \times cos63.2°}{1210} = 207\frac{kN}{m} = 207 \times 1.21 = \mathbf{250.47\ kN}$$

A.3 Special Steel Plate Walls:

According to [25], the shear resistance of the infill plates of a steel plate wall can be taken as:

$$V_r = 0.5F_y wLsin2\alpha \quad \text{(A.11)}$$

where;

- F_y = yield strength of the infill plate
- w = thickness of the wall
- L = centre-to-centre distance between columns.
- α = angle of inclination which is determined from the following expression and is limited between 38° and 45°:

$$\tan^4 \alpha = \frac{1 + \frac{wL}{2A_c}}{1 + wh(\frac{1}{A_b} + \frac{h^3}{360I_cL})}$$

where;

  - h = height of the wall
  - A_b = beam cross-sectional area
  - A_c = column cross-sectional area

- I_c = moment of inertia of the column

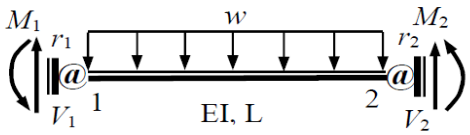
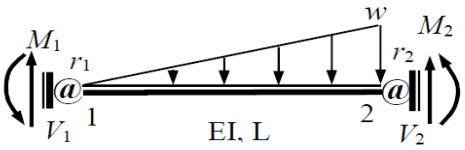
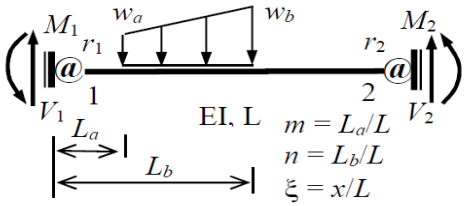
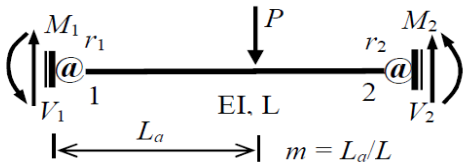
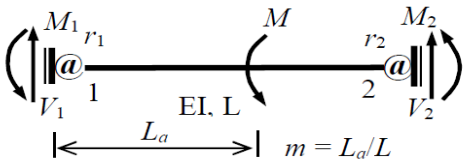
$$\tan^4 \alpha = \frac{1 + \frac{0.8 \times 1050}{2 \times 1675}}{1 + 0.8 \times 2100(\frac{1}{951} + \frac{2100^3}{360 \times 1050 \times 5663490})} = 30.7°$$

Therefore, α is taken as 38°.

$$V_r = 0.5 \times 167 \times 0.8 \times 1050 \times \sin(2 \times 38°) = \quad \boldsymbol{68.1\ kN}$$

Appendix B: Semi-rigid Structures and Beam Design Tables [90]:

Table 18: End-reactions of semi-rigid members.

Member Span Loads	Member End-Reactions
	$M_1 = (wL^2/12)[3r_1(2-r_2)/(4-r_1r_2)]$ $M_2 = -(wL^2/12)[3r_2(2-r_1)/(4-r_1r_2)]$ $V_1 = (M_1+M_2)/L + wL/2$ $V_2 = -(M_1+M_2)/L + wL/2$
	$M_1 = (wL^2/30)[r_1(7-4r_2)/(4-r_1r_2)]$ $M_2 = -(wL^2/60)[r_2(16-7r_1)/(4-r_1r_2)]$ $V_1 = (M_1+M_2)/L + wL/6$ $V_2 = -(M_1+M_2)/L + wL/3$
	$M_1 = \frac{r_1}{4-r_1r_2}\left(\frac{L^2}{60}\right)(n-m)\{w_a(2+r_2)[3(n-m)^3+15m(n^2+m^2)]$ $+10w_a(4-r_2)(n+2m)-30w_a[(n+m)^2+2m^2]$ $+w_b(2+r_2)[3(m-n)^3+15n(m^2+n^2)]$ $+10w_b(4-r_2)(m+2n)-30w_b[(m+n)^2+2n^2]\}$ $M_2 = \frac{r_2}{4-r_1r_2}\left(\frac{L^2}{60}\right)(n-m)\{w_a(2+r_1)[3(n-m)^3+15m(n^2+m^2)]$ $-20w_a(1-r_1)(n+2m)-15r_1w_a[(n+m)^2+2m^2]$ $+w_b(2+r_1)[3(m-n)^3+15n(m^2+n^2)]$ $-20w_b(1-r_1)(m+2n)-15r_1w_b[(m+n)^2+2n^2]\}$ $V_1 = \frac{(M_1+M_2)}{L}+\frac{(n-m)L}{6}[w_a(3-2m-n)+w_b(3-m-2n)]$ $V_2 = -\frac{(M_1+M_2)}{L}+\frac{(n-m)L}{6}[w_a(2m+n)+w_b(m+2n)]$
	$M_1 = \frac{r_1}{4-r_1r_2}m(1-m)[2(2-m)-r_2(1+m)]PL$ $M_2 = -\frac{r_2}{4-r_1r_2}m(1-m)[2(1+m)-r_1(2-m)]PL$ $V_1 = (M_1+M_2)/L + P(1-m)$ $V_2 = -(M_1+M_2)/L + Pm$
	$M_1 = -\frac{r_1}{4-r_1r_2}[6(1-m)^2-2+r_2(3m^2-1)]M$ $M_2 = -\frac{r_2}{4-r_1r_2}[2(3m^2-1)-3r_1(1-m)^2-r_1]M$ $V_1 = -V_2 = (M+M_1+M_2)/L$